Title

Optogenetic control of morphogen signaling in embryonic stem cells

Author

Repina, Nicole Anne

Publication Date

2019

Optogenetic control of morphogen signaling in embryonic stem cells

by

Nicole Repina

A dissertation submitted in partial satisfaction of the

requirements for the degree of

Joint Doctor of Philosophy
with University of California, San Francisco

in

Bioengineering

in the

Graduate Division

of the

University of California, Berkeley

Committee in charge:

Professor David Schaffer, Chair
Professor Xavier Darzacq
Professor Todd McDevitt
Professor Laura Waller

Summer 2019

The dissertation of Nicole Repina, titled Optogenetic control of morphogen signaling in embryonic stem cells, is approved:

Chair ______________________ Date __________

______________________ Date __________

______________________ Date __________

______________________ Date __________

University of California, Berkeley

Optogenetic control of morphogen signaling in embryonic stem cells

Abstract

Optogenetic control of morphogen signaling in embryonic stem cells

by

Nicole Repina

Joint Doctor of Philosophy
with University of California, San Francisco in Bioengineering

University of California, Berkeley

Professor David Schaffer, Chair

The processes of cell proliferation, differentiation, migration, and self-organization during early embryonic development are governed by spatially and temporally varying morphogen signals. Such dynamic morphogen patterns drive cell fate specification at the proper location and time. However, current *in vitro* methods typically do not allow for precise, dynamic, spatiotemporal control of morphogen signaling and are thus insufficient to readily study how morphogen dynamics impact cell behavior. In embryonic stem cell (ESC) models for early development, for example, analogous tissue patterns spontaneously emerge but mechanistic insight into this self-organization has been limited. In this dissertation, we combine engineered methods for optogenetic stimulation and biological analysis to photoactivate Wnt/β-catenin signaling and to study morphogen dynamics and self-organization of human pluripotent stem cells.

First, we show that optogenetic Wnt/β-catenin pathway activation can be controlled at user-defined intensities, temporal sequences, and spatial patterns in human ESCs (hESCs). We expressed a fusion of the plant blue-light photoreceptor Cryptochrome 2 (Cry2) to the Wnt co-receptor LRP6 (the optoWnt system) in hESCs and induce Cry2-LRP6c oligomerization and subsequent canonical Wnt/β-catenin activation using novel engineered illumination devices for optogenetic photostimulation and light activation at variable amplitudes (LAVA). Such LAVA devices are a LED-based, programmable illumination system for photostimulation of multi-well plates that can be readily incorporated into the workflow of routine cell culture and allow controlled and quantitative spatiotemporal light patterning. We optimized the LAVA board optical configuration for illumination uniformity and achieve programmable photostimulation of independent wells of 24-well or 96-well culture plates kept in standard $37°C$ tissue culture incubators. Each well can be wirelessly programmed through a graphical user interface (GUI) at user-defined intensities ($0 - 20$ $\mu W mm^{-2}$, 0.005 $\mu W mm^{-2}$ resolution), temporal sequences (10 ms resolution), and spatial patterns (100 μm resolution). We demonstrate LAVA board performance by modulating the intensity, timing, and spatial location of canonical Wnt/β-catenin signaling in hESC cultures using the optoWnt optogenetic

system. We show that Wnt pathway activation and hESC differentiation is dose-responsive to light intensity and duration of illumination, and that spatial patterning can be used to simulate the embryonic, spatially polarized presentation of the Wnt ligand.

In parallel, we engineered a microscope capable of dynamic photostimulation and high-resolution imaging with structured illumination microscopy (SIM). A digital micromirror device (DMD) is used to project user-defined photostimulation sequences onto the sample with diffraction-limited spatial resolution (800 nm). For fluorescence imaging, a series of multi-spot patterns is projected onto the sample to reconstruct a high-resolution SIM image with a 2-fold resolution improvement over the diffraction limit. Such multi-color, user-defined photostimulation and SIM imaging (opto-SIM) allows live-cell timelapse imaging while localizing Wnt/β-catenin photoactivation to specific regions within hESC cultures. Unlike LED-based illumination devices, such as the LAVA board system, the opto-SIM system enables pattern projection at subcellular resolution. Furthermore, projected patterns can be dynamically updated based on feedback from measurements acquired during experiment progression. The opto-SIM system also enables temporal control of signaling at a resolution of 60 Hz, as well as 8-bit greyscale modulation to achieve dose-dependent optoWnt activation. Such flexibility in spatiotemporal patterning gives the unprecedented ability to stimulate stem-cell based model systems, organoids, or embryos with time-varying patterns of morphogen gradients.

Lastly, we implement optogenetic control of canonical Wnt signaling to determine whether differential Wnt signaling can model human gastrulation and lead to emergence of organized shape and structure through collective cell rearrangement. We achieve optogenetic control of Wnt signaling in hESCs by illuminating hESC cultures expressing the optoWnt system with LAVA devices. Wnt/β-catenin signaling was activated over a high dynamic range ($>$500-fold) and drove broad transcriptional changes and mesendoderm differentiation of human ESCs at high efficiency ($>$95% cells). Furthermore, activating Wnt signaling in subpopulations of ESCs in 2D and 3D cultures induced cell self-organization and morphogenesis reminiscent of human gastrulation, including changes in cell migration and epithelial to mesenchymal transition. We thus developed an hESC model for studying Wnt-mediated morphogenesis in early development. Using this gastrulation model in combination with transcriptomic analysis and single-cell migration studies, we show that Wnt signaling is sufficient for inducing self-organization of cells in an EMT-dependent manner. Our findings thus reveal an instructive role for Wnt in directing cell patterning in this ESC model for early embryogenesis.

In summary, we developed and utilized engineered methods for spatial and temporal light patterning to photoactivate Wnt signaling in a precise location and at a given time within embryonic stem cell cultures. Such optogenetic activation of morphogen signaling in specific cell subpopulations allows studies of cell-cell interactions and signaling dynamics that regulate early embryonic development.

To my family

Contents

List of Figures

List of Tables

Acknowledgments

The work described in this dissertation would not have been possible without the mentorship, training, support, and encouragement that I am honored to have received over the course of my life and education. Below, I will attempt to express my deepest gratitude to the teachers, colleagues, family, and friends who have all helped shape my perspective and brought me to this point in my career.

First, I would like to thank Prof. Dave Schaffer for the opportunity to work on such an interdisciplinary thesis project. Beyond providing the intellectual, infrastructural, and financial resources for a supportive research environment, Dave also gave me the freedom and independence to pursue my interests. I am grateful for the trust he placed in me as a young researcher in the lab and for fostering my creativity and curiosity for developmental biology and optical engineering.

Second, I would like to thank Prof. Laura Waller. Without Laura's generosity and willingness to provide her lab resources to develop and house the opto-SIM microscope, I would have almost no knowledge of microscopy and optical engineering. Her curiosity for science as well as personal development has been a catalyst for my growth as a researcher and engineer.

Throughout my time working in the Schaffer lab, I have been fortunate to work with incredibly talented and kind colleagues. In particular, I would like to thank Xiaoping Bao, who taught me embryonic stem cell biology and genetic engineering. Most importantly, though, Xiaoping is always willing to engage in thoughtful discussions, listen to my questions and ideas, and provide honest feedback. I am incredibly grateful for his kindness, patience, and encouragement during my moments of doubt. I am also thankful to Josh Zimmermann for our thought-provoking discussions and his helpful suggestions on scientific writing, as well as Hunter Johnson for his endless curiosity and positivity. My friends and colleagues in the Schaffer lab have been a source of constant support and inspiration, including Sabrina, Andrew, Christina, Olivia, Phil, Rocio, Chris, Lukasz, Dawn, and Sisi.

Within the Waller lab, I would particularly like to thank Li-Hao Yeh, with whom I built initial versions of the opto-SIM microscope and who taught me the theory behind SIM imaging. It has been an honor to work with such a passionate mathematician and optical engineer, and especially one who had the talent and patience to answer all of my questions. I am also grateful to Nick Antipa for his help with Zemax modeling, Shwetadwip Chowdhury for his friendship, help with optical alignment, and SIM imaging, and Herbert Liu, for his help with DMD arrays. Through this collaboration with the Waller lab, I feel extremely fortunate to have met fantastic scientists and friends, including Emrah, Volker, Zack, and Henry.

I would also like to give special thanks to my two undergraduate students, Sarah Rockwood and Thomas McClave. From my experience mentoring Sarah and Thomas, I have learned at least as much from them as they did from me. Through her perseverance and curiosity, Sarah became a talented and dedicated researcher, whose enthusiasm and hard work I could always rely on. Thomas clarified for me the mysteries of computer science, and

his dedication, attention to detail, and cheerfulness made it a pleasure to work together. I feel incredibly lucky to have worked with both of you and am so proud of the things you are already achieving after graduation.

I would also like to thank the members of my qualifying exam and dissertation committees: Prof. Xavier Darzacq, Prof. Todd McDevitt, and Prof. Steve Conolly. To Xavier, I am particularly thankful for his thoughtful and considerate curiosity. In addition, Xavier generously allowed us to use his lab's lasers in the opto-SIM microscope. To Steve, I am grateful for his constant encouragement and optimism, as well as a wonderful GSI experience with Xinyi Zhou. To Todd, I am thankful for his helpful suggestions and engaged discussions, as well as the fruitful and helpful collaboration with David Joy.

While fabricating LAVA devices, Chris Myers from the CITRIS Invention Lab has been an incredible source of mentorship and support. His good humor while teaching me rapid prototyping techniques played an enormous role in encouraging me to continue learning and improving my engineering skills. I would also like to thank Kevin Tian and Mitchell Karchemsky for the helpful discussions and creating a warm and cheerful lab environment. Phil Simon from the Chemistry Machine Shop was also an invaluable help, and his thorough training, funny stories, and good cheer always brightened my day. In addition, I am incredibly grateful to Mary West from the SSCF who found the time and resources to provide the Nikon microscope and various equipment that was critical in allowing me to build the opto-SIM microscope. Thank you also to Berkeley Light Inc and Jimena Loureiro for the optical equipment donation.

I am also incredibly grateful to my mentors and teachers before graduate school, who gave me the skills, enthusiasm, and guidance I needed along every step of the way. In particular, thank you to Claudia Dall'Osso, Prof. Amy Wagers, Prof. Tom Gilmore, Danika Khong, Lotte Bruens, Sharif Tabebordbar, Chris Zhu, Leila Haery, Mr. Crosby, Mr. Petrizzi, and Dr. Kraus. Thank you also to Ira Kan, a fantastic interpreter and dear friend.

I would also like to thank the incredible teams and activities that I have been part of and that have enriched my life at UC Berkeley. I am grateful to the Berkeley Science Review, an incredibly team of artists, writers, and editors who I had the honor to work with, particularly Katie Deets, Dat Mai, Emily Gonthier, Emily Hartman, and Hayley McCausland. Thank you also to the Tablescope team and members of the Fletcher lab, particularly Prof. Dan Fletcher, Arunan Skandarajah, Kevin Yamauchi, Malav Desai, Elaine Yu, Matt Adams, Frankie Myers, Matt Bakalar, and Johannes-Geert Hagmann at the Deutsches Museum.

I would also like to thank the organizations that financially supported our research: the National Science Foundation, the National Institutes of Health, the Siebel Foundation, and the UC Berkeley Graduate Division. Without their financial support, our work would not have been possible.

My final thank you goes to the people whose love and support brought me to where I am today. To my mom, Лена, you are a strong, intelligent, and independent woman, and I am so grateful that you who have passed on these qualities to me. Thank you for love, support, and the immense sacrifices you have made to give me a good education and to constantly find opportunities for me to grow. To my dad, Папа, thank you for your creativity, love for engineering, and unwavering support, love, and curiosity. Thank you to my grandma, Бабуля, you have shown me the beauty of love and kindness. Thank you to my family in New York – Люба, Сеня, и Дима, Steph, Jen, Ариша, и Ися – for all the fun times in the city and on Cape Cod. Thank you to my family in Russia – Мими, Аня, и Дедушка – for the happy holidays and childhood memories. Thank you also to my relatives in СПб и Иваново, for showing me the meaning of family unity and hospitality – Димик, Алексей, Оля, Алена, Никита, Маша, Аня и Саша.

To Kevin, I cannot begin to express how much your love and support has meant to me. You have been an unwavering source of thoughtfulness, respect, and wisdom, a fantastic partner and friend. I don't think that my PhD would have been possible without you. I am also forever grateful to Муся, who has been with me through all my adventures, my fuzziest and most adorable companion.

Thank you also to all my dear friends. Colin and Jimena, thank you for the wonderful company, late night conversations, and constant care and help. To Elie, thank you for your cheerfulness, good humor, and banter, you are a constant source of laughter and epic skiing adventures. Thank you to Katie and Allegra, for our thoughtful conversations, tasty dinners, and climbing and yoga adventures. Thank you also to Paul, Will, Varun, Jake, Jeanne, Jane, Sophie and Donald, John, Nina, Matt B, and my climbing partners, Paul, George, Katie, Niklas, Jose, and David. You have all made the Bay Area feel like home to me. Thank you also to my friends far away and abroad, who are a constant source of love and inspiration: Мура, Ale, Jonas, Andrew G, Chrissi, and Egle. Finally, thank you to the mountains, valleys, and lakes of Tahoe, Yosemite, and the Sierras that have been a serene and beautiful haven from the bustle of work and daily life.

Chapter 1

Introduction

1.1 The early mammalian embryo

A majority of our knowledge of mammalian embryonic development comes from studies of the early mouse embryo. Unlike the extensively studied frog, chick, and fly embryos that develop in an external environment, the mouse embryo develops within the maternal uterine tissue. Despite the associated challenges of embryo imaging and manipulation, gene expression patterns in the mouse can be readily perturbed with transgenic and embryonic stem (ES) cell technologies. Such genetic studies have lead to the discovery of the critical regulators of early mammalian development, including the signaling pathways and molecular mechanisms regulating morphogenesis, symmetry-breaking, and body axis patterning.

1.1.1 Mouse embryogenesis: from fertilization to gastrulation

The fertilized egg, or zygote, starts as a single totipotent cell that has the capacity to give rise to all embryonic and extra-embryonic tissues necessary to form an adult organism (Figure 1.1A) (*1*, *2*). As the zygote journeys through the oviduct toward the uterus, it undertakes a series of cell cleavages. The initial single-cell zygote splits into two cells, or blastomeres, that continue to asynchronously divide. Though morphologically identical, the individual blastomeres can display differences in developmental potential as early as the two-cell stage (*3–6*), and show heterogeneous gene regulation (*7–10*) and transcription factor dynamics (*11*) at the four-cell state. However, other studies detect no differences in gene expression and cell fate at the four-cell stage (*12–14*), and consequently the first symmetry-breaking event of the embryo remains to be definitively identified (*15*).

By embryonic day 2.5 (E2.5), the zygote is comprised of eight blastomeres that subsequently undergo the first morphogenetic event of the embryo known as compaction. The cells form a tightly packed arrangement that is stabilized by tight junctions (*16*, *17*), increased cell adhesion (*18*), and cell tension (*19*). Blastomeres concomitantly acquire an apico-basal polarity (*20*), and a round of division generates a 16-cell compact structure called a morula. The outer layer of cells in the morula largely gives rise to extra-embryonic trophectoderm

(TE) tissue, whereas a small group of internal cells develops into the inner cell mass (ICM) and the mouse embryo proper (*21*, *22*). Blastomere fate commitment to either Cdx2+ TE or Oct4+ ICM at E3.0 is the first lineage segregation and symmetry-breaking event of the embryo. Multiple models have been proposed to explain this inside-out self-organization of the TE outer layer and ICM (*20*, *21*). Though it remains unclear how cell adhesion, tension, apicobasal polarity, and cell division work together to mediate symmetry-breaking, the apical domain of polarized cells is emerging as a critical regulator of cell positioning within the morula (*23*–*26*).

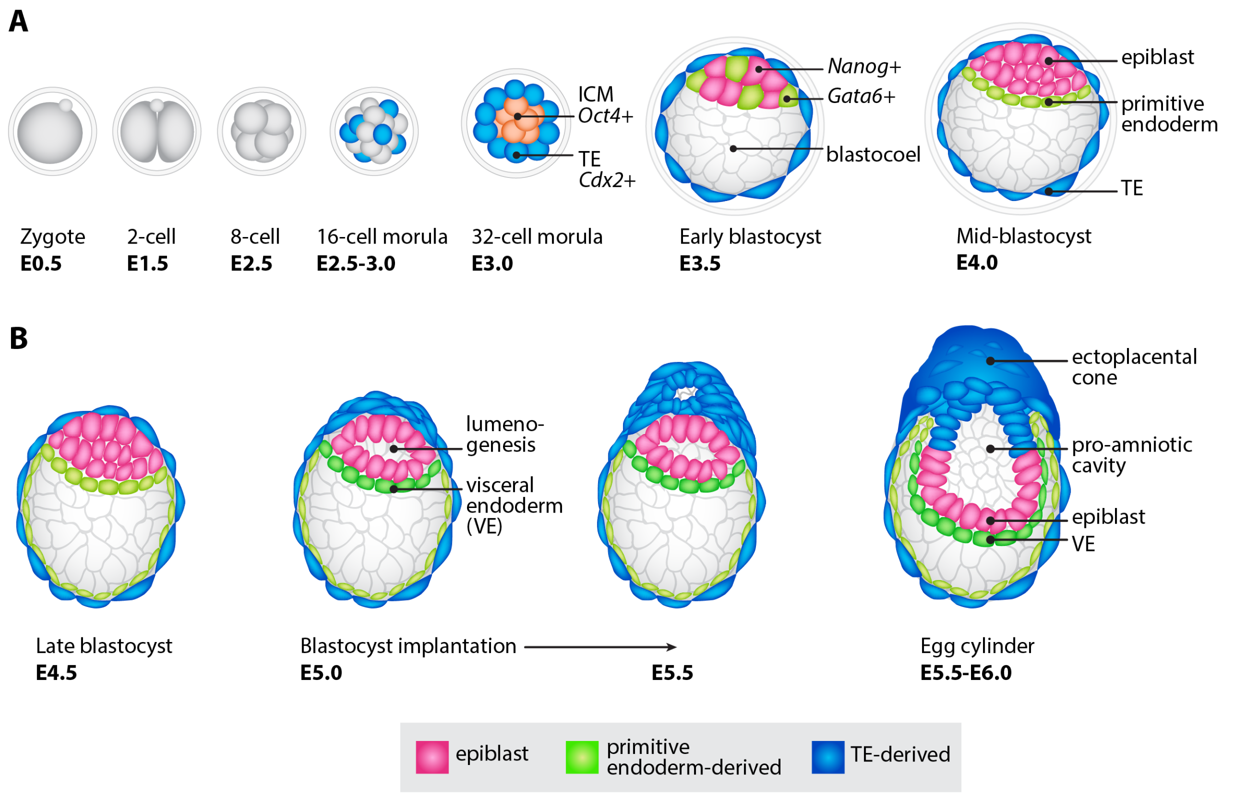

Figure 1.1: **Mouse embryo development from zygote to pregastrula**
A) Schematic outlining the first four days of mouse embryonic development, from zygote (E0.5) to mid-blastocyst (E4.0). Blue cells biased toward trophectoderm (TE) fate, orange cells biased toward inner cell mass (ICM) fate. Pink cells are Nanog+ epiblast, green cells are Gata6+ primitive endoderm and grey outline is zona pellucida. **B)** Schematic outlining mouse embryo development from the late blastocyst stage (E4.5) to the egg cylinder, pregastrula stage (E6.0).

Initially, the morula does not possess an internal cavity. However, during the process of cavitation, water passes via an osmotic gradient and via active transport by trophoblast aquaporins to the inside of the morula to form a hollow fluid-filled cavity called the blastocoel (Figure 1.1A) (*27*, *28*). At this stage, the ICM becomes positioned on one side of the spherical TE shell. The position of the blastocoel, and thus the embryonic-abembryonic axis, is determined by a balance of symmetric and asymmetric cell divisions coordinated in space and time (*29*), as well as possible signaling from the zona pellucida (*13*) and cleavage plane polarity (*6*). The TE is thereby separated into two populations: one that neighbors the ICM (polar trophectoderm) and one that surrounds the emerging cavity (mural trophectoderm) (*29–31*). The resulting spherical, spatially polarized structure, a hallmark of embryonic development called the blastocyst, continues to rapidly expand and proliferate through E4.5.

As the blastocyst expands, cells of the ICM differentiate to two distinct lineages: the epiblast and the primitive endoderm. A mosaic 'salt and pepper' pattern of cells emerges within the ICM marked by either Nanog or Gata6 transcription factor expression (*12, 32*). The source of this lineage allocation remains under debate, and could arise from stochastic changes in gene expression (*33, 34*) and/or patterned during successive rounds of polarized cell division (*32, 35, 36*). Nanog maintains pluripotency of epiblast progenitors (*37, 38*), whereas Gata6 drives primitive endoderm differentiation (*39*). Primitive endoderm cells spatially segregate to line the ICM surface and blastocoel cavity in a process thought to be regulated by differential cell movements and adhesion properties between ICM and PE cells, as well as selective apoptosis (*34, 40*). By E4.5, the late blastocyst thus contains three distinct cell lineages: (1) the trophectoderm, which mediates blastocyst implantation into the maternal uterine lining and forms progenitors of the placenta (extraembryonic ectoderm and the ectoplacental cone), (2) the primitive endoderm, which forms the extraembryonic parietal and visceral endoderm, and (3) the epiblast, which gives rise to the cell lineages of the embryo proper, including both the somatic tissue and germ cell lineages (Figure 1.1A) (*41*).

Once the three cell lineages successfully segregate, the blastocyst hatches from its surrounding glycoprotein shell, called the zona pellucida, so that it can adhere to the uterine wall (Figure 1.1B). Implantation of the blastocyst, mediated by extracellular matrix interactions (*42*) and protease secretion from the TE (*43*), results in growth of the embryonic and extraembryonic tissues, as well as dramatic changes in shape. By E5.0, the embryo implants into the uterine wall and transforms into an elongated structure called the egg cylinder. The cells of the epiblast acquire apicobasal polarity, and cavity forms at the center of the epiblast – a precursor of the amniotic cavity (*44*). Furthermore, the TE expands into the maternal tissue, while the primitive endoderm expands to form the parietal endoderm, which lines the extraembryonic tissue, and the visceral endoderm (VE), which lines the outside surface of the epiblast (*44*). In this way, the apical surface of epiblast cells faces the inside of the pro-amniotic cavity, whereas the basal surface faces the basement membrane and VE. In subsequent developmental steps, the VE plays a critical role in patterning the underlying epiblast and inducing signaling asymmetry and symmetry-breaking of the epiblast (*41*). During this process of implantation and epiblast morphogenesis, the epiblast cells also undergo transcriptional and epigenetic changes. Epiblast cells of the blastocyst exist in a naive pluripotent state, capable of producing all somatic and germ cell lineages and characterized by a transiently reactivated X chromosome in female cells (*45*). In contrast, upon implantation, epiblast cells transition to a primed state, where cells undergo X chromosome inactivation (*46*), show subtle transcriptional changes (*47*, *48*), and ultimately cannot contribute to blastocyst chimeras (*45*). The epiblast epithelial morphology in the egg cylinder stage thereby coincides with functional changes in cell signaling and lineage potential.

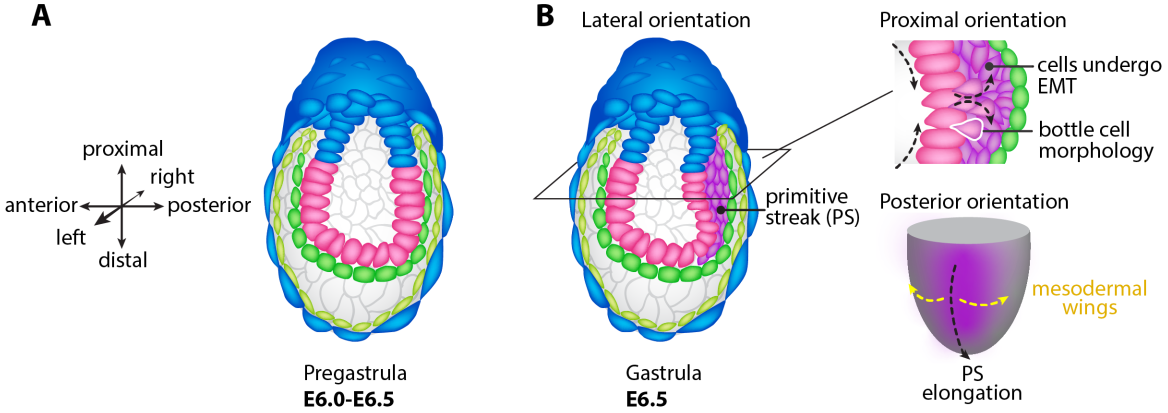

Figure 1.2: **Mouse primitive streak formation and gastrulation**
A) Schematic outlining the axes of the future body plan and pregastrula embryo. The primitive streak begins to form on the proximal posterior side of the pre-gastrulation embryo. **B)** Schematic of primitive streak formation in the mouse gastrula (E6.5). Cells undergo EMT and migrate through the region of the primitive streak (PS), highlighted purple. The apically constricted, bottle shape morphology of ingressing cells is highlighted in white.

After implantation, the epiblast also begins to acquire spatial asymmetry to establish the proximal – distal and anterior – posterior axes of the embryo. The first signs of asymmetry are evidenced by gradients of morphogen signals that pre-pattern the epiblast (see Section 1.1.2) (*41*). Consequently, gene expression patterns emerge in specific regions of the epiblast, which lay the foundation for the future site of primitive streak formation and gastrulation. Indeed, the establishment of signaling asymmetry is rapidly followed by dramatic morphological changes within the epiblast during the process of gastrulation (Figure 1.2A-B). During gastrulation, the three germ layers of the future organism are established: ectoderm, mesoderm, and endoderm. The spatial organization of these three layers is a critical step for establishment of the future body plan. Recent advances in live-embryo imaging have especially demonstrated the dynamic cell migration and cell morphology changes responsible for such embryonic morphogenesis (*49*, *50*). The onset of gastrulation is marked by the formation of a specialized structure called the primitive streak. At around E6.25, cells of the proximo-posterior epiblast converge toward the posterior and collectively migrate and ingress at the region of the primitive streak (*49*). In order to delaminate from the epithelial epiblast, epiblast cells undergo an epithelial to mesenchymal transition (EMT) and migrate away from the streak (*51*). Such motile cells undergo drastic changes in cytoskeletal rearrangement, acquiring a migratory, mesenchymal phenotype (*50*, *52*, *53*). As cells escape from the epithelial layer they acquire a bottle-shaped morphology within the streak, suggesting apical constriction as a method for ingression (Figure 1.2B) (*51*). Over the next 36 hrs, the primitive streak elongates and extends toward the distal and anterior side of the epiblast. The cells that migrate through the primitive streak acquire a mesendodermal cell lineage, with distinct mesoderm lineages allocated based on the timing and site of ingression through the primitive streak (*54, 55*). The earliest, most posterior subpopulations give rise to extraembryonic mesoderm tissue that have distinct migration trajectories (*50, 56*). Lateral plate, paraxial and cardiac mesoderm emerge slightly later from the intermediate and anterior levels of the streak via formation of the 'mesodermal wings' (Figure 1.2B) (*57*). Lastly, epiblast cells that migrate through the anterior portion of the primitive streak give rise to the prechordal plate, the notochord, as well as the definitive endoderm cell lineage (*58*) and pattern the underlying epiblast in the embryo anterior to form the neuroectoderm and notochord (*59, 60*). By the end of gastrulation at E7.5, the epiblast has broken its radial symmetry, differentiated, and self-organized to form the trilaminar structure of the mature gastrula.

1.1.2 Signal dynamics regulating primitive streak formation and gastrulation

Genetic and lineage analysis studies have identified the key signaling pathways and transcription factors that govern the process of axis patterning and cell lineage allocation. As the embryo implants into the uterine wall, it becomes patterned by gradients of morphogen signals, which activate or inhibit target transcriptional regulators that then mediate cell differentiation, morphology, and migration during gastrulation (*41*).

The first patterning event of the epiblast is formation of the proximal–distal axis. The proximal–distal axis (the long axis of the egg cylinder, and future dorsal–ventral axis) corresponds to the embryonic–abembryonic axis of the blastocyst, formed by the ICM and blastocoel cavity (Figure 1.1A). This embryonic–abembryonic axis can be regarded as the source of future dorsal-ventral polarity (*61*). Gene expression patterning within extramebryonic tissues is already evident at the blastocyst stage (*29–31*), but epiblast symmetry is thought to remain intact. During implantation, however, the epiblast breaks its proximal–distal signaling symmetry (Figure 1.3A). As the egg cylinder elongates along the proximal–distal axis, the PE also expands to form the parietal endoderm, which lines the surface of the mural TE, and the visceral endoderm (VE), which remains in contact with the embryo and plays a critical role in patterning the underlying epiblast. The TGFβ ligand Nodal, which is initially uniformly expressed across the epiblast (*62, 63*), activates Smad2 signaling in the distal VE (*64–67*). In turn, this initiates the expression of distal VE (DVE) marker genes including the transcription factors Hex, Foxa2, and Lim1 (*68–70*) that regulate the secretion of Wnt and Nodal signaling antagonists from the DVE, including Dickkopf homologue 1 (Dkk1), cerberus-like protein 1 (Cer1) and left–right determination factor 1 (Lefty1) (Figure 1.3B) (*68, 70–73*). Cells of the DVE are distinct from neighboring VE cells and develop a tall,

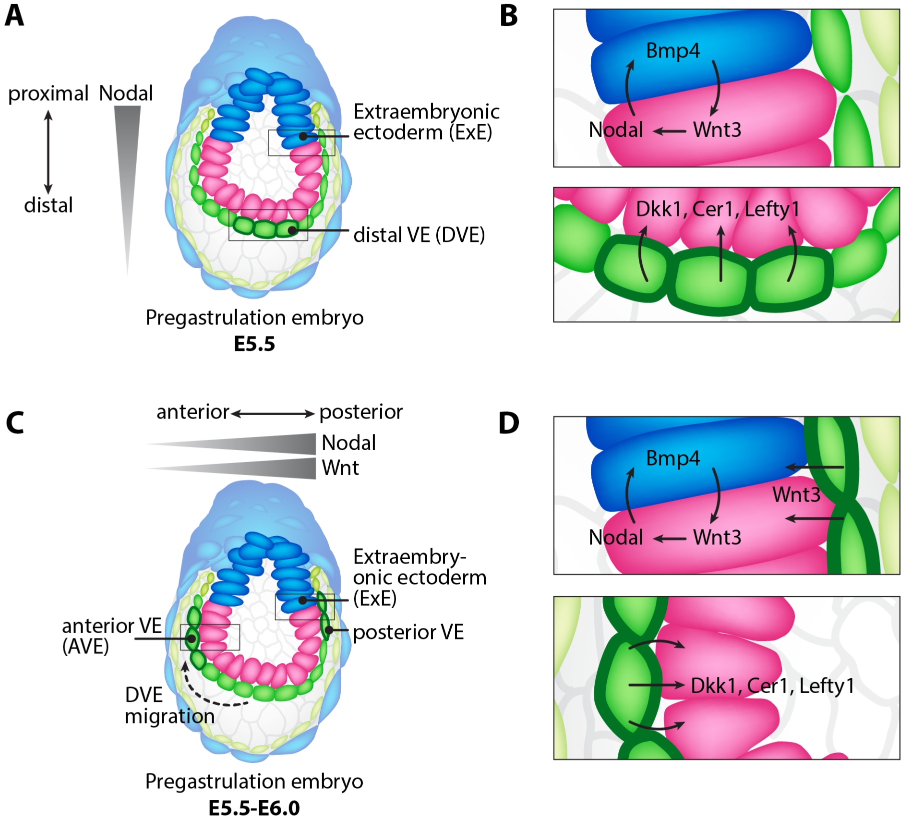

Figure 1.3: **Axis patterning in the mouse pre-gastrulation embryo**
A) Overview of P-D axis patterning in the E5.5 embryo. **B)** Top schematic shows zoom-in of signaling feedback between the proximal epiblast and extraembryonic ectoderm. Bottom schematic shows zoom-in of signaling feedback between the distal epiblast and distal VE, outlined in green. **C)** Overview of A-P axis patterning in the E5.5-E6.0 embryo. **D)** Top schematic shows zoom-in of signaling feedback between the proximal epiblast and extraembryonic ectoderm as well as feedback from the posterior VE onto the proximal epiblast. Bottom schematic shows zoom-in of signaling feedback between the anterior epiblast and anterior VE, outlined in green.

columnar epithelial morphology (*74*, *75*). These DVE cells thus secrete Wnt and Nodal antagonists that begin the pattern signaling in the underlying epiblast tissue.

In parallel, interactions between the epiblast and extraembryonic ectoderm (ExE) begin to pattern signaling on the proximal side of the epiblast (Figure 1.3A) (*64*). First, Nodal from the epiblast induces Furin and Pace4 covertases in the ExE, which cleave Nodal to its mature form. The mature Nodal signals back to the epiblast to further upregulate local Nodal expression (*76*). In a second feedback loop, Nodal secreted by the epiblast induces Bmp4 secretion by the ExE, which forms a self-sustaining positive feedback loop by in turn activating Wnt and Nodal in the adjacent epiblast (*56*, *64*, *76*) (Figure 1.3B). Such signal feedback between the ExE and epiblast upregulates Nodal, Wnt, and Bmp4 signaling at the proximal side of the epiblast.

At E6.0, shortly after the establishment of proximal–distal asymmetry, the DVE rapidly migrates to the anterior side of the epiblast, which effectively relocates the source of Nodal and Wnt inhibitors to the anterior VE (*77*). Such DVE migration initiates patterning of the anterior–posterior axis (Figure 1.3C). DVE cells activel migrate through cytoskeletal rearrangement and filopodial extension (*74*, *75*, *78*, *79*), a process that may be guided by directional cues from Nodal (*80*) and Wnt (*81*). Once localized to the anterior side, these cells are called the anterior VE (AVE), and they secrete Wnt and Nodal inhibitors such as Dkk1, Cer1, and Lefty1 (*70*, *71*) (Figure 1.3D). The antagonists secreted by the AVE block signalling and impart neurectodermal character to the epiblast anterior. In contrast, the posterior epiblast continues to reinforce Nodal, Wnt, and Bmp4 signaling through interaction with the ExE and instruct cells to acquire mesodermal and endodermal fates. In addition signal feedback with the ExE, Wnt signal induction from a localized source in extraembryonic tissue is thought to break anterior-posterior symmetry of the epiblast (*82*). Starting at E5.5, Wnt3 expression is evident first in the posterior visceral endoderm and then expands to the proximo-posterior epiblast a few hours later (Figure 1.3D) (*82*–*84*). However, conditional ablation of Wnt3 in the visceral endoderm delayed but did not inhibit axis formation and gastrulation (*85*), suggesting that the multiple signaling mechanisms patterning the epiblast may have compensatory effects.

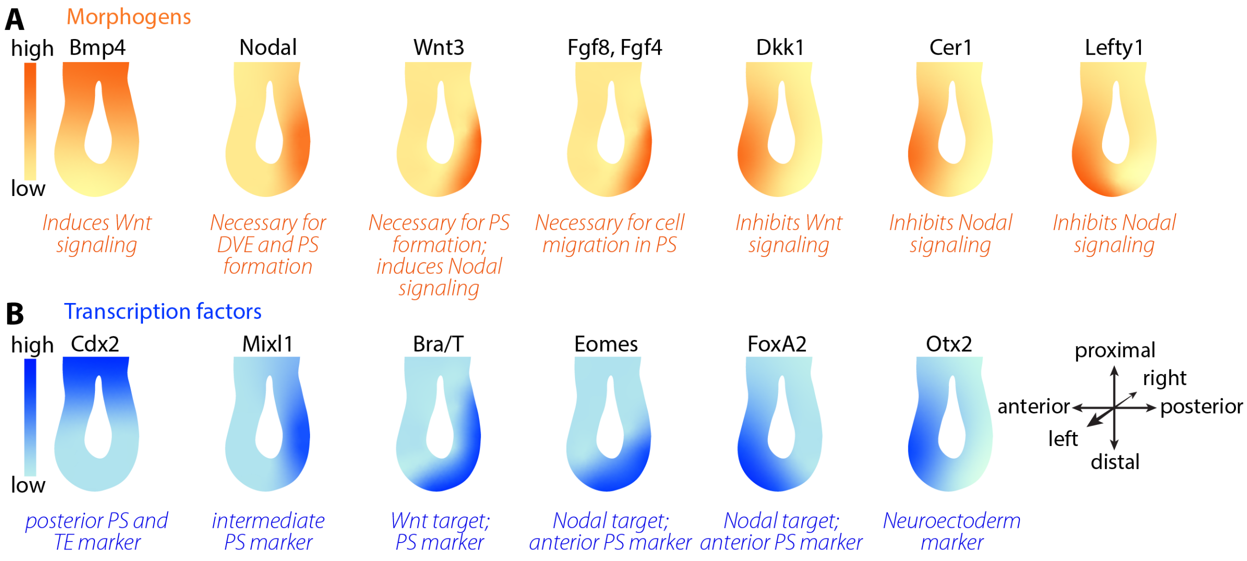

Figure 1.4: **Expression patterns of morphogens and transcription factors in the gastrulating E6.5-7.5 embryo**

A) Schematic of the mouse gastrula color-coded by morphogen expression level.

B) Schematic of the mouse gastrula color-coded by transcription factor expression level.

As a result of such signal feedback mechanisms, gradients of morphogens emerge across the epiblast prior to gastrulation (Figure 1.4A). In particular, canonical Wnt/β-catenin signaling has emerged as a master regulator of primitive streak formation across many organisms (*86*). In the mouse, embryos mutant for Wnt3, Lrp5;Lrp6, or β-catenin do not establish anterior–posterior polarity and fail to form mesoderm and endoderm (*87, 88*). Though a spatially localized pattern of Wnt3 mRNA is a hallmark of antero-posterior polarity, the spatial distribution of Wnt protein has yet to be established in the embryo, and it remains an open question how an initial Wnt stimulus is able to propagate through the embryo given the short range of Wnt protein diffusion (*89, 90*). Though Wnt signal in the embryo may propagate through membrane-tethered cell-cell contact during cell division (*90, 91*), the limited diffusion supports the hypothesis that Wnt is primarily activated through Nodal-mediated feedback loops (*76*) as opposed to localized diffusion from the posterior VE (*82*). Indeed, Nodal signaling is also required for successful primitive streak formation (*63, 92*), and Nodal-deficient embryos lack posterior markers including Wnt3 and Eomes, suggesting that Nodal is necessary for establishing posterior identity and the Wnt gradient (*64*).

As a consequence of the spatially localized Wnt signaling, the posterior epiblast begins expressing the early mesendoderm marker and transcriptional regulator Brachyury (Bra, also known by its gene name, T) (*93–95*). Bra is a direct transcriptional target of Wnt signaling (*82, 96, 97*), and, similar to Wnt3-null embryos, embryos mutant for Bra fail to form a primitive streak (*95*).

After the establishment of Wnt asymmetry, cells at the epiblast posterior also delaminate from the epithelial cell layer and undergo EMT. Within the context of mouse gastrulation, the regulation of EMT remains poorly understood. Fibroblast growth factor (FGF) signaling has emerged as a key regulator of migration (*98*). FGF signaling is present at the primitive streak, and it has been proposed that FGF ligands, specifically Fgf4 and Fgf8, act as an extracellular guidance cue for cell migration (*99, 100*). Studies from *Drosophila* suggest that strength of FGF signaling can have a dose-dependent effect on migration trajectory (*101*), though correlation of cell migration with Fgf signal strength during mouse gastrulation has not yet been performed. Nevertheless, activation of FGF receptor Fgfr1 via Fgf4 or Fgf8 binding upregulates the EMT regulator Snail, which in turn down-regulates E-cadherin (*52, 98, 102, 103*). The resulting EMT and loss of cell-cell junctions allows cells to detach from the epithelial layer, lose apico-basal polarity, and change cell shape and motility within the primitive streak (*52*). Though cell migration through the streak is a dynamic progress, presumably regulated by signal gradients that direct cell migration trajectories as well as cell fate (*54, 55*), the signaling dynamics remain unstudied. For example, it is unclear how the spatial and temporal dynamics of morphogens regulate cell lineage commitment and link cell fate outcome to migration dynamics through the primitive streak (*50, 54, 55, 104*). Whether mesoderm fate patterning within the streak is regulated by duration of cell migration through the streak or strength of exposure to extracellular guiding cues remains to be determined. A potential missing mechanistic link between cell fate and EMT could be β-catenin, which associates with E-cadherin at tight junctions. Thus, changes in cytoplasmic β-catenin levels upon E-cadherin downregulation may result in β-catenin-mediated transcriptional regulation.

1.1.3 Human embryonic development

Though the mouse embryo is the model system for mammalian development, the egg cylinder shape is unique to rodent development. Human embryos instead form a disk-shaped structure called the bilaminar disk, where the epiblast is flat but similarly sandwiched between the hypoblast (primitive endoderm and VE equivalent) and trophectoderm. Though human embryo geometry is markedly different from mouse, the cell-cell interactions and signaling are thought to remain conserved. Analogous processes occur in the human embryo, albeit at different time scales: blastocyst formation at E4-5, zona pellucida hatching at E6-7, implantation at E7-E9, epiblast polarization and pro-amniotic cavity formation at E9-14, and gastrulation at E15-16. Knowledge of such processes largely comes for early studies of human embryos (*105*, *106*) or monkey embryos (*107*). Currently, bioethical guidelines restrict the study of human embryos beyond E14 so human gastrulation remains entirely unstudied (ISSCR, NRC). The development of in vitro fertilization (IVF) techniques has spurred studies of human fertilization and early cleavage (*108*, *109*), but mechanistic studies of blastocyst development and implantation have been limited by the challenge of *in vitro* culture of human embryos.

However, recent advances in culture methods have given unprecedented insight into early human development prior to gastrulation (*110–112*). Such studies have found that human embryos retain the capacity to self-organize and develop outside of the maternal environment, and have noted key differences between mouse and human early embryonic development. In particular, whereas mouse epiblast and PE segregation occurs in the pre-implantation blastocyst, human epiblast and hypoblast segregation is delayed and occurs after implantation, (*110*, *113*). Advances in single-cell sequencing have also allowed transcriptomic profiling of preimplantation human embryos along different developmental stages (*114*, *115*). Furthermore, the isolation of human embryonic stem cells (see Section 1.1.4) has vastly expanded our understanding of early embryonic regulation and has led to the development of a variety of *in vitro* model systems for different developmental stages (*116*). Such advances have now set the stage for new discoveries of human embryonic regulation, which will broaden our understanding of molecular mechanisms of human development and shed light on novel advances in IVF technologies and infertility treatments.

1.2 Embryonic stem cell models for early development

Stem cell culture systems that recapitulate *in vivo* processes of early development have been an invaluable resource for modeling the signal patterning of the epiblast and enable genetic and molecular perturbation for insight into the mechanistic details of embryogenesis (*117*). Since the isolation of mouse (*118*, *119*) and human (*120*) embryonic stem cells (ESCs) from the pre-implantation blastocyst, a variety of cell-based systems have been developed for modeling embryo morphogenesis and patterning at the blastocyst and gastrula stage.

1.2.1 Stem cell-based models of the mouse embryo

To gain mechanistic insight into morphogenesis, embryonic stem cell culture systems have recently been developed to emulate *in vivo* processes of early mouse development (*116*). Such model systems use cells derived from the pre-implantation epiblast (*118, 119*), i.e. mouse embryonic stem cells (mESCs), which represent the naive pluripotent state of early embryonic tissue *in vitro* (*45*). Grown in specific culture conditions to recapitulate the signal patterning of early development, mESC-based model systems enable genetic and molecular perturbation for insight into the mechanistic details of embryogenesis (*116*).

In particular, aggregates of mESCs have been recently combined with trophoblast stem cells (TSCs) (*121*) to create an *in vitro* model of the early E3.5 blastocyst (*122*). The two cell populations self-organize to form the spherical, spatially polarized structure of the blastocyst and, remarkably, are able to implant *in vivo* into the mouse uterine wall. The gene expression patterns of such ESC-based blastoids show high similarity to natural E3.5 blastocysts, and have been used to study the signaling regulating of mural and polar trophectoderm patterning (*31*).

The majority of current ESC-based models have focused on recapitulating the process of primitive streak formation and gastrulation. In one approach, mESCs were grown adjacent to TSCs (called ETS embryos) (*123*) or adjacent to TCSs and extraembryonic endoderm (called ETX embryos) (*124*) to recapitulate the cell-cell interactions and signaling between these cell populations. Remarkably, the morphological structures and signaling patterns that emerged had many parallels with natural embryos. In ETS embryos, the cells self-organizes and formed luminized structures that ultimately unified to form a central cavity resembling the pro-amniotic cavity (*123*). The process of cavitation required Nodal signaling, and some ETS embryos (38% ETS embryos) expressed localized Wnt and Bra signaling on one side of the embryo. The origin of this signaling asymmetry remains unknown, but is likely a result of the cell-cell interactions between the ESC and TSC compartments. In ETX embryos, where ESCs are grown adjacent to TSCs and extraembryonic endoderm (XEN) cells (*125*), the phenotype of symmetry-breaking and gastrulation-like events is even more pronounced (*124*). These synthetic embryos also developed localized Wnt and Bra signaling at similar efficiency (42% ETX embryos) and stronger signal strength than in ETS embryos. Interestingly, synthetic embryos consisting only of ESC and XEN cells, without TSCs, did not develop signaling asymmetry, which reflects *in vivo* findings that the TE is critical for symmetry-breaking and may be regulated or enhanced by signaling from the VE. In ETX embryos, the XEN cell layer segregated into morphologically distinct compartments dependent on proximity to ES vs. TS cells. Furthermore, in a small fraction of ETX embryos, the XEN layer formed a signaling center where a group of cells expressed Lefty1 and Cer1, thus mimicking AVE specification and localization. Such signaling asymmetry led to morphological changes in the embryo, where a subset of Bra+ cells expressed EMT markers, acquired a bottle cell-shaped morphology and migratory phenotype, and underwent a gastrulation-like event to generate cells that expressed axial mesoderm and definitive endoderm markers (*124*). Furthermore, transcriptomic analysis of these ETX embryos at different developmental time points confirmed gene expression similarity with natural embryos (*124*). Though certain challenges remain to increase efficiency of synthetic embryo formation and morphogenesis and develop fully defined culture conditions, these studies show that stem cell culture models can be a powerful tool for recapitulating early embryonic morphogenesis and signaling dynamics.

Intriguingly, self-organization of mESC aggregates could also be induced in the absence of extra-embryonic tissues. Early efforts showed that spherical aggregates of mESCs, called embryoid bodies, spontaneously developed Wnt expression on one side of the aggregate when exposed to uniform treatment with Wnt agonists (*126*). Wnt expression resulted in spatially asymmetric expression of Bra and EMT markers. Subsequent studies optimized culture and aggregate formation protocols to show that mESC aggregates could also spontaneously elongate, an important morphological distinction that suggests axis patterning (*127–129*). Interestingly, Bra signal asymmetry was also detected such mESC aggregates without exposure to Wnt signaling, though an exogenous pulse of Wnt treatmen enhanced signal strength and polarization (*130*). Remarkably, these 'gastruloids' were able to spontaneously develop mesoderm and Hox gene expression patterns that resemble certain gene expression patterns of the natural embryo (*131*). However, the polarization and cell morphology of such aggregates is distinct from the natural epiblast, as cells do not form a centralized lumen or organized apicobasal polarity. Further, such gastruloid models rely on spontaneous symmetry-breaking as opposed to controlled perturbation of signaling dynamics and cell-cell interactions, precluding mechanistic insight into morphogenesis.

Compared to the use of natural mouse embryos, ESC-based model systems allow greater ease of genetic and molecular perturbation of signaling to study mechanism. However, symmetry-breaking still relies on spontaneous emergence of signaling or undefined cell-cell interactions. Though embryoids and gastruloids can be treated with signal agonists or inhibitors, their spatial location cannot be controlled and signal strength is dependent on protein diffusion and receptor expression. Thus, future efforts will likely focus on engineering methods for controlled signal activation in target cells or cell subpopulations, which will enable more intricate studies of signal dynamics and regulatory mechanisms of symmetry-breaking and morphogenesis.

1.2.2 Stem cell-based models of the human embryo

Excitingly, human ESCs (hESCs) have extended such developmental models from mouse to human embryogenesis, which, due to ethical restrictions, has long been a mystery (*116*, *117*). Human ESCs are derived from the inner cell mass of the human blastocyst (*120*), and differ significantly from mouse ESCs in terms of culture requirements, morphology, and molecular signature (*45*). Due to their flattened cell morphology and expression of certain early differentiation markers like WNT and FGF (*115*), the pluripotency state of hESCs has been under debate (*45*). It has been argued that some hESC molecular signatures resemble the primed state of mouse epiblast stem cells (*115*, *132–134*). However, unlike epiblast stem cells, hESCs are derived from the same developmental state as mESCs–the pre-implantation blastocyst–and are able to differentiate into a trophoblast lineage (*135*). Though certain genetic signatures of hESCs more closely resemble mouse epiblast stem cells than mESCs (*115*), the biological significance of such observations is unclear given the species differences between mouse and human embryology (*45*). Further, the classical functional assays for pluripotency developed in mouse systems, such as blastocyst chimeras, cannot be applied to human ESCs. It has been also shown that the primed state itself is flexible, as both human (*136*, *137*) and mouse (*138*) cells can be reprogrammed to a more naive state by culturing cells in a cocktail of inhibitors. Thus, though hESCs may not represent a true naive pluripotent state, they are able to model the early processes of human development.

Specifically, hESCs have been used to model the process of human gastrulation. Geometrically confined to two-dimensional circular micropatterns, hESCs differentiate and self-organize into radially symmetric patterns of germ lineages in response to uniform addition of BMP4 (*139*). Within the disk-shaped pattern, hESCs differentiate to form concentric rings of TE-like, endoderm, mesoderm, and ectoderm cell lineages. Subsequent studies determined the molecular explanation for such spatial patterning in response to a uniform morphogen cue. The geometric confinement of hESCs resulted in an asymmetric distribution of BMP4 receptors, so that cells at the edge of the colony were more receptive to the BMP4 ligand (*140*). In addition, BMP4 signaling activated secretion of the BMP4 protein inhibitor NOGGIN (*141*), which, due to protein diffusion, accumulated in the colony center, further reinforcing the spatial asymmetry in BMP4 signaling (*140*). This pioneering work established a system for modeling the cell-cell interactions and signal regulation between the adjacent germ layers. It has since been used to show that the WNT/NODAL/BMP4 signaling cascade found in the mouse epiblast (*76*) is conserved in hESCs (*142*) and that the combination of WNT and NODAL signaling can establish a signaling center (‘organizer’) for patterning the ectoderm cell lineage (*142*, *143*).

Human ESCs have also been recently used to develop three-dimensional (3D) cell culture models of the epiblast. Due to the apicobasal polarization of hESCs, cell aggregates self-organize into spherical lumenized structures termed spheroids when cultured in an extracellular matrix such as Matrigel (*112*). In a study that parallels mESC-based gastruloid models, hESC aggregates were grown in the absence of extraembryonic tissues or external signal asymmetry. Such aggregates broke symmetry and induced gastrulation-like events like EMT and mesoderm differentiation in response to uniform BMP4, mediated through downstream Wnt and Dkk1 signaling (*144*). In addition, a model for post-implantation amniotic sac development has also been developed using hESCs (*145*, *146*). Cultures of hESC aggregates grown on a gel substrate induced symmetry-breaking to generate squamous, amniotic ectoderm-like epithelium at one side and a columnar, embryonic disc-like epithelium on the other side, mediated through BMP signaling (*145*). Though a promising model for studies of amniotic sac development, patterning of the epiblast was limited and aggregate symmetry-breaking was mediated by undefined factors from the tumor-derived gel bed. Future hESC-based studies would therefore benefit from novel engineered methods for defined and spatiotemporal control of signal cues as well as cell co-culture systems with human extraembryonic tissues such as trophoblast stem cells (*117, 147*). For both mESC and hESC-based models, mechanistic insight into morphogenesis has been limited since their self-organization is a result of spontaneous and heterogeneous differentiation along diverse cell lineages rather than specific control of cell signaling pathways. How specific morphogen signals direct self-organization, cell fate specification, and migration in such early developmental models remains unknown.

1.3 Optogenetic control of cellular signaling

The field of optogenetics has sought to address the need for biological methods for controlling signal dynamics. Optogenetic approaches use light-responsive photoreceptor domains from plants, algae, and bacteria to control signaling and protein-protein interactions in mammalian cells (*148*). This approach enables specific control of target pathways with the unique advantage of using optics and illumination patterning to stimulate signaling in a specific location and at a specific time (Figure 1.5A) (*149*).

Optogenetics originated with the discovery of channelrhodopsins, a class of ion channels that open in response to a stimulus of light within the green algae *Chlamydomonas reinhardtii* (*150, 151*). When expressed in neurons of other organisms, light-gated channel opening resulted in an influx of cations that initiated an action potential in target cells, including mammalian neurons, mouse retina, spines of chicken embryos, and worms (*152–156*) (Figure 1.5B). Such seminal studies have led to a transformation of the field of neuroscience (*157–159*). To complement optical activation of neural signaling, light-sensitive domains have also been discovered or engineered that inhibit neural firing through membrane hyperpolarization (*160–165*).

Beyond rhodopsins, organisms have developed a vast variety photoreceptors over the course of evolution, including the major classes of photosensory proteins: BLUF domains (blue light utilizing flavin adenine dinucleotide), LOV domains (light-oxygen-voltage-sensing domains), cryptochromes, phototropins, phytochromes, and UVR8 (ultraviolet-B receptor 8). Since their discovery, such photosensory domains have been optimized and repurposed to place intracellular signaling pathways and protein-protein interactions under light control in mammalian cells (*149, 166*). These optogenetic techniques now allow activation of target signals with spatial and temporal precision (Figure 1.5C).

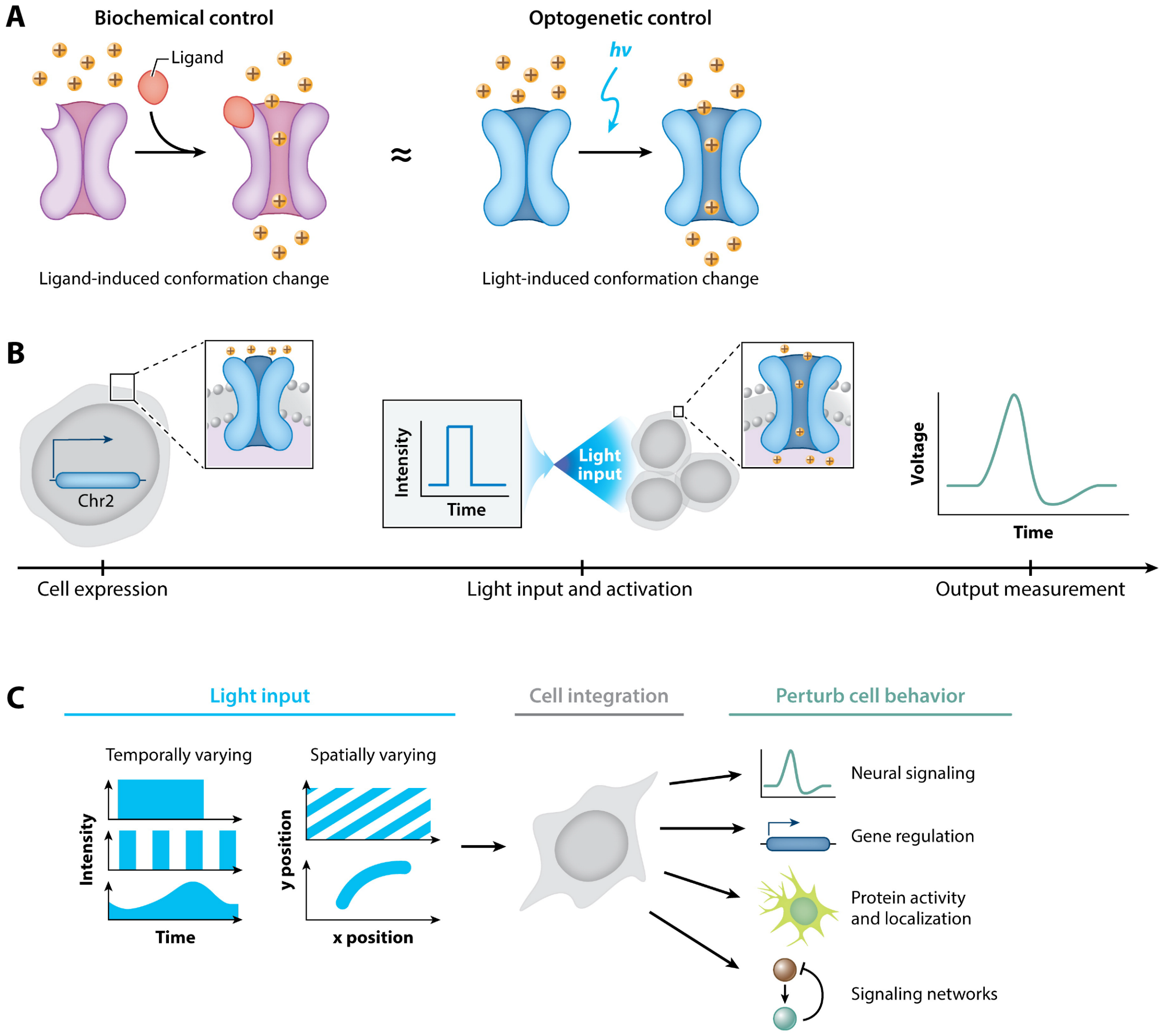

Figure 1.5: **User-defined control of protein behavior using optogenetics**
A) Light-activated channelrhodopsins (blue, right) mimic neurotransmitter-activated ion channel opening (violet, left). **B)** Experimental workflow of a typical optogenetic experiment. Optogenetic constructs are stably expressed in a cell (left); user-defined illumination patterns activate optogenetic proteins (middle); cell output, such as an action potential, is measured (right). **C)** Biological applications of optogenetic methods. Temporally and/or spatially varying input signals (left) are integrated by a cell (middle) to control and study a variety of cell behaviors (right).

1.3.1 Optogenetic photosensors for light-regulated control of cellular signaling pathways

1.3.1.1 Caged proteins

Light control over a protein's activation state is a powerful tool for investigating and controlling cell behavior in a precise, noninvasive manner. Optogenetic systems have been developed to retain a target protein in an inactive (i.e., caged) state via steric hindrance from a specialized, light- responsive domain; however, light stimulation induces a conformational change that liberates the protein to interact with its substrate or target protein (i.e., light-induced uncaging). Such optogenetic tools, predominantly based on a plant light, oxygen, and voltage photosensory domain, allow reversible control over protein signaling.

A widely studied and used caging domain is the light, oxygen, and voltage (LOV) domain isolated from the plant photosensor phototropin 1 (phot1). Originally studied for its involvement in light-responsive plant growth, phot1 contains two LOV domains that mediate the activity of its kinase effector domain through blue light– responsive uncaging (*167*, *168*). The second LOV domain, LOV2, plays the dominant role in kinase activation (*169*) and has been engineered as an optogenetic tool for light control of mammalian protein activity (*170*). In the dark state, the Avena sativa (oat) LOV2 domain (AsLOV2) binds its C-terminal helix, Jα, which resides in a folded state against the LOV domain core (*171*) (Figure 1.5B). Photoactivation with blue light converts the noncovalent interaction between the LOV core and its bound flavin chromophore, FMN, into a covalent one through a conserved cysteine residue. The accompanying light-induced conformational change displaces the Jα helix away from the protein core, leading to uncaging of a fused effector domain (e.g., the kinase domain of phot1) (*171*, *172*). The Jα helix reverts to its dark-state caged conformation within minutes owing to spontaneous decay of the protein-cofactor bond (Table 1). Optogenetic methods can mimic this light-induced uncaging of the phot1 kinase domain by fusing signaling domains of interest to AsLOV2, in place of the phot1 domain.

However, several limitations of the native AsLOV2 domain have motivated efforts to engineer improved variants. First, when fused to foreign protein domains, spontaneous undocking of the Jα helix can lead to a relatively high dark-state activity, resulting in a low dynamic range upon AsLOV2 uncaging (*173*). For example, the light-inducible DNA-binding system LovTAP has only a fivefold change in DNA affinity between the dark and illuminated states (*174*). To address this issue, Strickland et al. (*173*) used rational design to introduce four mutations into AsLOV2 that stabilized the docking of Jα to the LOV core. This increased the dynamic range of LovTAP from 5-fold to 70-fold, an approach that can be applied to other LOV domain optogenetic systems to reduce dark-state activity. AsLOV2 fusions are also particularly sensitive to linker lengths and the size and structure of attached domains (*175*, *176*), and as a result, each new fusion protein switch requires optimization to achieve low dark-state and high light-state activity in mammalian cells.

Various light-responsive domains can also be integrated into a target protein to replace ligand-binding domains with light-sensing domains. For example, addition of rhodopsin domains or LOV domains into a protein of interest can place transmembrane receptors under light control (*177–179*).

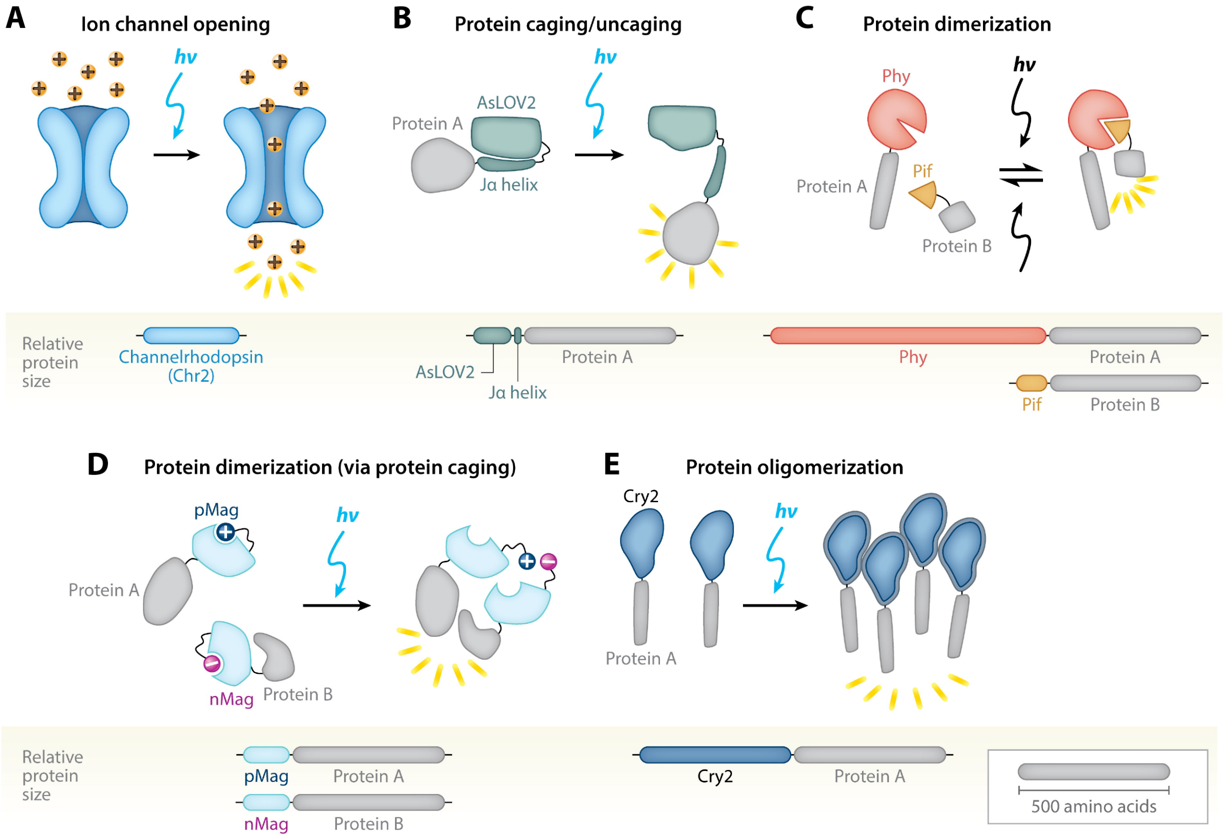

Figure 1.6: **Overview of the major classes of optogenetic systems**
Protein size indicated by relative size of bars, and sample proteins A/B are drawn to a scale of 500 amino acids. **A)** Light-induced ion channel (blue) opens in response to blue light to allow cation passage (yellow balls). **B)** Jα helix unfolds from AsLOV2 core (green) to uncage a fused protein (gray). **C)** Reversible interaction between Phy (red) and Pif (orange) leads to dimerization of attached domains (gray). **D)** Light-induced uncaging of affinity domains [positive domain of pMag (dark blue) and negative domain of nMag (pink)] results in dimerization of attached domains (gray). **E)** Cry2 (blue) clusters an attached protein (gray) in response to light.

1.3.1.2 Dimerizing systems

Protein-protein interactions are a frequent driver of molecular processes. The ability to control such interactions with light is a powerful tool for controlling many aspects of cell behavior. Light- inducible dimerizers are the most diverse class of optogenetic systems, with varying properties such as homo- versus heterodimerization, binding kinetics, reversibility, and absorption spectra, which allow for a wide variety of applications to biological systems.

A recent study has performed a detailed and systematic comparison of commonly used blue-light dimerization systems to identify optimal systems for desired biological applications (*180*).

Phytochromes Phytochromes are a class of proteins that regulate plant growth and develop- ment in response to red light. The mechanism of Arabidopsis thaliana phytochrome B (PhyB) is particularly well studied and has been harnessed for optogenetic control of protein-protein association (*181*, *182*). PhyB contains two primary structural domains: a light-absorbing N-terminal photosensory domain and a C-terminal effector domain that interacts with downstream pathway components (*183*). The PhyB light-sensing capability arises from a tetrapyrrole chromophore, such as phycocyanobilin, covalently bound by the photosensory domain. Absorption of red (650-nm) light triggers chromophore photoisomerization, a rotation about a carbon-carbon double bond that is reversed with the absorption of far-red (750-nm) light (*182*). This light-induced structural change triggers a conformational change in the surrounding protein that in turn modulates the biological activity of the photoreceptor. In the dark, or after absorption of far-red light, PhyB is biologically inactive and does not bind effector proteins; however, upon illumination with red light, PhyB binds to a class of target transcription factors termed phytochrome-interacting factors (Pifs) (*184*) (Figure 1.6C). This light-induced, reversible Phy/Pif dimerization is harnessed to optogenetically stimulate protein-protein interactions in mammalian cells (*181*). Fusion of proteins or localization signals of interest to optimized, truncated versions of PhyB and Pif6 (the so-called Phy/Pif system) can be used to control the interaction state of the attached domains with red and far-red light (*181*). Recently, a near-infrared-responsive alternative to the Phy/Pif system has been engineered based on the reversible interaction of bacterial phytochrome BphP1 with its partner PpsR2 (*185*)(Table 1). Since its discovery, the BphP1-PpsR2 system has been further engineered to enhance dimerization and decrease the size of the dimerizing domains (*186*, *187*).

The main advantages of the Phy/Pif and BphP1/PpsR2 systems are their triggered reversibility and speed. That is, unlike most optogenetic systems whose excited state decays spontaneously, the dissociation of these systems can be induced with light. Moreover, the fast on/off rate of Phy/Pif (with half-times on the order of seconds) allows for studies that perturb protein behavior at precise and/or short timescales. Such tools are particularly valuable for studying the dynamics of intracellular signaling networks and of signal presentation during cell development. Lastly, such phytochrome-based dimerizing systems are responsive to long-wavelength (red to near- infrared) light, whose lower-energy photons are less phototoxic to cells compared with blue or UV light and can penetrate deeper into tissues. That said, several considerations remain for Phy/Pif and BphP1/PpsR2 expression in mammalian cells. Whereas the BphP1 chromophore is endogenously present in mammalian cells, the PhyB chromophore is not and requires purification and supplementation to the cell culture medium or injection in vivo for cell uptake prior to photoactivation (*181*, *188*, *189*). Pharmacokinetic considerations could lead to variable outcomes in vivo. In addition, the cell expression levels of the phytochromes, as well as the expression ratio between them and their binding partners, have an effect on the dimerization efficiency (*190*). Lastly, phytochromes are large proteins that can be sensitive to fusions and linker lengths, potentially complicating the development of more complex systems (*188*).

Cryptochromes for dimerization Another such dimerizing module is the cryptochrome 2 (Cry2) and CIB1 protein pair, derived from the flowering plant *A. thaliana*. It consists of a basic helix-loop-helix protein, CIB1, and a blue light–sensitive protein, Cry2, that binds CIB1 in its photoexcited state. Unlike several such dimerizers, this module does not require any exogenously added cofactors, as it uses chromophores ubiquitously present in biological systems. Specifically, Cry2 becomes light responsive as it binds the flavin and pterin chromophores in its conserved N-terminal photolyase homology region (PHR). Kennedy et al. (*191*) showed that the PHR domain of Cry2 (Cry2PHR) alone, when used with a full-length CIB1 or CIB1 lacking the basic helix-loop-helix domain (CIBN), was sufficient to mediate robust and specific light-sensitive protein dimerization. Both Cry2/CIBN and Cry2PHR/CIBN pairs had very similar association and dissociation kinetics: The dimerization reached ∼90% completion within a matter of seconds of exposure to a 100-ms blue-light (488-nm) pulse, whereas the dissociation took place more gradually over an ∼10 min period (Table 1). The observed dimerization and dissociation kinetics were highly reproducible over successive blue light–exposure cycles, indicating stable maintenance of a high level of efficacy in the system. In addition, two-photon excitation at ∼860 nm was reported to be sufficient to activate the interaction (*191*). Finally, Taslimi et al. (*192*) recently reported two truncated versions of Cry2, Cry2(515) and Cry2(535), that exhibit significantly reduced background interaction with CIB1 in the dark. Also, two mutants of Cry2, L348F and W349R, showing slower and faster dissociation kinetics with CIB1 were reported. The Cry2-CIBN dimerization has, for example, been used for optogenetic control of epigenetic state (*193*) and gene expression (*194*).

Caged proteins for dimerization Another optogenetic method to induce protein dimerization makes use of the light-induced uncaging of LOV domain-based proteins (see section titled Light, Oxygen, and Voltage Domain Caging). Certain photoreceptors that contain LOV domains possess the inherent ability to dimerize upon blue light exposure, whereas others have been engineered to dimerize using synthetic dimerization domains. The most prominent examples of the former are the FKF1/Gigantea, EL222, and Vivid (VVD)-based systems, while the tunable light-inducible protein (TULIP) and improved light-inducible dimerization system (iLID) systems are examples of the latter (Table 1). The unifying principal is that, upon illumination, a conformational change in the protein exposes a binding site for a specific second protein, resulting in homo- or heterodimerization (Figure 1.6D).

FKF1 is an A. thaliana photoreceptor that regulates flowering onset by sensing blue light levels with its LOV domain (*195*). In particular, blue light stimulation triggers an FKF1 conformational change that stimulates heterodimerization with its binding partner Gigantea

(*195, 196*), a capability that has been adapted for optogenetic control of protein association in mammalian cells (*197*). Unlike the canonical Phot1-based LOV uncaging system, however, the dark-state reversion of FKF1/Gigantea binding is on the order of tens of hours (*196*), allowing long-lasting dimer formation after a single light stimulation, a property that is useful for long-term activation studies but occurs at the expense of temporal and spatial resolution.

The natural homodimerization properties of the bacterial transcription factor EL222 have also been harnessed for optogenetics. Homodimerization is mediated by a LOV domain that, in dark, binds and inhibits a helix-turn-helix DNA-binding domain (*198*). Upon light activation, the helix-turn-helix domain is uncaged and mediates the dimerization, yielding a complex that binds a target DNA sequence (*198–200*). Thus, the most direct application of the EL222 system is for transcriptional control or DNA modification (*200*). However, upon truncation of its target DNA- binding sequence, EL222 could also be used for the regulation of protein association with rapid on-off kinetics (Table 1). Indeed, the EL222 system has been recently used to engineer synthetic biological circuits and regulate cellular metabolism and chemical production in microbes (*201, 202*).

The fungal photoreceptor VVD is the smallest LOV domain–containing protein. Its N-terminal helix undergoes a conformational change upon photoexcitation (*203*), leading to homo- dimerization (*204*) and thus to close association of attached domains of interest (*205*). However, VVD's slow off kinetics (half-life of dissociation, $T_{d1/2} = 2.8$ h) and limitation to homodimerization prompted the development of an improved optogenetic system that incorporated either positive or negative amino acids into the VVD N-terminal helix. These so-called Magnets, one with negative (nMag) and one with positive (pMag) residues, preferentially heterodimerize because electrostatic repulsion impairs the natural homodimerization (*206*) (Figure 1.6D). Furthermore, multiple variants with faster dissociation kinetics (on the order of seconds) and optimized dimerization efficiencies were created (*206, 207*). Its small size and fast kinetics make Magnets one of the most robust dimerization systems and allow for precise subcellular control of protein association with high spatiotemporal resolution.

Another class of light-inducible dimerizers uses engineered synthetic peptides to mediate protein interactions. Specifically, the TULIP optogenetic system harnesses LOV domain uncaging to induce dimerization. In the dark state, a peptide epitope fused to the Jα helix of AsLOV2 (LOVpep) is sterically blocked from interaction with the coexpressed synthetic PDZ affinity clamp protein domain (ePDZ) (*208, 209*). After photostimulation, light-induced unwinding of the LOVpep Jα helix exposes the epitope, leading to dimerization between LOVpep and ePDZ (*208*). One question that remains to be explored is whether this system is orthogonal to endogenous proteins and signaling pathways, as proteins containing PDZ domains or their binding targets are ubiquitously present in yeast and mammalian cells (*210*). To address this issue, an iLID was generated using AsLOV2-based uncaging of SsrA, an Escherichia coli peptide that binds the SspB adapter protein (*211*). Through a phage display selection, this system was engineered to have low dark-state binding, a high dynamic range, and fast on/off kinetics (*211*).

Finally, LOV domains from a variety of organisms have been screened to identify variants with desired characteristics (*212*). For example, an aureochrome LOV domain was identified that is able to activate receptor tyrosine kinase signaling through dimerization (*213*). In addition, photosensors unrelated to LOV domains have been modified to introduce light-responsive dimerization ability. For example, the fluorescent protein Dronpa was mutated to dimerize in response to cyan light and dissociate in response to violet light (*214*, *215*). In the future, LOV domains and other new photosensors with novel properties will likely be discovered in a variety of other organisms.

1.3.1.3 Oligomerizing systems

Many signal transduction receptors and effectors undergo oligomerization as part of their signal activation. Hence, optogenetic systems that form multimeric clusters in response to light are useful tools for regulating biological activities that depend on protein oligomerization.

In 2013, Bugaj et al. (*216*) demonstrated that upon blue light stimulation, Cry2PHR —- a system previously explored for mediating heterodimerization with partner CIBN —- can, on its own, oligomerize in mammalian cells to generate visible protein clusters within ∼10 s (Figure 1.6E). The number of clusters increased sigmoidally over time, with a half-maximal time of association (Ta1/2) that varied inversely with illumination intensity and had a mean of 30 s. Furthermore, upon light withdrawal, the number of Cry2 clusters decreased exponentially with a half-life of dissociation ($T_{d1/2}$) of ∼5.5 min (Table 1). Like the Cry2PHR/CIBN pair, Cry2PHR exhibited very little loss in maximal response upon repeated clustering and declustering, indicating the system can be harnessed intracellularly for extended times. Researchers also reported dynamic exchange of Cry2 subunits between different clusters as well as the bulk protein, colocalization of CIB1 along with the Cry2 clusters, and a level of homooligomerization that depended on overall Cry2 expression levels (*216*). Recent protein purification studies along with multiangle light scattering (SEC-MALS) experiments have shown that Cry2PHR most likely forms a tetramer (*217*), which may be subject to higher-order oligomerization. Recently, an E490G mutation in the protein has been shown to greatly enhance the amount of clustering in the Cry2 system (*218*). It was shown that 40–90% of this cytosolic protein, named Cry2olig, immediately formed clusters when exposed to blue light. The clustering kinetics were again reported to be dependent on both the protein concentration in the cell and the light dose, with the half-maximal time of association (Ta1/2) varying between 15 and 75 s. In contrast, the half-life of dissociation ($T_{d1/2} = 23.1$ min) is significantly longer in Cry2olig than in wild-type Cry2PHR. Additionally, Cry2olig is capable of incorporating Cry2PHR in its cluster, and the photoresponse can be triggered by using two-photon excitation at a wavelength of 850 nm.

A recent study has shed light on the paradox of Cry2–Cry2 homo-oligomerization versus Cry2–CIB1 hetero-dimerization. The N-terminal charges of Cry2 were found to be critical for Cry2–CIB1 interaction, whereas two C-terminal residues mediate Cry2 oligomerization (*219*). Electrostatic interactions between Cry2 molecules at the C-terminal Arg489 and Glu490 are critical for oligomerization, and if Glu490 is replaced with a neutral or positively-charged residue, oligomerization is enhances. Indeed, this prediction is consistent the E490G mutation of Cry2olig, which enhances oligomerization over the naturally ocurring Cry2. Conversely, engineering C-terminal residues to be negatively-charged reduces oligomerization and creates a Cry2 variant with enhanced dimerization capabilities (*219*).

Cry2 oligomerization systems have been further engineered to create a Cry2-based clustering module termed CLICR (clustering indirectly using Cry2). This system was used to achieve endogenous transmembrane clustering and subsequent activation in mammalian and neural stem cells (*220*). The Cry2/CIBN and Cry2 modules have also found application in several other cellular biological phenomena, including, but not limited to, signal transduction, transcription, and protein-protein interactions (*191*, *216*, *218*, *220*). Cry2 oligomerization has also been recently used to induce phase separation of transciption factors as a method to control gene regulation (*221–223*).

Beyond Cry-based oligomerization, a tetramerizing system has been discovered in bacteria based on the native light-responsive transcription factor CarH. The photoresponsive, cobalamin (vitamin B12) - binding domain, CarH, forms tetramers in the dark, which dissociate in response to green-light illumination (*224–226*). Such green light-induced inactivation has been used to control fibroblast growth factor receptors in zebrafish embryos (*227*) and gene regulation in plants (*228*).

1.3.2 Optogenetic control of signaling in stem cell and developmental biology

Within mammalian cells, optogenetic tools that control protein-protein interactions have been developed for diverse signaling pathways such as Ras/Raf/Mek/Erk (*190*, *229–231*), fibroblast growth factor (FGF) (*227*), and Rho-family GTPase signaling (*181*, *197*, *208*, *211*, *220*, *232*). Optogenetic methods have also been recently applied to studies in developmental biology in key model organisms (*166*). For example, in Drosophila and zebrafish embryos, dynamic control of signaling elucidated the spatiotemporal limits of ERK (*229*, *231*), Nodal (*233*), and Bicoid (*234*) patterning and how local modulation of cell migration and contractility drives tissue morphogenesis (*178*, *235*, *236*). However, optogenetic control of signaling has not yet been achieved in mouse embryos or in mouse and human embryonic stem cell systems.

1.4 Research purpose and dissertation overview

A variety of open questions remain regarding the origin of signaling asymmetry and molecular regulation of cell fate patterning in early development. The origin of symmetry-breaking remains ambiguous, as patterning from extra-embryonic tissues, stochastic fluctuations in gene expression, or intrinsic heterogeneity within epiblast cells have been proposed as potential mechanisms for emergence of asymmetry within the mouse embryo (*41*, *237–240*). Within ESC models for early gastrulation, similar ambiguities remain. The origin of symmetry-breaking could reside in extra-embryonic tissues, as exemplified by studies that use co-cultures of ESCs and extra-embryonic cell types (*117*, *123*, *124*), or could be due to internal self-patterning of cells, as supported by the spontaneous self-organization of ESC aggregates (*126*, *129–131*). In addition, due to the complex feedback loops that self-regulate BMP, Nodal, and Wnt signaling, the specific morphogen signals responsible for patterning and symmetry-breaking are poorly understood (*56*, *64*, *76*, *82*), as are the temporal dynamics, intensity and duration thresholds, and spatial limits for cell fate patterning . During gastrulation, such signaling dynamics likely regulate the cell fate outcome of differentiating epiblast cells as they mature toward a mesodermal, endodermal, and ectodermal lineage (*50*, *54*, *55*, *104*). However, the mechanistic regulation of such fate patterning in the context of a larger tissue environment remains a mystery. Furthermore, the cell migration properties, morphology, and surface receptors that mediate cell-cell interactions during this dynamic process of primitive streak formation and gastrulation have remained unstudied due to the experimental challenges of imaging and labelling of live embryos (*241*). Though it is clear that spatial and temporal signal patterns regulate early embryonic development, insight into the origins, mechanism, and signal dynamics of embryonic patterning has been limited by a lack of tools that are able to perturb patterns in space and time.

To address such open questions in the field, we sought develop a tool that is able to control morphogen patterns in space and time. We use an optogenetic approach based on the blue light-induced oligomerization of the Cry2 photoreceptor fused to the Wnt co-receptor LRP6c to activate canonical β-catenin signaling (*216*). In chapter 2, we engineer illumination devices that activate Wnt/β-catenin signaling in hESCs at user-defined intensities, temporal sequences, and spatial locations. In Chapter 3, we design a fluorescence microscope capable of optogenetic stimulation with user-defined, high-resolution, and dynamic patterns as well as super-resolution imaging. Lastly, in Chapter 4, we use our engineered optical and genetic tools to activate Wnt signaling in specific hESC subpopulations and investigate the cell-cell interactions and migration dynamics that regulate early embryonic symmetry-breaking. We develop an *in vitro* ESC model for studying Wnt-mediated patterning and find that Wnt plays an instructive role for mediating tissue self-organization through cell migration and EMT.

References

1. Ishiuchi, T. & Torres-Padilla, M.-E. Towards an Understanding of the Regulatory Mechanisms of Totipotency. *Current Opinion in Genetics & Development. Cell Reprogramming* **23,** 512–518 (2013).
2. Leung, C. Y. & Zernicka-Goetz, M. Mapping the Journey from Totipotency to Lineage Specification in the Mouse Embryo. *Current Opinion in Genetics & Development. Cell Reprogramming, Regeneration and Repair* **34,** 71–76 (2015).
3. Tarkowski, A. K. Experiments on the Development of Isolated Blastomeres of Mouse Eggs. *Nature* **184,** 1286 (1959).
4. Piotrowska, K., Wianny, F., Pedersen, R. A. & Zernicka-Goetz, M. Blastomeres Arising from the First Cleavage Division Have Distinguishable Fates in Normal Mouse Development. *Development (Cambridge, England)* **128,** 3739–3748 (2001).
5. Casser, E. *et al.* Totipotency Segregates between the Sister Blastomeres of Two-Cell Stage Mouse Embryos. *Scientific Reports* **7,** 8299 (2017).
6. Plusa, B. *et al.* The First Cleavage of the Mouse Zygote Predicts the Blastocyst Axis. *Nature* **434,** 391 (2005).
7. Piotrowska-Nitsche, K., Perea-Gomez, A., Haraguchi, S. & Zernicka-Goetz, M. Four-Cell Stage Mouse Blastomeres Have Different Developmental Properties. *Development* **132,** 479–490 (2005).
8. Goolam, M. *et al.* Heterogeneity in Oct4 and Sox2 Targets Biases Cell Fate in 4-Cell Mouse Embryos. *Cell* **165,** 61–74 (2016).
9. Torres-Padilla, M.-E., Parfitt, D.-E., Kouzarides, T. & Zernicka-Goetz, M. Histone Arginine Methylation Regulates Pluripotency in the Early Mouse Embryo. *Nature* **445,** 214–218 (2007).
10. Fujimori, T., Kurotaki, Y., Miyazaki, J.-i. & Nabeshima, Y.-i. Analysis of Cell Lineage in Two- and Four-Cell Mouse Embryos. *Development* **130,** 5113–5122 (2003).
11. White, M. D. *et al.* Long-Lived Binding of Sox2 to DNA Predicts Cell Fate in the Four-Cell Mouse Embryo. *Cell* **165,** 75–87 (2016).
12. Guo, G. *et al.* Resolution of Cell Fate Decisions Revealed by Single-Cell Gene Expression Analysis from Zygote to Blastocyst. *Developmental Cell* **18,** 675–685 (2010).
13. Kurotaki, Y., Hatta, K., Nakao, K., Nabeshima, Y.-i. & Fujimori, T. Blastocyst Axis Is Specified Independently of Early Cell Lineage But Aligns with the ZP Shape. *Science* **316,** 719–723 (2007).
14. Kelly, S. J. Studies of the Developmental Potential of 4- and 8-Cell Stage Mouse Blastomeres. *Journal of Experimental Zoology* **200,** 365–376 (1977).
15. Zhang, H. T. & Hiiragi, T. Symmetry Breaking in the Mammalian Embryo. *Annual Review of Cell and Developmental Biology* **34,** 405–426 (2018).

16. Ducibella, T. & Anderson, E. Cell Shape and Membrane Changes in the Eight-Cell Mouse Embryo: Prerequisites for Morphogenesis of the Blastocyst. *Developmental Biology* **47,** 45–58 (1975).

17. Moriwaki, K., Tsukita, S. & Furuse, M. Tight Junctions Containing Claudin 4 and 6 Are Essential for Blastocyst Formation in Preimplantation Mouse Embryos. *Developmental Biology* **312,** 509–522 (2007).

18. Hyafil, F., Morello, D., Babinet, C. & Jacob, F. A Cell Surface Glycoprotein Involved in the Compaction of Embryonal Carcinoma Cells and Cleavage Stage Embryos. *Cell* **21,** 927–934 (1980).

19. Maître, J.-L., Niwayama, R., Turlier, H., Nédélec, F. & Hiiragi, T. Pulsatile Cell-Autonomous Contractility Drives Compaction in the Mouse Embryo. *Nature Cell Biology* **17,** 849–855 (2015).

20. Johnson, M. H. & Ziomek, C. A. The Foundation of Two Distinct Cell Lineages within the Mouse Morula. *Cell* **24,** 71–80 (1981).

21. Tarkowski, A. K. & Wróblewska, J. Development of Blastomeres of Mouse Eggs Isolated at the 4- and 8-Cell Stage. *Development* **18,** 155–180 (1967).

22. Balakier, H. & Pedersen, R. A. Allocation of Cells to Inner Cell Mass and Trophectoderm Lineages in Preimplantation Mouse Embryos. *Developmental Biology* **90,** 352–362 (1982).

23. Nishioka, N. *et al.* The Hippo Signaling Pathway Components Lats and Yap Pattern Tead4 Activity to Distinguish Mouse Trophectoderm from Inner Cell Mass. *Developmental Cell* **16,** 398–410 (2009).

24. Hirate, Y. *et al.* Polarity-Dependent Distribution of Angiomotin Localizes Hippo Signaling in Preimplantation Embryos. *Current Biology* **23,** 1181–1194 (2013).

25. Korotkevich, E. *et al.* The Apical Domain Is Required and Sufficient for the First Lineage Segregation in the Mouse Embryo. *Developmental Cell* **40,** 235–247.e7 (2017).

26. Maître, J.-L. *et al.* Asymmetric Division of Contractile Domains Couples Cell Positioning and Fate Specification. *Nature* **536,** 344–348 (2016).

27. Chan, C. J. *et al.* Hydraulic Control of Mammalian Embryo Size and Cell Fate. *Nature* **571,** 112 (2019).

28. Barcroft, L. C., Offenberg, H., Thomsen, P. & Watson, A. J. Aquaporin Proteins in Murine Trophectoderm Mediate Transepithelial Water Movements during Cavitation. *Developmental Biology* **256,** 342–354 (2003).

29. Bischoff, M., Parfitt, D.-E. & Zernicka-Goetz, M. Formation of the Embryonic-Abembryonic Axis of the Mouse Blastocyst: Relationships between Orientation of Early Cleavage Divisions and Pattern of Symmetric/Asymmetric Divisions. *Development* **135,** 953–962 (2008).

30. Gardner, R. L. Flow of Cells from Polar to Mural Trophectoderm Is Polarized in the Mouse Blastocyst. *Human Reproduction* **15,** 694–701 (2000).

31. Frias-Aldeguer, J. *et al.* Embryonic Signals Perpetuate Polar-like Trophoblast Stem Cells and Pattern the Blastocyst Axis. *bioRxiv,* 510362 (2019).

32. Chazaud, C., Yamanaka, Y., Pawson, T. & Rossant, J. Early Lineage Segregation between Epiblast and Primitive Endoderm in Mouse Blastocysts through the Grb2-MAPK Pathway. *Developmental Cell* **10,** 615–624 (2006).

33. Ohnishi, Y. *et al.* Cell-to-Cell Expression Variability Followed by Signal Reinforcement Progressively Segregates Early Mouse Lineages. *Nature Cell Biology* **16,** 27–37 (2014).

34. Plusa, B., Piliszek, A., Frankenberg, S., Artus, J. & Hadjantonakis, A.-K. Distinct Sequential Cell Behaviours Direct Primitive Endoderm Formation in the Mouse Blastocyst. *Development* **135,** 3081–3091 (2008).

35. Yamanaka, Y., Lanner, F. & Rossant, J. FGF Signal-Dependent Segregation of Primitive Endoderm and Epiblast in the Mouse Blastocyst. *Development* **137,** 715–724 (2010).

36. Morris, S. A. *et al.* Origin and Formation of the First Two Distinct Cell Types of the Inner Cell Mass in the Mouse Embryo. *Proceedings of the National Academy of Sciences* **107,** 6364–6369 (2010).

37. Chambers, I. *et al.* Functional Expression Cloning of Nanog, a Pluripotency Sustaining Factor in Embryonic Stem Cells. *Cell* **113,** 643–655 (2003).

38. Mitsui, K. *et al.* The Homeoprotein Nanog Is Required for Maintenance of Pluripotency in Mouse Epiblast and ES Cells. *Cell* **113,** 631–642 (2003).

39. Fujikura, J. *et al.* Differentiation of Embryonic Stem Cells Is Induced by GATA Factors. *Genes & Development* **16,** 784–789 (2002).

40. Meilhac, S. M. *et al.* Active Cell Movements Coupled to Positional Induction Are Involved in Lineage Segregation in the Mouse Blastocyst. *Developmental Biology* **331,** 210–221 (2009).

41. Arnold, S. J. & Robertson, E. J. Making a commitment: cell lineage allocation and axis patterning in the early mouse embryo. *Nat. Rev. Mol. Cell Biol.* **10,** 91–103 (2009).

42. Brenner, C. A., Adler, R. R., Rappolee, D. A., Pedersen, R. A. & Werb, Z. Genes for Extracellular-Matrix-Degrading Metalloproteinases and Their Inhibitor, TIMP, Are Expressed during Early Mammalian Development. *Genes & Development* **3,** 848–859 (1989).

43. Perona, R. M. & Wassarman, P. M. Mouse Blastocysts Hatch in Vitro by Using a Trypsin-like Proteinase Associated with Cells of Mural Trophectoderm. *Developmental Biology* **114,** 42–52 (1986).

44. Bedzhov, I. & Zernicka-Goetz, M. Self-Organizing Properties of Mouse Pluripotent Cells Initiate Morphogenesis upon Implantation. *Cell* **156,** 1032–1044 (2014).

45. Nichols, J. & Smith, A. Naive and Primed Pluripotent States. *Cell Stem Cell* **4,** 487–492 (2009).

46. Payer, B. Developmental Regulation of X-Chromosome Inactivation. *Seminars in Cell & Developmental Biology. X Chromosome Inactivation* **56,** 88–99 (2016).

47. Cheng, S. *et al.* Single-Cell RNA-Seq Reveals Cellular Heterogeneity of Pluripotency Transition and X Chromosome Dynamics during Early Mouse Development. *Cell Reports* **26,** 2593–2607.e3 (2019).

48. Mohammed, H. *et al.* Single-Cell Landscape of Transcriptional Heterogeneity and Cell Fate Decisions during Mouse Early Gastrulation. *Cell Reports* **20,** 1215–1228 (2017).

49. McDole, K. *et al.* In Toto Imaging and Reconstruction of Post-Implantation Mouse Development at the Single-Cell Level. *Cell* **175,** 859–876.e33 (2018).

50. Saykali, B. *et al.* Distinct mesoderm migration phenotypes in extra-embryonic and embryonic regions of the early mouse embryo. *eLife* **8,** 91 (2019).

51. Williams, M., Burdsal, C., Periasamy, A., Lewandoski, M. & Sutherland, A. The Mouse Primitive Streak Forms in Situ by Initiation of Epithelial to Mesenchymal Transition without Migration of a Cell Population. *Developmental Dynamics* **241,** 270–283 (2012).

52. Thiery, J. P., Acloque, H., Huang, R. Y. J. & Nieto, M. A. Epithelial-mesenchymal transitions in development and disease. *Cell* **139,** 871–890 (2009).

53. Ciruna, B. & Rossant, J. FGF signaling regulates mesoderm cell fate specification and morphogenetic movement at the primitive streak. *Dev. Cell* **1,** 37–49 (2001).

54. Lawson, K. A., Meneses, J. J. & Pedersen, R. A. Clonal analysis of epiblast fate during germ layer formation in the mouse embryo. *Development* **113,** 891–911 (1991).

55. Kinder, S. J. *et al.* The orderly allocation of mesodermal cells to the extraembryonic structures and the anteroposterior axis during gastrulation of the mouse embryo. *Development* **126,** 4691–4701 (1999).

56. Winnier, G., Blessing, M., Labosky, P. A. & Hogan, B. L. Bone morphogenetic protein-4 is required for mesoderm formation and patterning in the mouse. *Genes Dev.* **9,** 2105–2116 (1995).

57. Tam, P. P. & Beddington, R. S. The Formation of Mesodermal Tissues in the Mouse Embryo during Gastrulation and Early Organogenesis. *Development* **99,** 109–126 (1987).

58. Kwon, G. S., Viotti, M. & Hadjantonakis, A.-K. The Endoderm of the Mouse Embryo Arises by Dynamic Widespread Intercalation of Embryonic and Extraembryonic Lineages. *Developmental Cell* **15,** 509–520 (2008).

59. Yamanaka, Y., Tamplin, O. J., Beckers, A., Gossler, A. & Rossant, J. Live Imaging and Genetic Analysis of Mouse Notochord Formation Reveals Regional Morphogenetic Mechanisms. *Developmental Cell* **13,** 884–896 (2007).

60. Viotti, M., Foley, A. C. & Hadjantonakis, A.-K. Gutsy moves in mice: cellular and molecular dynamics of endoderm morphogenesis. *Philosophical Transactions of the Royal Society B: Biological Sciences* **369,** 20130547–20130547 (2014).

61. Rossant, J. & Tam, P. P. L. Blastocyst Lineage Formation, Early Embryonic Asymmetries and Axis Patterning in the Mouse. *Development* **136,** 701–713 (2009).

62. Norris, D. P. & Robertson, E. J. Asymmetric and Node-Specific Nodal Expression Patterns Are Controlled by Two Distinct Cis-Acting Regulatory Elements. *Genes & Development* **13,** 1575–1588 (1999).

63. Zhou, X., Sasaki, H., Lowe, L., Hogan, B. L. M. & Kuehn, M. R. Nodal Is a Novel TGF-β-like Gene Expressed in the Mouse Node during Gastrulation. *Nature* **361,** 543 (1993).

64. Brennan, J. *et al.* Nodal Signalling in the Epiblast Patterns the Early Mouse Embryo. *Nature* **411,** 965 (2001).

65. Waldrip, W. R., Bikoff, E. K., Hoodless, P. A., Wrana, J. L. & Robertson, E. J. Smad2 Signaling in Extraembryonic Tissues Determines Anterior-Posterior Polarity of the Early Mouse Embryo. *Cell* **92,** 797–808 (1998).

66. Mesnard, D., Guzman-Ayala, M. & Constam, D. B. Nodal Specifies Embryonic Visceral Endoderm and Sustains Pluripotent Cells in the Epiblast before Overt Axial Patterning. *Development* **133,** 2497–2505 (2006).

67. Yamamoto, M. *et al.* Antagonism between Smad1 and Smad2 Signaling Determines the Site of Distal Visceral Endoderm Formation in the Mouse Embryo. *The Journal of Cell Biology* **184,** 323–334 (2009).

68. Thomas, P. Q., Brown, A. & Beddington, R. S. Hex: A Homeobox Gene Revealing Peri-Implantation Asymmetry in the Mouse Embryo and an Early Transient Marker of Endothelial Cell Precursors. *Development (Cambridge, England)* **125,** 85–94 (1998).

69. Perea-Gómez, A., Shawlot, W., Sasaki, H., Behringer, R. R. & Ang, S. HNF3beta and Lim1 Interact in the Visceral Endoderm to Regulate Primitive Streak Formation and Anterior-Posterior Polarity in the Mouse Embryo. *Development (Cambridge, England)* **126,** 4499–4511 (1999).

70. Belo, J. A. *et al.* Cerberus-like Is a Secreted Factor with Neutralizing Activity Expressed in the Anterior Primitive Endoderm of the Mouse Gastrula. *Mechanisms of Development* **68,** 45–57 (1997).

71. Yamamoto, M. *et al.* Nodal Antagonists Regulate Formation of the Anteroposterior Axis of the Mouse Embryo. *Nature* **428,** 387 (2004).

72. Perea-Gomez, A. *et al.* Nodal Antagonists in the Anterior Visceral Endoderm Prevent the Formation of Multiple Primitive Streaks. *Developmental Cell* **3,** 745–756 (2002).

73. Huelsken, J. *et al.* Requirement for β-Catenin in Anterior-Posterior Axis Formation in Mice. *The Journal of Cell Biology* **148,** 567–578 (2000).

74. Rivera-Pérez, J. A., Mager, J. & Magnuson, T. Dynamic Morphogenetic Events Characterize the Mouse Visceral Endoderm. *Developmental Biology* **261,** 470–487 (2003).

75. Srinivas, S., Rodriguez, T., Clements, M., Smith, J. C. & Beddington, R. S. P. Active Cell Migration Drives the Unilateral Movements of the Anterior Visceral Endoderm. *Development* **131,** 1157–1164 (2004).

76. Ben-Haim, N. *et al.* The nodal precursor acting via activin receptors induces mesoderm by maintaining a source of its convertases and BMP4. *Dev. Cell* **11,** 313–323 (2006).

77. Thomas, P. & Beddington, R. Anterior Primitive Endoderm May Be Responsible for Patterning the Anterior Neural Plate in the Mouse Embryo. *Current Biology* **6,** 1487–1496 (1996).

78. Rakeman, A. S. & Anderson, K. V. Axis Specification and Morphogenesis in the Mouse Embryo Require Nap1, a Regulator of WAVE-Mediated Actin Branching. *Development* **133,** 3075–3083 (2006).

79. Morris, S. A. *et al.* Dynamics of Anterior–Posterior Axis Formation in the Developing Mouse Embryo. *Nature Communications* **3,** 673 (2012).

80. Ding, J. *et al.* Cripto Is Required for Correct Orientation of the Anterior–Posterior Axis in the Mouse Embryo. *Nature* **395,** 702 (1998).

81. Kimura-Yoshida, C. *et al.* Canonical Wnt Signaling and Its Antagonist Regulate Anterior-Posterior Axis Polarization by Guiding Cell Migration in Mouse Visceral Endoderm. *Developmental Cell* **9,** 639–650 (2005).

82. Rivera-Pérez, J. A. & Magnuson, T. Primitive streak formation in mice is preceded by localized activation of Brachyury and Wnt3. *Developmental Biology* **288,** 363–371 (2005).

83. Tortelote, G. G. *et al.* Wnt3 function in the epiblast is required for the maintenance but not the initiation of gastrulation in mice. *Developmental Biology* **374,** 164–173 (2013).

84. Barrow, J. R. *et al.* Wnt3 signaling in the epiblast is required for proper orientation of the anteroposterior axis. *Developmental Biology* **312,** 312–320 (2007).

85. Yoon, Y. *et al.* Extra-embryonic Wnt3 regulates the establishment of the primitive streak in mice. *Developmental Biology* **403,** 80–88 (2015).

86. Loh, K. M., van Amerongen, R. & Nusse, R. Generating Cellular Diversity and Spatial Form: Wnt Signaling and the Evolution of Multicellular Animals. *Dev. Cell* **38,** 643–655 (2016).

87. Liu, P. *et al.* Requirement for Wnt3 in vertebrate axis formation. *Nat. Genet.* **22,** 361–365 (1999).

88. Kelly, O. G., Pinson, K. I. & Skarnes, W. C. The Wnt co-receptors Lrp5 and Lrp6 are essential for gastrulation in mice. *Development* **131,** 2803–2815 (2004).

89. Alexandre, C., Baena-Lopez, A. & Vincent, J.-P. Patterning and growth control by membrane-tethered Wingless. *Nature* **505,** 180–185 (2014).

90. Farin, H. F. *et al.* Visualization of a short-range Wnt gradient in the intestinal stem-cell niche. *Nature* **530,** 340–343 (2016).

91. Habib, S. J. *et al.* A localized Wnt signal orients asymmetric stem cell division in vitro. *Science* **339,** 1445–1448 (2013).

92. Schier, A. F. & Shen, M. M. Nodal Signalling in Vertebrate Development. *Nature* **403,** 385 (2000).

93. Beddington, R. S., Rashbass, P. & Wilson, V. Brachyury–a gene affecting mouse gastrulation and early organogenesis. *Development (Cambridge, England). Supplement,* 157–165 (1992).

94. Wilson, V. & Beddington, R. Expression of T protein in the primitive streak is necessary and sufficient for posterior mesoderm movement and somite differentiation. *Developmental Biology* **192,** 45–58 (1997).

95. Wilkinson, D. G., Bhatt, S. & Herrmann, B. G. Expression pattern of the mouse T gene and its role in mesoderm formation. *Nature* **343,** 657–659 (1990).

96. Yamaguchi, T. P., Takada, S., Yoshikawa, Y., Wu, N. & McMahon, A. P. T (Brachyury) is a direct target of Wnt3a during paraxial mesoderm specification. *Genes Dev.* **13,** 3185–3190 (1999).

97. Arnold, S. J. *et al.* Brachyury is a target gene of the Wnt/β-catenin signaling pathway. *Mechanisms of Development* **91,** 249–258 (2000).

98. Ciruna, B. & Rossant, J. FGF Signaling Regulates Mesoderm Cell Fate Specification and Morphogenetic Movement at the Primitive Streak. *Developmental Cell* **1,** 37–49 (2001).

99. Feldman, B., Poueymirou, W., Papaioannou, V. E., DeChiara, T. M. & Goldfarb, M. Requirement of FGF-4 for Postimplantation Mouse Development. *Science* **267,** 246–249 (1995).

100. Sun, X., Meyers, E. N., Lewandoski, M. & Martin, G. R. Targeted Disruption of Fgf8 Causes Failure of Cell Migration in the Gastrulating Mouse Embryo. *Genes & Development* **13,** 1834–1846 (1999).

101. Ghabrial, A. S. & Krasnow, M. A. Social Interactions among Epithelial Cells during Tracheal Branching Morphogenesis. *Nature* **441,** 746 (2006).

102. Ciruna, B. G., Schwartz, L., Harpal, K., Yamaguchi, T. P. & Rossant, J. Chimeric Analysis of Fibroblast Growth Factor Receptor-1 (Fgfr1) Function: A Role for FGFR1 in Morphogenetic Movement through the Primitive Streak. *Development (Cambridge, England)* **124,** 2829–2841 (1997).

103. Carver, E. A., Jiang, R., Lan, Y., Oram, K. F. & Gridley, T. The mouse snail gene encodes a key regulator of the epithelial-mesenchymal transition. *Mol. Cell. Biol.* **21,** 8184–8188 (2001).

104. Scialdone, A. *et al.* Resolving early mesoderm diversification through single-cell expression profiling. *Nature* **535,** 289–293 (2016).

105. Hertig, A. T., Rock, J. & Adams, E. C. A Description of 34 Human Ova within the First 17 Days of Development. *American Journal of Anatomy* **98,** 435–493 (1956).

106. O'Rahilly, R. & Müller, F. Developmental Stages in Human Embryos: Revised and New Measurements. *Cells Tissues Organs* **192,** 73–84 (2010).

107. Enders, A. C., Schlafke, S. & Hendrickx, A. G. Differentiation of the Embryonic Disc, Amnion, and Yolk Sac in the Rhesus Monkey. *American Journal of Anatomy* **177,** 161–185 (1986).

108. Edwards, R. G., Steptoe, P. C. & Purdy, J. M. Fertilization and Cleavage in Vitro of Preovulator Human Oocytes. *Nature* **227,** 1307 (1970).

109. Edwards, R. G., Bavister, B. D. & Steptoe, P. C. Early Stages of Fertilization in Vitro of Human Oocytes Matured in Vitro. *Nature* **221,** 632 (1969).

110. Shahbazi, M. N. *et al.* Self-organization of the human embryo in the absence of maternal tissues. *Nat. Cell Biol.* **18,** 700–708 (2016).

111. Deglincerti, A. *et al.* Self-organization of the in vitro attached human embryo. *Nature* **533,** 251–254 (2016).

112. Shahbazi, M. N. *et al.* Pluripotent state transitions coordinate morphogenesis in mouse and human embryos. *Nature* **552,** 239–243 (2017).

113. Niakan, K. K. & Eggan, K. Analysis of Human Embryos from Zygote to Blastocyst Reveals Distinct Gene Expression Patterns Relative to the Mouse. *Developmental Biology* **375,** 54–64 (2013).

114. Petropoulos, S. *et al.* Single-Cell RNA-Seq Reveals Lineage and X Chromosome Dynamics in Human Preimplantation Embryos. *Cell* **165,** 1012–1026 (2016).

115. Yan, L. *et al.* Single-Cell RNA-Seq Profiling of Human Preimplantation Embryos and Embryonic Stem Cells. *Nature Structural & Molecular Biology* **20,** 1131–1139 (2013).

116. Shahbazi, M. N. & Zernicka-Goetz, M. Deconstructing and reconstructing the mouse and human early embryo. *Nat. Cell Biol.* **20,** 878–887 (2018).

117. Shahbazi, M. N., Siggia, E. D. & Zernicka-Goetz, M. Self-Organization of Stem Cells into Embryos: A Window on Early Mammalian Development. *Science* **364,** 948–951 (2019).

118. Martin, G. R. Isolation of a pluripotent cell line from early mouse embryos cultured in medium conditioned by teratocarcinoma stem cells. *Proceedings of the National Academy of Sciences* **78,** 7634–7638 (1981).

119. Evans, M. J. & Kaufman, M. H. Establishment in culture of pluripotential cells from mouse embryos. *Nature* **292,** 154–156 (1981).

120. Thomson, J. A. *et al.* Embryonic stem cell lines derived from human blastocysts. *Science* **282,** 1145–1147 (1998).

121. Tanaka, S., Kunath, T., Hadjantonakis, A.-K., Nagy, A. & Rossant, J. Promotion of Trophoblast Stem Cell Proliferation by FGF4. *Science* **282,** 2072–2075 (1998).

122. Rivron, N. C. *et al.* Blastocyst-like structures generated solely from stem cells. *Nature* **557,** 106–111 (2018).

123. Harrison, S. E., Sozen, B., Christodoulou, N., Kyprianou, C. & Zernicka-Goetz, M. Assembly of embryonic and extra-embryonic stem cells to mimic embryogenesis in vitro. *Science,* eaal1810 (2017).

124. Sozen, B. *et al.* Self-assembly of embryonic and two extra-embryonic stem cell types into gastrulating embryo-like structures. *Nat. Cell Biol.* **20,** 979–989 (2018).

125. Kunath, T. *et al.* Imprinted X-Inactivation in Extra-Embryonic Endoderm Cell Lines from Mouse Blastocysts. *Development* **132,** 1649–1661 (2005).

126. Ten Berge, D. *et al.* Wnt Signaling Mediates Self-Organization and Axis Formation in Embryoid Bodies. *Cell Stem Cell* **3,** 508–518 (2008).

127. Turner, D. A. *et al.* Wnt/β-catenin and FGF signalling direct the specification and maintenance of a neuromesodermal axial progenitor in ensembles of mouse embryonic stem cells. *Development* **141,** 4243–4253 (2014).

128. Turner, D. A., Rué, P., Mackenzie, J. P., Davies, E. & Martinez Arias, A. Brachyury cooperates with Wnt/β-catenin signalling to elicit primitive-streak-like behaviour in differentiating mouse embryonic stem cells. *BMC Biol.* **12,** 63 (2014).

129. Van den Brink, S. C. *et al.* Symmetry breaking, germ layer specification and axial organisation in aggregates of mouse embryonic stem cells. *Development* **141,** 4231–4242 (2014).

130. Turner, D. A. *et al.* Anteroposterior polarity and elongation in the absence of extra-embryonic tissues and of spatially localised signalling in gastruloids: mammalian embryonic organoids. *Development* **144,** 3894–3906 (2017).

131. Beccari, L. *et al.* Multi-axial self-organization properties of mouse embryonic stem cells into gastruloids. *Nature* **5,** 277 (2018).

132. Brons, I. G. M. *et al.* Derivation of Pluripotent Epiblast Stem Cells from Mammalian Embryos. *Nature* **448,** 191–195 (2007).

133. Rossant, J. Stem Cells and Early Lineage Development. *Cell* **132,** 527–531 (2008).

134. Tesar, P. J. *et al.* New Cell Lines from Mouse Epiblast Share Defining Features with Human Embryonic Stem Cells. *Nature* **448,** 196–199 (2007).

135. Xu, R.-H. *et al.* BMP4 Initiates Human Embryonic Stem Cell Differentiation to Trophoblast. *Nature Biotechnology* **20,** 1261–1264 (2002).

136. Theunissen, T. W. *et al.* Systematic Identification of Culture Conditions for Induction and Maintenance of Naive Human Pluripotency. *Cell Stem Cell* **15,** 471–487 (2014).

137. Gafni, O. *et al.* Derivation of Novel Human Ground State Naive Pluripotent Stem Cells. *Nature* **504,** 282–286 (2013).

138. Bao, S. *et al.* Epigenetic Reversion of Post-Implantation Epiblast to Pluripotent Embryonic Stem Cells. *Nature* **461,** 1292–1295 (2009).

139. Warmflash, A., Sorre, B., Etoc, F., Siggia, E. D. & Brivanlou, A. H. A method to recapitulate early embryonic spatial patterning in human embryonic stem cells. *Nat. Methods* **11,** 847–854 (2014).

140. Etoc, F. *et al.* A Balance between Secreted Inhibitors and Edge Sensing Controls Gastruloid Self-Organization. *Dev. Cell* **39,** 302–315 (2016).

141. McMahon, J. A. *et al.* Noggin-Mediated Antagonism of BMP Signaling Is Required for Growth and Patterning of the Neural Tube and Somite. *Genes & Development* **12,** 1438–1452 (1998).

142. Martyn, I., Kanno, T. Y., Ruzo, A., Siggia, E. D. & Brivanlou, A. H. Self-organization of a human organizer by combined Wnt and Nodal signalling. *Nature* **558,** 132–135 (2018).

143. Martyn, I., Brivanlou, A. H. & Siggia, E. D. A wave of WNT signalling balanced by secreted inhibitors controls primitive streak formation in micropattern colonies of human embryonic stem cells. *Development,* dev.172791 (2019).

144. Simunovic, M. *et al.* A 3D Model of a Human Epiblast Reveals BMP4-Driven Symmetry Breaking. *Nature Cell Biology* **21,** 900 (2019).

145. Shao, Y. *et al.* A Pluripotent Stem Cell-Based Model for Post-Implantation Human Amniotic Sac Development. *Nature Communications* **8,** 208 (2017).

146. Shao, Y. *et al.* Self-Organized Amniogenesis by Human Pluripotent Stem Cells in a Biomimetic Implantation-like Niche. *Nature Materials* **16,** 419–425 (2017).

147. Okae, H. *et al.* Derivation of Human Trophoblast Stem Cells. *Cell Stem Cell* **22,** 50–63.e6 (2018).

148. Hegemann, P. & Nagel, G. From channelrhodopsins to optogenetics. *EMBO Molecular Medicine* **5,** 173–176 (2013).

149. Repina, N. A., Rosenbloom, A., Mukherjee, A., Schaffer, D. V. & Kane, R. S. At Light Speed: Advances in Optogenetic Systems for Regulating Cell Signaling and Behavior. *Annual review of chemical and biomolecular engineering* **8,** 13–39 (2017).

150. Nagel, G. *et al.* Channelrhodopsin-1: A Light-Gated Proton Channel in Green Algae. *Science (New York, N.Y.)* **296,** 2395–2398 (2002).

151. Nagel, G. *et al.* Channelrhodopsin-2, a directly light-gated cation-selective membrane channel. *Proceedings of the National Academy of Sciences* **100,** 13940–13945 (2003).

152. Nagel, G. *et al.* Light Activation of Channelrhodopsin-2 in Excitable Cells of Caenorhabditis Elegans Triggers Rapid Behavioral Responses. *Current biology: CB* **15,** 2279–2284 (2005).

153. Li, X. *et al.* Fast Noninvasive Activation and Inhibition of Neural and Network Activity by Vertebrate Rhodopsin and Green Algae Channelrhodopsin. *Proceedings of the National Academy of Sciences* **102,** 17816–17821 (2005).

154. Ishizuka, T., Kakuda, M., Araki, R. & Yawo, H. Kinetic Evaluation of Photosensitivity in Genetically Engineered Neurons Expressing Green Algae Light-Gated Channels. *Neuroscience Research* **54,** 85–94 (2006).

155. Boyden, E. S., Zhang, F., Bamberg, E., Nagel, G. & Deisseroth, K. Millisecond-Timescale, Genetically Targeted Optical Control of Neural Activity. *Nature Neuroscience* **8,** 1263–1268 (2005).

156. Bi, A. *et al.* Ectopic Expression of a Microbial-Type Rhodopsin Restores Visual Responses in Mice with Photoreceptor Degeneration. *Neuron* **50,** 23–33 (2006).

157. Yizhar, O., Fenno, L. E., Davidson, T. J., Mogri, M. & Deisseroth, K. Optogenetics in neural systems. *Neuron* **71,** 9–34 (2011).

158. Fenno, L., Yizhar, O. & Deisseroth, K. The Development and Application of Optogenetics. *The Development and Application of Optogenetics* **34,** 389–412 (2011).

159. Kim, C. K., Adhikari, A. & Deisseroth, K. Integration of Optogenetics with Complementary Methodologies in Systems Neuroscience. *Nature Reviews Neuroscience* **18,** 222–235 (2017).

160. Wiegert, J. S., Mahn, M., Prigge, M., Printz, Y. & Yizhar, O. Silencing Neurons: Tools, Applications, and Experimental Constraints. *Neuron* **95,** 504–529 (2017).

161. Berndt, A. *et al.* Structural Foundations of Optogenetics: Determinants of Channelrhodopsin Ion Selectivity. *Proceedings of the National Academy of Sciences* **113,** 822–829 (2016).

162. Wietek, J. *et al.* Conversion of Channelrhodopsin into a Light-Gated Chloride Channel. *Science* **344,** 409–412 (2014).

163. Berndt, A., Lee, S. Y., Ramakrishnan, C. & Deisseroth, K. Structure-Guided Transformation of Channelrhodopsin into a Light-Activated Chloride Channel. *Science* **344,** 420–424 (2014).

164. Wietek, J. *et al.* An Improved Chloride-Conducting Channelrhodopsin for Light-Induced Inhibition of Neuronal Activity in Vivo. *Scientific Reports* **5,** 14807 (2015).

165. Govorunova, E. G., Sineshchekov, O. A., Janz, R., Liu, X. & Spudich, J. L. Natural Light-Gated Anion Channels: A Family of Microbial Rhodopsins for Advanced Optogenetics. *Science* **349,** 647–650 (2015).

166. Johnson, H. E. & Toettcher, J. E. Illuminating developmental biology with cellular optogenetics. *Current opinion in biotechnology* **52,** 42–48 (2018).

167. Christie, J. M., Salomon, M., Nozue, K., Wada, M. & Briggs, W. R. LOV (light, oxygen, or voltage) domains of the blue-light photoreceptor phototropin (nph1): binding sites for the chromophore flavin mononucleotide. *Proceedings of the National Academy of Sciences* **96,** 8779–8783 (1999).

168. Huala, E. *et al.* Arabidopsis NPH1: a protein kinase with a putative redox-sensing domain. *Science* **278,** 2120–2123 (1997).

169. Christie, J. M., Swartz, T. E., Bogomolni, R. A. & Briggs, W. R. Phototropin LOV domains exhibit distinct roles in regulating photoreceptor function. *Phototropin LOV domains exhibit distinct roles in regulating photoreceptor function.* **32,** 205–219 (2002).

170. Christie, J. M., Gawthorne, J., Young, G., Fraser, N. J. & Roe, A. J. LOV to BLUF: Flavoprotein Contributions to the Optogenetic Toolkit. *LOV to BLUF: Flavoprotein Contributions to the Optogenetic Toolkit* **5,** 533–544 (2012).

171. Harper, S. M., Neil, L. C. & Gardner, K. H. Structural basis of a phototropin light switch. *Science* **301,** 1541–1544 (2003).

172. Harper, S. M., Christie, J. M. & Gardner, K. H. Disruption of the LOV-Jalpha helix interaction activates phototropin kinase activity. *Biochemistry* **43,** 16184–16192 (2004).

173. Strickland, D. *et al.* Rationally improving LOV domain-based photoswitches. *Nat. Methods* **7,** 623–626 (2010).

174. Strickland, D., Moffat, K. & Sosnick, T. R. Light-activated DNA binding in a designed allosteric protein. *Proceedings of the National Academy of Sciences* **105,** 10709–10714 (2008).

175. Wu, Y. I. *et al.* A genetically encoded photoactivatable Rac controls the motility of living cells. *Nature* **461,** 104–108 (2009).

176. Wu, Y. I., Wang, X., He, L., Montell, D. & Hahn, K. M. Spatiotemporal control of small GTPases with light using the LOV domain. *Meth. Enzymol.* **497,** 393–407 (2011).

177. Morri, M. *et al.* Optical functionalization of human Class A orphan G-protein-coupled receptors. *Nat Commun* **9,** 1950 (2018).

178. Čapek, D. *et al.* Light-activated Frizzled7 reveals a permissive role of non-canonical wnt signaling in mesendoderm cell migration. *eLife* **8,** 1025 (2019).

179. Möglich, A., Ayers, R. A. & Moffat, K. Design and signaling mechanism of light-regulated histidine kinases. *J. Mol. Biol.* **385,** 1433–1444 (2009).

180. Benedetti, L. *et al.* Light-activated protein interaction with high spatial subcellular confinement. *Proceedings of the National Academy of Sciences* **115,** E2238–E2245 (2018).

181. Levskaya, A., Weiner, O. D., Lim, W. A. & Voigt, C. A. Spatiotemporal control of cell signalling using a light-switchable protein interaction. *Nature* **461,** 997–1001 (2009).

182. Quail, P. H. Phytochromes. *Current Biology* **20** (2010).

183. Quail, P. H. Phytochrome photosensory signalling networks. *Nat Rev Mol Cell Biol* **3,** 85–93 (2002).

184. Ni, M., Tepperman, J. M. & Quail, P. H. Binding of phytochrome B to its nuclear signalling partner PIF3 is reversibly induced by light. *Nature* **400,** 781–784 (1999).

185. Kaberniuk, A. A., Shemetov, A. A. & Verkhusha, V. V. A bacterial phytochrome-based optogenetic system controllable with near-infrared light. *Nat. Methods* **13,** 591–597 (2016).

186. Redchuk, T. A., Omelina, E. S., Chernov, K. G. & Verkhusha, V. V. Near-infrared optogenetic pair for protein regulation and spectral multiplexing. *Nat. Chem. Biol.* **13,** 633–639 (2017).

187. Verkhusha, V., Redchuk, T., Karasev, M. & Omelina, E. Near-infrared light-controlled gene expression and protein targeting in neurons and non-neuronal cells. *Chembiochem* (2018).

188. Toettcher, J. E., Gong, D., Lim, W. A. & Weiner, O. D. Light control of plasma membrane recruitment using the Phy-PIF system. *Meth. Enzymol.* **497,** 409–423 (2011).

189. Buckley, C. E. *et al.* Reversible Optogenetic Control of Subcellular Protein Localization in a Live Vertebrate Embryo. *Dev. Cell* **36,** 117–126 (2016).

190. Toettcher, J. E., Gong, D., Lim, W. A. & Weiner, O. D. Light-based feedback for controlling intracellular signaling dynamics. *Nat. Methods* **8,** 837–839 (2011).

191. Kennedy, M. J. *et al.* Rapid blue-light-mediated induction of protein interactions in living cells. *Nat. Methods* **7,** 973–975 (2010).

192. Taslimi, A. *et al.* Optimized second-generation CRY2-CIB dimerizers and photoactivatable Cre recombinase. *Nat. Chem. Biol.* **12,** 425–430 (2016).

193. Rege, M. *et al.* LADL: Light-activated dynamic looping for endogenous gene expression control. *bioRxiv,* 349340 (2018).

194. Polstein, L. R., Juhas, M., Hanna, G., Bursac, N. & Gersbach, C. A. An Engineered Optogenetic Switch for Spatiotemporal Control of Gene Expression, Cell Differentiation, and Tissue Morphogenesis. *ACS Synth Biol* **6,** 2003–2013 (2017).

195. Sawa, M., Nusinow, D. A., Kay, S. A. & Imaizumi, T. FKF1 and GIGANTEA complex formation is required for day-length measurement in Arabidopsis. *Science* **318,** 261–265 (2007).

196. Zikihara, K. *et al.* Photoreaction cycle of the light, oxygen, and voltage domain in FKF1 determined by low-temperature absorption spectroscopy. *Biochemistry* **45,** 10828–10837 (2006).

197. Yazawa, M., Sadaghiani, A. M., Hsueh, B. & Dolmetsch, R. E. Induction of protein-protein interactions in live cells using light. *Nature Biotechnology* **27,** 941–945 (2009).

198. Nash, A. I. *et al.* Structural basis of photosensitivity in a bacterial light-oxygen-voltage/helix-turn-helix (LOV-HTH) DNA-binding protein. *Proceedings of the National Academy of Sciences* **108,** 9449–9454 (2011).

199. Rivera-Cancel, G., Motta-Mena, L. B. & Gardner, K. H. Identification of natural and artificial DNA substrates for light-activated LOV-HTH transcription factor EL222. *Biochemistry* **51,** 10024–10034 (2012).

200. Motta-Mena, L. B. *et al.* An optogenetic gene expression system with rapid activation and deactivation kinetics. *Nat. Chem. Biol.* **10,** 196–202 (2014).

201. Zhao, E. M. *et al.* Optogenetic regulation of engineered cellular metabolism for microbial chemical production. *Nature* **555,** 683–687 (2018).

202. Zhang, P. *et al.* OptoGranules reveal the evolution of stress granules to ALS-FTD pathology. *bioRxiv,* 348870 (2018).

203. Zoltowski, B. D. *et al.* Conformational Switching in the Fungal Light Sensor Vivid. *Science (New York, N.Y.)* **316,** 1054–1057 (2007).

204. Lamba, P., Bilodeau-Wentworth, D., Emery, P. & Zhang, Y. Morning and evening oscillators cooperate to reset circadian behavior in response to light input. *Cell Reports* **7,** 601–608 (2014).

205. Wang, X., Chen, X. & Yang, Y. Spatiotemporal control of gene expression by a light-switchable transgene system. *Nat. Methods* **9,** 266–269 (2012).

206. Kawano, F., Suzuki, H., Furuya, A. & Sato, M. Engineered pairs of distinct photoswitches for optogenetic control of cellular proteins. *Engineered pairs of distinct photoswitches for optogenetic control of cellular proteins* **6,** 6256 (2015).

207. Zoltowski, B. D., Vaccaro, B. & Crane, B. R. Mechanism-based tuning of a LOV domain photoreceptor. *Nat. Chem. Biol.* **5,** 827–834 (2009).

208. Strickland, D. *et al.* TULIPs: tunable, light-controlled interacting protein tags for cell biology. *Nat. Methods* **9,** 379–384 (2012).

209. Huang, J., Koide, A., Makabe, K. & Koide, S. Design of protein function leaps by directed domain interface evolution. *Proceedings of the National Academy of Sciences* **105,** 6578–6583 (2008).

210. Lee, H.-J. & Zheng, J. J. PDZ Domains and Their Binding Partners: Structure, Specificity, and Modification. *Cell Communication and Signaling* **8,** 8 (2010).

211. Guntas, G. *et al.* Engineering an improved light-induced dimer (iLID) for controlling the localization and activity of signaling proteins. *Proceedings of the National Academy of Sciences* **112,** 112–117 (2015).

212. Inglés-Prieto, Á. *et al.* Light-assisted small-molecule screening against protein kinases. *Nat. Chem. Biol.* **11,** 952–954 (2015).

213. Grusch, M. *et al.* Spatio-temporally precise activation of engineered receptor tyrosine kinases by light. *EMBO J* **33,** 1713–1726 (2014).

214. Zhou, X. X., Chung, H. K., Lam, A. J. & Lin, M. Z. Optical Control of Protein Activity by Fluorescent Protein Domains. *Science (New York, N.Y.)* **338,** 810–814 (2012).

215. Zhou, X. X., Fan, L. Z., Li, P., Shen, K. & Lin, M. Z. Optical Control of Cell Signaling by Single-Chain Photoswitchable Kinases. *Science (New York, N.Y.)* **355,** 836–842 (2017).

216. Bugaj, L. J., Choksi, A. T., Mesuda, C. K., Kane, R. S. & Schaffer, D. V. Optogenetic protein clustering and signaling activation in mammalian cells. *Nat. Methods* **10,** 249–252 (2013).

217. Hallett, R. A., Zimmerman, S. P., Yumerefendi, H., Bear, J. E. & Kuhlman, B. Correlating in Vitro and in Vivo Activities of Light-Inducible Dimers: A Cellular Optogenetics Guide. *ACS Synth. Biol.* **5,** 53–64 (2015).

218. Taslimi, A. *et al.* An optimized optogenetic clustering tool for probing protein interaction and function. *Nat Commun* **5,** 4925 (2014).

219. Duan, L. *et al.* Understanding CRY2 interactions for optical control of intracellular signaling. *Nat Commun* **8,** 547 (2017).

220. Bugaj, L. J. *et al.* Regulation of endogenous transmembrane receptors through optogenetic Cry2 clustering. *Nat Commun* **6,** 6898 (2015).

221. Sabari, B. R. *et al.* Coactivator condensation at super-enhancers links phase separation and gene control. *Science* **19,** eaar3958 (2018).

222. Dine, E., Gil, A. A., Uribe, G., Brangwynne, C. P. & Toettcher, J. E. Protein Phase Separation Provides Long-Term Memory of Transient Spatial Stimuli. *Cell Syst* **6,** 655–663.e5 (2018).

223. Brangwynne, C. P. *et al.* Germline P granules are liquid droplets that localize by controlled dissolution/condensation. *Science* **324,** 1729–1732 (2009).

224. Ortiz-Guerrero, J. M., Polanco, M. C., Murillo, F. J., Padmanabhan, S. & Elıas-Arnanz, M. Light-dependent gene regulation by a coenzyme B12-based photoreceptor. *Proceedings of the National Academy of Sciences* **108,** 7565–7570 (2011).

225. Jost, M. *et al.* Structural basis for gene regulation by a B12-dependent photoreceptor. *Nature* **526,** 536–541 (2015).

226. Kutta, R. J. *et al.* The photochemical mechanism of a B12-dependent photoreceptor protein. *Nat Commun* **6,** 7907 (2015).

227. Kainrath, S., Stadler, M., Reichhart, E., Distel, M. & Janovjak, H. Green-Light-Induced Inactivation of Receptor Signaling Using Cobalamin-Binding Domains. *Angew Chem Int Ed Engl* **56,** 4608–4611 (2017).

228. Chatelle, C. *et al.* A green light-responsive system for the control of transgene expression in mammalian and plant cells. *ACS Synth Biol* **7,** acssynbio.7b00450–1358 (2018).

229. Johnson, H. E. & Toettcher, J. E. Signaling Dynamics Control Cell Fate in the Early Drosophila Embryo. *Dev. Cell* **48,** 361–370.e3 (2019).

230. Toettcher, J. E., Weiner, O. D. & Lim, W. A. Using optogenetics to interrogate the dynamic control of signal transmission by the Ras/Erk module. *Cell* **155,** 1422–1434 (2013).

231. Johnson, H. E. *et al.* The Spatiotemporal Limits of Developmental Erk Signaling. *Dev. Cell* **40,** 185–192 (2017).

232. Wang, X., He, L., Wu, Y. I., Hahn, K. M. & Montell, D. J. Light-mediated activation reveals a key role for Rac in collective guidance of cell movement in vivo. *Nat Cell Biol* **12,** 591–597 (2010).

233. Sako, K. *et al.* Optogenetic Control of Nodal Signaling Reveals a Temporal Pattern of Nodal Signaling Regulating Cell Fate Specification during Gastrulation. *Cell Rep* **16,** 866–877 (2016).

234. Huang, A., Amourda, C., Zhang, S., Tolwinski, N. S. & Saunders, T. E. Decoding temporal interpretation of the morphogen Bicoid in the early Drosophila embryo. *eLife* **6,** 197 (2017).

235. Izquierdo, E., Quinkler, T. & De Renzis, S. Guided morphogenesis through optogenetic activation of Rho signalling during early Drosophila embryogenesis. *Nat Commun* **9,** 2366 (2018).

236. Guglielmi, G., Barry, J. D., Huber, W. & De Renzis, S. An Optogenetic Method to Modulate Cell Contractility during Tissue Morphogenesis. *Dev. Cell* **35,** 646–660 (2015).

237. Oates, A. C., Gorfinkiel, N., Gonzalez-Gaitan, M. & Heisenberg, C.-P. Quantitative approaches in developmental biology. *Nat. Rev. Genet.* **10,** 517–530 (2009).

238. Wennekamp, S., Mesecke, S., Nédélec, F. & Hiiragi, T. A self-organization framework for symmetry breaking in the mammalian embryo. *Nat. Rev. Mol. Cell Biol.* **14,** 452–459 (2013).

239. Eldar, A. & Elowitz, M. B. Functional roles for noise in genetic circuits. *Nature* **467,** 167–173 (2010).

240. Snijder, B. & Pelkmans, L. Origins of regulated cell-to-cell variability. *Nat. Rev. Mol. Cell Biol.* **12,** 119–125 (2011).

241. McDole, K. *et al.* In Toto Imaging and Reconstruction of Post-Implantation Mouse Development at the Single-Cell Level. *Cell* **175,** 859–876.e33 (2018).

Chapter 2

Engineered illumination devices for optogenetic control of cellular signaling dynamics

2.1 Introduction

Cell fate decisions are governed by dynamic, spatially and temporally varying signals from the cellular environment. In particular, during development, morphogen gradients orchestrate the dynamic, coordinated movement and differentiation of embryonic cell populations (*1*). Genetic perturbation and biomolecular treatment with pathway agonists or inhibitors have provided insight into the critical regulators of embryogenesis, yet spatially-varying interactions between cell subpopulations and time-varying signal dynamics and duration thresholds remain largely unstudied due to a lack of tools to perturb signaling dynamics in biological systems (*1*, *2*).

Optogenetic methods aim to address this need for techniques that control such cell signal dynamics. With optogenetics, light-responsive proteins from plants, algae, and bacteria have been adapted to control signaling and protein-protein interactions in mammalian cells (*3*–*5*). In particular, a variety of photosensory domains have been discovered, optimized, and repurposed to place intracellular signaling pathways under light control, capabilities that offer the unique advantage of using light patterns to stimulate signaling in a specific location and at a specific time (*6*). Within mammalian cells, optogenetic tools that control protein-protein interactions have for example been developed for diverse signaling pathways such as Wnt/β-catenin (*7*, *8*), Ras/Raf/Mek/Erk (*9*–*12*), fibroblast growth factor (FGF) (*13*), and Rho-family GTPase signaling (*14*–*19*). Optogenetic methods have also been recently applied to studies in developmental biology in key model organisms (*20*). For example, in Drosophila and zebrafish embryos, dynamic control of signaling elucidated the spatiotemporal limits of ERK (*10*, *12*), Nodal (*21*), and Bicoid (*22*) patterning and how local modulation of cell migration and contractility drives tissue morphogenesis (*23*–*25*). Furthermore, in embryonic stem cell models for mammalian development, we have recently achieved optogenetic control of canonical Wnt signaling and elucidated mechanisms of tissue self-organization during mesendoderm differentiation (*7*, *8*).

To activate the variety of photosensory domains developed for cellular signaling pathway control, there must be complementary development of optical tools for cell culture illumination. However, current optical methods lack practical applicability to routine cell culture stimulation and/or lack critical characterization and functionality. In particular, microscope-based systems are widely used for optogenetic photostimulation that implement one- or two-photon excitation to scan a single diffraction-limited spot (*26*–*30*) or project multi-spot light patterns (*31*–*34*) onto the biological sample. While such systems are essential for high-resolution in vivo experiments and precise manipulation of neural circuits, their application to intracellular signal pathway activation in cell cultures is limited by the system complexity, low throughput, high cost, and need for continuous environmental control (*35*). For manipulating signaling pathways where speed and single-cell spatial resolution are often less critical, the paramount photostimulation criteria are high-throughput control of multiple parallel biological conditions, defined illumination parameters, and compatibility with established cell culture formats and assays. Several methods have been developed for such photostimulation of signal pathways in cell cultures, though they can lack critical characterization and functionality. For example, a simple panel of light emitting diodes (LEDs) enables optogenetic activation of a tissue culture plate, but lacks multi-well, high-throughput control (*36*, *37*) and spatiotemporal patterning capability (*38*). Multi-well control can be achieved by incorporating a microcontroller and LED drivers that set user-defined intensities for separate wells (*39*, *40*). Though such multi-well devices have advanced the throughput of optogenetic studies, current implementations have not characterized key performance parameters such as uniformity of illumination, spatial or temporal light patterning resolution, and quantification of device overheating and cell toxicity (*39*–*46*). Several such designs also rely on modification of expensive equipment (*46*) or are limited to bacterial culture (*39*).

We have designed a programmable illumination system for photostimulation of multiwell plates that can be readily incorporated into the workflow of routine cell culture and allow controlled and quantitative spatiotemporal light patterning. Specifically, we engineer cell culture illumination devices for light activation at variable amplitudes, or LAVA boards. We optimize the LAVA board optical configuration for illumination uniformity and achieve programmable photostimulation of independent wells of 24-well or 96-well culture plates kept in standard $37°C$ tissue culture incubators. Each well can be wirelessly programmed through a graphical user interface (GUI) at user-defined intensities ($0 - 20\ \mu W mm^{-2}$, 0.005 $\mu W mm^{-2}$ resolution), temporal sequences (10 ms resolution), and spatial patterns (100 μm resolution). We demonstrate LAVA board performance by modulating the intensity, timing, and spatial location of canonical Wnt/β-catenin signaling in human embryonic stem cell (hESC) cultures using the optoWnt optogenetic system (*7*, *8*). We show that Wnt pathway activation and hESC differentiation is dose-responsive to light intensity and duration of illumination, and that spatial patterning can be used to simulate the embryonic, spatially polarized presentation of the Wnt ligand.

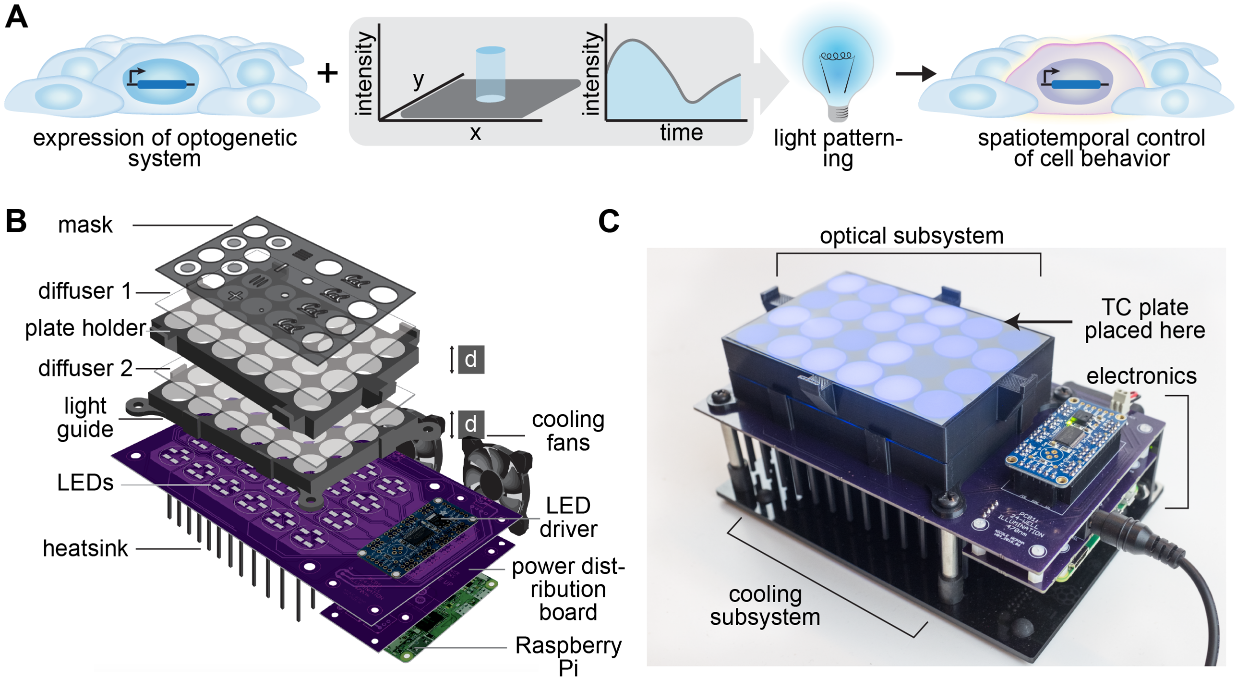

Figure 2.1: **Overview of illumination device, LAVA, for optogenetic stimulation of hESC cultures**
A) Schematic of typical optogenetic experiment, where spatiotemporal precision is conferred through light patterning. **B)** Diagram of illumination device design. LEDs illuminate a TC plate placed on top of device, with light passing through a series of two light guides, two optical diffusers, and a die-cut mask. LEDs are programmed through a Raspberry Pi and LED driver and are cooled with a heatsink and cooling fans. **C)** Image of assembled 24-well LAVA board, with optical, cooling, and electronics subsystems highlighted.

2.2 Design

2.2.1 Design requirements for spatiotemporal photostimulation of cell cultures

A number of design considerations should be considered to ensure controlled, long-term illumination of mammalian cell cultures. The primary requirement is illumination of cells with defined intensities of light and with illumination patterns that can vary in space and time. Also, the intensity range should be sufficient to activate the photosensory protein of interest, which can vary widely from continuous illumination at 1 $\mu W mm^{-2}$ (*8*) to short pulses at 1,000 – 10,000 $\mu W mm^{-2}$ (*35*). Moreover, the required temporal resolution also depends on the photosensory domain and experimental application: 1 to 100 ms pulses are typically used for control of neural circuits (*35*), whereas signal pathway dynamics are controlled on the second to multi-day timescales (*8*, *20*). Furthermore, for spatial resolution requirements, optimal resolution for subcellular stimulation would be 0.2 – 2 μm, but such resolutions are infeasible without complex optical systems. Since a typical cell size is 10 – 20 μm, multicellular resolution can be sufficient for many applications at 50 – 200 μm.

Beyond the requirement for light delivery, the illumination device must also be compatible with routine stem cell culture experiments. As a result, the electronics must be compatible with the warm ($37°C$) and humid environment used for mammalian tissue culture. Additionally, the device should also not induce cell damage from overheating or phototoxicity, which is a significant concern during optogenetic stimulation since such processes alter cell physiology and/or cause non-specific activation of signaling pathways (*35*, *47*–*50*). Illumination uniformity across a region of interest is critical as well. Since the strength of induced signaling is dependent on light dosage, nonuniformity can give rise to signal variation across the region of optogenetic stimulation. Lastly, cost, functionality, and ease of use can be significant barriers for optogenetic studies, so simple user-programmable control of many simultaneous illumination conditions is a significant advantage for complex and high-throughput biological experiments.

2.2.2 Design overview of engineered LAVA illumination devices

To enable precise control over the intensity, timing, and location of optogenetic stimulation, we engineered illumination devices, LAVA boards, that incorporateinto the workflow of stem cell culture (Figure 2.1A). LAVA boards project user-defined, programmable light patterns onto 24-well or 96-well tissue culture (TC) plates maintained inside a standard TC incubator (Figure 2.1B-C, Figure 2.2A-C). In brief, light emitted by LEDs located underneath the multiwell culture plate passes through diffusive optical elements that ensure uniform illumination of each well. For stimulation of cells expressing optoWnt, a system we previously engineered for optogenetic control of Wnt signaling (*7*, *8*), we chose blue LEDs emitting at a central wavelength of 470 nm to match the A. thaliana Cryptochrome 2 (Cry2) photosensory domain absorption spectrum (Figure 2.2D), though we note that LEDs of diverse colors can readily be substituted for use with other optogenetic systems. The LAVA board electronics are designed for programmable control of illumination intensity and temporal sequences, with independent control of each well. In addition, spatial precision is conveyed through an intensity mask attached to the culture plate. The hardware design also includes a cooling system and vibration isolation to ensure cell viability. Lastly, for ease of use, we developed a graphical user interface (GUI) to wirelessly program the illumination intensity and temporal sequences for each well.

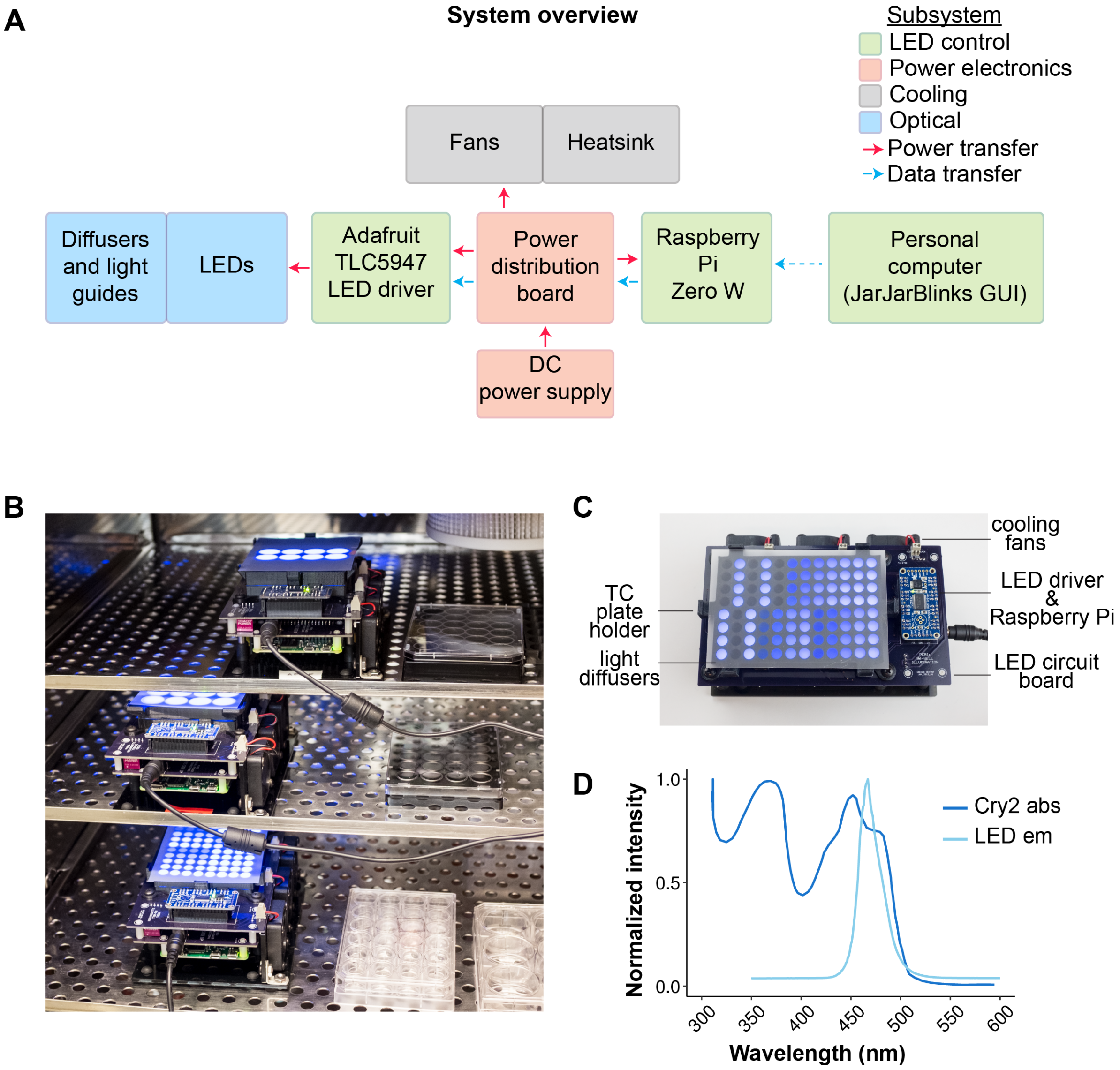

Figure 2.2: **Overview of 24-well and 96-well LAVA devices**
A) System block diagram of LAVA device. **B)** Image of 24-well and 96-well LAVA devices in TC incubator. **C)** Image of assembled 96-well LAVA board, with optical, cooling, and electronic subsystems highlighted. **D)** Emission spectrum of 470 nm blue LEDs match the absorption spectrum of Cry2. Cry2 spectrum adapted from reference (*51*)

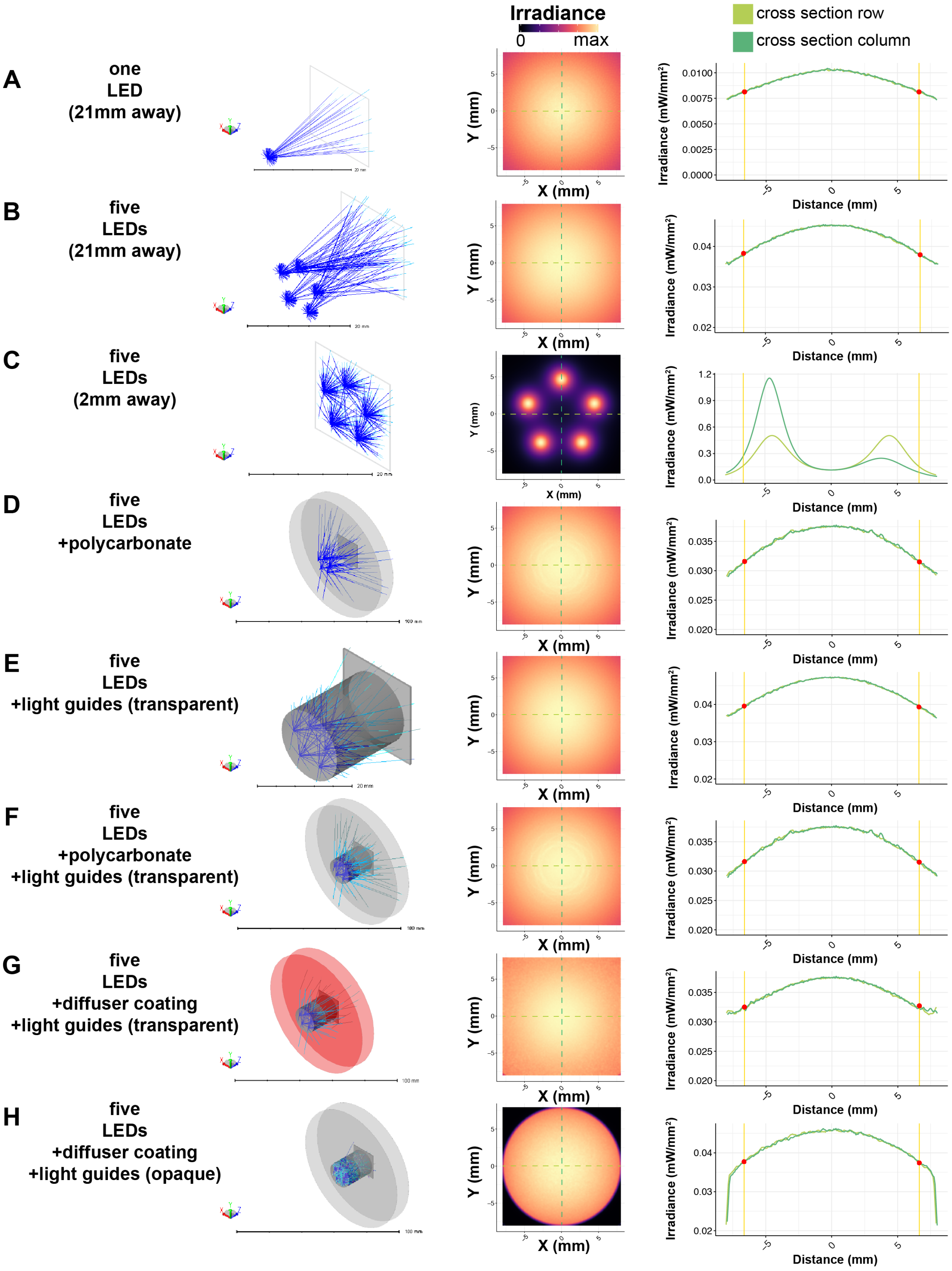

Figure 2.3: *See caption on next page*

Figure 2.3: **In silico validation of Zemax ray tracing model**
Schematic of LED configuration (left), modeling result at detector plane (middle), and column and row cross-sections (right) with well edge of 24-well plate indicated with red points. **A)** Single LED illuminating detector 21mm away. **B)** Five LEDs, distributed along a 1 *cm* diameter circle, illuminating detector 21mm away. **C)** Five LEDs illuminating detector 2mm away. **D)** Five LEDs illuminating detector 21mm away through two 0.01" thick sheets of polycarbonate. **E)** Five LEDs illuminating detector 21mm away through two 10mm transparent light guides. **F)** Five LEDs illuminating detector 21mm away through two 0.01" thick sheets of polycarbonate and two 10mm transparent light guides. **G)** Five LEDs illuminating detector 21mm away through two 0.01" thick sheets of polycarbonate with 80° diffuser coating and two 10mm transparent light guides. **H)** Five LEDs illuminating detector 21mm away through two uncoated 0.01" thick sheets of polycarbonate and two 10mm reflective light guides with Lambertian scattering.

2.2.3 Optimization of illumination uniformity

We established the LAVA optical system design by modeling the optical configuration of a single well in the optical ray tracing software Zemax OpticStudio (Figure 2.3A-H). We then optimized the optical configuration for uniform well illumination (Figure 2.4A). Due to spatial constraints of a TC incubator, we used optical diffusers, rather than lenses, in addition to optical scattering from the 3D-printed light guides to ensure illumination uniformity. In the Zemax model, parameters such as LED position on the circuit board, diffuser strength, and light guide dimensions were optimized to reduce intensity drop-off at the well edge (Figure 2.3A-H, Figure 2.5A-E). Modeling results showed that the parameter with the strongest effect on uniformity was the axial thickness, d, of the two 3D-printed light guides (labelled in Figure 2.1B). Based on these modeling results, we fabricated LAVA devices and experimentally validated the resulting well uniformity by imaging LAVA wells under a low-magnification microscope (Figure 2.4B, Figure 2.6A-C). Measurement of light intensity as a function of radial distance confirmed the improved illumination uniformity, which came at the expense of maximum illumination intensity (Figure 2.4B). Increasing d from 1 cm to 1.5 cm attenuated the intensity decrease at the well edge from 20.4% to 16.9%, i.e. a roughly 20% improvement in uniformity. A larger d also resulted in a two-fold improvement in well-to-well variability between the 24 independent wells (2.6% versus 1.2% coefficient of variation) (Figure 2.6D). For experimental applications where intensity of illumination is paramount to well uniformity, a lower d could be used to achieve higher illumination intensities. Thus, the LAVA boards can be used in two hardware configurations, which are summarized as follows: (1) a low-intensity, high-precision configuration at $d = 1.5\ cm$ where intensity can be programmed from $0 - 10 \mu W mm^{-2}$ in 0.0024 $\mu W mm^{-2}$ increments with high illumination uniformity and low well-to-well variability and (2) a high-intensity, low precision configuration at $d = 1\ cm$ where well intensity resolution, variability, and uniformity are sacrificed to achieve a doubling in light intensity ($0 - 20 \mu W mm^{-2}$ in 0.005 $\mu W mm^{-2}$ increments) (Figure 2.4C).

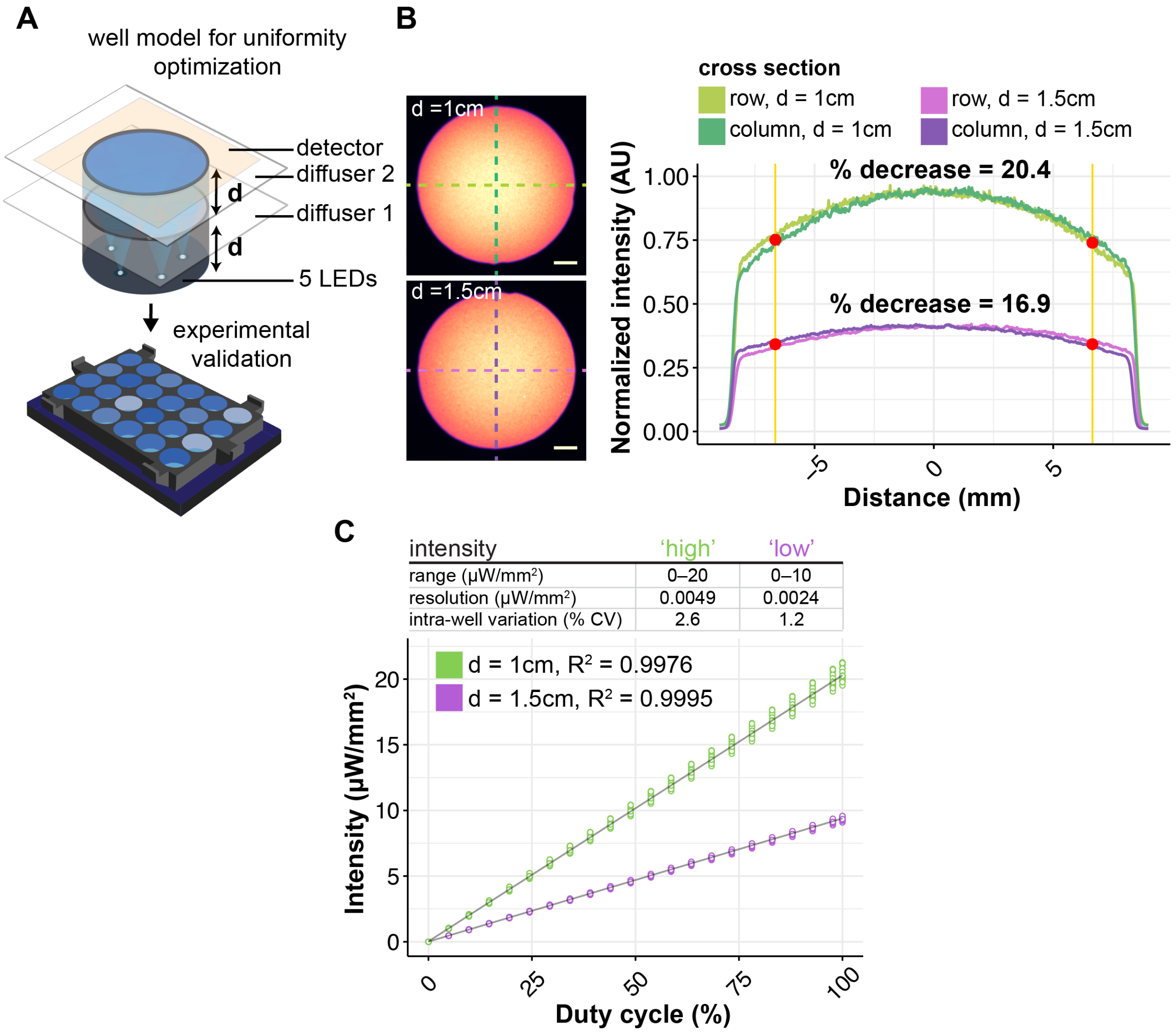

intensity	'high'	'low'
range (μW/mm²)	0–20	0–10
resolution (μW/mm²)	0.0049	0.0024
intra-well variation (% CV)	2.6	1.2

Figure 2.4: **Optical design for illumination uniformity of TC plate wells**
A) Schematic of Zemax model used for LAVA optical system optimization. **B)** Brightfield images of LAVA board wells (left) and graph of intensity linescans along indicated cross-sections (right) characterize the intensity uniformity of the 24-well LAVA device under two configurations, where light guide thickness, d, is either (1) 1 *cm* (top, green) or (2) 1.5 *cm* (bottom, purple). Percent decrease is calculated between intensity at center of well and intensity at highlighted red point, which indicates location of well edge of a 24-well culture plate. Graph shows mean normalized intensity over 4 independent wells. Scale bar 2.5 *mm*. **C)** Measured light intensity in response to the programmed duty cycle of the LED pulse-width modulation signal. Graph shows measured intensity from each well of a 24-well LAVA board and curve fit to a linear regression model.

2.3 Results

2.3.1 Intensity control of optogenetic stimulation reveals Brachyury expression level is dependent on LRP6 oligomer number and size

During mammalian embryonic development, gradients in Wnt signal intensity control the progression of cell lineage commitment and axis patterning (*1, 52–54*). In hESCs, the strength of Wnt signaling similarly modulates cell lineage commitment and differentiation potential (*55–58*). Equipped with a method for optogenetic stimulation of cell cultures, we used the LAVA boards to activate canonical Wnt/β-catenin signaling in a clonal hESC line expressing the optoWnt system (*8*). In addition to on/off control of Wnt signaling, we sought to determine whether optoWnt could be activated in a dose-responsive manner to better mimic the signal gradients present during development.

Since Cry2 oligomerization is a dynamic, reversible process wherein clustering is triggered upon photon absorption (*7, 59*), we reasoned that the fraction of photostimulated Cry2 proteins per cell could be controlled with light intensity (Figure 2.7A). Using the LAVA boards, we were able to set independent wells to different light intensities using pulse width modulation (PWM) (Figure 2.4C). Upon continuous photostimulation at variable intensities, we indeed observed that the number and size of visible LRP6 oligomers per cell increased monotonically with illumination intensity (Figure 2.7B). To determine whether increased Cry2 oligomerization translated to a stronger Wnt signal intensity, we probed for expression Brachyury (BRA, also known by its gene name, T), a direct transcriptional target of Wnt signaling and regulator of mesendoderm and primitive streak differentiation (*60–63*). Following a similar trend to Cry2 oligomerization, the mean intensity of BRA immunostaining increased with light intensity, suggesting that an increased number and size of LRP6 clusters results in a stronger differentiation signal (Figure 2.7C, Figure 2.8A).

To better quantify BRA expression at a single-cell level, we used a clonal hESC cell line co-expressing the optoWnt system and an eGFP reporter driven by the endogenous T locus (*8*). Live-cell analysis with flow cytometry showed a heterogeneous response to Wnt stimulation at both low (0.1 $\mu W mm^{-2}$) and high (1.4 $\mu W mm^{-2}$) light intensities, confirming BRA immunostaining results (Figure 2.8A-B). Maximal light-induced activation increased BRA expression by ~33-fold over unilluminated optoWnt hESCs, which notably showed no detectable activation in the dark. Quantification of the percentage eGFP-positive cells exhibited an exponential increase with light intensity that greatly exceeded activation achieved with recombinant Wnt3a protein (Figure 2.7D). Fitting to an increasing exponential decay function showed a very rapid increase in BRA expression at low light intensities (time constant $\tau = 0.07$ $\mu W mm^{-2}$/percent eGFP+, see methods), with saturation reached at ~0.4 $\mu W mm^{-2}$. The high sensitivity at lower light intensities suggests a binary switch for onset of BRA expression above a signaling threshold, followed by a monotonic increase in BRA expression levels in a light dose-dependent manner.

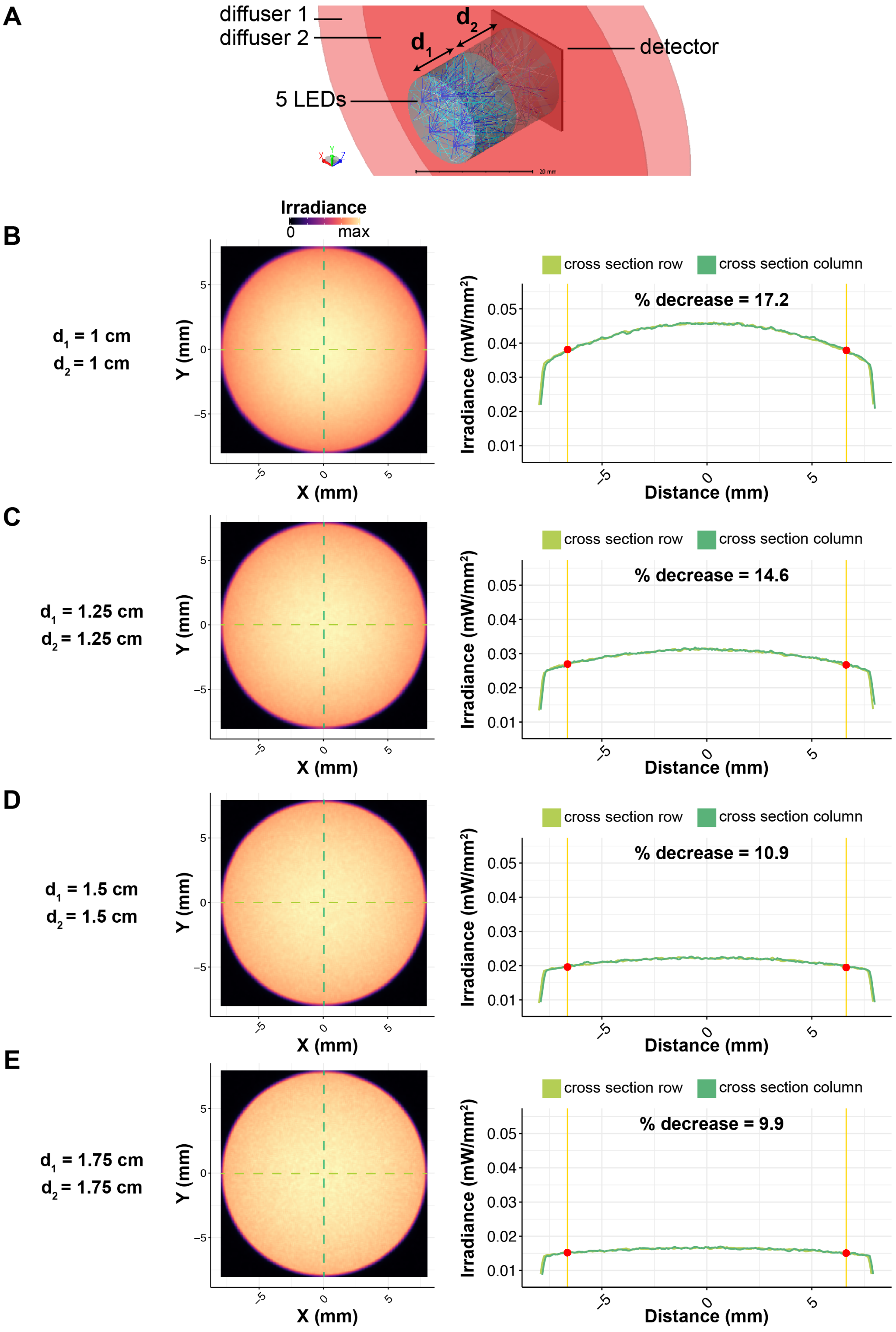

Figure 2.5: *See caption on next page.*

Figure 2.5: **Results of Zemax modeling at variable light guide thicknesses, d_1 and d_2**
A) Schematic of modeling setup. Five LEDs illuminate detector through two 0.01” thick sheets of polycarbonate with 80° diffuser coating (red) and two reflective light guides with Lambertian scattering (grey cylinder). **B-E)** Modeling results at indicated values of d_1, d_2. Image at detector plane (left) and column and row cross-sections (right) with well edge of 24-well plate indicated with red points show improved illumination uniformity at expense of light intensity with increasing light guide thickness.

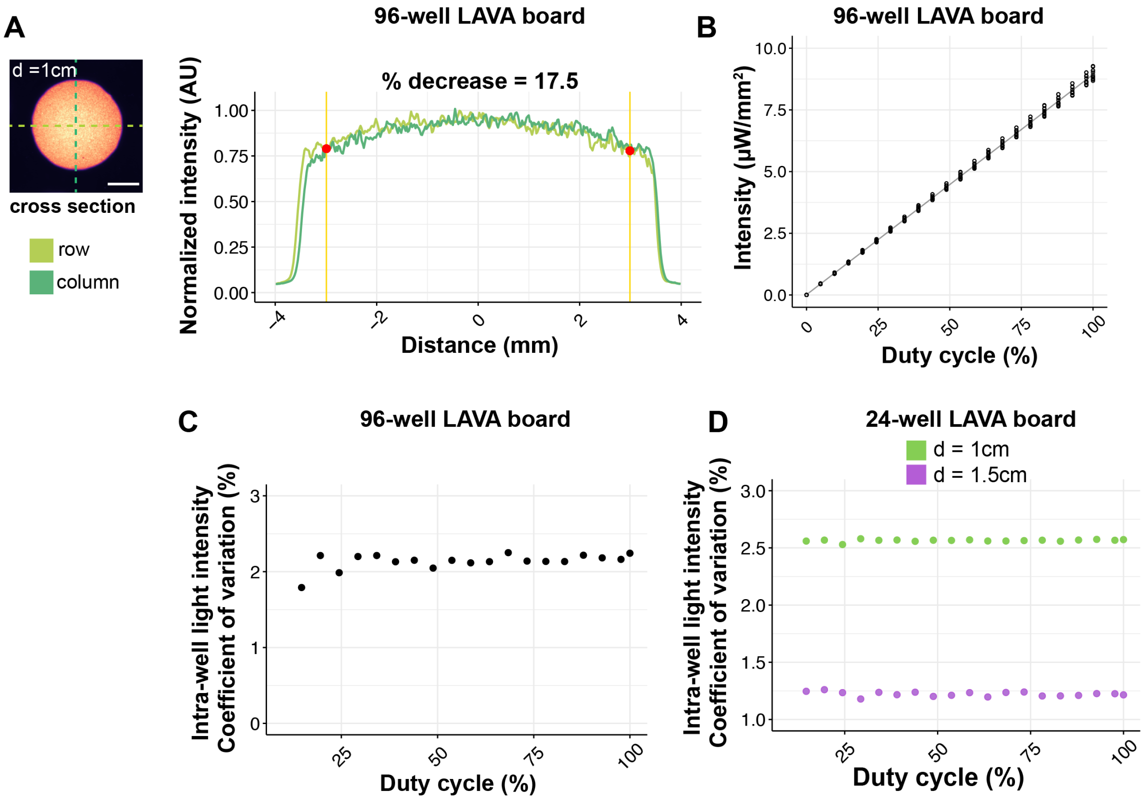

Figure 2.6: **Intensity characterization of 24-well and 96-well LAVA boards**
A) Brightfield images of well (left) and graph of intensity linescans along indicated cross-sections (right) characterize the intensity uniformity of the 96-well LAVA board when $d = 1\ cm$. Percent decrease is calculated between intensity at center of well and intensity at highlighted red point, which indicates location of well edge of a 96-well culture plate. Graph shows mean normalized intensity over 2 independent wells. Scale bar 2.5 mm. **B)** Measured light intensity in response to the programmed duty cycle of the LED pulse-width modulation signal. Graph shows measured intensity from wells of a 96-well LAVA board and curve fit to a linear regression model. **C)** Coefficient of variation of light intensity between the 24 independent light channels of a 96-well LAVA device measured at different programmed intensities. **D)** Coefficient of variation of light intensity between the 24 independent light channels of a 24-well LAVA device measured at different programmed intensities. Green points correspond to optical configuration with $d = 1\ cm$, violet points show optical configuration with $d = 1.5\ cm$.

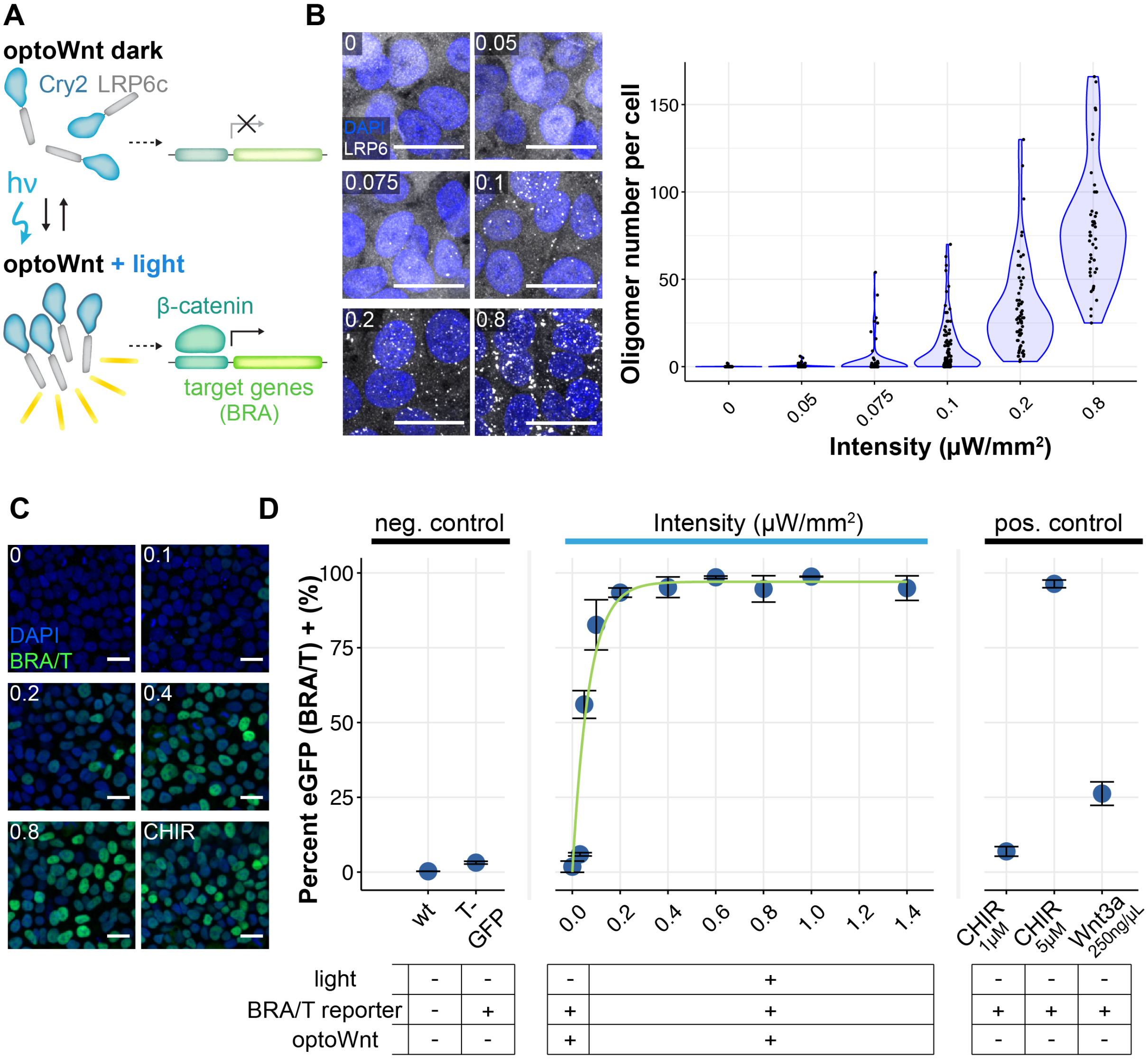

Figure 2.7: **Optogenetic induction of BRA expression is light dose dependent**
A) Schematic of optoWnt system. In the dark, the Cry2 photosensory domain is diffuse. Illumination induces LRP6c oligomerization and transcription of β-catenin target genes. **B)** Immunostaining for LRP6 (left) and quantification of cluster number per hESC in response to increasing light intensity after 1 hr illumination. Graph shows individual cell quantification, sith each point representing a single cell. Scale bar 25 μm. **C)** Immunostaining for BRA in response to increasing light intensity after 24 hr illumination or 3 μm CHIR treatment. Scale bar 25 μm. **D)** Flow cytometry of optoWnt hESCs expressing eGFP reporter for BRA/T treated with varying light intensities or with Wnt pathway agonists (Wnt3a recombinant protein or CHIR). Graph shows percent eGFP positive cells and nonlinear least squares fit to increasing exponential decay curve. Subset of data reproduced from (*8*). Graph shows mean ± 1 s.d., n = 3 biological replicates.

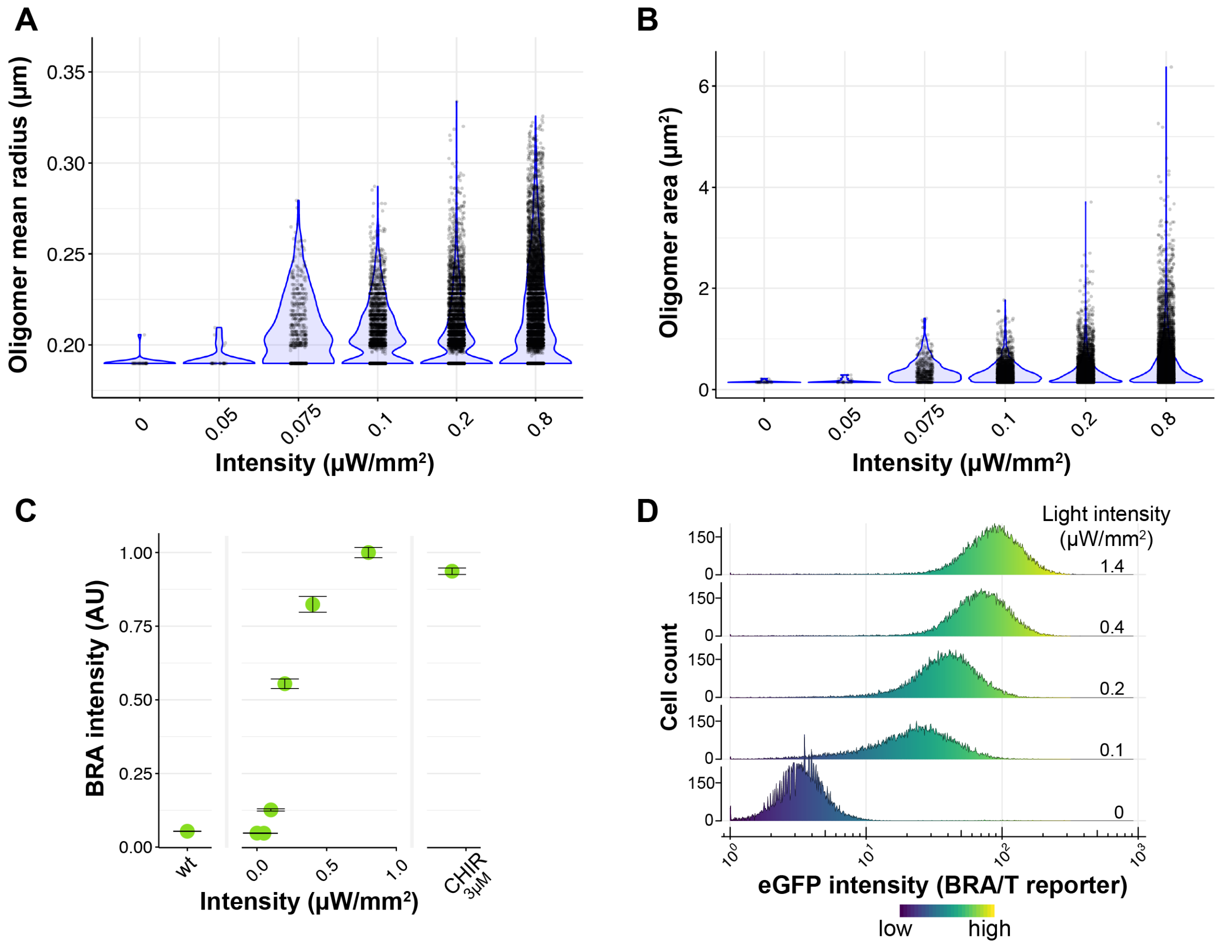

Figure 2.8: **LRP6 oligomer size and BRA expression in optoWnt cells is dose-responsive to light intensity**

A-B) Quantification of LRP6 oligomer size from immunostaining of optoWnt hESCs illuminated at indicated light intensities for 1 hr, Each point represents an LRP6 oligomer, with > 100 cells analyzed per condition. **C)** Quantification BRA immunostaining in response to increasing light intensity after 24 hr illumination or 3μm CHIR treatment. Average BRA intensity per hESC was calculated for each biological replicate. Graph shows mean of biological replicates ± 1 s.d., n = 3 replicates. **D)** Flow cytometry histograms of optoWnt hESCs expressing eGFP reporter for BRA/T after 24 hr illumination at varying light intensities. Graph shows sum of n = 3 replicates.

2.3.2 Analysis of phototoxicity reveals no detectable effects on hESC viability at maximal optoWnt activation

Since high intensity light can induce phototoxicity in cells (*35, 47–49*), we used the LAVA boards to analyze the phototoxicity threshold for hESC cultures. Inefficiencies in LED semiconductors cause heating, and though we incorporated a heat sink, cooling fans, and electrical vias in the circuit board design to conduct heat away from the cell culture plate, we observed heating of the LED dyes at continuous operation at high intensities (Figure 2.9A). Within the intensity range where we did not observe significant heating ($0 - 2\ \mu W mm^{-2}$), we assessed potential phototoxic effects on hESC cultures after 48 hrs of continuous illumination. Above 1 $\mu W mm^{-2}$, we observed a significant increase in apoptosis and membrane integrity markers Annexin IV and propidium iodide (PI), as well as a corresponding increase in cell debris and edge roughness of hESC colonies (Figure 2.9B-C). Thus, for all optogenetic stimulation we used light intensity under 1 $\mu W mm^{-2}$ (specifically, 0.8 $\mu W mm^{-2}$). At this intensity, we saw no decrease in pluripotency markers SOX2, NANOG, and OCT4 after 48 hrs of illumination of wild-type hESCs, as well as no spontaneous BRA+ mesendoderm differentiation (Figure 2.9D). Notably, since saturation in the percentage BRA+ optoWnt cells occurred at ~0.4 $\mu W mm^{-2}$ (Figure 2.7D), the optoWnt operating range falls below the 1 $\mu W mm^{-2}$ phototoxicity threshold.

Figure 2.9: **Phototoxicity during continuous optogenetic stimulation of hESC cultures)** **A)** Temperature of media after 24 hrs of continuous illumination. **B)** Brightfield images (top) of live wild-type hESC cultures illuminated at indicated light intensities for 48 hrs and flow cytometry results for Annexin V and propidium iodide (PI) stain. Scale bar 250 μm. **C)** Quantification of apoptosis marker Annexin V and dead cell stain PI shows a significant increase in apoptosis and cell death above $1 \mu W mm^{-2}$ illumination intensity (p_A=0.002, $p_P I$=0.001 at 0 vs. 1 $\mu W mm^{-2}$ and p_A=0.0005, $p_P I = 0.0005$ at 0 vs. 2 $\mu W mm^{-2}$). No difference was observed between 0 and $0.5 \mu W mm^{-2}$ (p_A=0.78, $p_P I$=0.50). ANOVA followed by Tukey test. Graph shows mean ± 1 s.d., n = 3 biological replicates. **D)** Representative fluorescence images (left) and quantification (right) of wild-type hESCs stained for cell fate markers SOX2, NANOG, OCT4, and BRA after 48 hrs illumination at 0.8 $\mu W mm^{-2}$. Student's t-test (two-tail). Graph shows mean ± 1 s.d., n = 3 biological replicates. Scale bar 25 μm.

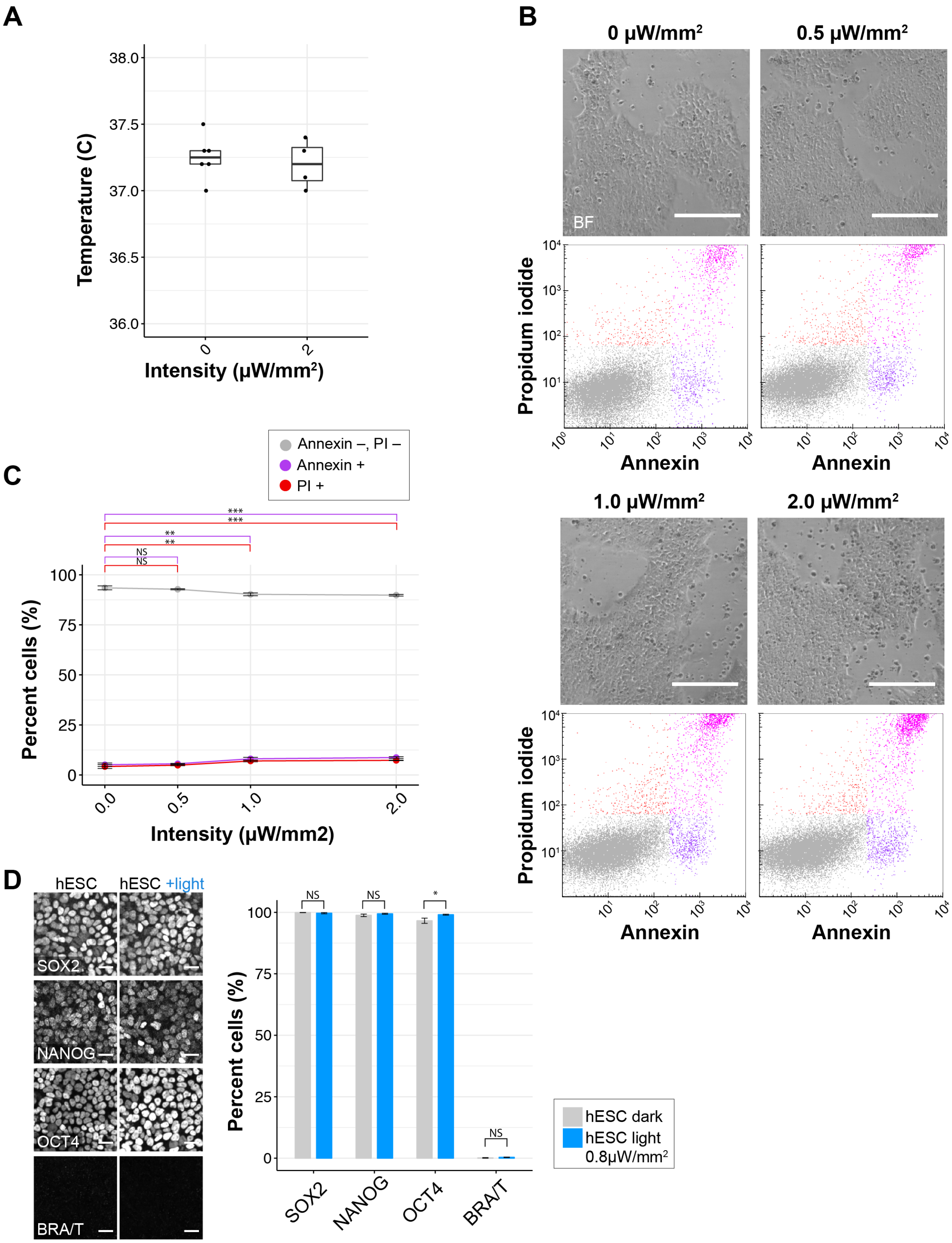

Figure 2.9: *See caption on previous page.*

2.3.3 Temporal control of optoWnt shows BRA downregulation after light withdrawal

In addition to intensity control, LAVA boards enable temporal control of illumination patterns (Figure 2.10A). Given the reversible oligomerization of Cry2 (7), we reasoned that the optoWnt system can be readily applied to regulation of Wnt temporal dynamics.

We designed a LAVA board GUI to allow users to input the desired temporal light patterns for each independent well (Figure 2.11A-C). After input of illumination parameters, the GUI wirelessly transmits the parameters to the LAVA device in the form of a JSON file. The file is parsed by the on-board Raspberry Pi microcontroller, which then to sets LED intensities and temporal patterns for the duration of the experiment. The user can set each of the 24 wells to one of three modes: (1) constant illumination at a specified intensity; (2) blinking at a specified intensity, duty cycle, and period; and (3) a series of linear or sinusoidal functions at specified function parameters. Multiple piecewise functions can be programmed in sequence, enabling an immense variety of complex, time-varying light patterns (Figure 2.10B, Supplementary video 1). The shortest possible blink, i.e. the temporal resolution of the device, is set to 1 ms in firmware, though we observed a significant drop in the accuracy and precision of stimulation at pulsewidths below 10 ms (Figure 2.10C, Figure 2.12).

We next asked whether sustained optoWnt activation is required to maintain BRA expression during hESC differentiation. We thus illuminated optoWnt cells expressing the T/eGFP reporter with varying durations of light and quantified eGFP fluorescence with flow cytometry at a fixed endpoint (Figure 2.10D). The duration of optoWnt stimulation determined endpoint eGFP intensity, suggesting that sustained illumination and optoWnt activation is necessary for a sustained β-catenin transcriptional response.

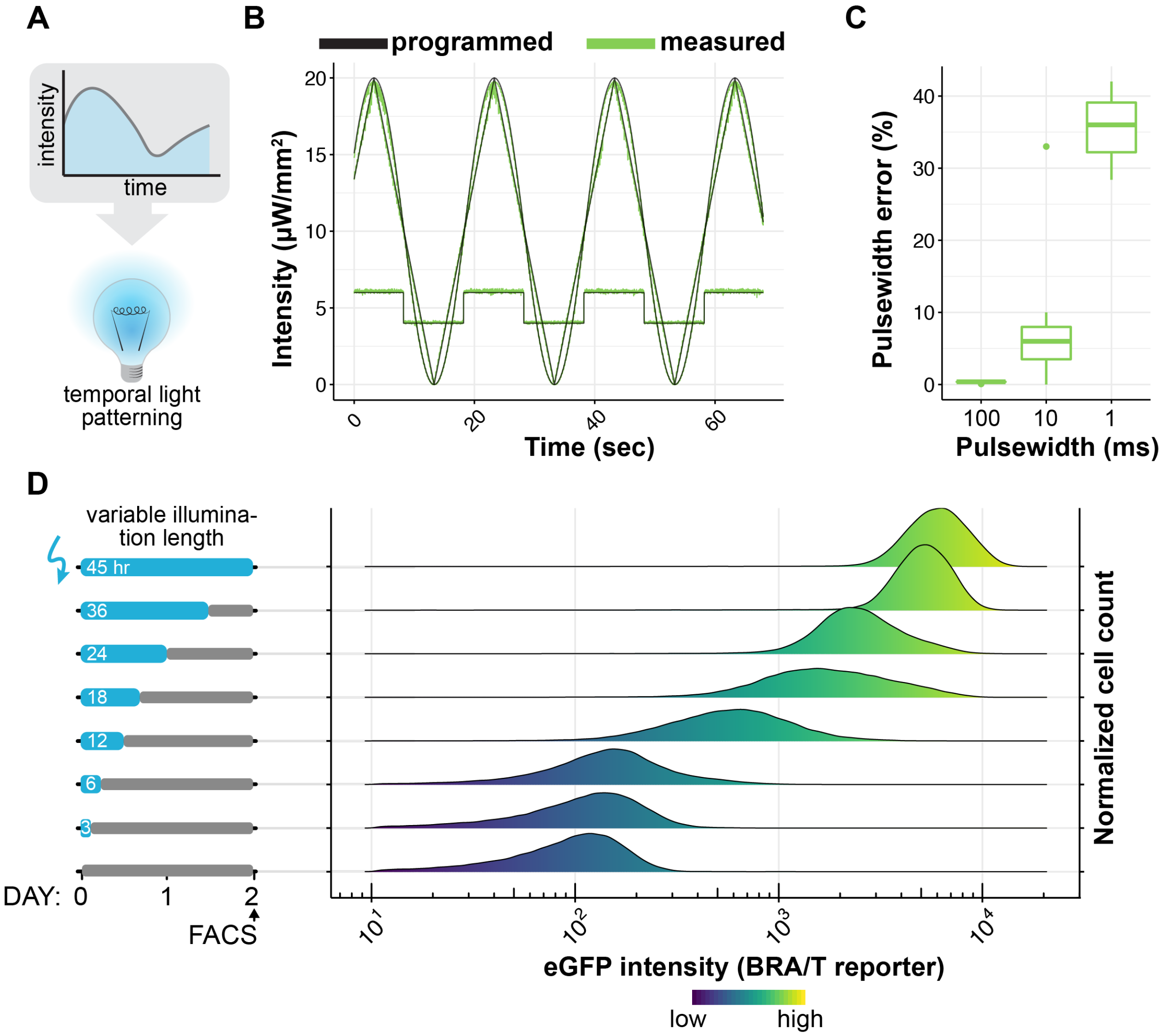

Figure 2.10: **Characterization of temporal control using LAVA devices**
A) Schematic of temporal light patterning in optogenetics. **B)** LAVA board well intensity as a function of time of various waveforms programmed through LAVA GUI. Programmed values shown in black, measured intensities shown in green. **C)** Percent error in measured pulsewidth relative to programmed pulsewidth for blinking sequences programmed through the LAVA GUI at 50% duty cycle and at indicated pulsewidth on-times. **D)** OptoWnt hESCs containing an eGFP reporter for endogenous BRA/T activity were illuminated for varying lengths of time and analyzed by flow cytometry at a fixed endpoint. Graph shows histograms of eGFP expression at each illumination condition. Cell count histograms normalized to total cells per condition (~30,000 cells), n = 3 biological replicates.

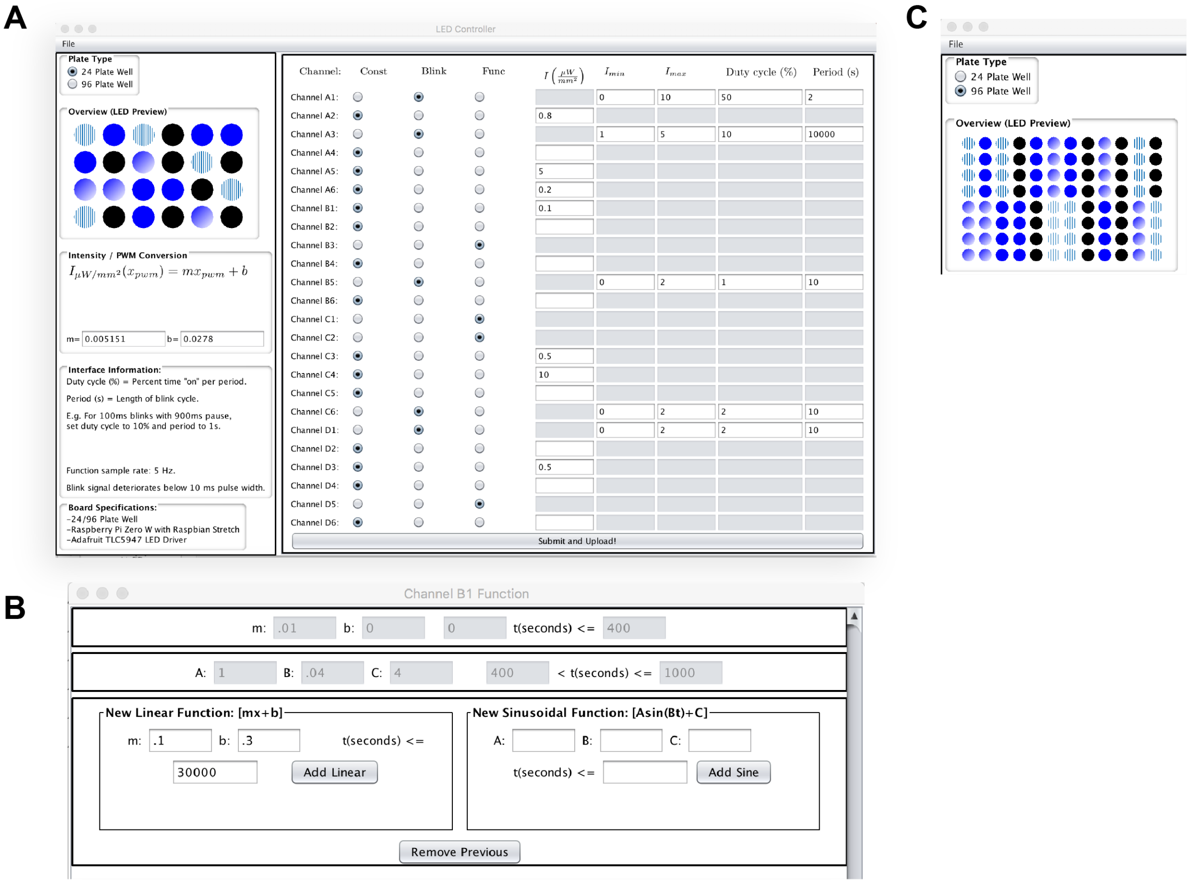

Plate Type
● 24 Plate Well
○ 96 Plate Well

Intensity / PWM Conversion

$I_{\mu W/mm^2}(x_{pwm}) = m x_{pwm} + b$

m= 0.005151 b= 0.0278

Interface Information:

Duty cycle (%) = Percent time "on" per period.

Period (s) = Length of blink cycle.

E.g. For 100ms blinks with 900ms pause, set duty cycle to 10% and period to 1s.

Function sample rate: 5 Hz.

Blink signal deteriorates below 10 ms pulse width.

Board Specifications:
-24/96 Plate Well
-Raspberry Pi Zero W with Raspbian Stretch
-Adafruit TLC5947 LED Driver

Channel:	Const	Blink	Func	$I\left(\frac{\mu W}{mm^2}\right)$	I_{min}	I_{max}	Duty cycle (%)	Period (s)
Channel A1:	○	●	○		0	10	50	2
Channel A2:	●	○	○	0.8				
Channel A3:	○	●	○		1	5	10	10000
Channel A4:	●	○	○					
Channel A5:	●	○	○	5				
Channel A6:	●	○	○	0.2				
Channel B1:	●	○	○	0.1				
Channel B2:	●	○	○					
Channel B3:	○	○	●					
Channel B4:	●	○	○					
Channel B5:	○	●	○		0	2	1	10
Channel B6:	●	○	○					
Channel C1:	○	○	●					
Channel C2:	○	○	●					
Channel C3:	●	○	○	0.5				
Channel C4:	●	○	○	10				
Channel C5:	●	○	○					
Channel C6:	○	●	○		0	2	2	10
Channel D1:	○	●	○		0	2	2	10
Channel D2:	●	○	○					
Channel D3:	●	○	○	0.5				
Channel D4:	●	○	○					
Channel D5:	○	○	●					
Channel D6:	●	○	○					

m: .01 b: 0 0 t(seconds) <= 400

A: 1 B: .04 C: 4 400 < t(seconds) <= 1000

New Linear Function: [mx+b]
m: .1 b: .3 t(seconds) <= 30000

New Sinusoidal Function: [Asin(Bt)+C]
A: B: C:
t(seconds) <=

Plate Type
○ 24 Plate Well
● 96 Plate Well

Figure 2.11: **Screenshot of GUI for LAVA board control**
A) Screenshot of GUI under 24-well TC plate setting. **B)** Screenshot of diaolog box for input of time-varying light patterns as piecewise functions. **C)** Screenshot of GUI under 96-well TC plate setting.

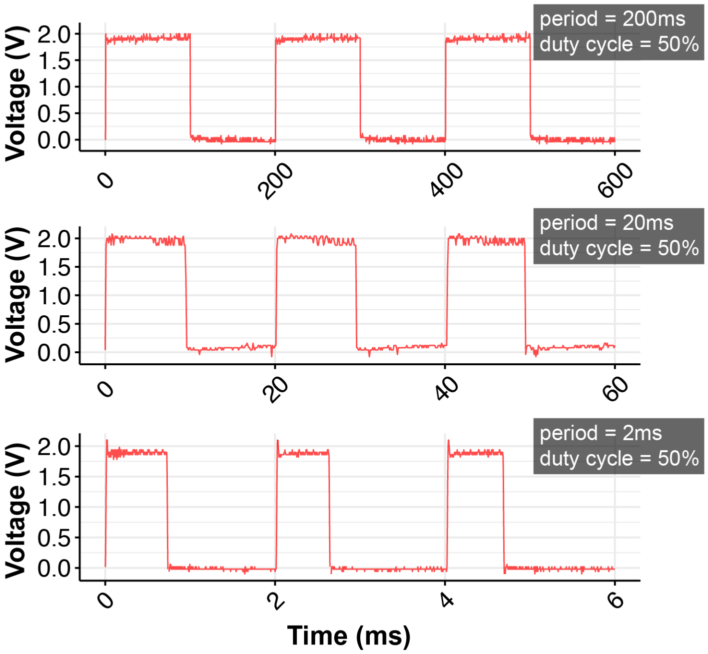

Figure 2.12: **Measured illumination intensity during programmed blink sequences show signal inaccuracy at 1 ms pulses**
Voltage signal from power meter measured with oscilloscope and is proportional to irradiance.

2.3.4 Spatial localization of Wnt signaling and hESC differentiation as a model for early embryonic Wnt patterning

Another advantage of optogenetic control is the ability to manipulate the spatial location of signal activation (Figure 2.13A). Though precise patterned illumination can be achieved with confocal scanning or the use of spatial light modulators (*6*), the cost and complexity of such microscope systems are restrictive, particularly for longer biological processes and/or large sample sizes. Instead, the majority of optogenetic studies leverage genetic specificity to target cell types of interest (*35*) or subcellular tagging to specific cell compartments (*64*) to achieve higher spatial resolutions. To easily incorporate spatial light patterning during cell culture, we designed die-cut photomasks that can be adhered to TC plates during illumination (Figure 2.14A). The mask feature size was limited by the cutting resolution of the die cutter to ∼150 μm (Figure 2.14B). Using such photomasks, we were able to illuminate wells with arbitrary light patterns and induce optoWnt clustering only in illuminated regions (Figure 2.13B). Since the mask was placed underneath the TC plate, we anticipated that there would be light scattering through the plate bottom (170 μm-thick coverglass) that would compromise the mask resolution (Figure 2.14C). To quantify the extent of light scattering, we measured the number of LRP6 clusters as a function of distance beyond the mask edge and found that clusters were induced ∼50 μm from the mask edge (Figure 2.13C). Thus, photomask feature size was limited to ∼150 μm while patterning resolution (full width at half maximum, see methods) was ∼100 μm (Figure 2.13C).

During mammalian development, a gradient of Wnt signaling emerges across the epiblast (*1*, *53*, *60*). Subsequently, cells in the posterior epiblast break away from the epithelial cell layer, migrating as single cells, which results in spatial rearrangement and morphological symmetry-breaking of the epiblast in the region of the primitive streak (*65–67*). We modeled this spatial pattern of Wnt signaling by activating optoWnt hESCs in defined regions within the culture. To determine whether optoWnt activation could trigger cell migration outside the area of illumination, we used the LAVA boards to illuminate cells with a 1.5 mm-diameter circular light pattern (Figure 2.15A). Indeed, immunostaining showed that BRA+ cells localized both within the illuminated region as well as up to ∼300 μm beyond the illumination boundary (Figure 2.15B). Given the ∼50 μm photomask scattering (Figure 2.13C), we excluded the possibility that cells were activated by scattered light. Intriguingly, within the illuminated circle, BRA+ cells grew vertically upwards and piled four to six cell diameters in height (∼70 μm). In contrast, BRA+ cells beyond the illumination boundary localized underneath the epithelial cell layer (Figure 2.15A). These cells likely underwent an epithelial-to-mesenchymal transition (EMT) and migrated below the hESC colony, reflecting a migratory phenotype that has been analogously observed in hESCs undergoing EMT in conditions of high cell density and confinement (*68*).

We next illuminated optoWnt cultures with a stripe of light to mimic the spatial geometry of Wnt gradients established across the epiblast (*60*). Cells in the illuminated stripe broke away from hESC colonies, adopted a mesenchymal morphology, and localized up to 500 μm beyond the boundary of the light pattern (Figure 2.15C). Immunostaining confirmed that these migratory cells expressed BRA, while surrounding unilluminated cells retained epithelial morphology with no detectable BRA expression. In addition, migratory cells showed a decrease in OCT4 expression, a shift in β-CAT localization away from the plasma membrane, and an increase in SLUG expression, all consistent with cells undergoing an EMT (Figure 2.15C). Taken together, these data show that optogenetic Wnt activation is sufficient for inducing a migratory cell phenotype and that patterned illumination can be used as a tool to further study Wnt patterning and gastrulation-like events in ESC culture.

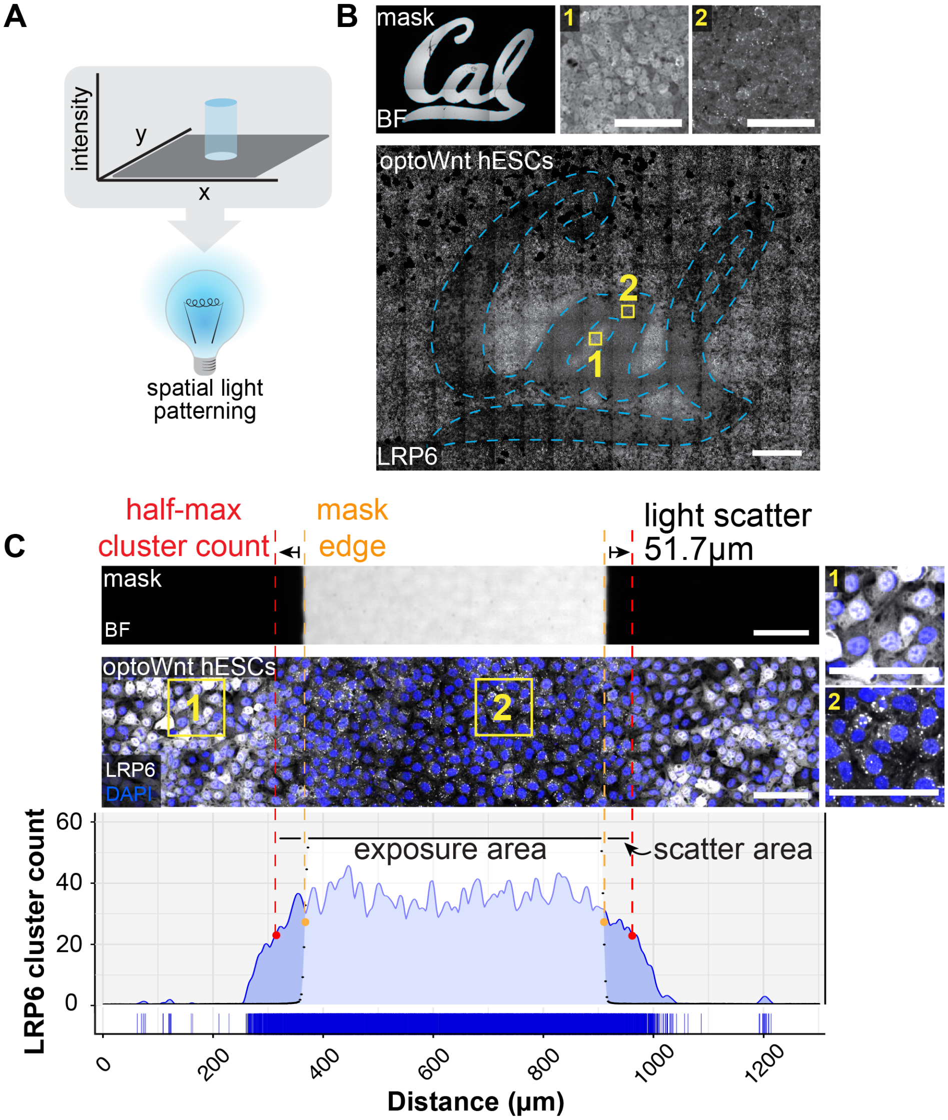

Figure 2.13: **Light patterning with LAVA devices for localized optoWnt activation**
A) Schematic of spatial light patterning in optogenetic experiments. **B)** Stitched brightfield and fluorescence confocal images of optoWnt hESCs illuminated with UC Berkeley (Cal) logo photomask. Immunostaining for LRP6 oligomers, with representative image of masked region (1) and illuminated region (2) as shown. Scale bar 100 μm (top), 1 mm (bottom). **C)** Quantification of light scattering through bottom of TC plate shows a ~50 μm spread (full width at half max, red line) of optoWnt oligomers beyond photomask edge (orange line). Figure shows brightfield image of photomask (top), fluorescence image of immunostaining for LRP6 (middle), and quantification of LRP6 cluster count (bottom). Insets (1) and (2) show masked and illuminated regions, respectively. Scale bars 100 μm.

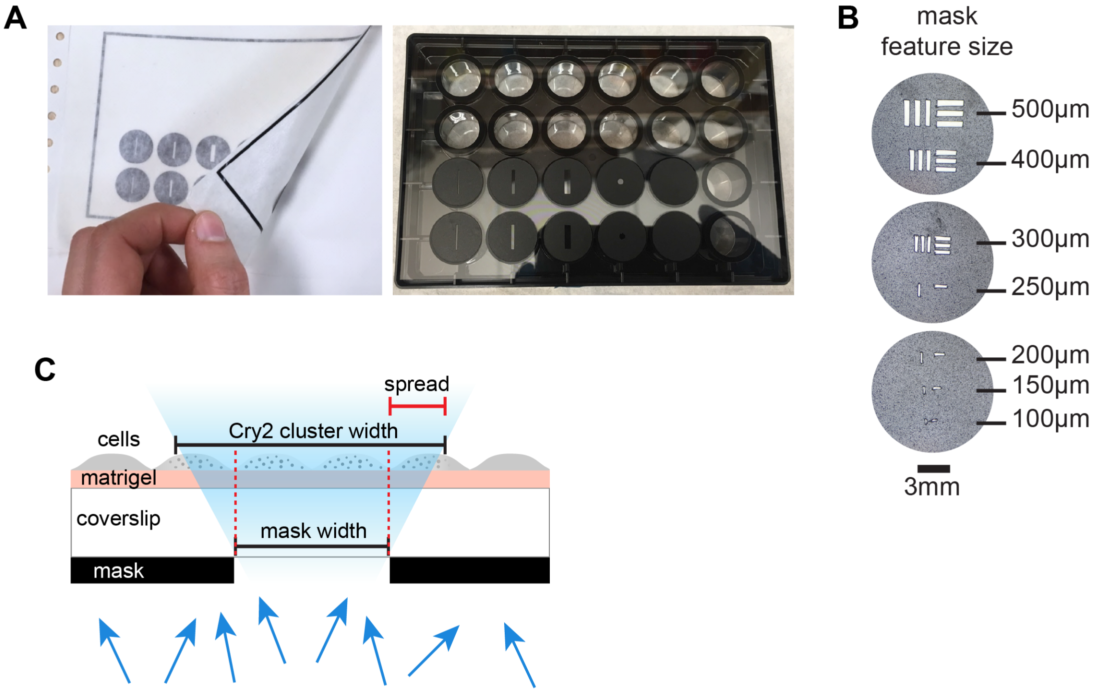

Figure 2.14: **Dye-cut photomask enables spatial control of illumination**
A) Images of adhesive die-cut masks applied using transfer tape (top) onto 24-well TC plate (bottom). **B)** Brightfield images of die-cut mask illustrate resolution limit of cutter. Scale bar 3 *mm*. **C)** Schematic of light scattering from photomask.

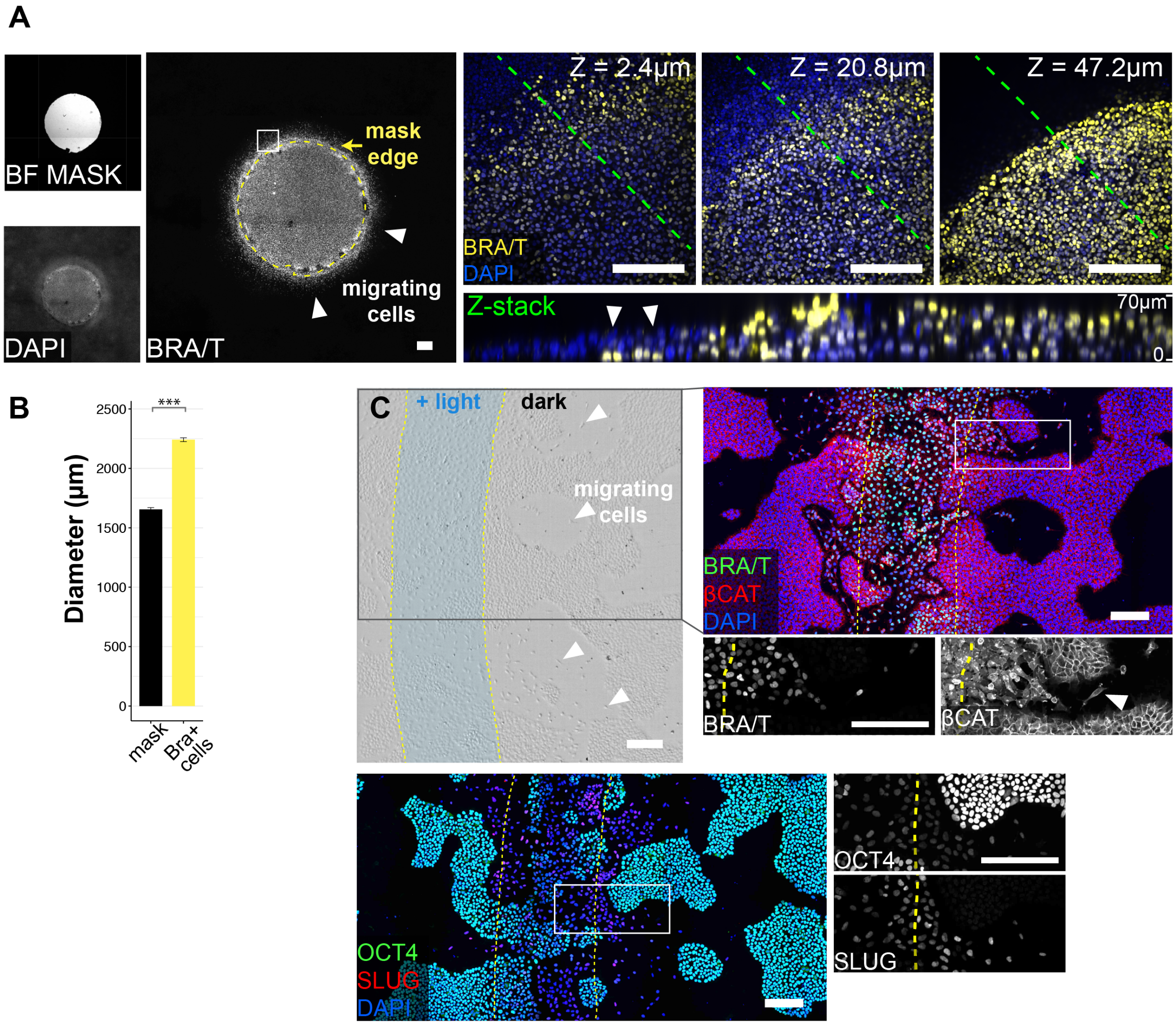

Figure 2.15: **Localized Wnt activation with LAVA devices activates localized ESC differentiation and EMT**

A) Patterned illumination with a 1.5 *mm* diameter circle of light. BRA immunostaining with photomask overlay shown in left panel. Confocal z-stacks of bottom (closest to coverslip, Z = 2.4 *μm*), middle (Z = 20.8 *μm*) and top (Z = 47.2 *μm*) cell layers show BRA+ cells localized beyond photomask boundary and under the epithelial cell layer (white arrows). Bottom panel shows z-slice through cross-section highlighted with green line. Scale bars 100 *μm*. **B)** Quantification of BRA+ cell localization beyond photomask edge. Mean diameter of circular photomask pattern was quantified using the brightfield image channel, and mean diameter of BRA+ cell pattern was quantified through immunostaining, as shown in (D). Graph shows mean measured diameter ± 1 s.d., n = 3 biological replicates. Student's t-test (two-tail). Scale bars 200 *μm*. *Continued on next page.*

Figure 2.15: **C)** Patterned illumination with stripe of light, 500 μm in width. Brightfield image (left panel) with overlay of light pattern shows cells with mesenchymal morphology localized beyond of region of illumination (white arrows). Immunostaining for BRA and β-CAT (middle panel); OCT4 and SLUG (right panel). Overlay of light pattern is highlighted in yellow, and zoom-in (white box) shown below. Scale bars 200 μm.

2.4 Discussion

Spatial and temporal morphogen gradients have long been known to exist during development, though there has been a paucity of tools to create and perturb such signaling patterns. In this study, we combined optogenetic control of Wnt signaling with novel engineered illumination devices, LAVA boards, to dynamically control hESC morphogen signaling in intensity, space, and time. Using this precise manipulation of morphogen signaling, we show that optogenetic Wnt patterning can be used to mimic embryonic morphogen patterning in vitro. This platform will enable future studies that elucidate spatial and temporal Wnt signaling thresholds and mechanisms of cell patterning in a variety of biological systems.

2.4.1 LAVA boards for quantitative, spatiotemporal control of Wnt signaling dynamics

With the continued development of new optogenetic proteins that perturb cell signaling and protein-protein interactions, there is a need for illumination devices that allow high-throughput intensity, spatial, and temporal control of stimulation. Previous illumination technologies for multi-well plate photostimulation have helped advance optogenetic studies, but have addressed only some of these individual design criteria and do not fully characterize intensity parameters, uniformity, spatial and temporal resolution, or undesired heating and toxicity (*40–45*). Thus, in designing LAVA boards, we addressed such concerns and engineered devices that programmatically control photostimulation intensity, timing, and location at 0.005 $\mu W mm^{-2}$, 10 ms, and 100 μm resolution, respectively. As optical system cost and ease of use can be significant barriers for adoption of optogenetic studies, we also developed a GUI for simple configuration and wireless upload of desired intensity patterns to LAVA devices from a personal computer. Further, to make optogenetic studies more accessible, we provide a detailed protocol, design files, and software source code for both 24-well and 96-well plate LAVA board assembly. Each device takes ∼8 hrs and less than $500 to fabricate and assemble.

One of the major optical design parameters we optimized during LAVA board design was illumination uniformity. Since the strength of induced Wnt signaling is dependent on light dosage (Figure 2.7D), nonuniformity can give rise to signal variation across the region of optogenetic stimulation. Specifically, the optoWnt dose response showed that Wnt activation can be sensitive to up to 0.025 $\mu W mm^{-2}$ differences in intensity, especially at photostimulation near 0.1 $\mu W mm^{-2}$ (Figure 2.7D). Despite this high sensitivity, the optimized LAVA board design is equipped to stimulate wells at sufficiently uniform levels. Illumination at 0.1 $\mu W mm^{-2}$, for example, would have a 0.017 $\mu W mm^{-2}$ intensity drop-off at the well edge (16.9% decrease) (Figure 2.4B), which is below the 0.025 $\mu W mm^{-2}$ design criterium and thus results in uniform Wnt signal activation within the well. Though characterization of uniformity is critical for controlled signal activation, surprisingly this design parameter has not been addressed in previous illumination systems (*39, 40*).

Equally important to illumination uniformity is programmable control of intensity for dose-responsive and time-varying signal activation. Because we observed dose-dependent Wnt signal activation in response to increasing light intensities (Figure 2.7D), the LAVA boards combined with the optoWnt system can be readily applied to various biological systems where Wnt signal strength directly regulates cell fate outcome. For example, different Wnt signal intensities can drive dose-dependent or divergent lineage specification during neural fate commitment (*69, 70*), hematopoiesis (*71*), and mesoderm differentiation (*55, 72*). In addition, the optoWnt dose response suggests a role for LRP6 oligomer size in regulating β-catenin degradation (*73, 74*), which can be used to further shed light on the molecular regulation of Wnt signaling. In parallel, temporal modulation with LAVA devices opens a range of possible studies of Wnt signal dynamics (Figure 2.10). Combined with optoWnt reversibility (*7*)(Figure 2.10D), intricate studies of Wnt signaling thresholds and timing of signaling oscillations during development (*75–78*) can now be performed with much greater ease compared with microfluidic approaches (*79*) or manual pipetting (*80*).

Lastly, for spatial control, we implement a dye-cut photomask to achieve spatial patterning at 100 μm resolution (Figure 2.13C), an improvement relative to previous innovative photomask approaches (*36, 37*). Patterned illumination thus enables the unprecedented ability to 'paint' Wnt activation onto target cells of interest and study how the shape, size, and intensity of spatial patterns influences differentiation and morphogenesis. Elegant optogenetic approaches for studying spatial signaling thresholds, like patterned ERK signaling during early Drosophila embryogenesis (*10, 12*), can now be extended to morphogen patterning in stem cell-based and organoid models for development.

2.4.2 Limitations

Having established proof of principle applications for LAVA devices and the optoWnt system, we would like to comment on their limitations as well as considerations for generalizability to other optogenetic systems. Many hardware components of LAVA boards are exchangeable, so that LEDs of other colors can readily be incorporated to activate red or UV-based light sensors. Currently, the hardware design allows independent control of a single color, but can be extended to multicolor stimulation by modifying the electronics design to incorporate more LED drivers.

To stimulate photosensory proteins, light delivered by LAVA devices must be of sufficiently high intensities. We have found that the achieved illumination intensities (0 – 20 $\mu W mm^{-2}$) are sufficient for optoWnt photostimulation, which requires merely 0.5 – 1 $\mu W mm^{-2}$ for maximal activation (Figure 2.7D). However, LAVA board intensities may be insufficient for less sensitive photosensory domains that can require pulses of up to 1,000 – 10,000 $\mu W mm^{-2}$ (*35*). LAVA board intensities can be increased by minimizing the light guide thickness, d (see Figure 2.4), but the maximal illumination intensity is still limited by the maximum forward current of LED dyes, as well as by the phototoxicity of light at higher intensities (*35*, *47*–*50*). Thus, for high-intensity applications, microscope-based systems and laser illumination would be more suitable.

Lastly, spatial patterning with a photomask is limited to a static, two-dimensional light pattern, with resolution limited by light scattering through the TC plate bottom surface. In the future, the pattern feature size can be improved by using chrome masks or laser-plotted mylar masks, which are limited to sub-micron and ∼5 – 10 μm features, respectively (*81*). Such methods can also be used to achieve greyscale modulation (*81*). In summary, LAVA devices are versatile tools for photostimulation of cell cultures, and can be applied to many biological systems for studies of cell signaling dynamics, high-throughput screens, and control of protein-protein interactions.

2.5 Methods

2.5.1 Zemax modeling and uniformity optimization

The ray-tracing software Zemax OpticStudio was used in Non-Sequential mode to model illumination of a 24-well plate. Based on modeling results, the optimized configuration parameters are as follows: 5 surface-mount LEDs are symmetrically radially distributed around a 5mm-radius circle; the radius of each light guide is 8.25 mm; one 80° circular optical diffuser is placed between the two light guides and another onto the top light guide (i.e. between light guide and TC plate); the thickness of each light guide is 1.5 cm; and light guides are manufactured from black 3D-printed acrylic.

2.5.2 LAVA device construction

LAVA devices are constructed using two custom printed circuit boards (PCB) designed in EAGLE (Autodesk). PCB1 contains electronics for LED control while PCB2 is the power distribution board. For 24-well illumination, PCB1 contains solder pads for a circular array of 5 LEDs per well, which are connected in series and illuminate each well through two 3D-printed light guides and a series of diffusers (optical configuration optimized in Zemax, see below). For 96-well illumination, PCB1 contains solder pads for 1 LED per well of a 96-well plate; given the 24-channel LED driver, independent illumination control is possible for each group of 4 wells. For each channel, the ground wire connects to TLC5947 driver and is modulated with pulse-width modulation, while the positive terminal connects to the power plane of PCB1. PCB1 also contains headers for electrical connection to cooling fans. A heatsink mounts onto the bottom of PCB1, using thermally conductive adhesive (Arctic Silver, ASTA-7G), in a region without silk screen and thermally conductive electrical vias that draw heat away from surface-mount LEDs.

In PCB2, a power supply connects through a barrel power jack to power the LEDs through an LED driver (TLC5947, Adafruit). Power is also supplied to three fans and the Raspberry Pi microcontroller through switching voltage regulators.

On top of PCB1, optical assembly and TC plate is mounted in such a way that TC plate is illuminated from the bottom. It is critical that TC plate is made of black, opaque plastic with a thin, 170 μm coverslip bottom (Eppendorf Cell Imaging Plate, 24-well) to avoid light bleed-through between wells and thus enhance high spatial patterning resolution. The LED driver, PCB2, and the Raspberry Pi microcontroller are all mounted and electrically connected to PCB1, and the entire assembly is mounted onto an acrylic laser-cut base through vibration-dampening mounts. The base contains rubber footpegs to reduce static or electrical shorting with the TC incubator racks.

For details of LAVA board design and fabrication, see supplemental methods which include a detailed protocol, design files, and software source code for 24-well and 96-well plate LAVA board assembly. In brief, LAVA boards were constructed in the CITRIS Invention Lab, a UC Berkeley rapid prototyping facility, using the following equipment: 3D printer

(Ultimaker 3), laser cutter (Speedy 400, Trotec), and standard soldering tools. Photomasks were dye-cut on a vinyl cutter (CAMM-1 GS-24, Roland).

2.5.3 LAVA software control and graphical user interface

The LEDs are controlled by an Adafruit 24-Channel 12-bit PWM LED driver with an SLI interface to a Raspberry Pi Zero W. The 12-bit PWM resolution allows 4086 unique illumination intensity levels over the LED operating range. For ease of use, a GUI has been written in Java and is conveniently packed into an executable file. This interface allows for independent control of each of the 24 channels. To accommodate the variety of experimental conditions, each LED can be programmed to a constant illumination, a blinking pattern, or a series of linear and sinusoidal patterns. Since each board has slightly different intensity characteristics, the intensity to PWM calibration parameters are input at runtime. Sinusoidal and linear functions are interpolated at a frequency of 1 Hz whereas blinking patterns have been tested up to 100 Hz. Since the LED board's USB port may be inaccessible during certain experiments, it is possible to wirelessly upload new illumination settings from any Wi-Fi capable computer. The Java program parses the illumination settings and PWM calibration parameters, packages them into a JSON file, and transmits these settings to the Pi over an SFTP channel.

Upon booting the Raspberry Pi, a C++ script executes, checks the device for previous illumination settings and resumes the patterned illumination if found. The Pi polls for changes in the JSON file every few seconds, so the changes of a newly uploaded pattern will be reflected without an additional reboot. It should be noted that the decision to use C++ was motivated by a desire to break through certain speed limitations posed by an interpreted language's rate of execution. A Python implementation was completed and included on the Pi operating system to easily generate custom pattern scripts, but only the compiled C++ version is able to drive the 24 channels at the desired refresh rate.

2.5.4 LAVA device intensity, uniformity, heating, and spectral characterization

For LAVA board characterization, light intensity was measured with a power meter (PM100D, Thorlabs) with a photodiode power sensor (S121C, Thorlabs) at 470 nm. For high-resolution measurement of temporal light patterns, the Thorlabs power meter was connected to an oscilloscope. Well uniformity measurements were performed by imaging wells on a Nikon Z100 microscope with a wide-field lens (Nicole AZ-Plan Apo 1x) and sCMOS monochrome camera (pco.edge 5.5). Image intensity was quantified as a function of distance in Fiji (*82*). Well temperature was measured with a digital multimeter (87-V, Fluke) with a Type-K thermocouple probe (80BK-A, Fluke). LED emission spectra were measured with a spectrometer (Red Tide USB650, Ocean Optics).

2.5.5 Embryonic stem cell culture

For routine culture and maintenance, all optogenetic and wild-type hESCs (H9, WiCell) (*83*) lines were grown on Matrigel (Corning, lot # 7268012, 7275006) coated plates in mTeSR1 medium (STEMCELL Technologies) and 1% penicillin/streptomycin (Life Technologies) at 37 °C and 5% CO2 with daily media changes. Optogenetic cells were cultured with hood lights off. For illumination experiments, cells were singularized with Accutase (STEMCELL Technologies) at 37°C for 5min and seeded onto Matrigel-coated 24-well plates (0030741021, Eppendorf, black-walled with 170 μm coverglass bottom) in E8 media (STEMCELL Technologies) with 5 μM ROCK inhibitor Y-27632 (Selleckchem) at a density of 35k – 70k cell cm^2. Wnt agonist CHIR99021 (Stemgent) or Wnt3a protein (StemRD) was diluted in E8 media and added to cells. Clonal optoWnt knock-in lines and clonal BRA/T reporter lines were generated through CRISPR/Cas9-mediated recombination as previously described (*8*).

2.5.6 Immunostaining and imaging

Cells were fixed with 3% PBS – paraformaldehyde (ThermoFisher) for 20min at room temperature and subsequently washed three times with PBS. Blocking and permeabilization was done with 5% donkey serum (D9663, Sigma-Aldrich) and 0.3% Triton X-100 (Fisher Scientific) (PBS-DT) for 1 hour. Cells were incubated with primary antibodies (Supplementary Table 1) at 4 °C overnight, then washed three times with PBS, and incubated with fluorescently conjugated secondary antibodies (Invitrogen) at 1:250 dilution for 1 hour at room temperature. Both primary and secondary antibodies were diluted in PBS-DT. Cells were washed with PBS and stained with 0.1 μmL^{-1} DAPI nuclear stain (ThermoFisher) prior to imaging. Confocal imaging was performed on a Perkin Elmer Opera Phenix system (QB3 High-Throughput Screening Facility). Brightfield and widefield fluorescence imaging was performed on a Zeiss AxioObserver epi-fluorescent microscope (CIRM/QB3 Shared Stem Cell Facility).

2.5.7 Image analysis

Microscopy image processing, including stitching and z-slice projection, was performed in Fiji (*82*) and image quantification was performed in CellProfiler (*84*) with custom analysis pipelines detailed below.

For quantification of BRA, SOX2, OCT4, and NANOG nuclear fluorescence intensity, nuclei stained with DAPI were identified and used to generate a binary mask applied to the appropriate fluorescence channel. The mean fluorescence intensity per cell nucleus was calculated for each cell in a given field of view. A threshold defining 'positive' cells was determined from signal intensity of negative control wells.

Spatial light patterning resolution was quantified by illuminating optoWnt hESC wells with a dye-cut photomask for 1 hr at 1 $\mu W mm^{-2}$ and immunostaining for LRP6. With mask attached to plate, wells were imaged in brightfield at varying focus positions, to capture images of both the photomask and cells. The mask was subsequently removed, and cells were imaged in brightfield and fluorescence channels (with 5x and 60x water-immersion objectives on a Perkin Elmer Opera Phenix confocal system). The mask image was aligned to the LRP6 fluorescence channel using the brightfield channel in Fiji (*82*). An identical alignment procedure was used for all spatial patterning data shown. For quantification of light scattering, multiple fields of view were stitched together and oligomers were manually counted in Fiji based on the LRP6 fluorescence channel. The pixel location of each identified LRP6 oligomer was recorded. Since the photomask pattern was a vertical stripe, the oligomer counts were summed vertically over multiple fields of view to quantify the spatial distribution of oligomers relative to the photomask. The spatial extent of photostimulation due to light scatter was calculated by determining the full width half maximum (FWHM) of the LRP6 oligomer distribution outside of the photomask.

2.5.8 Flow cytometry and analysis

Cells were lifted with Accutase at 37 $°C$ for 5 min, centrifuged, and resuspended in flow buffer (0.5% bovine serum albumin in PBS (w/v)) for analysis. For photoxicity experiments, centrifuged cells were resuspended in PBS and stained with AlexaFluor 488-conjugated annexin V and 1 $\mu g m L^{-1}$ propidium iodide (PI) as per kit manufacturer recommendations (V13241, ThermoFisher). Cells were analyzed on a BD LSR Fortessa X20 (UC Berkeley Cancer Research Laboratory Flow Cytometry Facility). Cell counting for proliferation assays was performed using a ThermoFisher Attune (UC Berkeley CIRM/QB3 Shared Stem Cell Facility) by measuring the number of cells per unit volume.

Data analysis was performed with FlowJo 10 software. To determine the fraction of BRA-eGFP+ cells after light treatment, gating was set such that less than 0.5% of undifferentiated wild-type hESCs were positive for eGFP and mCherry. Data were fit to an increasing exponential decay curve using a nonlinear least squares model in R:

$y \sim A_{max}(1 - e^{-x/\tau})$

where y represents the percent BRA-eGFP+ cells and x is light intensity ($\mu W mm^{-2}$). The curve asymptotically approaches the maximum percentage of BRA-eGFP+ cells ($A_{max} = 97.1\%$) with time constant $\tau = 0.07$.

2.5.9 Statistical analysis and graphing

Data are presented as mean ± 1 standard deviation (s.d.) unless otherwise specified. Statistical significance was determined by Student's t-test (two-tail) between two groups, and three or more groups were analyzed by one-way analysis of variance (ANOVA) followed by Tukey test. $P < 0.05$ was considered statistically significant (NS P>0.05, $*$P<0.05, $**$P<0.01, $***$P<0.001).

References

1. Arnold, S. J. & Robertson, E. J. Making a commitment: cell lineage allocation and axis patterning in the early mouse embryo. *Nat. Rev. Mol. Cell Biol.* **10,** 91–103 (2009).
2. Oates, A. C., Gorfinkiel, N., Gonzalez-Gaitan, M. & Heisenberg, C.-P. Quantitative approaches in developmental biology. *Nat. Rev. Genet.* **10,** 517–530 (2009).
3. Boyden, E. S., Zhang, F., Bamberg, E., Nagel, G. & Deisseroth, K. Millisecond-timescale, genetically targeted optical control of neural activity. *Millisecond-timescale, genetically targeted optical control of neural activity.* **8,** 1263–1268 (2005).
4. Nagel, G. *et al.* Channelrhodopsin-2, a directly light-gated cation-selective membrane channel. *Proceedings of the National Academy of Sciences* **100,** 13940–13945 (2003).
5. Hegemann, P. & Nagel, G. From channelrhodopsins to optogenetics. *EMBO Molecular Medicine* **5,** 173–176 (2013).
6. Repina, N. A., Rosenbloom, A., Mukherjee, A., Schaffer, D. V. & Kane, R. S. At Light Speed: Advances in Optogenetic Systems for Regulating Cell Signaling and Behavior. *Annual review of chemical and biomolecular engineering* **8,** 13–39 (2017).
7. Bugaj, L. J., Choksi, A. T., Mesuda, C. K., Kane, R. S. & Schaffer, D. V. Optogenetic protein clustering and signaling activation in mammalian cells. *Nat. Methods* **10,** 249–252 (2013).
8. Repina, N. A. *et al.* Optogenetic control of Wnt signaling for modeling early embryogenic patterning with human pluripotent stem cells. *bioRxiv* **8,** 665695 (2019).
9. Toettcher, J. E., Gong, D., Lim, W. A. & Weiner, O. D. Light-based feedback for controlling intracellular signaling dynamics. *Nat. Methods* **8,** 837–839 (2011).
10. Johnson, H. E. & Toettcher, J. E. Signaling Dynamics Control Cell Fate in the Early Drosophila Embryo. *Dev. Cell* **48,** 361–370.e3 (2019).
11. Toettcher, J. E., Weiner, O. D. & Lim, W. A. Using optogenetics to interrogate the dynamic control of signal transmission by the Ras/Erk module. *Cell* **155,** 1422–1434 (2013).
12. Johnson, H. E. *et al.* The Spatiotemporal Limits of Developmental Erk Signaling. *Dev. Cell* **40,** 185–192 (2017).
13. Kainrath, S., Stadler, M., Reichhart, E., Distel, M. & Janovjak, H. Green-Light-Induced Inactivation of Receptor Signaling Using Cobalamin-Binding Domains. *Angew Chem Int Ed Engl* **56,** 4608–4611 (2017).
14. Levskaya, A., Weiner, O. D., Lim, W. A. & Voigt, C. A. Spatiotemporal control of cell signalling using a light-switchable protein interaction. *Nature* **461,** 997–1001 (2009).
15. Yazawa, M., Sadaghiani, A. M., Hsueh, B. & Dolmetsch, R. E. Induction of protein-protein interactions in live cells using light. *Nature Biotechnology* **27,** 941–945 (2009).

16. Strickland, D. *et al.* TULIPs: tunable, light-controlled interacting protein tags for cell biology. *Nat. Methods* **9,** 379–384 (2012).

17. Guntas, G. *et al.* Engineering an improved light-induced dimer (iLID) for controlling the localization and activity of signaling proteins. *Proceedings of the National Academy of Sciences* **112,** 112–117 (2015).

18. Bugaj, L. J. *et al.* Regulation of endogenous transmembrane receptors through optogenetic Cry2 clustering. *Nat Commun* **6,** 6898 (2015).

19. Wang, X., He, L., Wu, Y. I., Hahn, K. M. & Montell, D. J. Light-mediated activation reveals a key role for Rac in collective guidance of cell movement in vivo. *Nat Cell Biol* **12,** 591–597 (2010).

20. Johnson, H. E. & Toettcher, J. E. Illuminating developmental biology with cellular optogenetics. *Current opinion in biotechnology* **52,** 42–48 (2018).

21. Sako, K. *et al.* Optogenetic Control of Nodal Signaling Reveals a Temporal Pattern of Nodal Signaling Regulating Cell Fate Specification during Gastrulation. *Cell Rep* **16,** 866–877 (2016).

22. Huang, A., Amourda, C., Zhang, S., Tolwinski, N. S. & Saunders, T. E. Decoding temporal interpretation of the morphogen Bicoid in the early Drosophila embryo. *eLife* **6,** 197 (2017).

23. Izquierdo, E., Quinkler, T. & De Renzis, S. Guided morphogenesis through optogenetic activation of Rho signalling during early Drosophila embryogenesis. *Nat Commun* **9,** 2366 (2018).

24. Guglielmi, G., Barry, J. D., Huber, W. & De Renzis, S. An Optogenetic Method to Modulate Cell Contractility during Tissue Morphogenesis. *Dev. Cell* **35,** 646–660 (2015).

25. Čapek, D. *et al.* Light-activated Frizzled7 reveals a permissive role of non-canonical wnt signaling in mesendoderm cell migration. *eLife* **8,** 1025 (2019).

26. Packer, A. M., Roska, B. & Häusser, M. Targeting neurons and photons for optogenetics. *Nat. Neurosci.* **16,** 805–815 (2013).

27. Prakash, R. *et al.* Two-photon optogenetic toolbox for fast inhibition, excitation and bistable modulation. *Nat. Methods* **9,** 1171–1179 (2012).

28. Packer, A. M., Russell, L. E., Dalgleish, H. W. P. & Häusser, M. Simultaneous all-optical manipulation and recording of neural circuit activity with cellular resolution in vivo. *Nat. Methods* **12,** 140–146 (2015).

29. Carrillo-Reid, L., Yang, W., Bando, Y., Peterka, D. S. & Yuste, R. Imprinting and recalling cortical ensembles. *Science* **353,** 691–694 (2016).

30. Nikolenko, V., Poskanzer, K. E. & Yuste, R. Two-photon photostimulation and imaging of neural circuits. *Nat. Methods* **4,** 943–950 (2007).

31. Papagiakoumou, E. *et al.* Scanless two-photon excitation of channelrhodopsin-2. *Nat. Methods* **7,** 848–854 (2010).

32. Pégard, N. C. *et al.* Three-dimensional scanless holographic optogenetics with temporal focusing (3D-SHOT). *Nat Commun* **8,** 1228 (2017).

33. Papagiakoumou, E., de Sars, V., Oron, D. & Emiliani, V. Patterned two-photon illumination by spatiotemporal shaping of ultrashort pulses. *Opt Express* **16** (2008).

34. Hernandez, O. *et al.* Three-dimensional spatiotemporal focusing of holographic patterns. *Nat Commun* **7,** 11928 (2016).

35. Yizhar, O., Fenno, L. E., Davidson, T. J., Mogri, M. & Deisseroth, K. Optogenetics in neural systems. *Neuron* **71,** 9–34 (2011).

36. Müller, K., Zurbriggen, M. D. & Weber, W. Control of gene expression using a red- and far-red light-responsive bi-stable toggle switch. *Nat Protoc* **9,** 622–632 (2014).

37. Shao, J. *et al.* Synthetic far-red light-mediated CRISPR-dCas9 device for inducing functional neuronal differentiation. *Proceedings of the National Academy of Sciences* **8,** 201802448 (2018).

38. Tucker, C. L., Vrana, J. D. & Kennedy, M. J. Tools for controlling protein interactions using light. *Curr Protoc Cell Biol* **64,** 17.16.1–20 (2014).

39. Olson, E. J., Hartsough, L. A., Landry, B. P., Shroff, R. & Tabor, J. J. Characterizing bacterial gene circuit dynamics with optically programmed gene expression signals. *Nat. Methods* **11,** 449–455 (2014).

40. Gerhardt, K. P. *et al.* An open-hardware platform for optogenetics and photobiology. *Sci Rep* **6,** 35363 (2016).

41. Davidson, E. A., Basu, A. S. & Bayer, T. S. Programming microbes using pulse width modulation of optical signals. *J. Mol. Biol.* **425,** 4161–4166 (2013).

42. Lee, J. M., Lee, J., Kim, T. & Lee, S. K. Switchable gene expression in Escherichia coli using a miniaturized photobioreactor. *PLoS ONE* **8,** e52382 (2013).

43. Hannanta-Anan, P. & Chow, B. Y. Optogenetic Control of Calcium Oscillation Waveform Defines NFAT as an Integrator of Calcium Load. *Cell Syst* **2,** 283–288 (2016).

44. Bugaj, L. J. *et al.* Cancer mutations and targeted drugs can disrupt dynamic signal encoding by the Ras-Erk pathway. *Science* **361,** eaao3048 (2018).

45. Hennemann, J. *et al.* Optogenetic Control by Pulsed Illumination. *Chembiochem* **19,** 1296–1304 (2018).

46. Richter, F. *et al.* Upgrading a microplate reader for photobiology and all-optical experiments. *Photochem Photobiol Sci* **14,** 270–279 (2015).

47. Tyssowski, K. M. & Gray, J. M. Blue light induces neuronal-activity-regulated gene expression in the absence of optogenetic proteins. *bioRxiv* **12,** 572370 (2019).

48. Acker, L., Pino, E. N., Boyden, E. S. & Desimone, R. FEF inactivation with improved optogenetic methods. *Proceedings of the National Academy of Sciences* **113,** E7297–E7306 (2016).

49. Allen, B. D., Singer, A. C. & Boyden, E. S. Principles of designing interpretable optogenetic behavior experiments. *Learning & memory (Cold Spring Harbor, N.Y.)* **22,** 232–238 (2015).

50. Owen, S. F., Liu, M. H. & Kreitzer, A. C. Thermal constraints on in vivo optogenetic manipulations. *Nat. Neurosci.* 1–9 (2019).

51. Banerjee, R. *et al.* The signaling state of Arabidopsis cryptochrome 2 contains flavin semiquinone. *J. Biol. Chem.* **282,** 14916–14922 (2007).

52. Zeng, L. *et al.* The mouse Fused locus encodes Axin, an inhibitor of the Wnt signaling pathway that regulates embryonic axis formation. *Cell* **90,** 181–192 (1997).

53. Liu, P. *et al.* Requirement for Wnt3 in vertebrate axis formation. *Nat. Genet.* **22,** 361–365 (1999).

54. Kimura-Yoshida, C. *et al.* Canonical Wnt Signaling and Its Antagonist Regulate Anterior-Posterior Axis Polarization by Guiding Cell Migration in Mouse Visceral Endoderm. *Developmental Cell* **9,** 639–650 (2005).

55. Davidson, K. C. *et al.* Wnt/β-catenin signaling promotes differentiation, not self-renewal, of human embryonic stem cells and is repressed by Oct4. *Proceedings of the National Academy of Sciences* **109,** 4485–4490 (2012).

56. Blauwkamp, T. A., Nigam, S., Ardehali, R., Weissman, I. L. & Nusse, R. Endogenous Wnt signalling in human embryonic stem cells generates an equilibrium of distinct lineage-specified progenitors. *Nat Commun* **3,** 1070 (2012).

57. Sumi, T., Tsuneyoshi, N., Nakatsuji, N. & Suemori, H. Defining early lineage specification of human embryonic stem cells by the orchestrated balance of canonical Wnt/beta-catenin, Activin/Nodal and BMP signaling. *Development* **135,** 2969–2979 (2008).

58. Bernardo, A. S. *et al.* BRACHYURY and CDX2 mediate BMP-induced differentiation of human and mouse pluripotent stem cells into embryonic and extraembryonic lineages. *Cell Stem Cell* **9,** 144–155 (2011).

59. Duan, L. *et al.* Understanding CRY2 interactions for optical control of intracellular signaling. *Nat Commun* **8,** 547 (2017).

60. Rivera-Pérez, J. A. & Magnuson, T. Primitive streak formation in mice is preceded by localized activation of Brachyury and Wnt3. *Developmental Biology* **288,** 363–371 (2005).

61. Yamaguchi, T. P., Takada, S., Yoshikawa, Y., Wu, N. & McMahon, A. P. T (Brachyury) is a direct target of Wnt3a during paraxial mesoderm specification. *Genes Dev.* **13,** 3185–3190 (1999).

62. Arnold, S. J. *et al.* Brachyury is a target gene of the Wnt/β-catenin signaling pathway. *Mechanisms of Development* **91,** 249–258 (2000).

63. Lindsley, R. C., Gill, J. G., Kyba, M., Murphy, T. L. & Murphy, K. M. Canonical Wnt signaling is required for development of embryonic stem cell-derived mesoderm. *Development* **133,** 3787–3796 (2006).

64. Benedetti, L. *et al.* Light-activated protein interaction with high spatial subcellular confinement. *Proceedings of the National Academy of Sciences* **115,** E2238–E2245 (2018).

65. Thiery, J. P., Acloque, H., Huang, R. Y. J. & Nieto, M. A. Epithelial-mesenchymal transitions in development and disease. *Cell* **139,** 871–890 (2009).

66. Thiery, J. P. & Sleeman, J. P. Complex networks orchestrate epithelial–mesenchymal transitions. *Nat. Rev. Mol. Cell. Biol.* **7,** 131–142 (2006).

67. Williams, M., Burdsal, C., Periasamy, A., Lewandoski, M. & Sutherland, A. Mouse primitive streak forms in situ by initiation of epithelial to mesenchymal transition without migration of a cell population. *Developmental dynamics : an official publication of the American Association of Anatomists* **241,** 270–283 (2012).

68. Warmflash, A., Sorre, B., Etoc, F., Siggia, E. D. & Brivanlou, A. H. A method to recapitulate early embryonic spatial patterning in human embryonic stem cells. *Nat. Methods* **11,** 847–854 (2014).

69. Kirkeby, A. *et al.* Generation of regionally specified neural progenitors and functional neurons from human embryonic stem cells under defined conditions. *Cell Rep* **1,** 703–714 (2012).

70. Kiecker, C. & Niehrs, C. A morphogen gradient of Wnt/beta-catenin signalling regulates anteroposterior neural patterning in Xenopus. *Development* **128,** 4189–4201 (2001).

71. Luis, T. C. *et al.* Canonical wnt signaling regulates hematopoiesis in a dosage-dependent fashion. *Cell Stem Cell* **9,** 345–356 (2011).

72. Kempf, H. *et al.* Bulk cell density and Wnt/TGFbeta signalling regulate mesendodermal patterning of human pluripotent stem cells. *Nat Commun* **7,** 13602 (2016).

73. Kim, S.-E. *et al.* Wnt stabilization of β-catenin reveals principles for morphogen receptor-scaffold assemblies. *Science* **340,** 867–870 (2013).

74. Li, V. S. W. *et al.* Wnt signaling through inhibition of β-catenin degradation in an intact Axin1 complex. *Cell* **149,** 1245–1256 (2012).

75. Bao, X. *et al.* Long-term self-renewing human epicardial cells generated from pluripotent stem cells under defined xeno-free conditions. *Nature Biomedical Engineering* **1,** 0003 (2016).

76. Aulehla, A. *et al.* Wnt3a plays a major role in the segmentation clock controlling somitogenesis. *Dev. Cell* **4,** 395–406 (2003).

77. Lian, X. *et al.* Robust cardiomyocyte differentiation from human pluripotent stem cells via temporal modulation of canonical Wnt signaling. *Proceedings of the National Academy of Sciences* **109,** E1848–57 (2012).

78. Yu, W., McDonnell, K., Taketo, M. M. & Bai, C. B. Wnt signaling determines ventral spinal cord cell fates in a time-dependent manner. *Development* **135,** 3687–3696 (2008).

79. Sonnen, K. F. *et al.* Modulation of Phase Shift between Wnt and Notch Signaling Oscillations Controls Mesoderm Segmentation. *Cell* **172,** 1079–1090.e12 (2018).

80. Massey, J. *et al.* Synergy with TGFβ ligands switches WNT pathway dynamics from transient to sustained during human pluripotent cell differentiation. *Proceedings of the National Academy of Sciences* **116,** 4989–4998 (2019).

81. Folch, A. *Introduction to BioMEMS* 1st ed. (CRC Press, 2016).

82. Schindelin, J. *et al.* Fiji: an open-source platform for biological-image analysis. *Nat. Methods* **9,** 676–682 (2012).

83. Thomson, J. A. *et al.* Embryonic stem cell lines derived from human blastocysts. *Science* **282,** 1145–1147 (1998).

84. Carpenter, A. E. *et al.* CellProfiler: image analysis software for identifying and quantifying cell phenotypes. *Genome biology* **7,** R100 (2006).

Chapter 3

Design of a DMD-based microscope for structured illumination microscopy and optogenetic stimulation of biological samples

3.1 Introduction

Spatially and temporally-varying signals from the cellular environment orchestrate the coordinated cell fate decisions and patterning during embryonic development (*1*, *2*). Optogenetic approaches have recently enabled studies of such signal dynamics through the use of light-responsive photosensors to perturb signaling and protein-protein interactions (*3*, *4*). Light stimulation results in specific activation of target signal pathways with the unique advantage of using optics and illumination patterning to activate signaling in a specific location and at a specific time. The expanding optogenetics toolkit enables light control of pathways such as Wnt/β-catenin (*5*, *6*), Nodal (*7*), Ras/Raf/Mek/Erk (*8–11*), fibroblast growth factor (FGF) (*12*), and Rho-family GTPase signaling (*13–18*), and such optogenetic methods have also been recently applied to studies in developmental biology in key model organisms and stem cell-based model systems (*4*, *6*, *19*).

To activate the variety of photosensory domains with precise spatial and temporal control, there has been complementary, extensive development of optical tools for optogenetic stimulation and imaging. For example, devices for high-throughput illumination of cell culture plates allow programmable control of intensity and timing sequences (*19–23*) as well as spatial control with dye-cut masks (*19*, *24*, *25*). However, such approaches are limited to static spatial patterns that have relatively low resolution (50-100μm, see Chapter 2) (*19*).

For dynamic and high-resolution optogenetic stimulation, microscope-based systems are widely used that both activate and image the sample. Recently, the technologies developed primarily for neuroscience applications have been extended to developmental biology studies.

As opposed to the short (ms time-scale), high-intensity light pulses necessary for neural action potential stimulation (*26*), cell and developmental systems typically use long-term activation at relatively low illumination powers (*3*, *4*). For example, confocal or two-photon microscopes — the most common means used — incorporate two scanning mirrors that direct the position of a single diffraction-limited spot onto the sample, which can be used both for photoexcitation and imaging (*27–31*). As with fluorescence imaging, the laser intensity is tunable, and the spatial location of illumination can often be specified in software. Because of the small point size (1 - 0.25 μm in diameter), the spatial resolution of activation is high, and the resulting biological effects can be immediately imaged with confocal fluorescence imaging. Such single-spot scanning systems have been used to confine optogenetic stimulation to user-defined regions of interest in a variety of model systems, e.g. for photoactivation of Rac1 (*32*), Nodal (*7*), or non-canonical Wnt signaling in the zebrafish embryo, as well as cell contractility in the *Drosphila* embryo (*33*, *34*). However, single-spot scanning systems are typically limited to a single region of interest and have an inherent time delay due to optical scanning.

To photoactivate multiple regions within a field of view without a time delay (i.e. multi-spot patterning), systems have been engineered that incorporate a spatial light modulator, such as a digital micromirror device (DMD) (*35*). A DMD is an array of individually switchable mirrors that allows projection of user-defined light patterns to stimulate multiple cells and regions simultaneously (*36–38*). Indeed, such DMD-based systems have been used to pattern Erk signaling in space and time within the developing *Drosophila* embryo (*9*, *11*). However, these DMD-based systems are solely used for patterning of optogenetic stimulation, whereas subsequent widefield or confocal fluorescence readout is typically performed by an external light source and separate beampath. This de-coupling of photostimulation from imaging can result in expensive and complex optical system configurations, which can be prohibitive to optogenetic experiments. Furthermore, the fluorescence readout is restricted to the native capability of the modified microscope system, typically a confocal microscope.

To address the need for a system that allows dynamic photostimulation and high-resolution imaging, we have designed a microscope capable of multispot optogenetic patterning as well as structured illumination microscopy (SIM). A DMD is used to project user-defined photostimulation sequences onto the sample with diffraction-limited spatial resolution. For fluorescence imaging, a series of multi-spot patterns is projected onto the sample to reconstruct a high-resolution SIM image with a 2-fold resolution improvement over the diffraction limit. Such multi-color, user-defined photostimulation and imaging sequences allow live-cell timelapse imaging during localized and dynamic Wnt/β-catenin photoactivation in human embryonic stem cells.

3.2 Design

3.2.1 Principle of structured illumination microscopy

Super-resolution imaging techniques have transformed our ability to image small features in biological samples (*39*). Due to the finite nature of optical systems, wide-field fluorescence microscopy is limited to a lateral resolution of ~250 nm and an axial resolution of 500-700 nm. This 'diffraction limit' prohibits imaging of cellular features below these size scales. However, super-resolution techniques, such as stimulated emission depletion (STED) (*40*, *41*), photo-activated localization microscopy/stochastic optical reconstruction microscopy (PALM/STORM) (*42*, *43*), and SIM (*44*, *45*), have allowed sub-diffractive imaging to length scales as small as ~20 nm (*39*). Of these imaging methods, SIM has a relatively modest 2-fold resolution improvement but is most amenable to live-cell imaging as a result of its reduced phototoxicity, fast acquisition speed, and high signal-to-noise ratio (*46*).

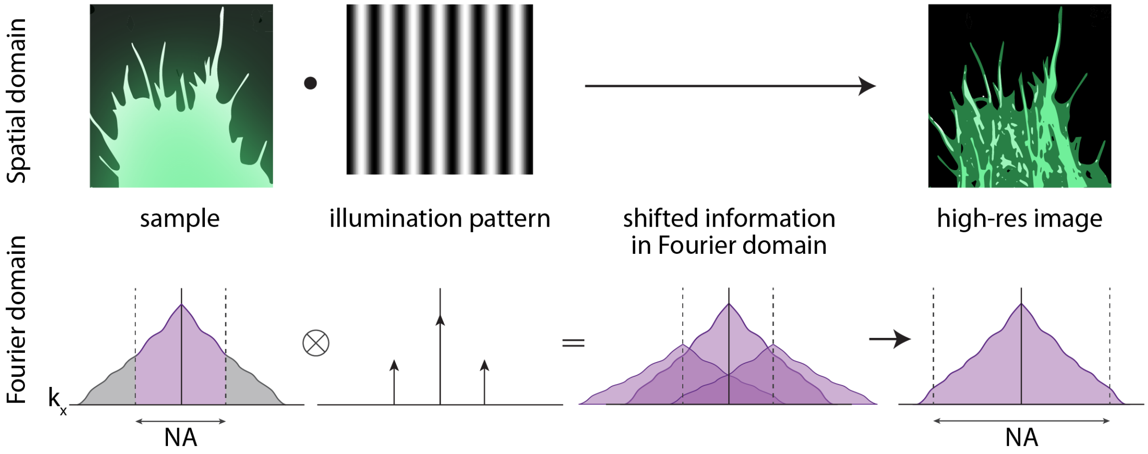

Figure 3.1: **Principles of structured illumination microscopy**
Schematic of spatial domain (top) and frequency domain (bottom) information during SIM imaging.

The principle of SIM imaging relies on imaging a fluorescent sample that is illuminated by a sequence of excitation patterns, to generate multiple images from which a higher-resolution image is reconstructed (Figure 3.1). In fluorescence microscopy, the illumination I_{ex} multiplies the fluorescently-labeled object $O(x, y)$ to elicit a fluorescence emission, which is blurred by diffraction, yielding the image I_{em}:

$$I_{em}(x, y) = (I_{ex}(x, y) \cdot O(x, y)) \otimes h(x, y)$$

where $\otimes$ denotes convolution (blurring) and $h(x, y)$ is the emission point spread function (PSF). The object is thereby blurred by the PSF. In widefield imaging, the illumination is spatially uniform and image resolution is limited by $h(x, y)$ to approximately $\lambda_{em}/2\text{NA}$, where λ_{em} is the wavelength of emission and NA is the numerical aperture of the objective. In the Fourier (frequency) domain, the image equation becomes:

$$\tilde{I}_{em}(k_x, k_y) = (\tilde{I}_{ex}(k_x, k_y) \otimes \tilde{O}(k_x, k_y)) \cdot \tilde{h}(k_x, k_y)$$

where $\tilde{h}(k_x, k_y)$ is called the optical transfer function (OTF) that limits the spatial frequecies (k_x, k_y) collected by the optical system. The spatial frequency cutoff, k_em, corresponds to $2\mathrm{NA}/\lambda_{em}$. In widefield imaging where illumination is uniform, $\tilde{I}_{ex}(k_x, k_y)$ takes the form of a delta function and the equation simplifies to:

$$\tilde{I}_{em}(k_x, k_y) = \tilde{O}(k_x, k_y) \cdot \tilde{h}(k_x, k_y)$$

where the Fourier transform of the object is simply multiplied by the OTF to set the detection passband. In contrast, the key principle of SIM is to illuminate the sample with a pattern of illumination. The first implementations of SIM use a sinusoidal pattern (*44*), expressed as $I_{ex}(x, y) = 1 + cos(k_{x0}x + k_{y0}y + \phi)$, where ϕ is the phase and k_{x_0} and k_{y_0} are the cartesian components that determine the frequency and angle of the sinusoidal pattern, to yield:

$$\tilde{I}_{em}(k_x, k_y) = (\tilde{O}(k_x, k_y) + \frac{1}{2}e^{i\phi}\tilde{O}(k_x - k_{x_0}, k_y - k_{y0}) + \frac{1}{2}e^{-i\phi}\tilde{O}(k_x + k_{x_0}, k_y + k_{y0})) \cdot \tilde{h}(k_x, k_y)$$

which can be redefined as:

$$\tilde{I}_n = \tilde{O} + \frac{1}{2}e^{i\phi_n}\tilde{O}^{+} + \frac{1}{2}e^{-i\phi_n}\tilde{O}^{-}$$

where

$$\begin{aligned}
\tilde{O}\ \ &= \tilde{O}(k_x, k_y) \cdot \tilde{h} \\
\tilde{O}^{+} &= \tilde{O}(k_x - k_{x_0}, k_y - k_{y0}) \cdot \tilde{h} \\
\tilde{O}^{-} &= \tilde{O}(k_x + k_{x_0}, k_y + k_{y0}) \cdot \tilde{h}
\end{aligned}$$

At a given phase, frequency, and angle, the sinusoidal pattern corresponds to three delta functions in the Fourier domain that, when convolved with $\tilde{O}(k_x, k_y)$, shift the the object spectrum in Fourier space to generate three overlapping copies: $\tilde{O}$, $\tilde{O}^{+}$, and $\tilde{O}^{-}$ (Figure 3.1). Such shifting brings the high spatial-frequency information of the object, typically cut off by the OTF, into the passband. For each angle of illumination, solving for $\tilde{O}$, $\tilde{O}^{+}$, and $\tilde{O}^{-}$ is a linear inverse problem that requires three measurements, obtained by illuminating the sample with three different phases, $\{\phi_n \mid n = 1, 2, 3\}$. Thus, to cover the two-dimensional Fourier domain, typically three angles, with three phases each, are used to reconstruct a full super-resolution image from 9 measurements.

The first SIM implementations used a rotating diffraction grating or interference of two coherent laser beams to generate sinusoidal illumination patterns (*44*, *47*, *48*). However, various other patterns can be used to generate the shifted copies in the frequency domain, such as multi-spot patterns (*49–51*) or random speckle (*52–54*). DMDs have been used in both traditional (*55*, *56*) and multi-spot scanning (*49*, *57*) SIM microscopes to enable rapid and flexible pattern generation.

3.2.2 Opto-SIM microscope design

A standard widefield inverted microscope (Nikon TE2000) was modified to incorporate a DMD into the optical beam path (Figure 3.2). In brief, the DMD was placed conjugate to the sample plane to project user-defined optogenetic stimulation and SIM excitation patterns onto the sample. Two fiber-coupled lasers were collimated and expanded to fully illuminate the DMD: the blue (458 nm) laser channel was used for optogenetic stimulation and the green (514 nm) laser channel for imaging (e.g. YFP or mVenus fluorescent proteins). In addition, a red long-pass filter was added to the brightfield illumination beampath to allow continuous phase or differential interference contrast (DIC) imaging without unintended activation of the optogenetic system. The two lasers were aligned to illuminate the DMD at slightly different incident angles to compensate for the wavelength-dependent light dispersion from the DMD array. The angle of incidence to the surface normal was ∼24° for the green laser and ∼26.8° for the blue laser. Furthermore, the DMD array was rotated by 45° so that incident light was reflected in the plane of the optical axis. After reflection from the DMD, the patterned light was projected through the back port of the microscope to illuminate the sample. A multi-band dichroic was placed in the fluorescence filter cube to remove the need for mechanical movement of filters during switching of excitation channels. Fluorescence emission was collected through the dichroic and emission filters with an sCMOS camera (Andor Zyla 4.2) rotated by 45° to align with the orientation of the DMD array (Figure 3.3).

The optical system was designed to reduce aberrations and enable high-contrast and multicolor projection of optogenetic and SIM patterns. For maximal SIM resolution, each spot of a multi-spot SIM pattern must correspond to a diffraction-limited spot at the sample, with optimal reconstruction achieved at lateral shifts of the multi-spot pattern by less than 0.6 times the PSF diameter (*49*, *57*). Thus, each DMD mirror (7.6 x 7.6 μm) was demagnified to a diffraction-limited spot at the sample through a relay system. Previous optical designs for DMD-based microscopes have used a 4f system, which provides space for the illumination optics and illumination coupling into the microscope along with additional demagnification of the DMD pattern (*49*, *55*). However, such designs have strong chromatic aberrations that reduce image quality in multicolor experiments, so that refocusing may be required for different wavelengths. We thus sought to model the optical system design in the ray-tracing optical modeling software Zemax to test the performance of alternative lens designs.

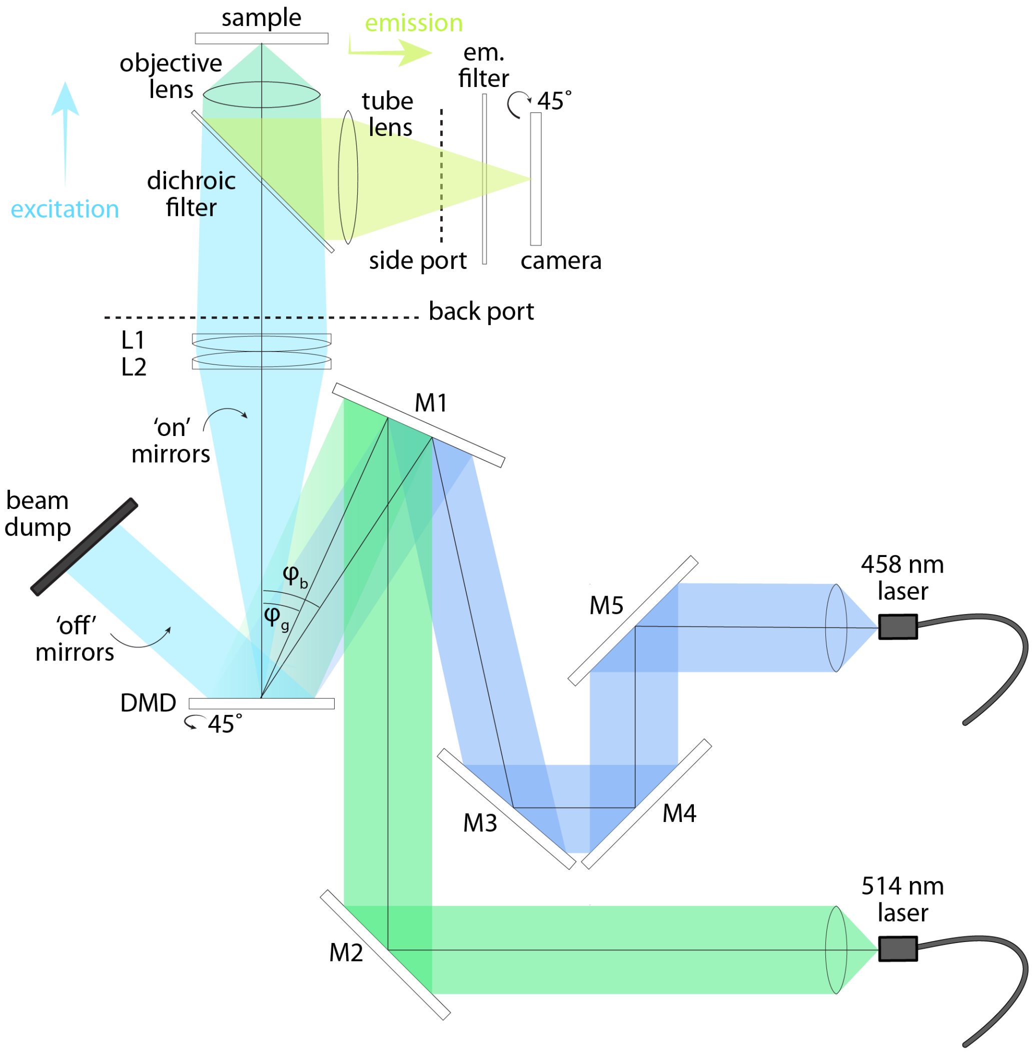

Figure 3.2: **Layout of opto-SIM microscope**
Schematic of opto-SIM microscope with labelled optical elements. Light passes from two fiber-coupled lasers (458 nm and 514 nm laser lines) and reflected off of mirror M1 onto the DMD microscope at $\phi_b = \sim 26.8°$ and $\phi_g = \sim 24°$. Light reflected from DMD mirrors in the 'on' position pass through lenses L1 and L2 (the eyepiece design) and enter into the microscope back port to illuminate the sample. Fluorescence emission is collected through the dichroic and emission filters with a camera mounted on the microscope side port.

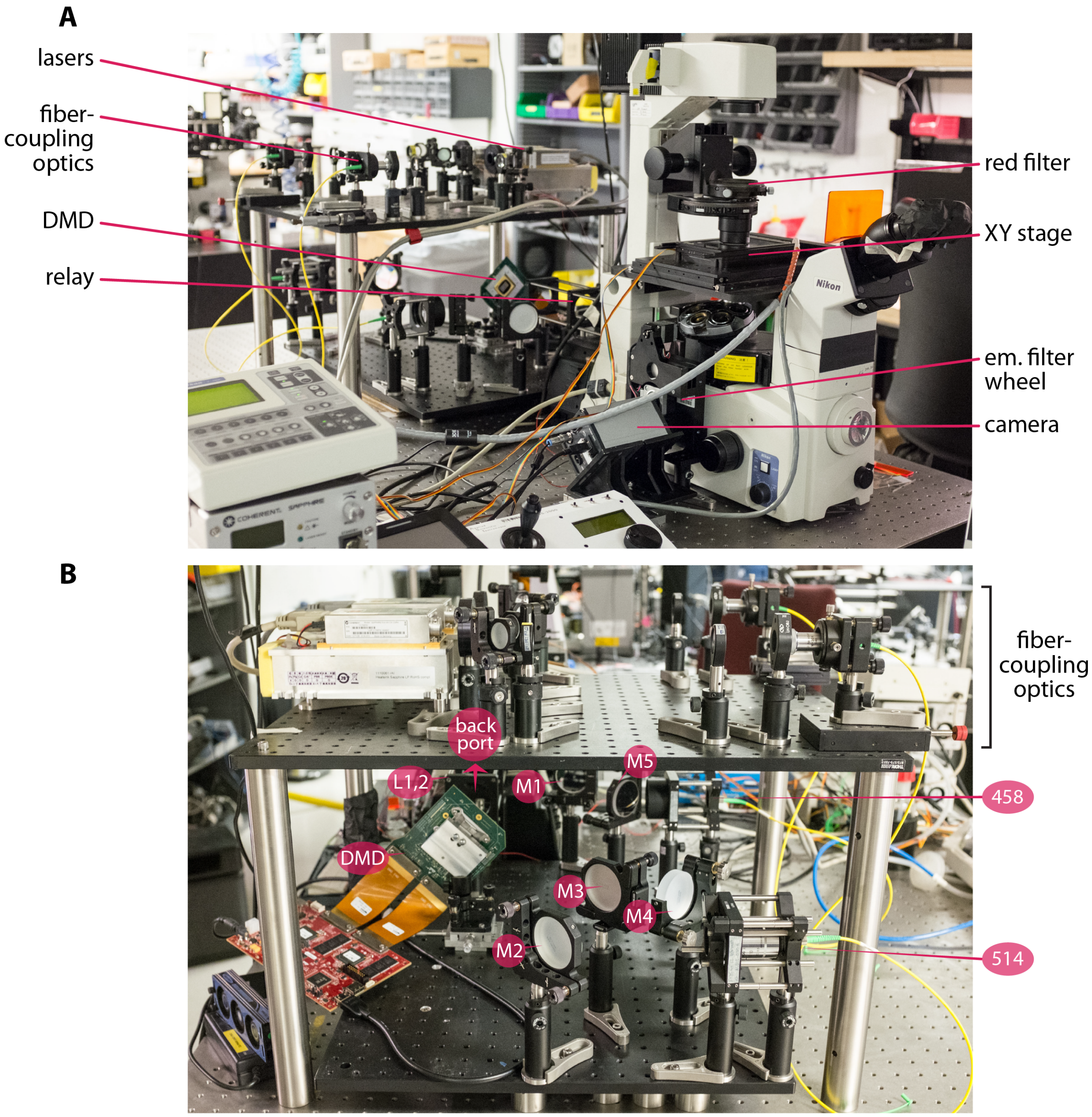

Figure 3.3: **Image of opto-SIM microscope**
A) Side view of opto-SIM microscope showing side camera port and sample stage with illumination optics in rear. **B)** Rear view of opto-SIM microscope showing optical elements that correspond to labels in Figure 3.3.

We first generated a Zemax model of a system that uses a standard 4f system with two lenses (f=125 mm, f=225 mm) that relay the projected image to the back focal plane of the microscope tube lens (Figure 3.4A). This design showed strong aberrations, which were dominated by chromatic aberrations (Figure 3.4B-C). When the system was focused on the green wavelength, the Airy disk radius was ~16 μm at the DMD surface (Figure 3.4D). However, at this focal plane, the Airy disk for the blue wavelength was barely visible due to severe chromatic aberrations (Figure 3.4D-E).

We thus optimized the system and replaced the 4f system and microscope tube lens with an eyepiece lens design (Figure 3.5A). Two achromatic doublets (f=750 mm) were placed adjacent to each other, similarly resulting in a 2-fold demagnification of the DMD array. This design showed dramatically decreased chromatic aberrations (Figure 3.5B-C; note the 10-fold change in axis length), as well as high contrast and spatial resolution in both color channels within a single focal plane (Figure 3.5D-E). We therefore implemented this eyepiece design in the opto-SIM microscope.

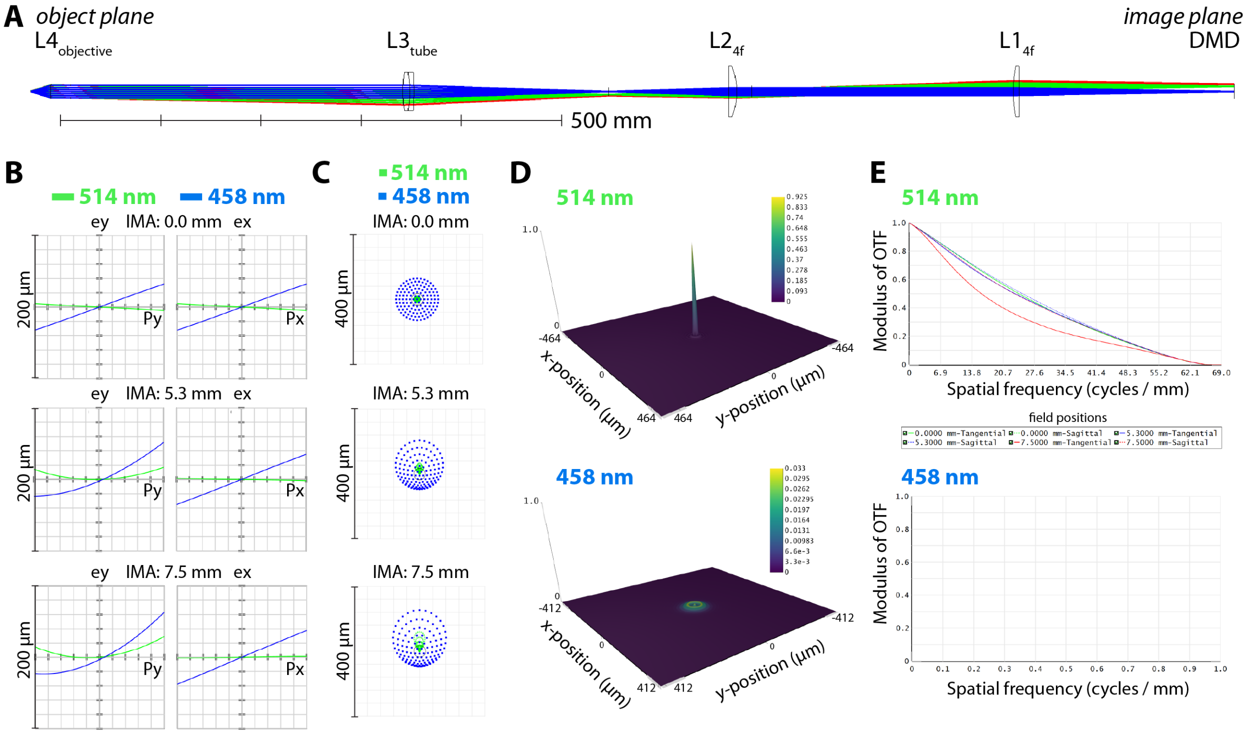

Figure 3.4: **Zemax modeling of opto-SIM microscope with a 4f optical system**
A) Layout of Zemax model. **B)** Transverse ray fan plots of Zemax model at image (IMA) plane at indicated field point. **C)** Spot diagram at image (IMA) plane at indicated field point, with airy radius of 17.9 μm shown with black outline. **D)** Point spread function of a point projected from object plane to the image plane (FFT PSF) for each wavelength. **E)** MTF curve for each wavelength.

For all subsequent imaging experiments, we used the optimized system design with a 10x microscope objective (Nikon Plan Apochromat, NA = 0.45). Given the application of the opto-SIM microscope for photostimulation of 2D cell colonies or 3D cell aggregates or spheroids, we reasoned that a large field of view is paramount for imaging as many cells or aggregates per imaging experiment as possible. We thus chose to use a 10x microscope objective, which would give a ∼0.8 μm widefield fluorescence imaging and optogenetic patterning resolution, as calculated in the Zemax model (Figure 3.5E). Cells could thus be imaged at a large field of view (0.9 x 0.9 mm), photostimulated at subcellular resolution (0.8 μm), and, given the theoretical ∼2-fold image resolution improvement of SIM, imaged at ∼0.4 μm resolution.

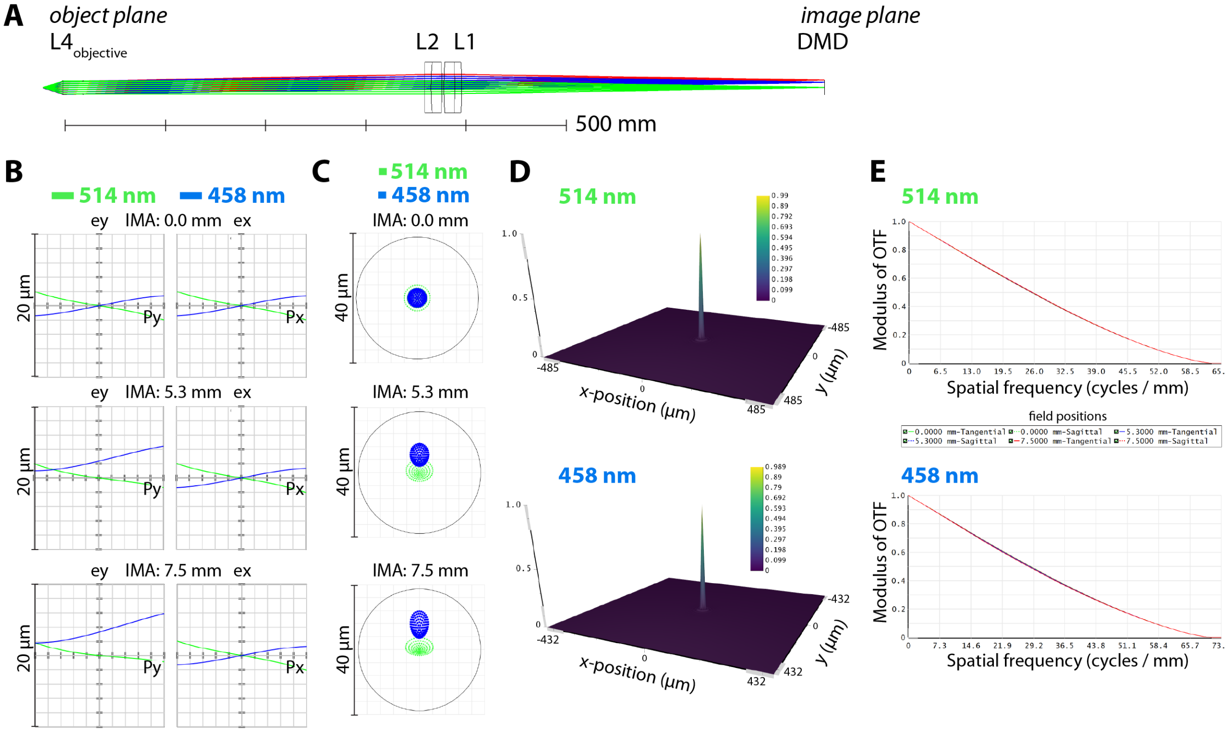

Figure 3.5: **Zemax modeling of opto-SIM microscope with an eyepiece design**
A) Layout of Zemax model. **B)** Transverse ray fan plots of Zemax model at image (IMA) plane at indicated field point. **C)** Spot diagram at image (IMA) plane at indicated field point, with airy radius of 18.8 μm shown with black outline. **D)** Point spread function of a point projected from object plane to the image plane (FFT PSF) for each wavelength. **E)** MTF curve for each wavelength.

3.3 Results

3.3.1 Illumination patterning at diffraction-limited resolution

To characterize the system design of the optimized opto-SIM microscope, we first measured the contrast and resolution of projected light patterns. By placing a beamsplitter in the microscope filter cube and a mirror at the sample, the illumination patterns could be directly imaged by the camera. Image contrast (Michelson contrast) was defined as:

$$\frac{I_{max} - I_{min}}{I_{max} + I_{min}}$$

where I_{max} and I_{min} represent the highest and lowest pixel intensity so that contrast values range from 0 (no contrast) to 1 (maximal contrast). A projected pattern of the UC Berkeley Cal logo had high contrast at 0.96 (Figure 3.6A). The ringing artifacts are attributed to inference of the coherent laser beam, which is inherent to placing a mirror at the sample plane for these measurements. The gaussian beam profile of the laser is also evident in these images, as the image center is brighter than the periphery.

To measure the contrast of the highest possible spatial frequency projected by the DMD, we projected a linear pattern where each row alternated between 'on' and 'off'-state DMD mirrors. Due to diffraction, such a pattern resembles a sinusoidal pattern with a period of two times the diffraction-limited resolution of the illumination optics. Though this pattern showed decreased contrast (0.46 in center region, 0.27 at periphery), the illumination pattern clearly showed the expected sinusoidal pattern with a period of 1.8 μm (Figure 3.6B). To quantify the contrast of SIM excitation patterns, we projected grid arrays onto the sample. The pattern is composed of a repeat array of a cluster of mirrors in the 'on' position (either a single mirror, 1x1, or four mirrors, 2x2) that directs excitation light to the sample. Such 'apertures' are arranged in either a 6x6, 8x8, or 10x10-mirror array so that the aperture is shifted 36, 64, or 100 times, respectively, to acquire a SIM image. Each pattern showed strong contrast, with, as expected, higher intensity at the image center and brighter signal from 2x2 apertures compared to 1x1 apertures (Figure 3.6C). Due to increased distance between apertures, the 10x10 array SIM pattern had highest contrast (0.90 center contrast for 2x2 apertures), followed by the 8x8 array (0.78 contrast) and the 6x6 array (0.54 contrast).

A similar approach was used to characterize the blue laser used for photoexcitation. Projection of a Cal logo also had high contrast (0.94) (Figure 3.7A). User-defined illumination patterns could be projected from an input image file, Matlab matrix, or hand-drawn using the MicroManager Projector plugin (Figure 3.7B) (*58*, *59*). As with projection of multi-spot patterns, multiple user-drawn regions of interest (ROIs) could be projected onto the sample. As expected, the smallest photostimulation region was measured to be diffraction-limited at 0.8 μm (Figure 3.7C).

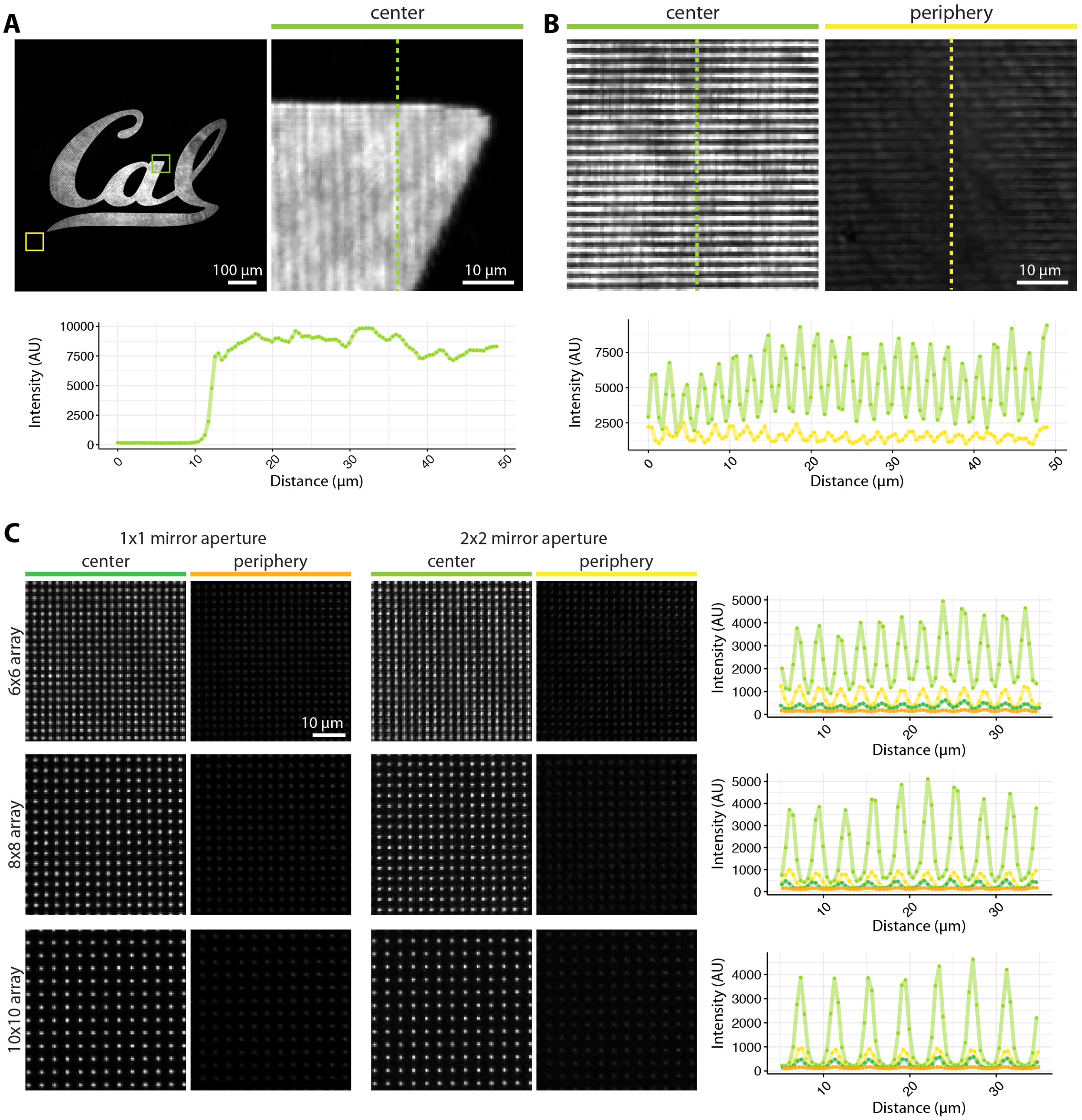

Figure 3.6: *See caption on next page*

Figure 3.6: **Contrast and resolution of 514 nm illumination for fluorescence SIM imaging** Figures (A)-(C) show green-channel excitation light pattern. Optical system was modified to add a beamsplitter in microscope filter wheel and a mirror at sample plane. **A)** Cal pattern projected from DMD. Full camera field of view shown on left, and center zoom (green outline) shown on right. Region for peripheral zoom in subsequent images indicated with yellow outline. Vertical linescan along dotted line is plotted on graph below. Graph shows raw 16-bit pixel intensity values as a function of sample distance. **B)** 1 by 1 horizontal pattern projected from DMD. Center zoom is shown on left, periphery zoom is shown on right. Vertical linescan along dotted lines is plotted on graph below. **C)** Multispot SIM patterns projected from DMD, using a 1x1-mirror aperture (left) or a 2x2-mirror aperture (right). Center and peripheral zoom shown for each, as indicated. Linescan along vertical line plotted on graphs on right for each array configuration.

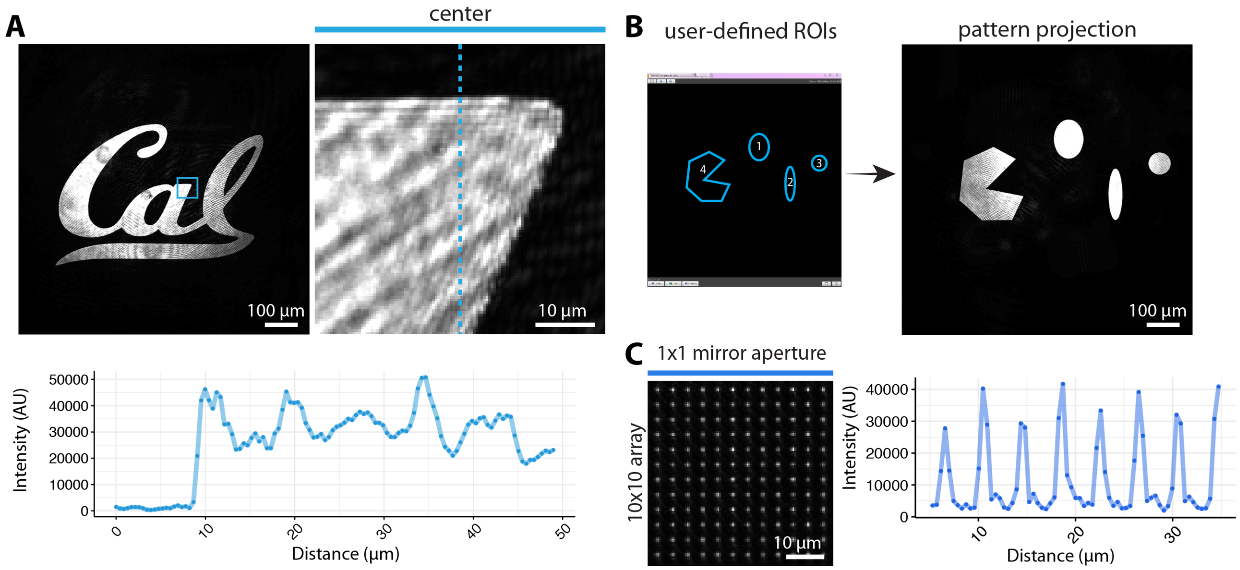

Figure 3.7: **Contrast and resolution of 458 nm illumination for photostimulation** Figures (A)-(C) show blue-channel photostimulation light pattern. Optical system was modified to add a beamsplitter in microscope filter wheel and a mirror at sample plane. **A)** Cal pattern projected from DMD. Full camera field of view shown on left, and center zoom (blue outline) shown on right. Region for peripheral zoom in subsequent images indicated with yellow outline. Vertical linescan along dotted line is plotted on graph below. Graph shows raw 16-bit pixel intensity values as a function of sample distance. **B)** Left image shows screenshot of user-defined ROIs drawn in FIJI. The ROIs are displayed on DMD using the MicroManager Projector plugin and projected onto sample. Right image shows image of projected patterns. **C)** Multispot pattern projected from DMD using a 1x1-mirror aperture shows resolution and contrast of blue-light photostimulation. Linescan along vertical line plotted on graph on right.

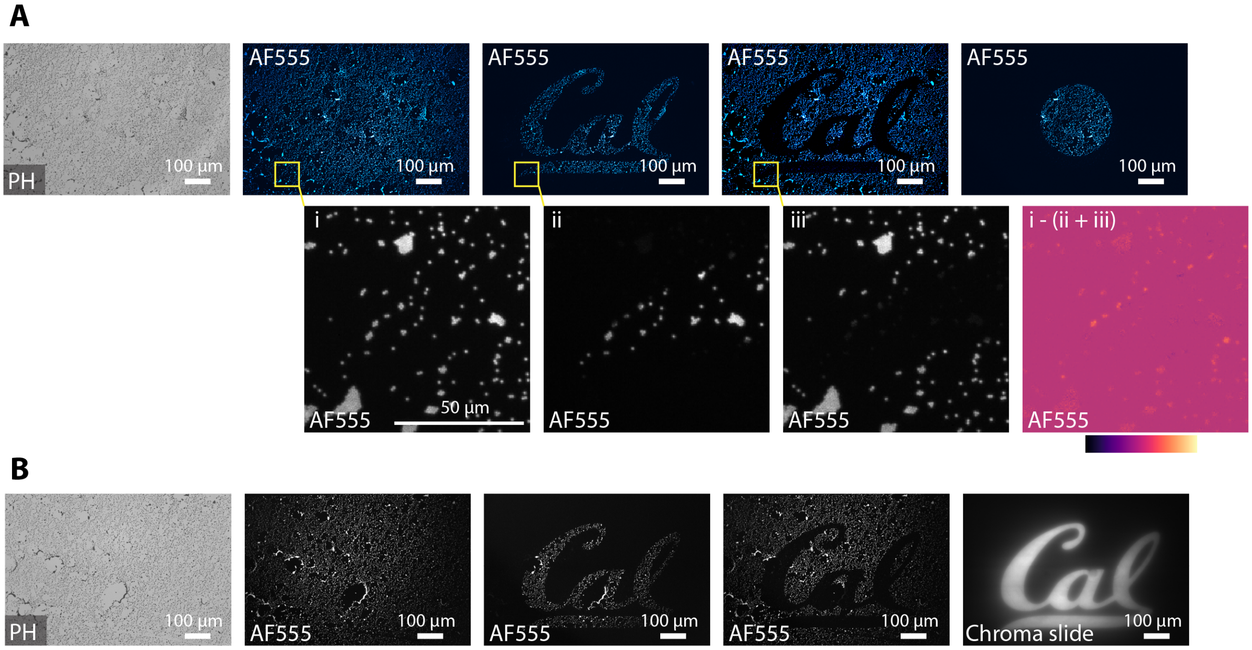

Figure 3.8: **Two-color illumination patterning and imaging of fluorescent beads**
A) Fluorescence image of $1\mu m$ beads under 514 nm excitation. From left to right: phase channel, fluorescence channel (DMD pixels all 'on'),fluorescence channel (Cal logo pattern), fluorescence channel (inverted Cal logo pattern), fluorescence channel (circle pattern). Zoom-in region marked by yellow rectangle. Right-most zoom image shows the sum of image (ii) and (iii) subtracted from image (i). **B)** Fluorescence image of $1\mu m$ beads under 458 nm excitation. From left to right: phase channel, fluorescence channel (DMD pixels all 'on'),fluorescence channel (Cal logo pattern), fluorescence channel (inverted Cal logo pattern). Right-most image shows Cal logo projected onto a fluorescent slide (Chroma).

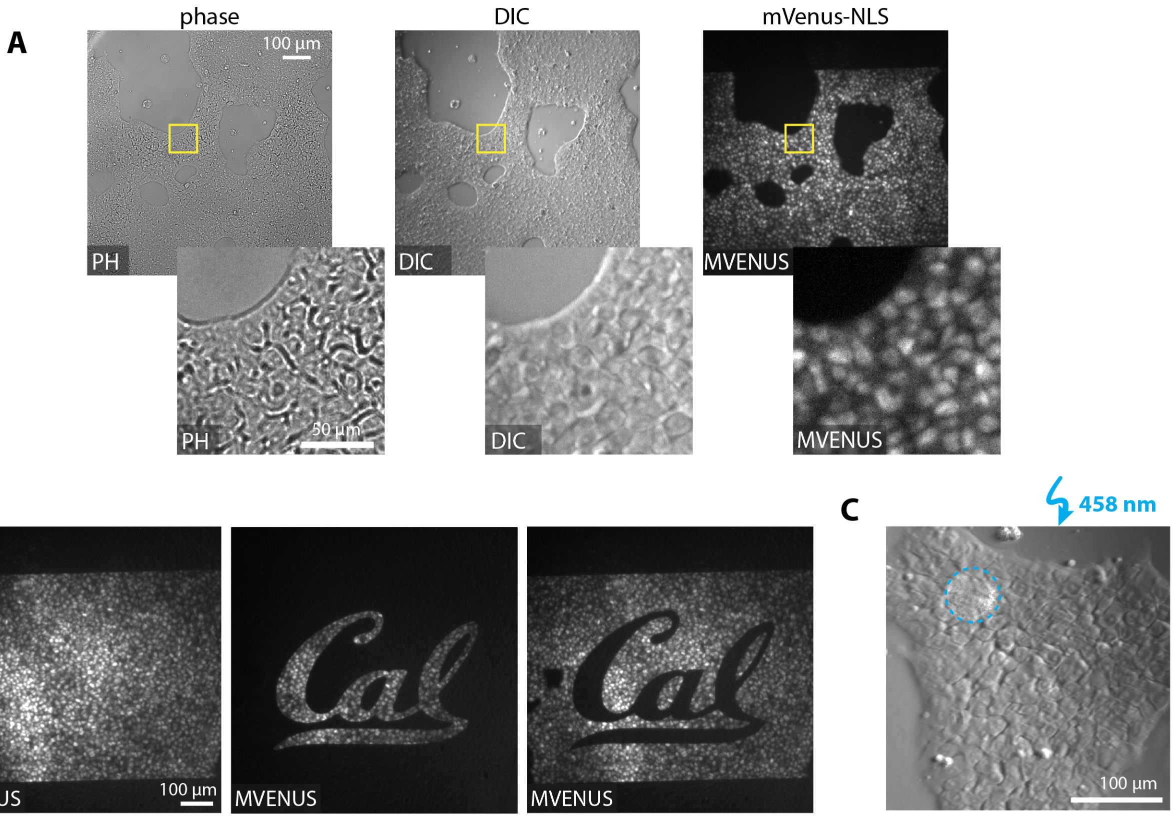

Figure 3.9: **Widefield phase, DIC, and fluorescence imaging and photopatterning of live optoWnt hESCs**

A) Phase, DIC, and fluorescence images and zoom inset (marked by yellow rectangle) of optoWnt hESCs expressing nuclearly-localized mVenus. **B)**Patterning of excitation illumination using opto-SIM setup while imaging of live optoWnt hESCs. **C)** Photostimulation with user-defined ROI using 458 nm channel. Image in DIC channel shows backreflection from illuminated region.

3.3.2 Widefield fluorescence imaging using on the opto-SIM microscope

To characterize the brightfield and widefield fluorescence imaging capability of the opto-SIM microscope, we first imaged samples of 1 μm beads. Given the 0.8 μm resolution limit of the system, such beads are barely resolved under widefield fluorescence. Widefield fluorescence imaging was achieved by setting all DMD mirrors to the 'on' position (Figure 3.8A). Next, the excitation patterning capability of the microscope was demonstrated by illuminating the bead sample with patterns of light, so that fluorescence signal was only detected in illuminated regions (Figure 3.8A). Fluorescence imaging and excitation patterning could also be performed in the blue channel (Figure 3.8B).

We next tested the opto-SIM microscope imaging capability on live human embryonic stem cells (hESCs) co-expressing the optoWnt optogenetic system and a nuclearly-localized mVenus fluorescent protein (*6*, *19*). To identify cell morphology, we performed phase contrast and differential interference contrast (DIC) imaging (Figure 3.9A). The far-red illumination ensured no background activation of the optoWnt system during imaging. The mVenus signal was measured in the 514 nm channel, and showed nuclearly-localized signal and densely packed epithelial morphology, as expected for hESC colonies (Figure 3.9A). Similar to bead sample fluorescence, we demonstrated 514 nm illumination patterning by projecting Cal logo patterns onto the hESC sample (Figure 3.9B). For optogenetic stimulation, we projected a user-defined ROI onto the sample, which can be observed under the brightfield imaging mode as a subtle higher-intensity region that is visible due to back-reflection from the sample (Figure 3.9C).

3.3.3 SIM imaging using on the opto-SIM microscope

For DMD-based SIM imaging, we projected multispot patterns from the DMD so that the lateral shift between each pattern corresponded to half of the PSF size ($\sim 0.4\ \mu m$) (*57*). The SIM image was subsequently reconstructed using an algorithm that estimated the multispot SIM pattern, based on previously published work (*57*). Since pattern estimation utilizes measured data, it provides the advantage of accounting for any aberrations in the system that may distort the theoretical projected pattern. Such self-calibration can give robust image reconstruction in the presence of system aberrations (*57*).

We first imaged a sample of 1 μm fluorescent beads. Comparison of the widefield image, deconvolved widefield image, not deconvolved SIM image, and deconvolved SIM image show a ∼2-fold resolution improvement after SIM reconstruction (Figure 3.10A-B). While beads were not resolved under widefield imaging, they were clearly resolved after reconstruction.

Since different multispot illumination patterns can be used for SIM, we compared different patterns – 6x6, 8x8, or 10x10 arrays, as well as 1x1 or 2x2-mirror apertures – to determine the optimal pattern for SIM imaging (Figure 3.11). We found that 2x2-mirror apertures have higher SNR, as expected due to the higher excitation power. Though using a larger aperture comes at the expense of resolution, we found a negligible difference in the SIM reconstruction.

Thus, using 2x2-mirror apertures would be particularly advantageous for dimmer samples. Because larger arrays (ex. 10x10) have higher contrast (see Figure 3.6), we expected to see more robust reconstruction results with these patterns. However, all arrays yielded high quality SIM results. The difference between array patterns was primarily in acquisition and SIM algorithm time. For 10x10 arrays, a sequence of 100 images needs to be taken, whereas for 6x6 arrays a sequence of 36 images is acquired. Having a shorter image sequence reduces the acquisition time, which is particularly important for reducing reconstruction artifacts during live imaging, where cell movement during acquisition can result in significant motion artifacts.

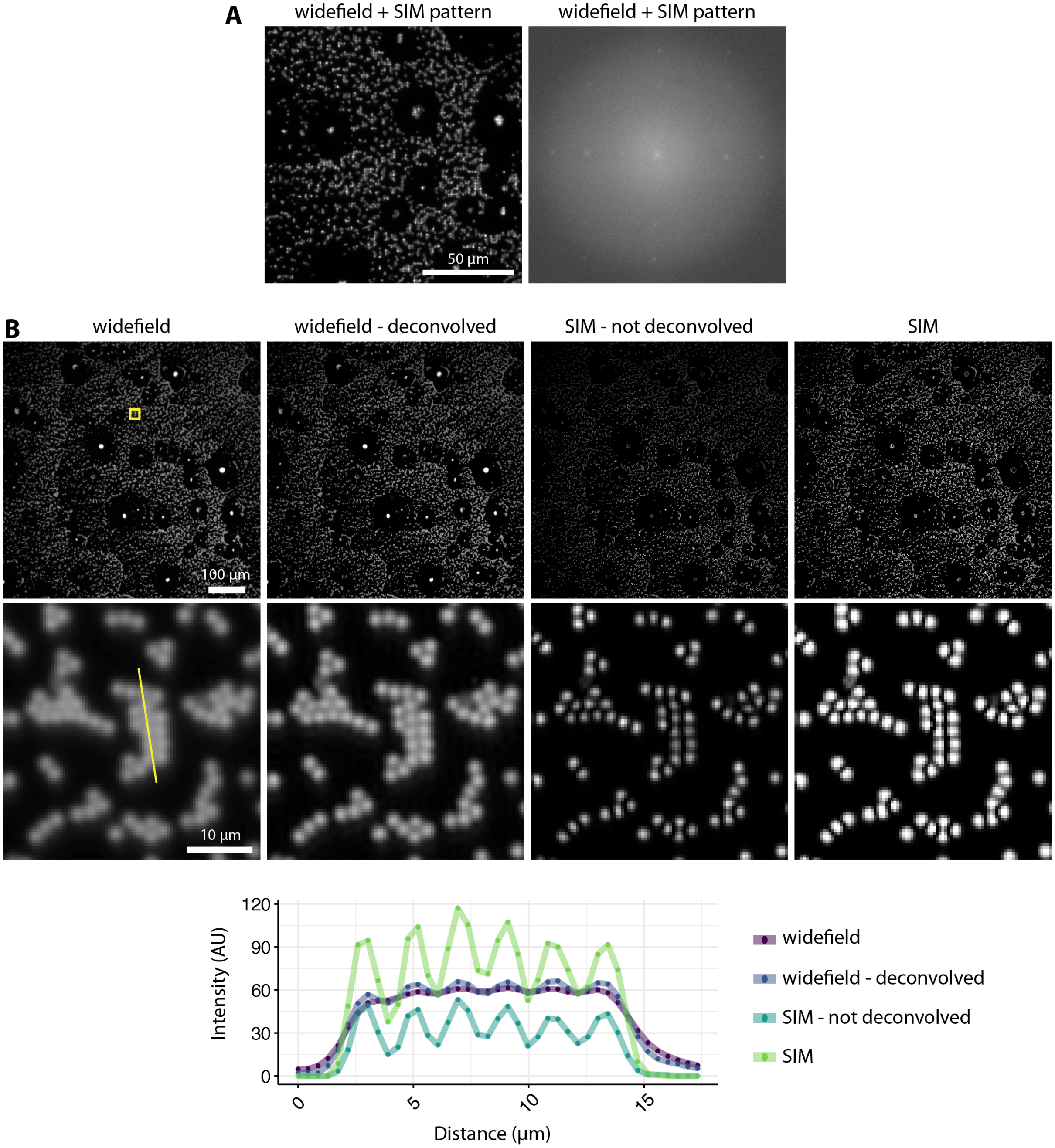

Figure 3.10: **SIM imaging of fluorescent beads**

A) Image of bead sample illuminated with a 8x8 array, 2x2 mirror aperture (left) and fourier transform (FFT, right) showing replicates of comb pattern in frequency space. **B)** Images of widefield, deconvolved widefield, SIM before deconvolution, and SIM after deconvolution (left to right) are shown for a 8x8 array, 2x2 mirror pattern. Bottom row shows zoom-in of top row in the region highlighted in yellow. Graph of linescan along yellow line is shown to compare the contrast and resolution of the four images.

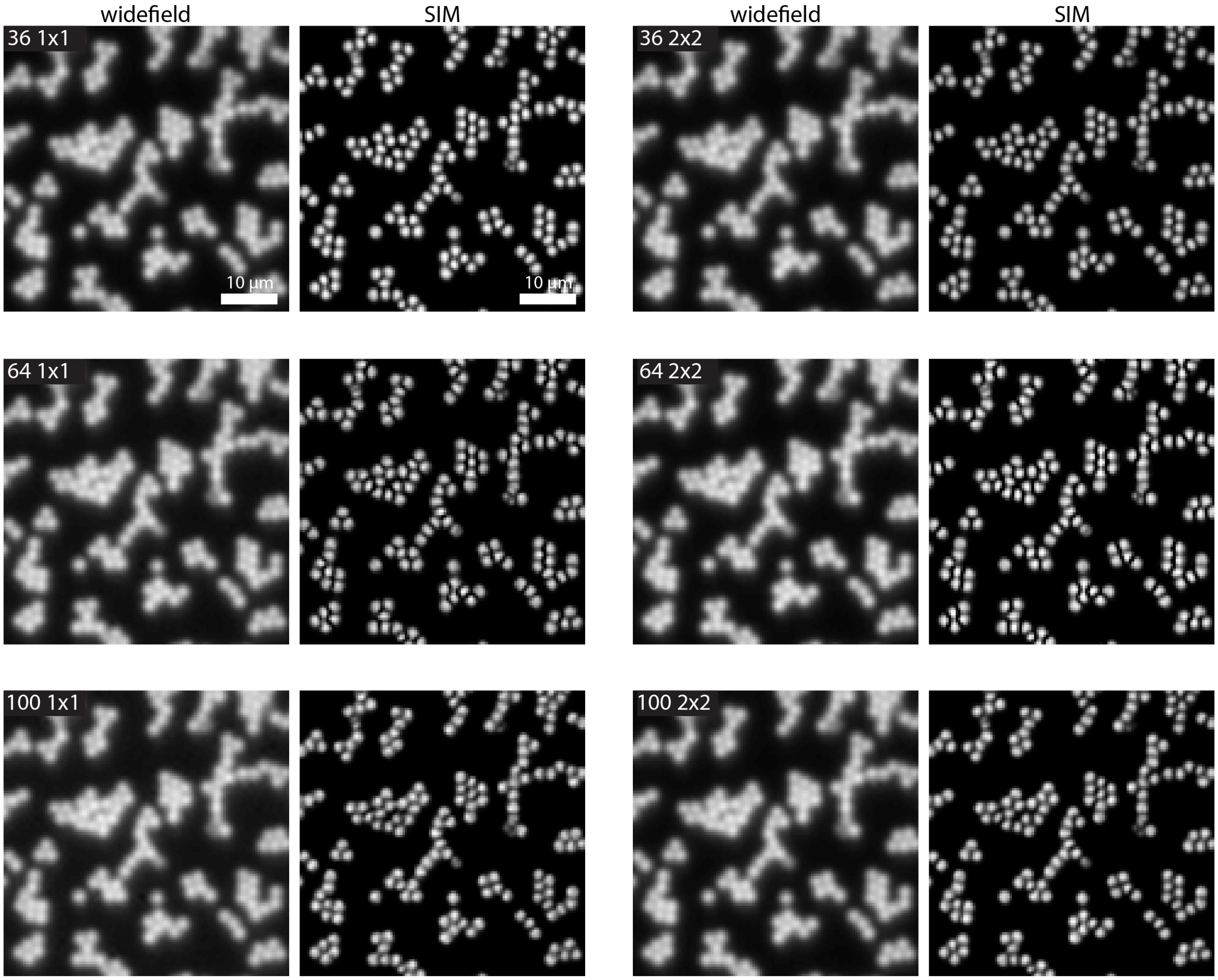

Figure 3.11: **Comparison of multispot illumination patterns**
Example zoom-in of widefield and SIM image shown for each indicated illumination pattern, e.g. '36 1x1' refers to a 6x6 array and 1x1 mirror aperture pattern.

3.4 Discussion

Dynamic perturbation of cell signaling pathways with spatiotemporal precision requires the development of illumination technologies that are capable of high-resolution optogenetic photostimulation and imaging. Here we combined optogenetic photostimulation and high-resolution imaging to create an optical system that can be used for localized signal perturbation in cell-based systems. The optimized optical design allows multi-color photopatterning and SIM imaging. We demonstrate the utility of this opto-SIM system with photopatterning and imaging of hESC cultures that express the optoWnt optogenetic system.

In the future, the opto-SIM system can be used for photoactivation of target cells to study cell-cell interactions and migration at a single-cell level. Such studies may provide insight into the molecular mechanisms of Wnt-induced tissue patterning and symmetry-breaking. Unlike LED-based illumination devices, such as the LAVA board system (see Chapter 2), the opto-SIM system enables dynamic pattern projection at high resolution. The use of diffraction-limited optics yields a high photopatterning resolution that is determined by the numerical aperture of the objective lens as opposed to the mask-limited resolution of LAVA devices. Furthermore, projected patterns can be dynamically updated based on feedback from measurements acquired during experiment. For example, existing cell tracking algorithms can be implemented to identify cell migration trajectories and modify the projection pattern to continuously illuminate target cells or locations during live-cell timelapse experiments. The opto-SIM system also enables temporal control of signaling at a resolution of 60 Hz, as well as 8-bit greyscale modulation to achieve dose-dependent optoWnt activation (*19*). Such flexibility in spatiotemporal patterning gives the unprecedented ability to stimulate stem-cell based model systems, organoids, or embryos with time-varying patterns of morphogen gradients.

Furthermore, with the opto-SIM system optogenetic stimulation can also be extended to subcellular scales. At the current 0.8 μm resolution, subcellular localization can already be achieved. Microscope objectives of higher numerical aperture can be used to further enhance the phototargeting resolution, which would enable precise subcellular stimulation up to $\sim$ 250 nm in resolution. Such phototargeting would allow localized activation of signaling at specific organelles or cytoplasmic regions to investigate how subcellular asymmetry in Wnt signaling, or other target pathways, can control cell fate commitment. For example, an intriguing study using Wnt-coated beads has shown that asymmetric presentation of the extracellular Wnt3a ligand can result in asymmetric fate allocation upon cell division of mouse epiblast stem cells (*60*). An exciting application of the opto-SIM system would be to further investigate the spatial patterning and duration thresholds that control this potential symmetry-breaking behavior. Though the subcellular resolution of phototargeting will be inherently compromised by protein diffusion, the target optogenetic proteins can be tethered to organelle or cytoskeletal structures to mitigate such effects.

In summary, the opto-SIM system allows user-defined, programmable control of light patterning and high-resolution imaging during optogenetic experiments. This system opens the door to a variety of future studies that investigate signaling dynamics and fate commitment during embryonic development.

3.5 Methods

3.5.1 Zemax modeling

The ray-tracing software Zemax OpticStudio was used in Sequential mode to model the opto-SIM optical configuration. Distances between lenses were set as variables and optimized to minimize on-axis spot size. In both system designs, the objective was assumed to be a perfect, aberration-free paraxial lens. In the 4f model, f = 125 mm (LA1384-A-ML, Thorlabs) and f = 225 mm (KPX201, Newport) lenses were used in the 4f system, and an f = 200 mm achromatic doublet as a tube lens (PAC077, Newport). In the eyepiece model, two f = 750 mm achromatic doublets were used (PAC094, Newport). The model configuration is described in Figure 3.12.

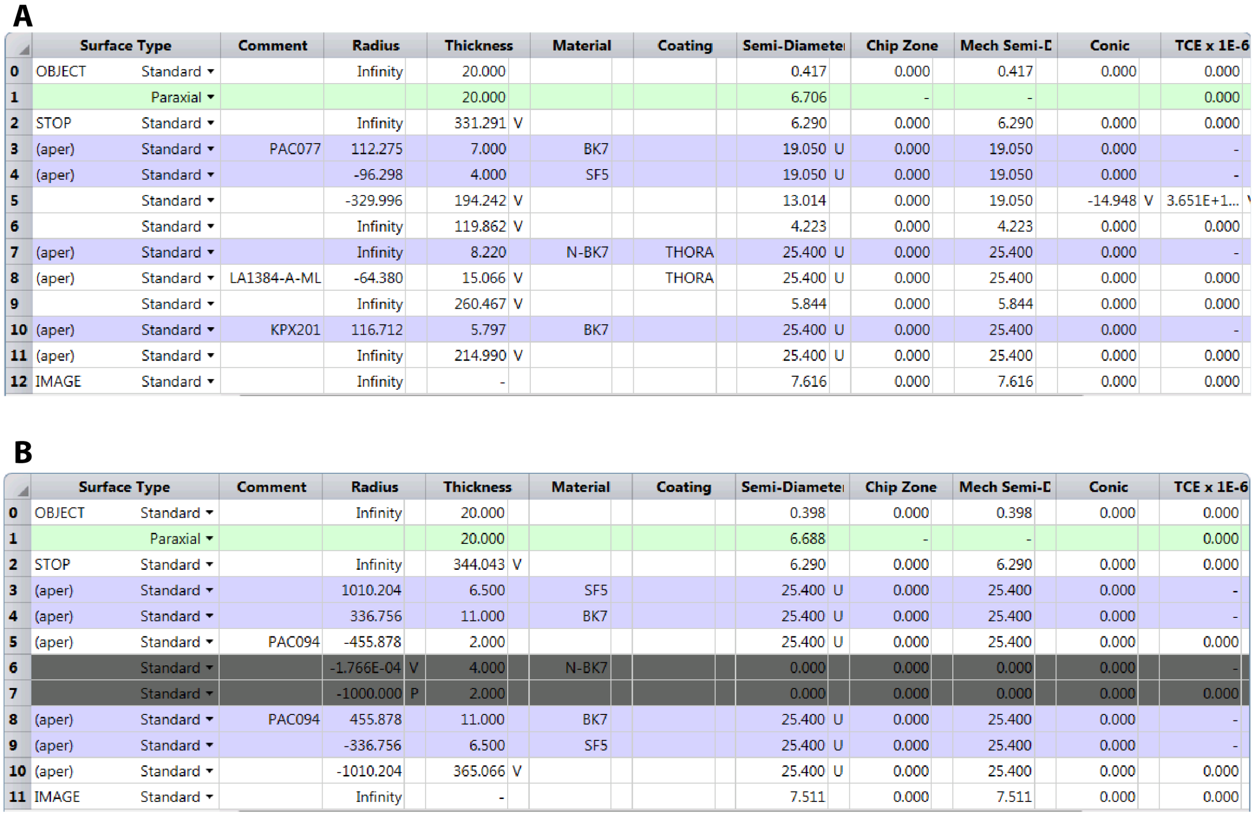

A

	Surface Type		Comment	Radius	Thickness	Material	Coating	Semi-Diamete	Chip Zone	Mech Semi-D	Conic	TCE x 1E-6
0	OBJECT	Standard ▾		Infinity	20.000			0.417	0.000	0.417	0.000	0.000
1		Paraxial ▾			20.000			6.706	-	-		0.000
2	STOP	Standard ▾		Infinity	331.291 V			6.290	0.000	6.290	0.000	0.000
3	(aper)	Standard ▾	PAC077	112.275	7.000	BK7		19.050 U	0.000	19.050	0.000	-
4	(aper)	Standard ▾		-96.298	4.000	SF5		19.050 U	0.000	19.050	0.000	-
5		Standard ▾		-329.996	194.242 V			13.014	0.000	19.050	-14.948 V	3.651E+1...
6		Standard ▾		Infinity	119.862 V			4.223	0.000	4.223	0.000	0.000
7	(aper)	Standard ▾		Infinity	8.220	N-BK7	THORA	25.400 U	0.000	25.400	0.000	-
8	(aper)	Standard ▾	LA1384-A-ML	-64.380	15.066 V		THORA	25.400 U	0.000	25.400	0.000	0.000
9		Standard ▾		Infinity	260.467 V			5.844	0.000	5.844	0.000	0.000
10	(aper)	Standard ▾	KPX201	116.712	5.797	BK7		25.400 U	0.000	25.400	0.000	-
11	(aper)	Standard ▾		Infinity	214.990 V			25.400 U	0.000	25.400	0.000	0.000
12	IMAGE	Standard ▾		Infinity	-			7.616	0.000	7.616	0.000	0.000

B

	Surface Type		Comment	Radius	Thickness	Material	Coating	Semi-Diamete	Chip Zone	Mech Semi-D	Conic	TCE x 1E-6
0	OBJECT	Standard ▾		Infinity	20.000			0.398	0.000	0.398	0.000	0.000
1		Paraxial ▾			20.000			6.688	-	-		0.000
2	STOP	Standard ▾		Infinity	344.043 V			6.290	0.000	6.290	0.000	0.000
3	(aper)	Standard ▾		1010.204	6.500	SF5		25.400 U	0.000	25.400	0.000	-
4	(aper)	Standard ▾		336.756	11.000	BK7		25.400 U	0.000	25.400	0.000	-
5	(aper)	Standard ▾	PAC094	-455.878	2.000			25.400 U	0.000	25.400	0.000	0.000
6		Standard ▾		-1.766E-04 V	4.000	N-BK7		0.000	0.000	0.000	0.000	-
7		Standard ▾		-1000.000 P	2.000			0.000	0.000	0.000	0.000	0.000
8	(aper)	Standard ▾	PAC094	455.878	11.000	BK7		25.400 U	0.000	25.400	0.000	-
9	(aper)	Standard ▾		-336.756	6.500	SF5		25.400 U	0.000	25.400	0.000	-
10	(aper)	Standard ▾		-1010.204	365.066 V			25.400 U	0.000	25.400	0.000	0.000
11	IMAGE	Standard ▾		Infinity	-			7.511	0.000	7.511	0.000	0.000

Figure 3.12: **Zemax model parameters of opto-SIM microscope**
A) Parameters for 4f system design. **B)** Parameters for eyepiece design.

	Part	Manufacturer	Model
1	Microscope	Nikon	TE 2000
2	514 nm laser	Coherent	Sapphire 514 LP 120 mW
3	458 nm laser	Coherent	Sapphire 458 LP 90 mW
4	Laser shutters	Edmund Optics	C-mount motorized shutter
5	Laser fiber	Thorlabs	F/APC single-mode patch cable
6	M1-M5	Thorlabs	2-inch mirror AR coated
7	DMD	Digital Light Innovations	DLP LightCrafter 9000
8	L1-L2	Newport	f=750 mm achromatic doublet
9	Dichroic filter	Chroma	Multi-band dichroic (458/ 514/ 594 nm) uf2
10	Sample stage	ASI	MS 2000 XY stage
11	Environmental control	OKO Labs	UNO-T-H-Premixed
12	Objective lens	Nikon	10x plan apochromat DIC NA = 0.45
13	Red brightfield filter	Edmund Optics	600nm longpass glass color filter (Hoya-R60)
14	Filter wheel	Sutter Instrument	Lambda 10-B
15	Emission filter (YFP)	Chroma	ET480/30m 25mm diameter
16	Emission filter (BV480)	Chroma	ET535/30m 25mm diameter
17	Camera	Andor	sCMOS Zyla 4.2p
18	Software	MicroManager	Gamma 2.0

Table 3.1: Opto-SIM microscope components

3.5.2 Microscope optical configuration

A Nikon TE 2000 microscope was modified to incorporate a DMD (DLi, DLP 9000) in the illumination beam path, coupled into the rear port of the microscope through an eyepiece lens design (two f = 750 mm achromatic doublets, PAC094, Newport). Hardware components used in final design are listed in Table 1, and hardware specifications detailed in Table 2-4. The 458 nm laser intensity was tuned so that illumination at the sample plane corresponded to 10-50 $\mu W mm^{-2}$. To achieve such low laser powers, an OD = 1 absorptive ND filter was placed into the 458 nm beam path (Thorlabs).

Software control was achieved through the open-source microscope control software MicroManager (version 2.0-gamma) (58, 59). The camera, DMD, laser shutters, and filter wheel were controlled through MicroManager run through MATLAB. Custom acquisition

	Camera Specification	**Value**
1	QE	82%
2	Sensor dimension	2048x2048
3	Mpixel	4.2 Mp
4	Pixel size	6.5 μm
5	Shutter	Rolling
6	Dynamic range	33000:1
7	Read noise (e/p/s)	0.9-1.1

Table 3.2: Andor Zyla 4.2p camera specifications

	DMD Specification	**Value**
1	Mirror pitch	7.6 μm
2	Mirror tilt angle	12 degrees
3	Array size	2560x1600 mirrors
4	Greyscale pattern rate (video)	60 Hz
5	Greyscale resolution	8-bit
6	Software control	HDMI
7	Array dimensions	19.5 x 12.2 mm
8	Array diagonal	0.9 inch

Table 3.3: DLP 9000 (WQXGA) DMD specification

	Objective Specification	**Value**
1	Magnification	10x
2	NA	0.45
3	Theoretical resolution (500nm light)	0.55 μm
4	Field of view (camera)	0.89 x 0.89 mm
5	Chromatic correction	3-color

Table 3.4: Nikon 10x plan apochromat objective specifications

sequences were programmed through MATLAB, and user-defined photostimulation and SIM patterns uploaded from an image file, MATLAB matrix, or user-defined through the Micro-Manager Projector plugin. Laser shutter control was achieved by powering the shutters (see Table 1) through an Arduino Uno microcontroller, which was controlled through MicroManager over a serial connection.

3.5.3 Sample preparation

Bead samples were prepared by coating 1 μm - diameter fluorescent beads (FluoroSpheres 505/515, Life Technologies F8762) onto a microscope slide. A drop of isopropanol was placed onto the slide, and 1 μL of bead solution was mixed in with a pipette tip and allowed to dry.

Clonal human embryonic stem cell lines (H9, Wicell) expressing the optoWnt optogenetic system (Cry2-LRP6c-2A-mVenus-2xNLS) were generated using a CRISP-based knock-in strategy at the AAVS1 locus as previously described (*6*). For imaging experiments, optoWnt hESCs were seeded on a 35 mm tissue culture plate coated with Matrigel (Corning) grown in mTeSR1 medium (STEMCELL Technologies) and 1% penicillin/streptomycin (Life Technologies) at 37 $°C$ and 5% CO2 with daily media changes. Cells were imaged in the native tissue culture plate and in maintenance self-renewal medium, mTeSR1.

References

1. Arnold, S. J. & Robertson, E. J. Making a commitment: cell lineage allocation and axis patterning in the early mouse embryo. *Nat. Rev. Mol. Cell Biol.* **10,** 91–103 (2009).
2. Oates, A. C., Gorfinkiel, N., Gonzalez-Gaitan, M. & Heisenberg, C.-P. Quantitative approaches in developmental biology. *Nat. Rev. Genet.* **10,** 517–530 (2009).
3. Repina, N. A., Rosenbloom, A., Mukherjee, A., Schaffer, D. V. & Kane, R. S. At Light Speed: Advances in Optogenetic Systems for Regulating Cell Signaling and Behavior. *Annual review of chemical and biomolecular engineering* **8,** 13–39 (2017).
4. Johnson, H. E. & Toettcher, J. E. Illuminating developmental biology with cellular optogenetics. *Current opinion in biotechnology* **52,** 42–48 (2018).
5. Bugaj, L. J., Choksi, A. T., Mesuda, C. K., Kane, R. S. & Schaffer, D. V. Optogenetic protein clustering and signaling activation in mammalian cells. *Nat. Methods* **10,** 249–252 (2013).
6. Repina, N. A. *et al.* Optogenetic control of Wnt signaling for modeling early embryogenic patterning with human pluripotent stem cells. *bioRxiv* **8,** 665695 (2019).
7. Sako, K. *et al.* Optogenetic Control of Nodal Signaling Reveals a Temporal Pattern of Nodal Signaling Regulating Cell Fate Specification during Gastrulation. *Cell Rep* **16,** 866–877 (2016).
8. Toettcher, J. E., Gong, D., Lim, W. A. & Weiner, O. D. Light-based feedback for controlling intracellular signaling dynamics. *Nat. Methods* **8,** 837–839 (2011).
9. Johnson, H. E. & Toettcher, J. E. Signaling Dynamics Control Cell Fate in the Early Drosophila Embryo. *Dev. Cell* **48,** 361–370.e3 (2019).
10. Toettcher, J. E., Weiner, O. D. & Lim, W. A. Using optogenetics to interrogate the dynamic control of signal transmission by the Ras/Erk module. *Cell* **155,** 1422–1434 (2013).
11. Johnson, H. E. *et al.* The Spatiotemporal Limits of Developmental Erk Signaling. *Dev. Cell* **40,** 185–192 (2017).
12. Kainrath, S., Stadler, M., Reichhart, E., Distel, M. & Janovjak, H. Green-Light-Induced Inactivation of Receptor Signaling Using Cobalamin-Binding Domains. *Angew Chem Int Ed Engl* **56,** 4608–4611 (2017).
13. Levskaya, A., Weiner, O. D., Lim, W. A. & Voigt, C. A. Spatiotemporal control of cell signalling using a light-switchable protein interaction. *Nature* **461,** 997–1001 (2009).
14. Yazawa, M., Sadaghiani, A. M., Hsueh, B. & Dolmetsch, R. E. Induction of protein-protein interactions in live cells using light. *Nature Biotechnology* **27,** 941–945 (2009).
15. Strickland, D. *et al.* TULIPs: tunable, light-controlled interacting protein tags for cell biology. *Nat. Methods* **9,** 379–384 (2012).

16. Guntas, G. *et al.* Engineering an improved light-induced dimer (iLID) for controlling the localization and activity of signaling proteins. *Proceedings of the National Academy of Sciences* **112,** 112–117 (2015).

17. Bugaj, L. J. *et al.* Regulation of endogenous transmembrane receptors through optogenetic Cry2 clustering. *Nat Commun* **6,** 6898 (2015).

18. Wang, X., He, L., Wu, Y. I., Hahn, K. M. & Montell, D. J. Light-mediated activation reveals a key role for Rac in collective guidance of cell movement in vivo. *Nat Cell Biol* **12,** 591–597 (2010).

19. Repina, N. A., McClave, T., Bao, X., Kane, R. S. & Schaffer, D. V. Engineered illumination devices for optogenetic control of cellular signaling dynamics. *bioRxiv* **8,** 675892 (2019).

20. Chen, M., Mertiri, T., Holland, T. & Basu, A. S. Optical Microplates for High-Throughput Screening of Photosynthesis in Lipid-Producing Algae. *Lab on a Chip* **12,** 3870–3874 (2012).

21. Olson, E. J., Hartsough, L. A., Landry, B. P., Shroff, R. & Tabor, J. J. Characterizing bacterial gene circuit dynamics with optically programmed gene expression signals. *Nat. Methods* **11,** 449–455 (2014).

22. Gerhardt, K. P. *et al.* An open-hardware platform for optogenetics and photobiology. *Sci Rep* **6,** 35363 (2016).

23. Bugaj, L. J. & Lim, W. A. High-Throughput Multicolor Optogenetics in Microwell Plates. *Nature Protocols* **14,** 2205 (2019).

24. Müller, K., Zurbriggen, M. D. & Weber, W. Control of gene expression using a red- and far-red light-responsive bi-stable toggle switch. *Nat Protoc* **9,** 622–632 (2014).

25. Shao, J. *et al.* Synthetic far-red light-mediated CRISPR-dCas9 device for inducing functional neuronal differentiation. *Proceedings of the National Academy of Sciences* **8,** 201802448 (2018).

26. Yizhar, O., Fenno, L. E., Davidson, T. J., Mogri, M. & Deisseroth, K. Optogenetics in neural systems. *Neuron* **71,** 9–34 (2011).

27. Packer, A. M., Roska, B. & Häusser, M. Targeting neurons and photons for optogenetics. *Nat. Neurosci.* **16,** 805–815 (2013).

28. Prakash, R. *et al.* Two-photon optogenetic toolbox for fast inhibition, excitation and bistable modulation. *Nat. Methods* **9,** 1171–1179 (2012).

29. Packer, A. M., Russell, L. E., Dalgleish, H. W. P. & Häusser, M. Simultaneous all-optical manipulation and recording of neural circuit activity with cellular resolution in vivo. *Nat. Methods* **12,** 140–146 (2015).

30. Carrillo-Reid, L., Yang, W., Bando, Y., Peterka, D. S. & Yuste, R. Imprinting and recalling cortical ensembles. *Science* **353,** 691–694 (2016).

31. Nikolenko, V., Poskanzer, K. E. & Yuste, R. Two-photon photostimulation and imaging of neural circuits. *Nat. Methods* **4,** 943–950 (2007).
32. Yoo, S. K. *et al.* Differential Regulation of Protrusion and Polarity by PI(3)K during Neutrophil Motility in Live Zebrafish. *Developmental Cell* **18,** 226–236 (2010).
33. Izquierdo, E., Quinkler, T. & De Renzis, S. Guided morphogenesis through optogenetic activation of Rho signalling during early Drosophila embryogenesis. *Nat Commun* **9,** 2366 (2018).
34. Guglielmi, G., Barry, J. D., Huber, W. & De Renzis, S. An Optogenetic Method to Modulate Cell Contractility during Tissue Morphogenesis. *Dev. Cell* **35,** 646–660 (2015).
35. Bansal, V. & Saggau, P. Digital Micromirror Devices: Principles and Applications in Imaging. *Cold Spring Harbor Protocols* **2013,** pdb.top074302 (2013).
36. Papagiakoumou, E. *et al.* Scanless two-photon excitation of channelrhodopsin-2. *Nat. Methods* **7,** 848–854 (2010).
37. Pégard, N. C. *et al.* Three-dimensional scanless holographic optogenetics with temporal focusing (3D-SHOT). *Nat Commun* **8,** 1228 (2017).
38. Hernandez, O. *et al.* Three-dimensional spatiotemporal focusing of holographic patterns. *Nat Commun* **7,** 11928 (2016).
39. Sahl, S. J., Hell, S. W. & Jakobs, S. Fluorescence Nanoscopy in Cell Biology. *Nature Reviews Molecular Cell Biology* **18,** 685–701 (2017).
40. Hell, S. W. & Wichmann, J. Breaking the Diffraction Resolution Limit by Stimulated Emission: Stimulated-Emission-Depletion Fluorescence Microscopy. *Optics Letters* **19,** 780–782 (1994).
41. Klar, T. A., Jakobs, S., Dyba, M., Egner, A. & Hell, S. W. Fluorescence Microscopy with Diffraction Resolution Barrier Broken by Stimulated Emission. *Proceedings of the National Academy of Sciences* **97,** 8206–8210 (2000).
42. Betzig, E. *et al.* Imaging Intracellular Fluorescent Proteins at Nanometer Resolution. *Science* **313,** 1642–1645 (2006).
43. Rust, M. J., Bates, M. & Zhuang, X. Sub-Diffraction-Limit Imaging by Stochastic Optical Reconstruction Microscopy (STORM). *Nature Methods* **3,** 793 (2006).
44. Gustafsson, M. G. L. Surpassing the Lateral Resolution Limit by a Factor of Two Using Structured Illumination Microscopy. *Journal of Microscopy* **198,** 82–87 (2000).
45. Gustafsson, M. G. L. *et al.* Three-Dimensional Resolution Doubling in Wide-Field Fluorescence Microscopy by Structured Illumination. *Biophysical Journal* **94,** 4957–4970 (2008).
46. Wu, Y. & Shroff, H. Faster, Sharper, and Deeper: Structured Illumination Microscopy for Biological Imaging. *Nature Methods* **15,** 1011 (2018).

47. Heintzmann, R. & Cremer, C. G. *Laterally Modulated Excitation Microscopy: Improvement of Resolution by Using a Diffraction Grating Optical Biopsies and Microscopic Techniques III* **3568** (International Society for Optics and Photonics, 1999), 185–196.

48. Demmerle, J. *et al.* Strategic and Practical Guidelines for Successful Structured Illumination Microscopy. *Nature Protocols* **12,** 988–1010 (2017).

49. York, A. G. *et al.* Resolution Doubling in Live, Multicellular Organisms via Multifocal Structured Illumination Microscopy. *Nature Methods* **9,** 749–754 (2012).

50. Schulz, O. *et al.* Resolution Doubling in Fluorescence Microscopy with Confocal Spinning-Disk Image Scanning Microscopy. *Proceedings of the National Academy of Sciences* **110,** 21000–21005 (2013).

51. York, A. G. *et al.* Instant Super-Resolution Imaging in Live Cells and Embryos via Analog Image Processing. *Nature Methods* **10,** 1122–1126 (2013).

52. Mudry, E. *et al.* Structured Illumination Microscopy Using Unknown Speckle Patterns. *Nature Photonics* **6,** 312–315 (2012).

53. Yeh, L.-H., Chowdhury, S. & Waller, L. Computational Structured Illumination for High-Content Fluorescence and Phase Microscopy. *Biomedical Optics Express* **10,** 1978–1998 (2019).

54. Yeh, L.-H., Chowdhury, S., Repina, N. A. & Waller, L. Speckle-Structured Illumination for 3D Phase and Fluorescence Computational Microscopy. *Biomedical Optics Express* **10,** 3635–3653 (2019).

55. Dan, D. *et al.* DMD-Based LED-Illumination Super-Resolution and Optical Sectioning Microscopy. *Scientific Reports* **3,** 1116 (2013).

56. Cheng, L.-C. *et al.* Nonlinear Structured-Illumination Enhanced Temporal Focusing Multiphoton Excitation Microscopy with a Digital Micromirror Device. *Biomedical Optics Express* **5,** 2526–2536 (2014).

57. Yeh, L.-H., Tian, L. & Waller, L. Structured Illumination Microscopy with Unknown Patterns and a Statistical Prior. *Biomedical Optics Express* **8,** 695–711 (2017).

58. Edelstein, A., Amodaj, N., Hoover, K., Vale, R. & Stuurman, N. Computer Control of Microscopes Using μManager. *Current Protocols in Molecular Biology* **92,** 14.20.1–14.20.17 (2010).

59. Edelstein, A. D. *et al.* Advanced Methods of Microscope Control Using μManager Software. *Journal of Biological Methods* **1,** e10 (2014).

60. Habib, S. J. *et al.* A localized Wnt signal orients asymmetric stem cell division in vitro. *Science* **339,** 1445–1448 (2013).

Chapter 4

Optogenetic control of Wnt signaling for modeling early embryogenic patterning with human pluripotent stem cells

4.1 Introduction

Molecular regulation of embryonic morphogenesis, a process where seemingly identical cells differentiate and organize into spatially defined regions, remains poorly understood in mammalian developmental biology (*1*). The emergence of such spatial organization is attributed to cell-intrinsic differences in gene expression (*2*, *3*) or extrinsic asymmetries within the cell environment (*4*, *5*). The resulting variability in intracellular signaling leads to changes in cell migration, cell-cell interactions, and/or cell polarity that in turn drive the coordinated organization of specific cell populations (*6*, *7*).

Self-organization within the embryonic tissue proper, or epiblast, is first evident during gastrulation, where subpopulations of cells reorganize and differentiate along distinct cell lineages to form the three germ layers of the future organism (*4*). Initially, asymmetric patterns of molecular signals – morphogens such as Wnt, BMP, Nodal, and FGF – emerge across the morphologically symmetric epiblast of the mouse embryo (*4*, *8*–*12*). The establishment of such signaling asymmetry is followed by morphological symmetry-breaking, where a subpopulation of posterior epiblast cells undergoes mesendoderm differentiation and an epithelial to mesenchymal transition (EMT), then migrates away from the epithelial epiblast cells in the region of the primitive streak (*13*, *14*). During this dynamic process of gastrulation, the temporal order and location of cell migration through the primitive streak is correlated with downstream cell fate outcome, resulting in organization of the developing cell lineages into defined regions within the embryo (*13*, *15*–*17*).

However, while advances in live embryo imaging and transcriptomic analysis have unveiled dynamics of cell migration and identified molecular signatures of lineage trajectories (*17*–*19*), a mechanistic and causal understanding of the molecular regulation of gastrulation is lacking. Morphogen signals are necessary for successful gastrulation (*8*, *10–12*), but which specific signals are sufficient for inducing cell self-organization are unknown. Furthermore, it is unclear how the spatial and temporal dynamics of morphogens regulate cell lineage commitment and link cell fate outcome to migration dynamics through the primitive streak (*13*, *15–17*).

To gain mechanistic insight into morphogenesis, embryonic stem cell (ESC) culture systems have recently been developed to emulate in vivo processes of early mammalian development (*20*). Such embryoid or gastruloid models can show remarkable gene expression similarity to natural embryos (*21–23*) and also enable molecular perturbation to study mechanism. As one example, aggregates of mouse ESCs (mESCs), derived from the pre-implantation blastocyst (*24*, *25*), spontaneously self-organize and initiate mesendoderm differentiation, an effect enhanced by an exogenous pulse of Wnt agonist (*26–28*). Gastrulation-like events are also observed in mESC aggregates grown adjacent to extraembryonic tissue, an effect suppressed by the Wnt antagonist Dkk1 (*22*, *29*). Excitingly, human ESCs (hESCs) have extended such developmental models from mouse to human embryogenesis, which, due to ethical restrictions, has long been a mystery (*20*, *30*). For example, hESCs geometrically confined to two-dimensional circular micropatterns self-organize into radially symmetric patterns of germ lineages in response to uniform addition of BMP4 or Wnt agonists, (*5*, *31*, *32*) as well as establish signal feedback loops between Wnt/Nodal/BMP4 pathways (*33*). However, as with exogenous molecular perturbation of natural embryos, such ESC-based models rely on uniform addition of signal pathway agonists or inhibitors, which lack dynamic and spatial control. Furthermore, such models are confounded by variations in molecular diffusion of agonists within embryoids (*34*), cell variation in morphogen receptor expression (*3*, *5*), and geometric asymmetries in the cell environment (*29*, *35*). As a result, mechanistic insight into morphogenesis has been limited in such models since their self-organization is a result of spontaneous and heterogeneous differentiation along diverse cell lineages rather than specific control of cell signaling pathways. How specific morphogen signals direct self-organization, cell fate specification, and migration in gastrulation models thus remains unknown.

To address this critical need for dynamic and specific control of embryonic morphogen signaling, we developed an optogenetic approach to perturb Wnt signaling in hESCs. Light-sensitive protein domains that induce protein-protein interactions and/or modify protein activity in response to illumination allow optogenetic control of signaling in space and time (*36*, *37*). Optogenetic strategies have recently been applied for spatiotemporal control of transcription and intracellular signaling in the Drosophila (*38–41*) and zebrafish embryo (*42–44*). Here, we implement optogenetic control of canonical Wnt signaling to determine whether differential Wnt signaling can model human gastrulation and lead to emergence of organized shape and structure through collective cell rearrangement. We achieve optogenetic control of Wnt signaling in hESCs by illuminating hESC cultures expressing a fusion of the plant blue-light photoreceptor Cryptochrome 2 (Cry2) to the Wnt co-receptor LRP6 (*45*). By mimicking differential Wnt presentation with optogenetic stimulation of cell subpopulations, we developed an hESC model for studying Wnt-mediated morphogenesis in early development. Using this gastrulation model in combination with transcriptomic analysis and single-cell migration studies, we show that Wnt signaling is sufficient for inducing self-organization of cells in an EMT-dependent manner.

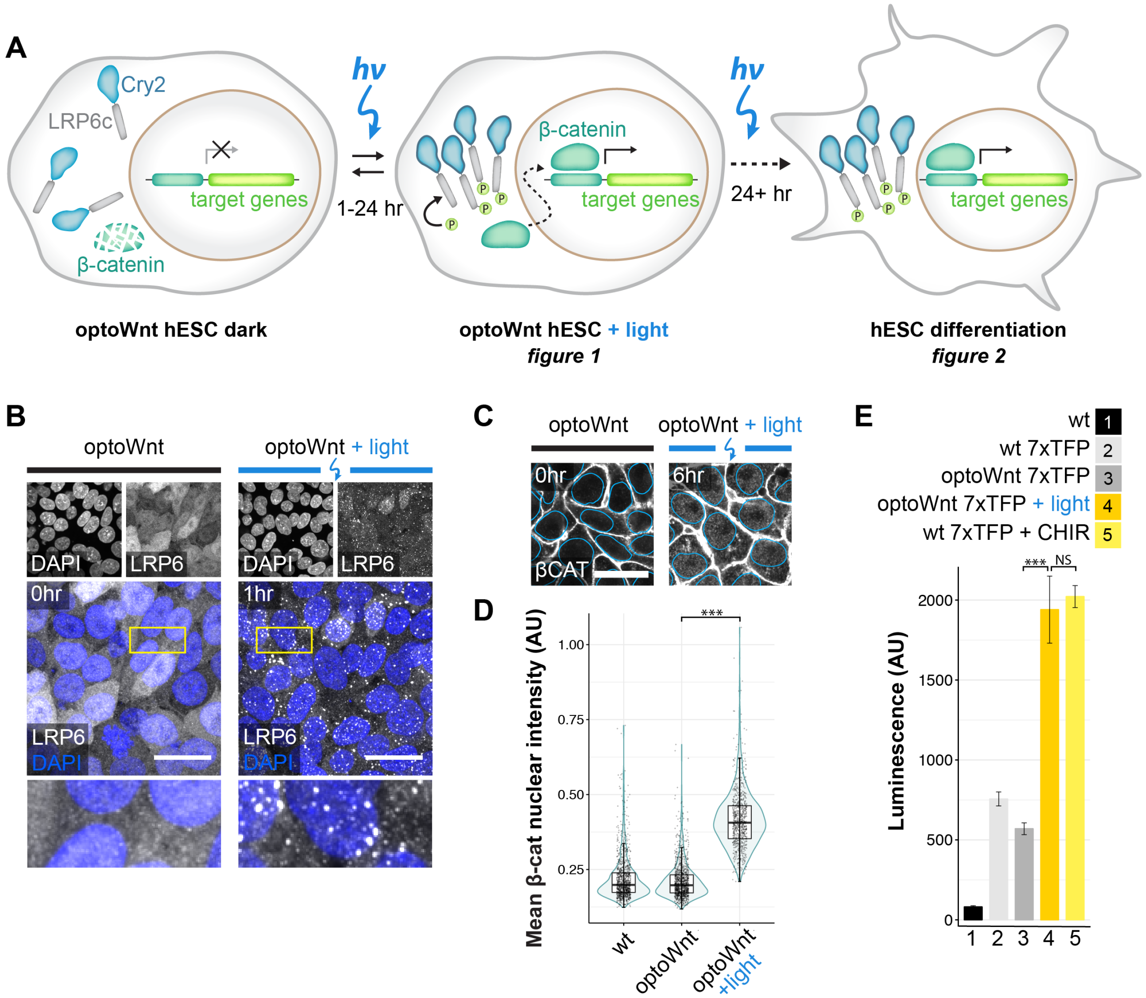

Figure 4.1: **Optogenetic activation of Wnt/β-catenin signaling in hESCs**
A) Schematic of optogenetic Wnt/β-catenin pathway activation (optoWnt) in hESCs. **B)** Immunostaining for LRP6 in optoWnt hESCs in the dark (left) and after 1 hr of 0.8 $\mu W mm^{-2}$ illumination (right). Scale bar 25 μm. **C)** Representative images of immunostaining for β-catenin in optoWnt hESCs in the dark (left) and after 6 hr illumination (right). Nuclear outline from DAPI stain overlaid in blue. Scale bar 25 μm. **D)** Quantification of β-catenin nuclear intensity. Graph shows pooled analysis of 14 fields of view per biological replicate (n = 3), each point representing a single cell. Unpaired two-samples Wilcoxon test (p = 1 x 10-16). **E)** Luciferase assay in WT and optoWnt hESCs carrying a 7xTFP reporter for β-catenin activity. Wnt signaling was induced for 24 hr with 0.8 $\mu W mm^{-2}$ illumination or with CHIR99021 (CHIR, 3 μM). ANOVA followed by Tukey test (p = 4.6 x 10-7 (3 vs. 4); p = 0.86 (4 vs. 5)). Graph shows mean ± 1 s.d., n = 3 biological replicates.

4.2 Results

4.2.1 Optogenetic activation of Wnt/β-catenin signaling in hESCs

Canonical Wnt/β-catenin signaling initiates when extracellular Wnt protein binds to transmembrane receptor Frizzled, an event that triggers multimeric clustering of the Wnt coreceptor low-density lipoprotein receptor-related protein 6 (LRP6) (*46*). LRP6 oligomers are subsequently phosphorylated and induce an intracellular signaling cascade that stabilizes the downstream Wnt effector β-catenin, which in turn transcriptionally activates target genes (*47*). To render Wnt signaling light-inducible, we previously developed an optogenetic system consisting of the photolyase homology domain of A. thaliana blue-light photoreceptor Cryptochrome 2 (Cry2) fused to the cytoplasmic domain of LRP6 (LRP6c) (*45*) (Figure 4.1A).

Here, we extend the application of the Cry2-LRP6c optogenetic system, hereafter named 'optoWnt', to hESCs by knocking the optoWnt transgene into the AAVS1 safe harbor locus for stable expression (*48*) (Figure 4.2A-C). Specifically, we used CRISPR/Cas9-mediated homology-directed repair to generate a clonal, heterozygous hESC line that constitutively expresses Cry2-LRP6c for light-induced Wnt activation and a P2A-linked mCherry for cell identification. The resulting optoWnt hESCs uniformly expressed mCherry and retained a pluripotent phenotype (Figure 4.2D-E). We also generated clonal induced pluripotent stem cell (iPSC) lines expressing the optoWnt system (Figure 4.2B-C), **F)**. Blue (470 nm) light stimulation of hESC cultures was achieved with specialized LED illumination devices (light activation at variable amplitude, or LAVA, devices) that allow precise control of the intensity, timing, and uniformity of stimulation (Figure 4.2G-I) (*49*).

To confirm that Cry2 is functional in hESCs, we illuminated optoWnt hESC cultures and examined the induction of LRP6 oligomers. In the dark, LRP6 was diffusely distributed throughout the cell cytoplasm, but upon blue light stimulation LRP6 formed distinct oligomers, confirming the functionality of multimeric Cry2 clustering in hESCs (Figure 4.1B).

Since activation of canonical Wnt signaling is characterized by β-catenin nuclear translocation in hESCs (*47*), we probed for accumulation of nuclear β-catenin upon optogenetic stimulation. From an initial membrane-associated state, reflecting its role in stabilizing adherens junctions, β-catenin protein translocated to the cell cytoplasm and nucleus (Figure 4.1C). Single-cell quantification of the mean nuclear intensity of β-catenin showed a significant accumulation of nuclear β-catenin following 6 hrs of optogenetic stimulation ($p < 1E-16$), with no apparent accumulation in the dark (Figure 4.1D).

To assess transcriptional activity of the nuclearly localized β-catenin, we used an established β-catenin-responsive luciferase reporter, 7xTFP (*50*), introduced into optoWnt hESCs via lentiviral infection. Consistent with the lack of observable dark-state LRP6 clustering or nuclear β-catenin, unilluminated optoWnt hESCs showed no activation of β-catenin transcriptional activity, suggesting minimal background Wnt pathway activation from optoWnt expression (Figure 4.1E). In contrast, illumination over 24 hrs at a constant intensity of 0.8 $\mu W mm^{-2}$ led to a $\sim$3-fold increase in luciferase reporter expression ($p < 1E-7$), with activation levels comparable to those induced by the small-molecule Wnt pathway agonist CHIR99021 (CHIR, 3 μM).

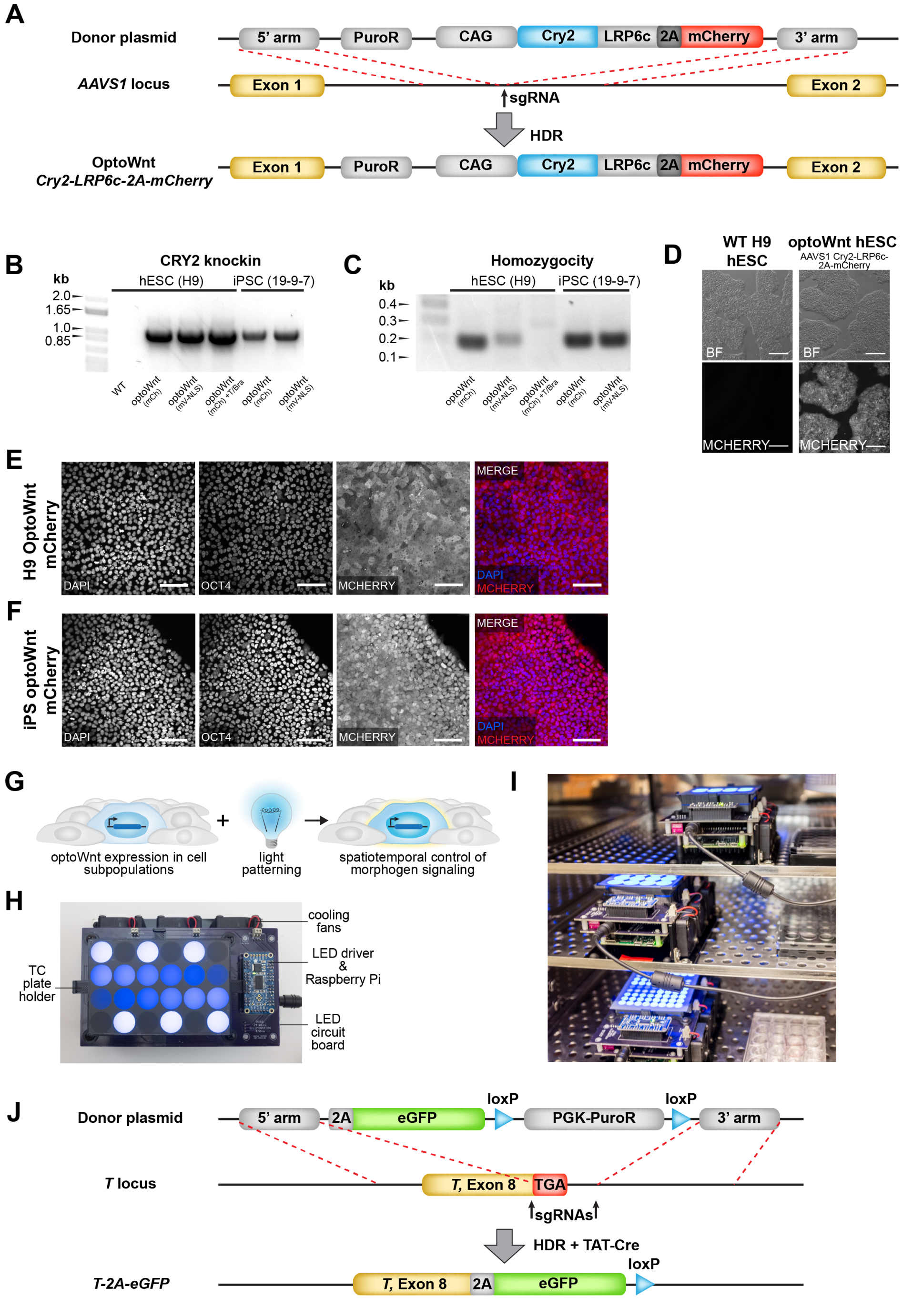

Figure 4.2: *See caption on next page*

Figure 4.2: **OptoWnt cell line characterization and optical stimulation**
A) Schematic of optoWnt knock-in strategy using CRISPR-mediated modification of AAVS1 locus. OptoWnt expression driven by synthetic CAG promoter. **B)** PCR genotyping of hESC and iPSC clones after puromycin selection. Expected PCR product for correctly targeted AAVS1 locus is 1.1 kbp. **C)** PCR homozygosity assay on knock-in clones. Clones without a ∼200 bp PCR product were homozygous. **D)** Representative brightfield (BF) and mCherry fluorescence images of live WT and optoWnt hESCs. Scale bar 250 μm. **E)** Representative images of immunostaining for OCT4 and mCherry in optoWnt hESCs in routine cell culture, kept in the dark. Scale bar 100 μm. **F)** Representative images of immunostaining for OCT4 and mCherry in optoWnt iPSCs in routine cell culture, kept in the dark. Scale bar 100 μm. **G)** Schematic of optogenetic experimental setup for stimulation of cell subpopulations. **H)** Image of illumination device, LAVA board, used for optogenetic stimulation of hESC cultures. **I)** Image of LAVA boards kept inside a TC incubator. **J)** Schematic of eGFP knock-in strategy to make BRA/T reporter line using CRISPR-mediated modification of endogenous BRA/T locus.

4.2.2 OptoWnt stimulation induces hESC differentiation and expression of primitive streak marker Brachyury

Recombinant Wnt3a protein or Wnt pathway small-molecule agonists induce ESC differentiation along a mesendoderm lineage (*51*, *52*). To determine whether optoWnt can analogously induce hESC and iPSC differentiation, we analyzed the light-induced expression of self-renewal and differentiation markers. We first examined expression of the mesendoderm transcriptional regulator and primitive streak marker Brachyury (BRA, also known by its gene name, T), a direct transcriptional target of Wnt signaling (*9*, *53*, *54*). After 48 hrs of light activation, we saw a ∼40-fold increase in BRA/T protein expression in optoWnt hESCs and iPSCs (Figure 4.3A, Figure 4.4A-B). The resulting >99.9% pure BRA+ population was comparable to the CHIR (5 μM) positive control, and by contrast BRA expression was not observed in dark-state cells (Figure 4.3B).

To better quantify BRA expression at a single-cell level, we generated an hESC reporter cell line co-expressing the optoWnt system and an eGFP reporter for endogenous BRA expression (Figure 4.2J). Live-cell analysis with flow cytometry showed that $>$ 95% cells expressed BRA after 24 hrs of illumination, with the mean eGFP intensity increasing ∼33-fold over unilluminated optoWnt hESCs (Figure 4.3C). Quantification of eGFP-positive cells between multiple control conditions showed that signal levels achieved with optoWnt stimulation greatly exceeded activation by high concentrations of recombinant Wnt3a protein (250 $ngmL^{-1}$) and were comparable to 5 μM CHIR treatment (Figure 4.3D). In contrast, unilluminated optoWnt reporter cells showed no significant eGFP expression relative to wild-type reporter cells, further demonstrating the low dark-state activation. We validated these protein expression results with qPCR for the T gene following variable lengths of illumination (Figure 4.3E). Onset of T transcription was observed after as quickly as 4 hr of illumination (∼14-fold increase in mRNA expression), with expression saturating at ∼500-fold by 32 hr of illumination (Figure 4.3E).

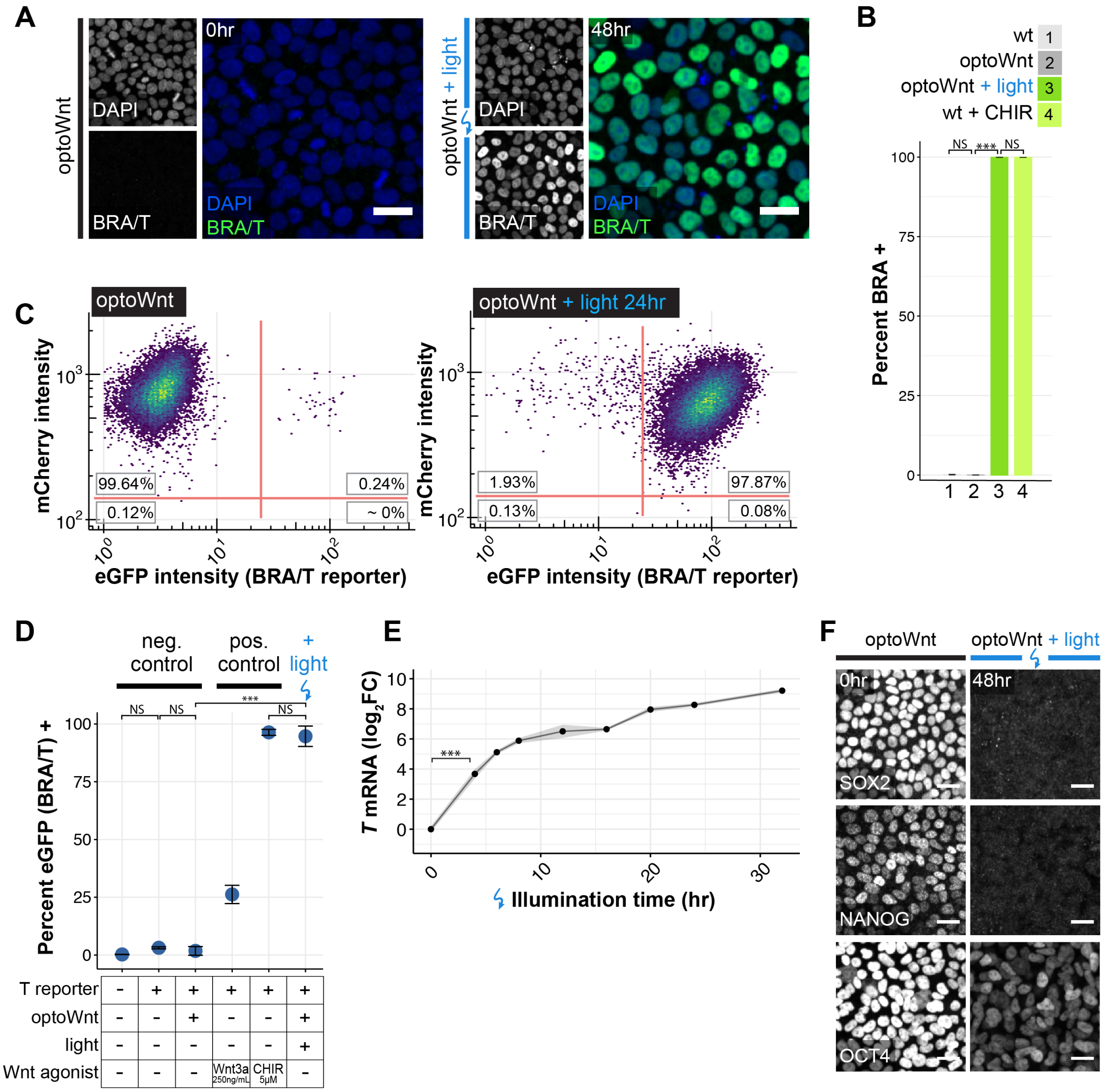

Figure 4.3: **OptoWnt induces BRA expression and hESC differentiation**
A) Representative images of immunostaining for BRA in optoWnt hESC in the dark (top) or after 48 hrs illumination (bottom). Scale bar 25 μm. **B)** Quantification of immunostaining for BRA in WT and optoWnt hESCs following 48 hrs illumination or CHIR (5 μM) treatment. ANOVA followed by Tukey test. Graph shows mean ± 1 s.d., n = 3 biological replicates. **C)** FACS analysis of optoWnt hESCs (mCherry+) modified with an eGFP reporter at the endogenous BRA/T gene locus ('BRA/T reporter'), kept in the dark (left) or illuminated for 24 hrs (right). Graph shows pooled data from 3 biological replicates, ~30,000 cells per condition. **D)** FACS quantification of percent eGFP-positive cells under indicated conditions for 24 hrs, e.g. Wnt3a recombinant protein (250 $ngmL^{-1}$) or CHIR (5 μM). ANOVA followed by Tukey test (p < 10-12). Graph shows mean ± 1 s.d., n = 3 to 6 biological replicates. *Caption continued on next page*

Figure 4.3: **E)** qPCR timecourse of T mRNA expression in optoWnt hESCs at indicated durations of illumination. Graph shows mean log fold change in mRNA expression (log_2FC) relative to dark (0 hr) condition ± 1 S.E.M, n = 3 biological replicates. **F)** Representative images of immunostaining for pluripotency markers SOX2, NANOG, and OCT4 in optoWnt hESCs kept in the dark (left) and following 48 hrs illumination (right). Scale bar 25 μm.

Next, we assayed for expression of ESC pluripotency markers SOX2, NANOG, and OCT4. Cells kept in the dark retained pluripotency markers at levels indistinguishable from wild-type (WT) hESCs (Figure 4.3F, Figure 4.4C-F). Conversely, as anticipated for cells undergoing differentiation, optoWnt stimulation led to a decrease in expression of all three pluripotency markers to levels similar to CHIR treatment. The incomplete reduction in OCT4 levels following 48 hrs of illumination is consistent with longer OCT4 persistence during differentiation compared to NANOG or SOX2 (*55*). Global transcriptional profiling of optogenetic stimulation confirms light-induced mesendoderm lineage commitment

To establish a molecular fingerprint for optoWnt-induced differentiation, we measured global transcriptional changes using bulk-population RNA-seq of optoWnt and WT hESCs after 48 hrs of light stimulation (Figure 4.5A), Table S1). Illuminated WT cells served as a phototoxicity control, and unilluminated optoWnt cells controlled for potential CRISPR/Cas9 knock-in effects, cell perturbation due to optoWnt expression, and dark-state Wnt pathway activation. Principal component analysis (PCA) showed clustering of biological triplicates for each condition and strong transcriptional changes upon optoWnt stimulation that account for 97% gene variance among samples (Figure 4.5B). Dark and illuminated WT cells clustered together, and differential analysis showed minimal gene expression differences, demonstrating minimal phototoxicity effects after 48 hrs of continuous 0.8 $\mu W mm^{-2}$ blue light stimulation (Figure 4.5C). The remaining 3% of variance was captured by the second principle component, which accounted for slight transcriptional differences between the unilluminated WT vs. optoWnt cells (Figure 4.5D). Notably, none of the differentially expressed genes (DEGs, highlighted red) are members of the Wnt/β-catenin pathway, suggesting that transcriptional differences are due to gene knock-in or protein overexpression effects and not background Wnt pathway activation.

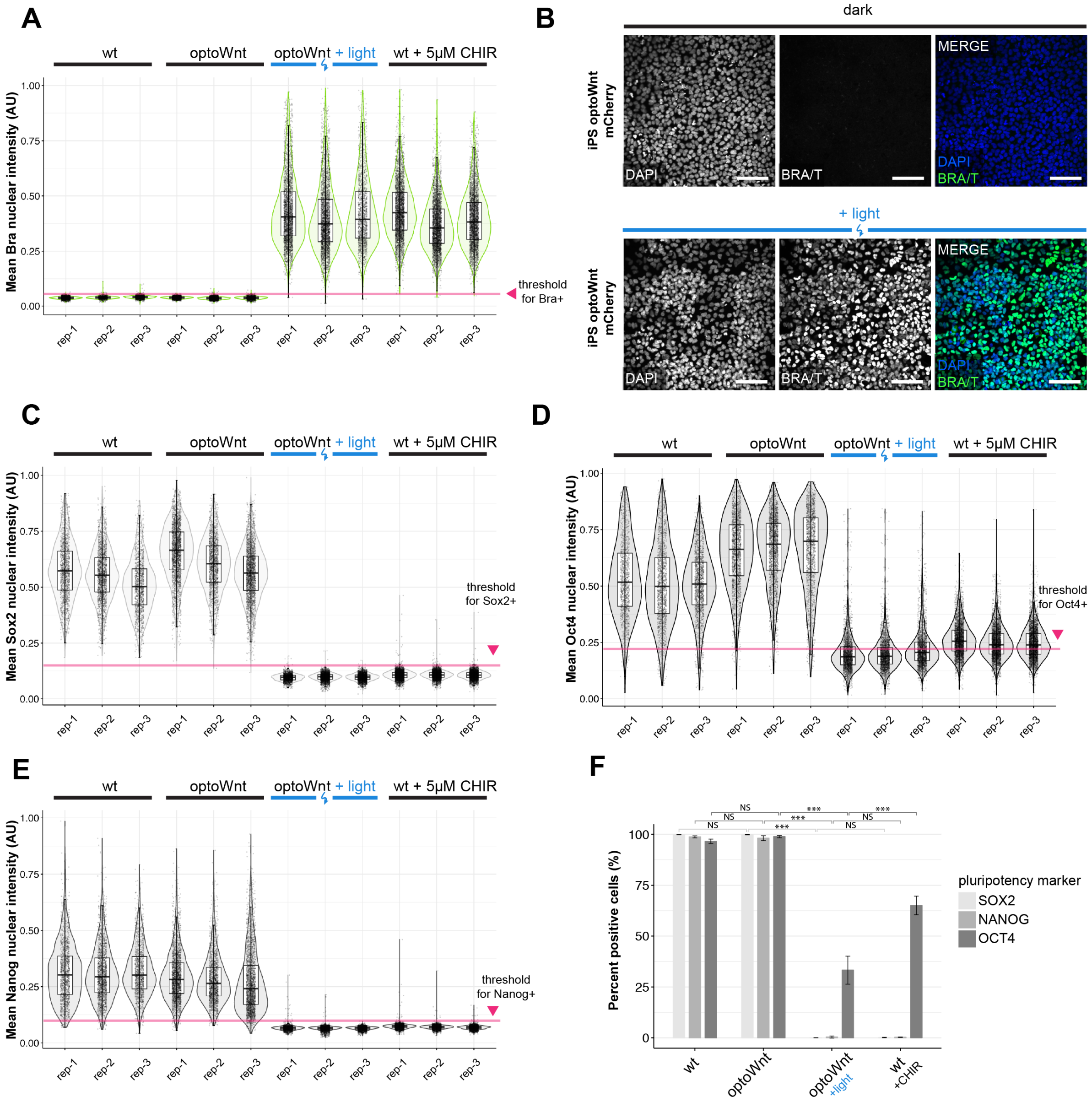

Figure 4.4: **Lineage marker expression in optoWnt hESCs and iPSCs**
A) Quantification of mean BRA nuclear intensity from immunostaining shown in (Figure 4.3A-B). Graph shows analysis of biological replicates (rep 1-3) after 48 hrs illumination or CHIR99021 (5 μM) treatment. Each point represents a single cell. Threshold for BRA+ classification indicated with red arrow. **B)** Representative images of immunostaining for BRA in optoWnt iPSCs. Scale bar 100 μm. **C-E)** Quantification of mean SOX2 (C), OCT4 (D), and NANOG (E) nuclear intensity from immunostaining shown in (Figure 4.3F). Threshold for SOX2+, OCT4+, or NANOG+ classification indicated with red arrow. **F)** Quantification of percent positive cells for pluripotency markers based on immunostaining shown in (C)-(E) and (Figure 4.3F). Graph shows percent positive cells ± 1 s.d., n = 3 biological replicates. ANOVA followed by Tukey test.

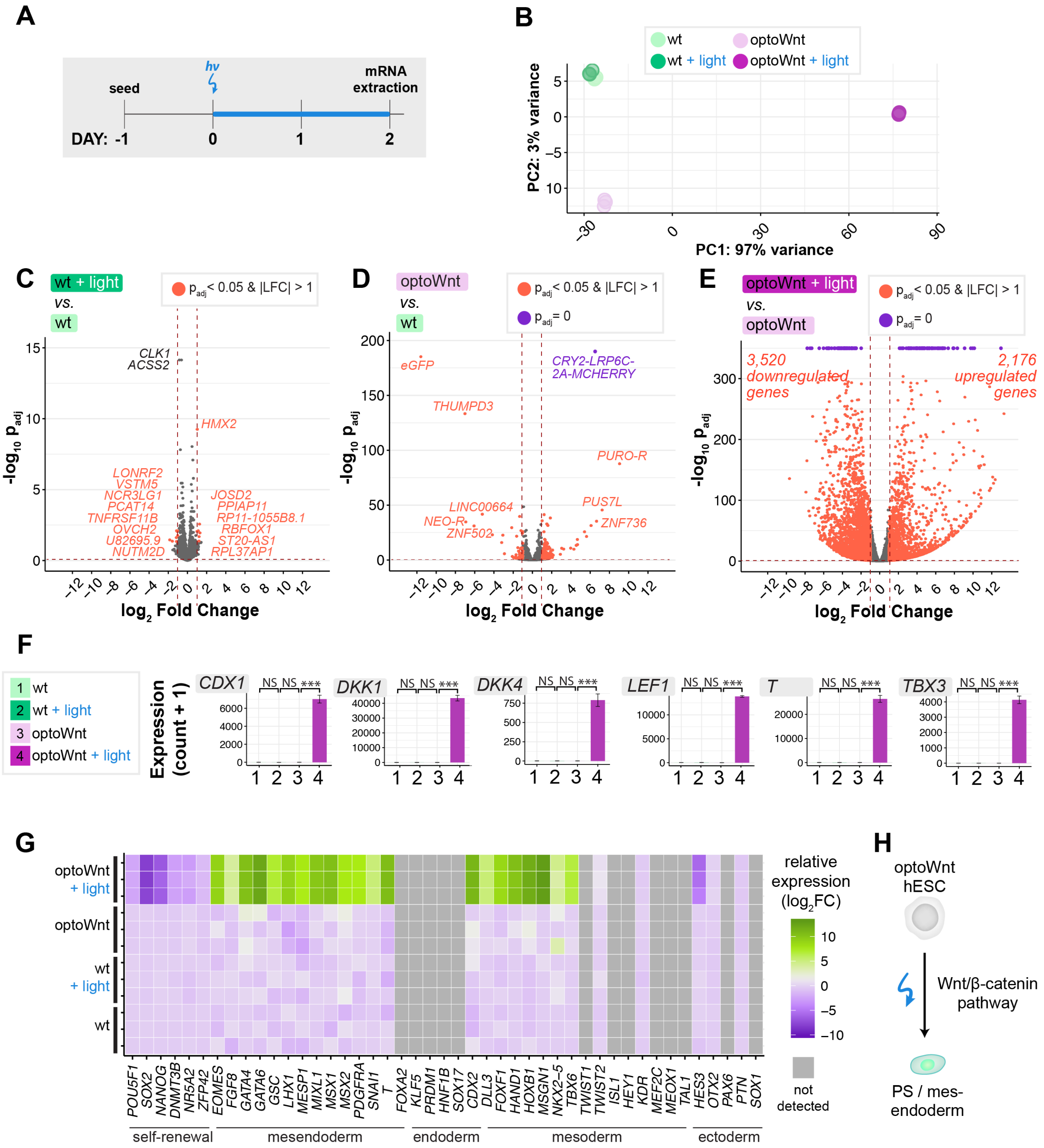

Figure 4.5: **RNA-seq of optoWnt hESCs shows mesendoderm differentiation, low phototoxicity, and low optoWnt dark-state activity**
A) Schematic of experimental timeline. WT and optoWnt cells were kept in the dark or illuminated at 0.8 $\mu W mm^{-2}$ for 48 hrs. **B)** PCA of RNA-seq results. Colors designate the four experimental conditions. Each point is a biological replicate. *Caption continued on next page*

Figure 4.5: **C-E)** Volcano plots of RNA-seq differential expression analysis, with DEGs (adjusted p-value < 0.05 and log_2 fold change > 1) highlighted red and DEGs saturated at $p = 0$ highlighted purple. (C) Illuminated WT vs. unilluminated WT hESCs (phototoxicity control); (D) unilluminated optoWnt vs. unilluminated WT hESCs, (dark-state activity control); (E) illuminated optoWnt vs. unilluminated optoWnt hESCs. **F)** β-catenin target gene expression. ANOVA followed by Tukey test. Graphs show mean expression (read counts + 1) ± 1 s.d., n = 3 biological replicates. **G)** Heat map of log_2 fold change in lineage markers normalized to WT hESC expression level. Biological replicates displayed for each condition, with undetected genes (read count < 150) shown in grey. **H)** Schematic of light-induced mesendoderm differentiation.

In contrast, optoWnt stimulation induced a broad transcriptional effect, with ~5,500 differentially expressed genes between the dark and illuminated conditions (Figure 4.5E). Direct β-catenin target genes, such as CDX1, DKK1, T, and TBX3, are among the most differentially expressed genes, all with a log fold change (LFC) of $\sim 9-13$ (Figure 4.5F), Figure 4.6A-B). To determine whether optoWnt stimulation induced hESC differentiation along a mesendoderm lineage, we analyzed transcriptional changes in fate markers associated with embryonic germ layer specification (Figure 4.5G, Figure 4.6C-E). OptoWnt stimulation for 48 hrs induced strong upregulation of the primitive streak and mesendoderm markers T, EOMES, MIXL1, GATA6, MSX1, and GATA4 with a corresponding decrease in self-renewal markers POU5F1, SOX2, and NANOG. Endodermal markers, such as FOXA2 and SOX17, and ectodermal markers, such as SOX1 and PAX6, remained low or were downregulated. Conversely, certain mesodermal markers, such as TBX6, FOXF1, and HOXB1, were upregulated consistent with the role of Wnt in inducing mesoderm differentiation in the absence of high TGFβ signaling (*33*). In summary, global RNA sequencing analysis confirmed that optogenetic stimulation of optoWnt hESCs induced robust mesendoderm differentiation with undetectable phototoxicity, low background activity, and large dynamic range (Figure 4.5H).

Figure 4.6: **Validation of RNA-seq study of optoWnt-induced hESC differentiation**
A) RNA-seq results of indicated genes that mark WT (eGFP+, Neomycin-resistant) and optoWnt (Cry-LRP6c-2A-mCherry+, Puromycin-resistant) cells. Graphs show mean expression (read count + 1) ± 1 s.d., n = 3 biological replicates. **B)** Top upregulated (red) and downregulated (grey) genes in illuminated optoWnt vs. unilluminated optoWnt hESCs. Graph shows mean log_2 fold change for each indicated gene. **C)** Heat map of mRNA expression (read count + 1) of indicated lineage markers. Biological replicates displayed for each condition, with undetected genes (read count $<$ 150) shown in grey. **D)** qPCR validation of RNA-seq results with indicated lineage markers and comparison to CHIR (3 μM) treatment. Graphs show mean fold change ± 1 s.d., n = 3 biological replicates. ANOVA followed by Tukey test. **E)** Heat map of mean log_2 fold change in lineage markers normalized to WT expression level, from qPCR data shown in (d).

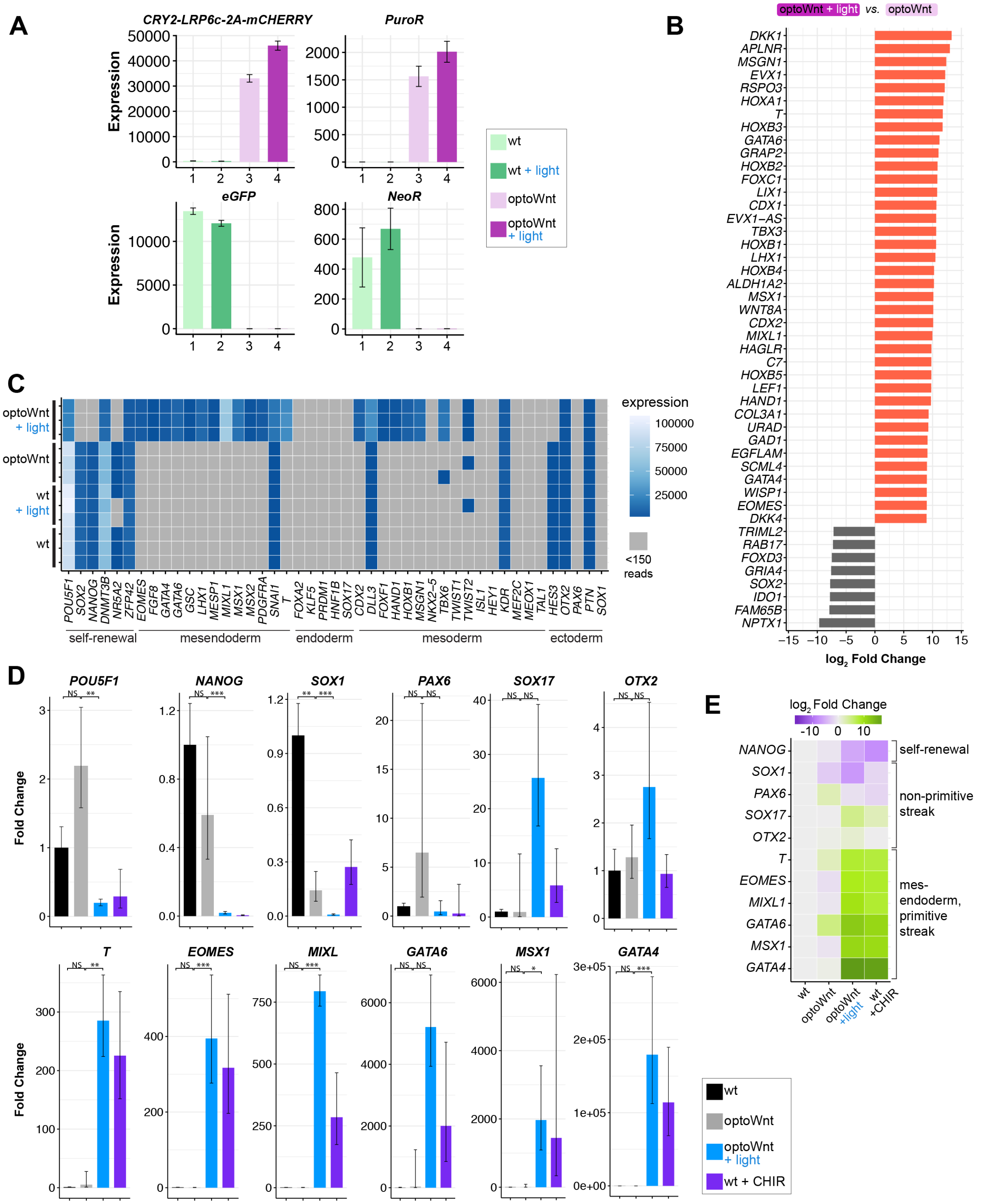

Figure 4.6: *See caption on previous page*

4.2.3 Wnt signaling is sufficient for inducing cell self-organization in 2D and 3D hESC culture

Equipped with a method for optogenetic control of Wnt signaling, we investigated whether Wnt signaling is sufficient for inducing cell self-organization. Specifically, optoWnt and WT hESCs were mixed into a 1:1 heterogeneous culture such that illumination would activate Wnt signaling in only the optoWnt subpopulation of an hESC colony (Figure 4.7A). Kept in the dark, the mCherry-positive optoWnt hESCs remained heterogeneously mixed with WT hESCs. Strikingly, illuminated co-cultures showed a strong segregation between the two cell populations, where optoWnt and WT cells separated and created sharp boundaries between the two resulting domains (Figure 4.7B, Figure 4.8A-B). This was a surprising observation as spontaneous Wnt activation has been reported in mESC gastrulation models but did not appear to cause a distinct spatial segregation between cell populations (*21*, *29*). In addition to segregating, axial cross-sections showed that WT cells remained in an epithelial monolayer. However, optoWnt cells piled into vertical stacks up to ∼60 μm in height, apparently minimized contact area with WT cells by forming steep boundaries at domain edges, and displayed a mesenchymal morphology with increased cell protrusions and scattering of single cells from hESC colonies (Figure 4.7B, Figure 4.8C-D). In contrast, in illuminated monocultures optoWnt cells piled vertically only in certain regions and with less defined boundaries (Figure 4.8E). We tested different optoWnt:WT seeding ratios to determine whether there existed an optoWnt dosage threshold for segregation, but we observed clear segregation at all seeding ratios (Figure 4.9).

We quantified the extent of segregation by counting the cell neighbors of optoWnt (mCherry+) cells (Figure 4.7C, Figure 4.8F-G). If the two populations were fully mixed in a 1:1 ratio, the percentage of ‘like’ (i.e. mCherry+) neighbors for each optoWnt cell would average 50%, whereas if the two populations were perfectly segregated, the percentage of ‘like’ neighbors (for optoWnt cells away from population boundaries) would be 100%. Dark co-cultures remained well-mixed with a wide distribution of neighbor counts that were slightly skewed toward higher ‘like’ neighbor percentages, reflecting the clonal expansion that occurs over the 3-day experiment duration (Figure 4.7C). In contrast, illuminated co-cultures displayed a ∼4-fold higher level ($p < 0.001$) of optoWnt cells that were entirely surrounded by cells of their own kind, a result consistent with cell segregation (Figure 4.7C-D). Strong segregation was observed in all culture media conditions tested, including basal media lacking pluripotency factors like FGF2 and TGFβ, suggesting that Wnt signaling alone is sufficient to drive the observed cell self-organization (Figure 4.10A-E).

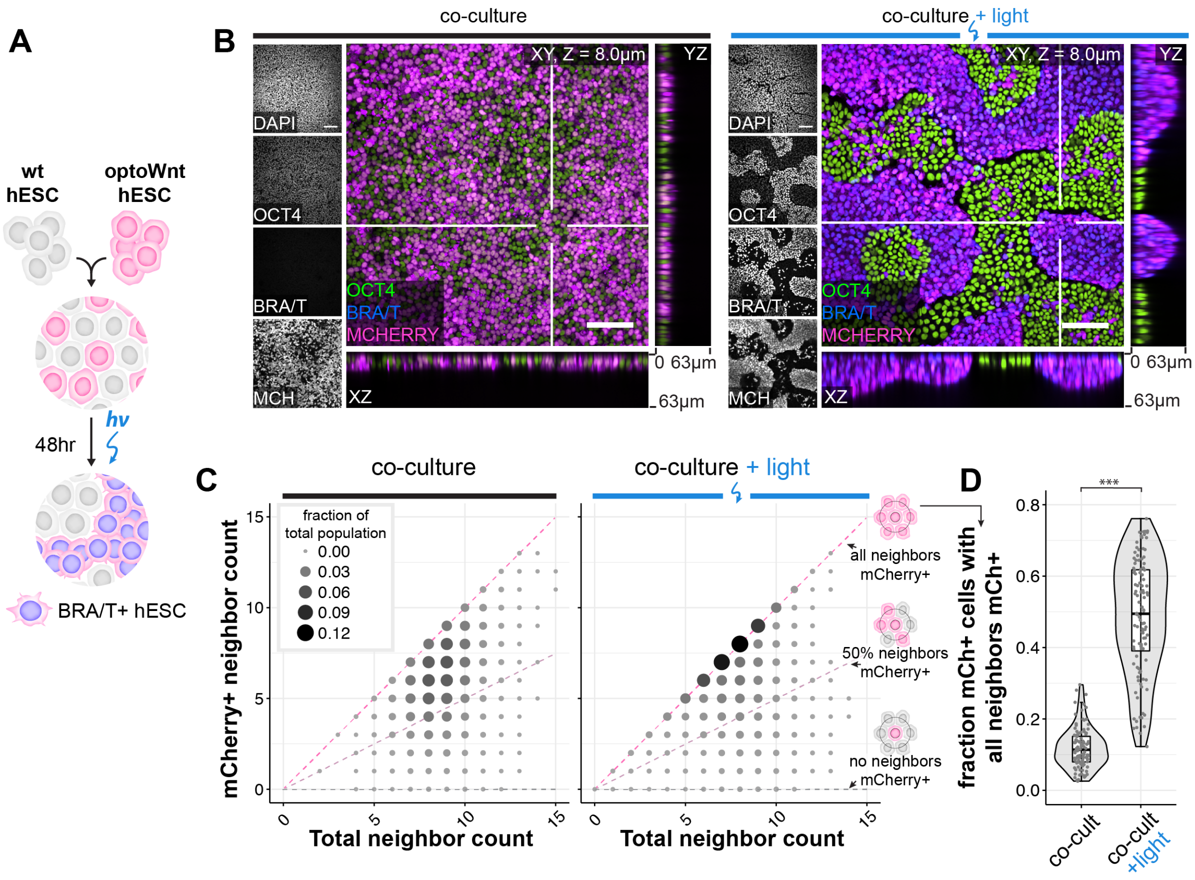

Figure 4.7: **Cell self-organization upon optoWnt stimulation of cell subpopulations** **A)** Schematic of experimental setup of optWnt/WT hESC co-cultures in 2D culture. **B)** Confocal images of optWnt/WT co-cultures in the dark (left panel) and after 48 hrs illumination (right panel), stained for OCT4 and BRA/T. OptoWnt cells are labelled with mCherry (mCh) expression. Scale bar 100 μm, YZ and XZ axial cross-sections shown through indicated slices (white lines), 64 μm in height. **C)** Cell neighbor analysis of optoWnt (mCh+) cells kept in the dark (left) or illuminated for 48 hrs (right). Graph shows the count of total cell neighbors vs. count of mCh+ cell neighbors across total population of analyzed mCh+ cells (95,685 cells analyzed, pooled analysis from n = 3 biological replicates). Area and color of points is proportional to the fraction of total population. Constant ratios of mCh+ to total neighbors are highlighted with pink and grey lines. **D)** Quantification of fraction of optoWnt (mCh+) cells whose neighbors are all mCh+. Each point represents an analyzed field of view (108 fields of view analyzed, n = 3 biological replicates). Unpaired two-samples Wilcoxon test ($p < 2.2$ x 10-16).

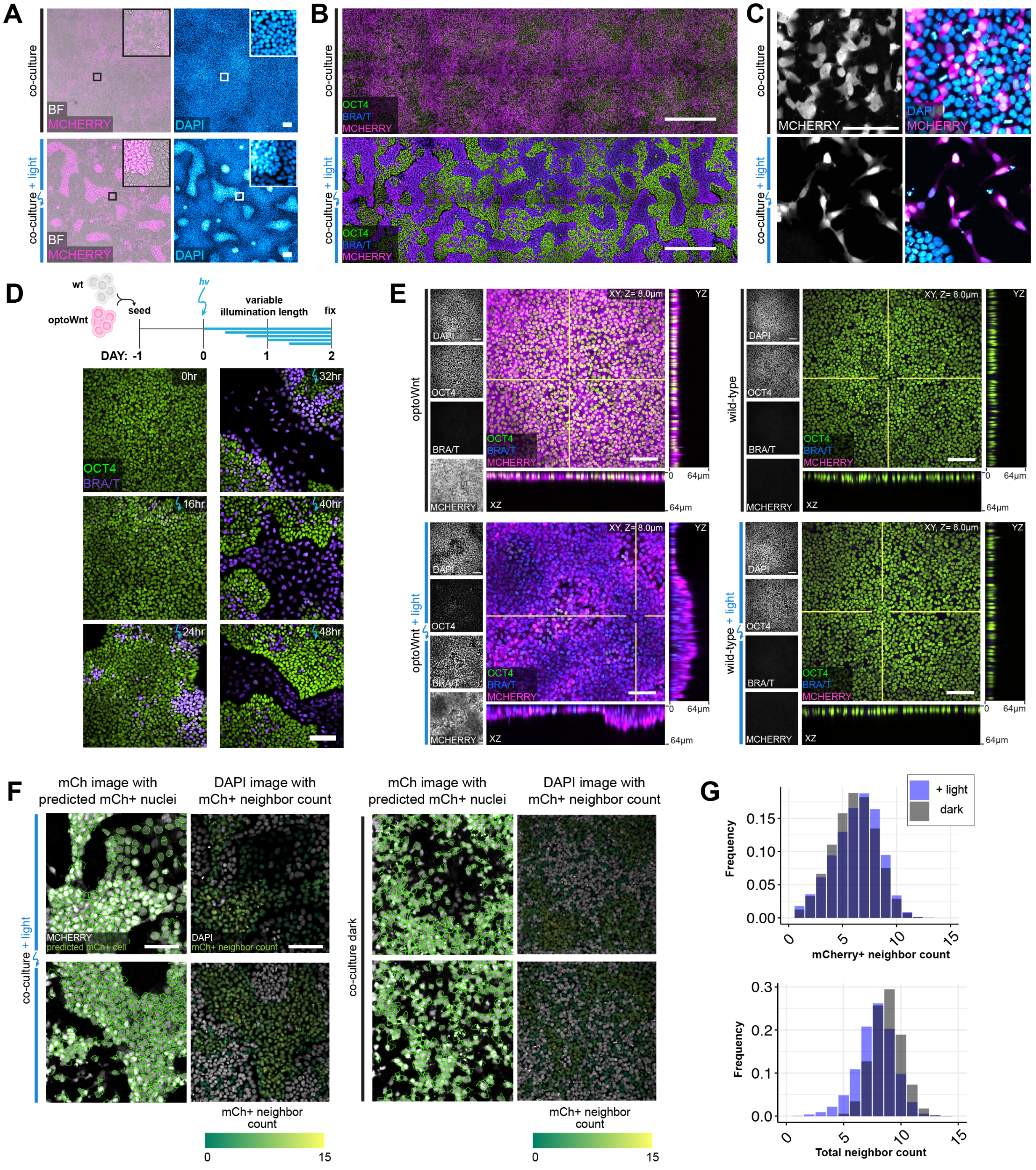

Figure 4.8: **Quantification of cell self-organization upon optoWnt stimulation of cell subpopulations**

A) Representative images of brightfield (BF), mCherry fluorescence (expressed in optoWnt cells), and DAPI nuclear stain of fixed optoWnt/WT co-cultures in the dark (top panel) after 48 hrs of illumination (bottom panel). Scale bar 100 μm. *Caption continued on next page*

Figure 4.8: **B)** Stitched images of optoWnt/WT co-cultures show large-scale pattern of cell self-organization. Scale bar 500 μm. **C)** Representative image of optoWnt/WT co-cultures seeded at lower cell density (20k cell cm-2) show single-cell scattering and morphology changes in optoWnt (mCh+) cells after 48 hrs illumination. Scale bar 100 μm. **D)** Representative fluorescence images of optoWnt/WT co-cultures after indicated durations of illumination, stained for OCT and BRA/T. Scale bar 100 μm. **E)** Confocal images of optoWnt monocultures (left panels) and WT monocultures (right panels) in the dark or after 48 hrs illumination, stained for OCT4 and BRA/T. OptoWnt cells labelled with mCh. Scale bar 100 μm, YZ and XZ axial cross-sections shown through indicated slices (white lines), 64 μm in height. **F)** Sample images of cell neighbor analysis in CellProfiler of illuminated (left panel) and dark (right panel) co-cultures. Nuclear outline of mCh+ nuclei (green) overlaid on mCh channel image (left column). DAPI channel image (right column) shown with overlay of mCh+ nuclei colored by mCh+ positive neighbor count. Scale bar 100 μm. **G)** Histogram of total cell neighbor counts (bottom) and mCh+ cell neighbor counts (top) across all analyzed cells show comparable cell densities between light and dark conditions.

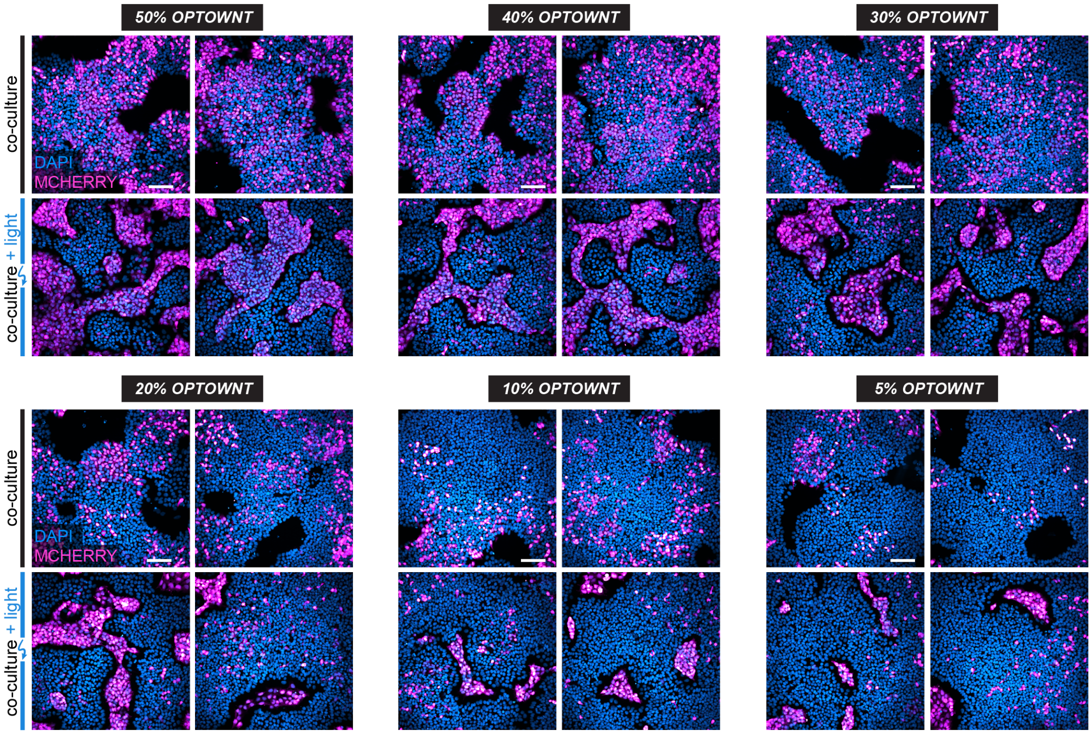

Figure 4.9: **Cell self-organization evident at variable dosages of optoWnt cells in optoWnt/WT co-cultures**

A) Representative fluorescence images of optoWnt/WT co-cultures at indicated seeding doses (e.g. 40% optoWnt indicates 2:3 ratio of optoWnt:WT cells). OptoWnt cells are mCh+. Scale bar 100 μm.

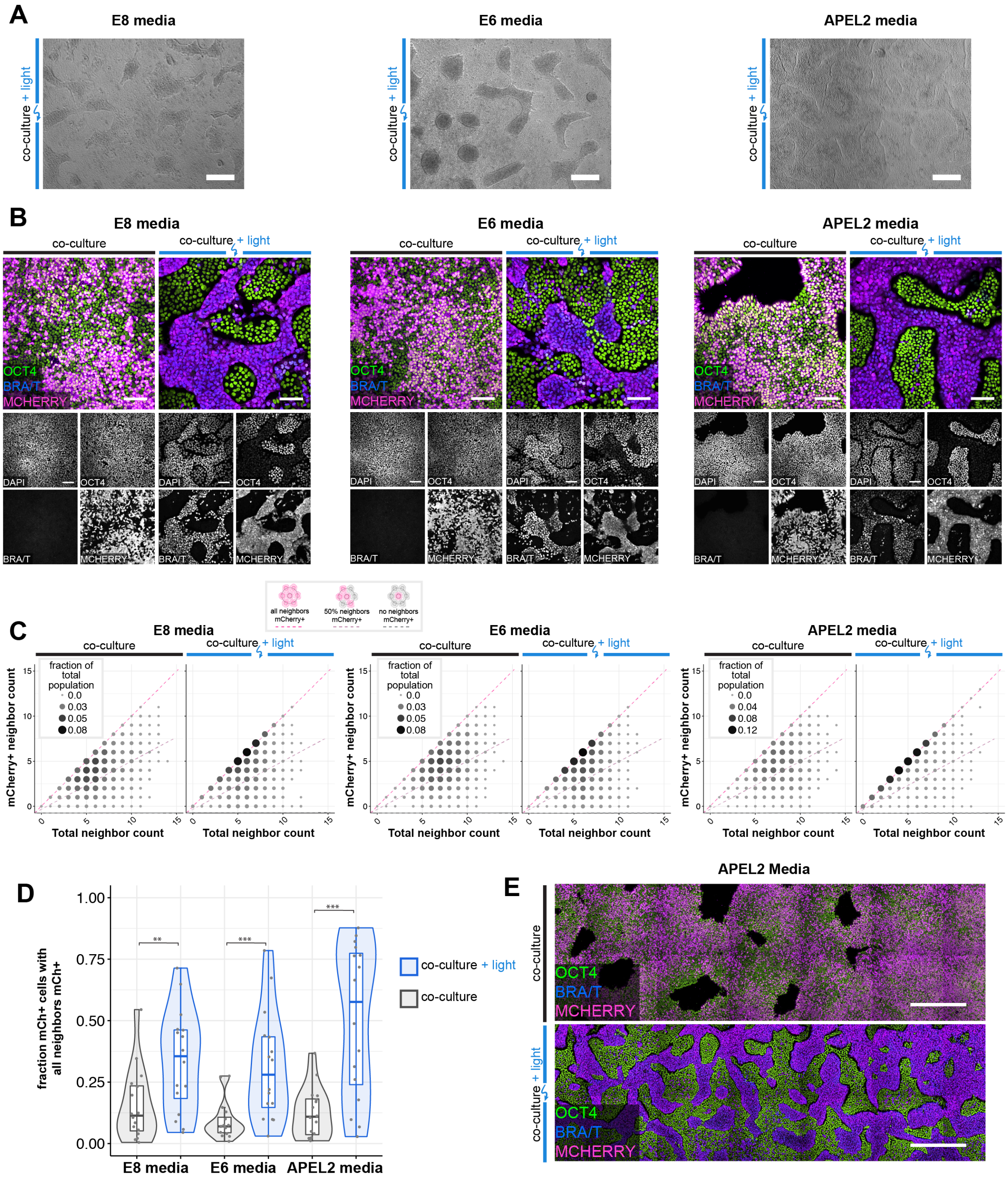

Figure 4.10: *See next page for caption*

Figure 4.10: **Cell self-organization occurs in media without FGF and TGFβ agonists** **A)** Representative brightfield images of optoWnt/WT co-cultures after 48 hrs illumination in E8, E6, and APEL2 media. Scale bar 250 μm. **B)** Confocal images of optoWnt/WT co-cultures in indicated media conditions, stained for OCT4 and BRA/T. OptoWnt cells labelled with mCh. Scale bar 100 μm. **C)** Cell neighbor analysis of optoWnt (mCh+) cells in co-culture. Graph shows count of total cell neighbors vs. count of mCh+ cell neighbors across total population of analyzed mCh+ cells (25,742 cells analyzed, pooled analysis from n=3 biological replicates for each condition). Area and color of points is proportional to the fraction of total population. Constant ratios of mCh+ to total neighbors are highlighted with pink and grey lines. **D)** Quantification of fraction of optoWnt (mCh+) cells whose neighbors are all mCh+. Each point represents an analyzed field of view (16 fields of view analyzed per condition, n=3 biological replicates). Unpaired two-samples Wilcoxon test (pE8 = 0.011 ; pE6 = 3.3 x 10-4 ; pAPEL2 = 3.9 x 10-4). **E)** Stitched images of optoWnt/WT co-cultures in APEL2 media show large-scale pattern of cell self-organization. Scale bar 500 μm.

Self-organization also occurred in three dimensions (3D) when co-cultures of WT and optoWnt hESCs were grown as spheroid aggregates (Figure 4.11A). In the dark, WT and optoWnt cells were uniformly distributed throughout the spheroid surrounding a central lumen, as previously observed (*56*) (Figure 4.11B). After illumination, however, spheroids displayed a striking difference in morphology, with a subpopulation of cells that organized radially outward from the central lumen, preserving radial symmetry of the aggregate. Fluorescent labelling of the two cell populations showed that the outer layer of cells was composed of optoWnt cells, while the inner, central lumen was composed of WT cells (Figure 4.11C, Supplementary Video 1). Quantification of the radial distribution of WT (dsRed+) and optoWnt (mVenus-NLS+) cells confirmed segregation of the two populations, as shown by the shift in optoWnt fluorescence toward the spheroid periphery as well as compaction of the WT radial distribution (Figure 4.11D-E). Furthermore, illuminated optoWnt cells developed cell protrusions that dynamically interacted with the surrounding gel matrix (Supplementary Video 1). These results suggest that the lumenized core of WT cells retained an epithelial phenotype, whereas optoWnt cells obtained a mesenchymal morphology. Such observed self-organization is consistent with the 2D culture results and is reminiscent of the morphogenetic movements of mammalian gastrulation, where mesendoderm similarly segregates radially outward from an epithelial cell layer (*57*).

4.2.4 Self-organization occurs through optogenetic induction of epithelial to mesenchymal transition and cell migration

A key component of embryonic patterning is the coordinated movement of cell populations. Cells of the primitive streak undergo an EMT (*14*, *58*), a process regulated at least in part by Wnt signaling as mouse embryos mutant in Wnt3 or β-catenin do not ingress or form a primitive streak (*8*, *59*). To determine whether optoWnt activation is sufficient for EMT induction, we assayed for hallmarks of EMT upon light stimulation (Figure 4.12A).

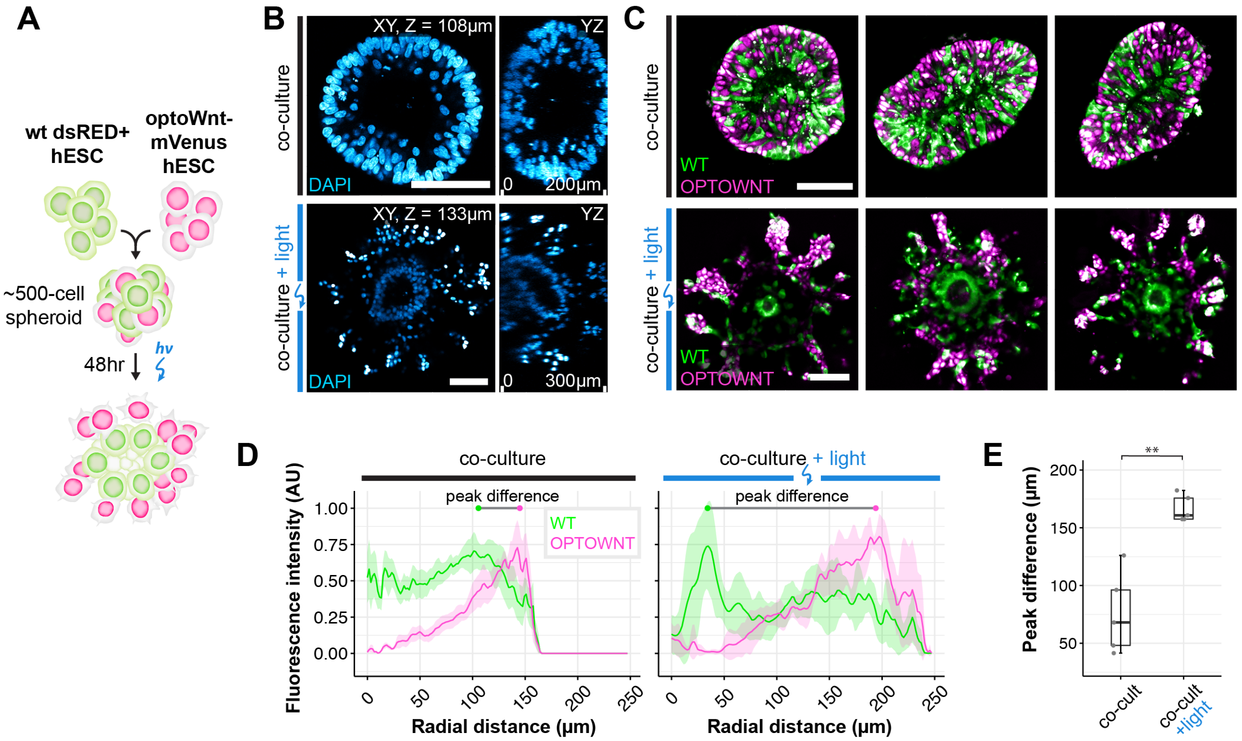

Figure 4.11: **OptoWnt-induced cell self-organization in hESC spheroids**
A) Schematic of experimental setup of optoWnt/WT co-cultures in 3D spheroid cultures. **B)** Two-photon imaging of co-cultures kept in the dark (top) and after 48 hrs illumination (bottom) with DAPI staining of cell nuclei. Scale bars 100 μm, YZ axial cross-sections 200 μm in height. **C)** Two-photon imaging of co-cultures kept in the dark (top) and after 48 hrs illumination (bottom). WT cells are labelled with dsRed, optoWnt cells are labelled with mVenus-NLS expression. Scale bars 100μm. **D)** Radial quantification of cell segregation in 3D spheroids. Normalized intensity of mean fluorescence signal is graphed as a function of radial distance from spheroid center. Graph shows mean of $n = 5$ spheroids, ± 1 S.E.M. **E)** Radial distance between peak intensities of WT and optoWnt fluorescence distribution, i.e. 'peak difference', labelled in (h). Unpaired two-samples Wilcoxon test ($p = 0.0079$), $n = 5$ spheroids.

Global RNA sequencing showed EMT-associated transcriptional changes upon illumination (Figure 4.12B). In particular, E-cadherin (CDH1) levels markedly decreased after 48hrs of illumination while N-cadherin (CDH2) levels increased, a switch in cell adhesion proteins characteristic of EMT (*58*). In addition, other indicators of EMT such as cytoskeletal protein Vimentin (VIM) and E-cadherin transcriptional repressors Snail and Slug (SNAI1, SNAI2) were upregulated. Similar trends were observed at the transcriptional level through qPCR and at the protein level with immunostaining for E- and N-cadherin (Figure 4.13A-C). These results confirmed that EMT was occurring in response to optoWnt activation.

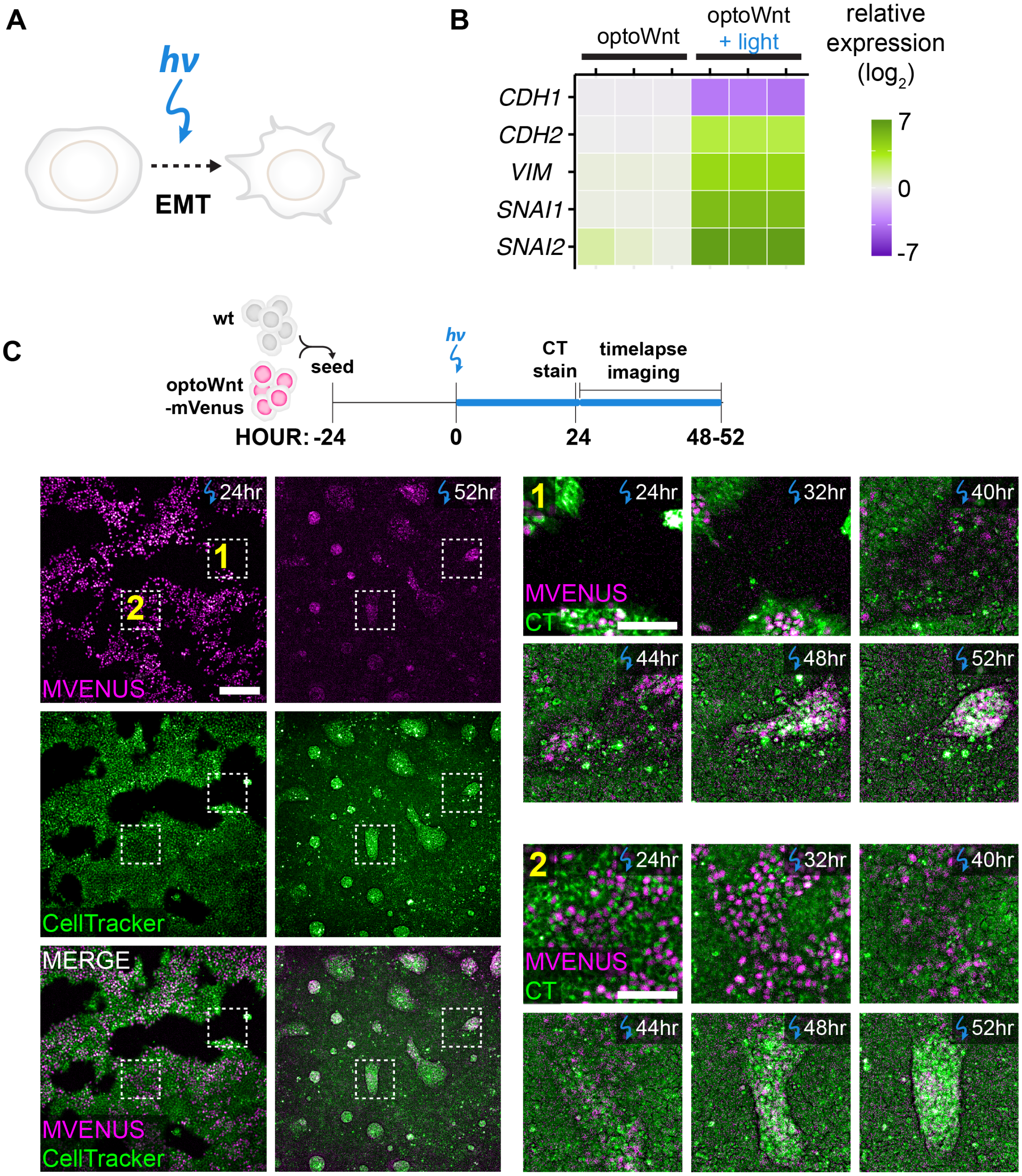

Figure 4.12: **Cell self-organization is mediated by Wnt-induced cell migration and EMT** **A)** Schematic of optogenetic induction of EMT **B)** RNA-seq heat map of log_2 fold change in EMT marker genes normalized to mean gene expression of WT hESCs. Biological replicates displayed for each condition. **C)** Live-cell timelapse fluorescence imaging of 2D optoWnt/WT co-cultures during optogenetic stimulation at indicated time points. OptoWnt cells are labelled with mVenus-NLS expression, all cells are labelled with CellTracker (CT) dye. Zoom in (right) of regions 1 (cell aggregation outside hESC colony) and 2 (cell aggregation inside hESC colony) at indicated time points. Scale bar 250 μm (left), 100 μm (zoom in).

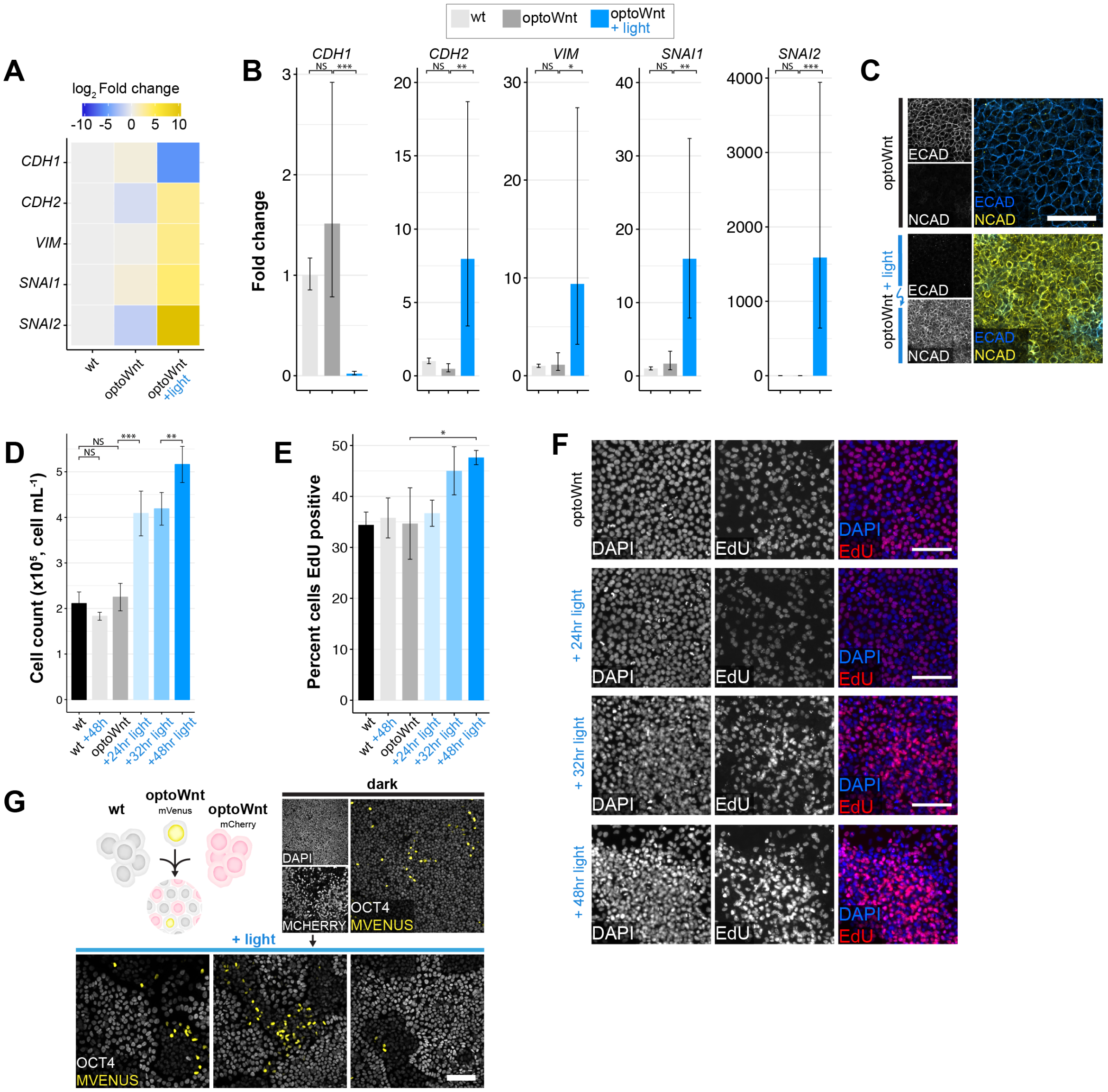

Figure 4.13: **EMT and increased cell proliferation upon optoWnt stimulation**
A-B) qPCR for EMT markers in WT and optoWnt hESC monocultures cultured in APEL2 media. Graphs show heatmap of mean log_2 fold change (A) and mean fold change (B) over WT hESCs ± 1 s.d., n = 3 biological replicates. ANOVA followed by Tukey test. **C)** Representative images of immunostaining for ECAD and NCAD in unilluminated (top) and illuminated (bottom) optoWnt cells. Scale bar 100 μm. **D)** Endpoint cell count of optoWnt cells after indicated illumination duration. Graph shows mean ± 1 s.d., n=3 replicates. ANOVA followed by Tukey test. **E-F)** EdU stain of optoWnt cells after indicated illumination duration, with quantification of percent EdU+ cells (E) and representative images of EdU staining (F). Graph shows mean ± 1 s.d., n=3 replicates. ANOVA followed by Tukey test. Scale bar 100 μm. **G)** No observed clonal expansion of optoWnt cells. Scale bar 100 μm.

EMT is often accompanied by a migratory cell phenotype (*13, 19, 58*). As clear segregation of cell populations was observed upon optoWnt activation of hESC co-cultures, we analyzed the specific role that cell migration may play during the apparent EMT occurring in this self-organization process. We thus performed live-cell timelapse imaging during optogenetic stimulation, in contrast to endpoint analysis, to determine whether cell migration was driving the observed self-organization. Timelapse imaging of 2D cultures showed that optoWnt cells became increasingly migratory and led to visible aggregation after 30-40 hrs of illumination (Figure 4.12C, Supplementary Video 2). We observed that segregation resulted from both (1) cells migration out of the epithelial hESC colonies and aggregation in the empty space between colonies and (2) cells migration and aggregate formation within the colony (Figure 4.15A, Supplementary Video 2-3). Once formed, the dynamic behavior of aggregates was particularly striking, with aggregates migrating rapidly as a group, merging with nearby aggregates, or detaching from the plate surface entirely (Supplementary Video 4). We considered whether apparent segregation could be mediated by an increased proliferation of a rapidly expanding subpopulation of optoWnt cells, but we observed no evidence of such expansion in proliferation and imaging studies (Figure 4.13D-G).

To quantify changes in cell migration upon optoWnt stimulation, we performed single-cell tracking of optoWnt hESCs expressing a nuclearly-localized mVenus (mVenus-NLS) fluorescent tag grown in 2D co-culture with WT hESCs (Figure 4.14A-C). During the first 24 hrs of illumination, optoWnt hESCs showed no change in cell migration speed, velocity, or mean-squared displacement (MSD); however, within the ∼24-32 hr time window these metrics increased ∼2-fold, confirming that cells gain a migratory phenotype upon Wnt stimulation (Figure 4.15B, Figure 4.16A-C). After ∼32 hrs of illumination, both MSD and velocity were observed to plateau and then decline in response to aggregation of optoWnt cells, reflecting the increasing role of cellular confinement in determining migration dynamics. Indeed, these time scales align with the emergence of segregation following ∼40 hr of illumination (Figure 4.12C, Figure 4.8D). The ratio of cell displacement over distance and the percentage of time a cell migrated without turning remained constant over time (Figure 4.16D,I-J), indicating that cells did not increase directionality of their migration. We also observed a large heterogeneity in mean cell migration velocities across the cell population and binned cells into three groups (slow, medium, fast) based on their mean velocity (Figure 4.16E-H). Over time, the velocity and speed for each group increased but cells maintained their individual migration heterogeneity (Figure 4.15C). In summary, these findings support the conclusion that Wnt drives self-organization of differentiating mesendoderm and hESCs through changes in cell migration.

To confirm that self-organization was driven in an EMT-dependent manner, we performed genetic knockdown of target genes in optoWnt hESCs. We found that knockdown of SNAI1 (encoding SNAIL protein), a regulator of EMT, reduced the segregation capacity of optoWnt and WT co-cultures, whereas knockdown of SNAI2 (encoding SLUG protein) had no detectable effect (Figure 4.15D, Figure 4.17). Interestingly, these results mimic the phenotype of knockout mice deficient in Snai1, which die at gastrulation due to failure to undergo EMT and mesoderm formation (*60*), in contrast to Snai2-deficient mice, which

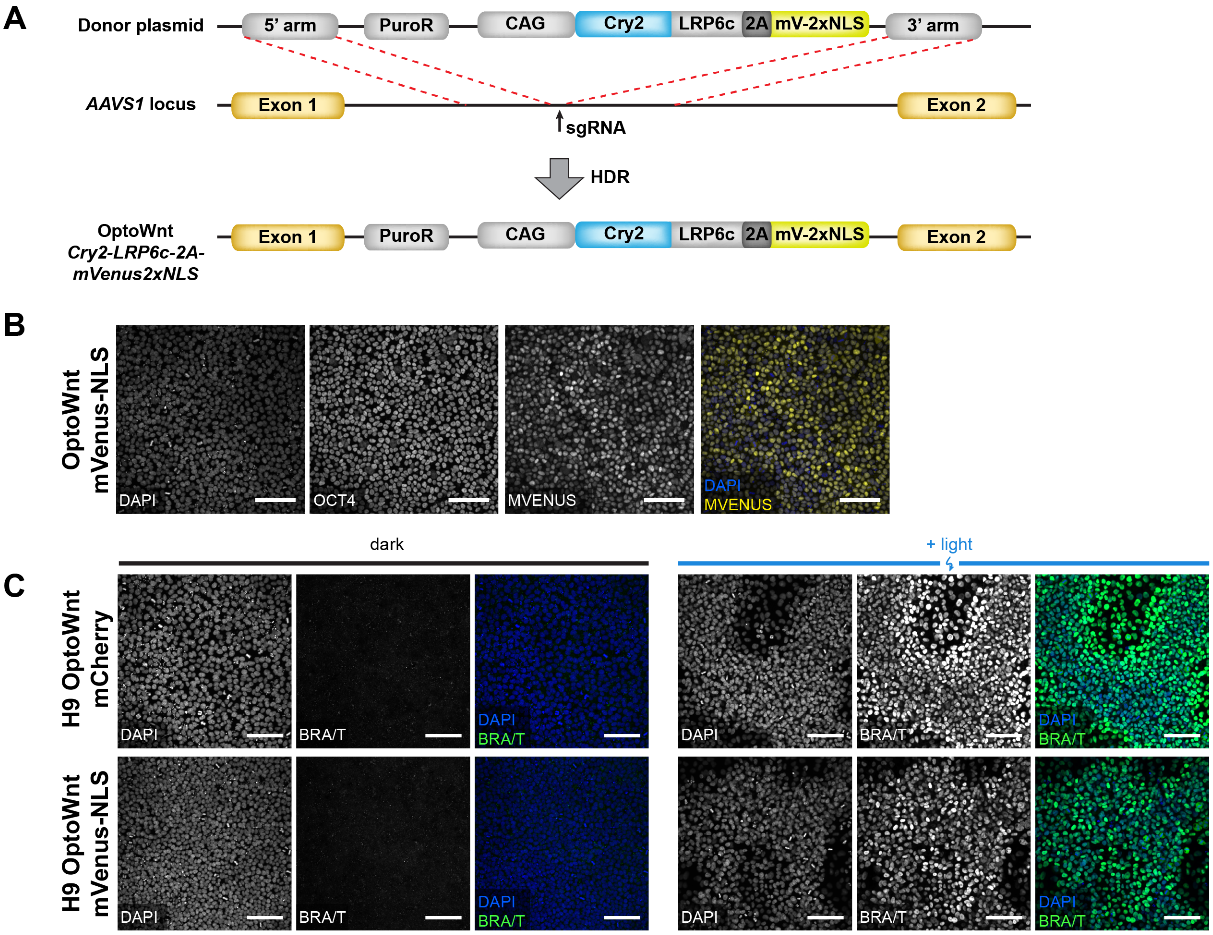

Figure 4.14: **Characterization of optoWnt-mVenus-NLS hESC line**
A Schematic diagram of knock-in strategy at the AAVS1 locus. **B)** Representative images of immunostaining for OCT4 and mVenus in optoWnt-mVenus-NLS hESCs in routine cell culture, kept in the dark. Scale bar 100 μm. **C)** Light-induced BRA expression of optoWnt-mVenus-NLS line is comparable to optoWnt-mCherry line. Scale bars 100 μm.

remain viable (*61*). This finding suggests that EMT is required for the observed segregation. In conclusion, we show that differential Wnt signal activation can lead to emergence of organized shape and structure through cell migration and EMT.

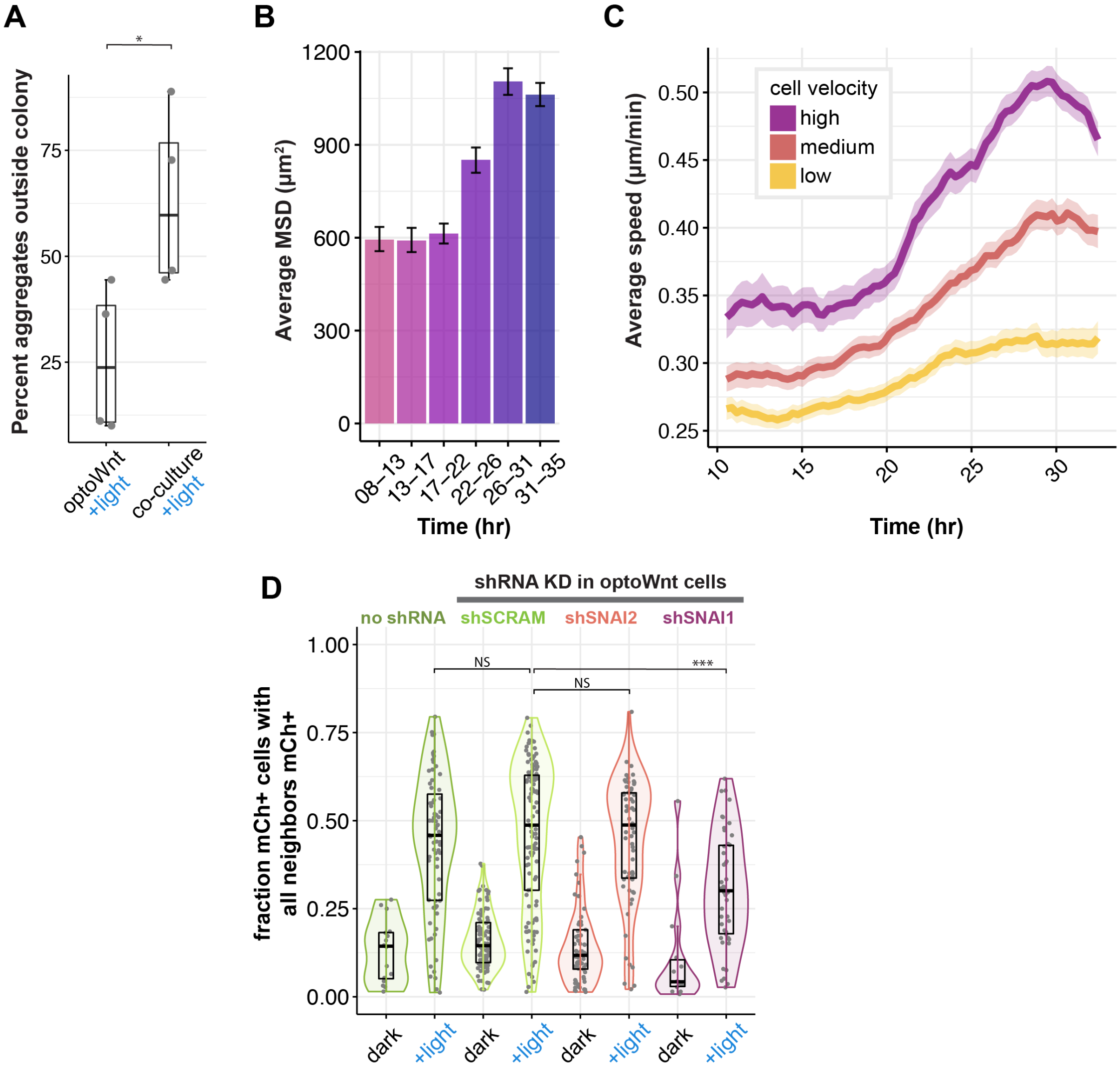

Figure 4.15: **Single-cell imagining of self-organization shows Wnt-induced cell migration** **A)** Percentage of aggregates forming outside of hESC colonies (as shown in region 1) over total formed aggregates. Graph shows analysis of n = 4 fields of view, ANOVA followed by Tukey test (p = 0.034). **B)** Average mean squared displacement (MSD) of single-cell trajectories of optoWnt cells in optoWnt/WT co-cultures at indicated time intervals after onset of light stimulation. Graph shows mean (>1,000 tracks over 5 fields of view) ± 95% confidence interval. **C)** Average cell speed over time of optoWnt single-cell trajectories binned by median cell velocity (low: 0-0.15 $\mu m min^{-1}$; medium: 0.15-0.18 $\mu m min^{-1}$; high: 0.18-0.6 $\mu m min^{-1}$). Graph shows mean ± 95% confidence interval. **D)** Neighbor analysis of optoWnt/WT co-cultures following shRNA knockdown of EMT regulators SNAI1 and SNAI2 in optoWnt cells. Quantification of fraction of optoWnt (mCh+) cells whose neighbors are all mCh+ in co-cultures kept in the dark or illuminated for 48 hrs. Each point represents an analyzed field of view (>16 fields of view analyzed per condition, n = 3 biological replicates). Unpaired two-samples Wilcoxon test (p = 0.00027).

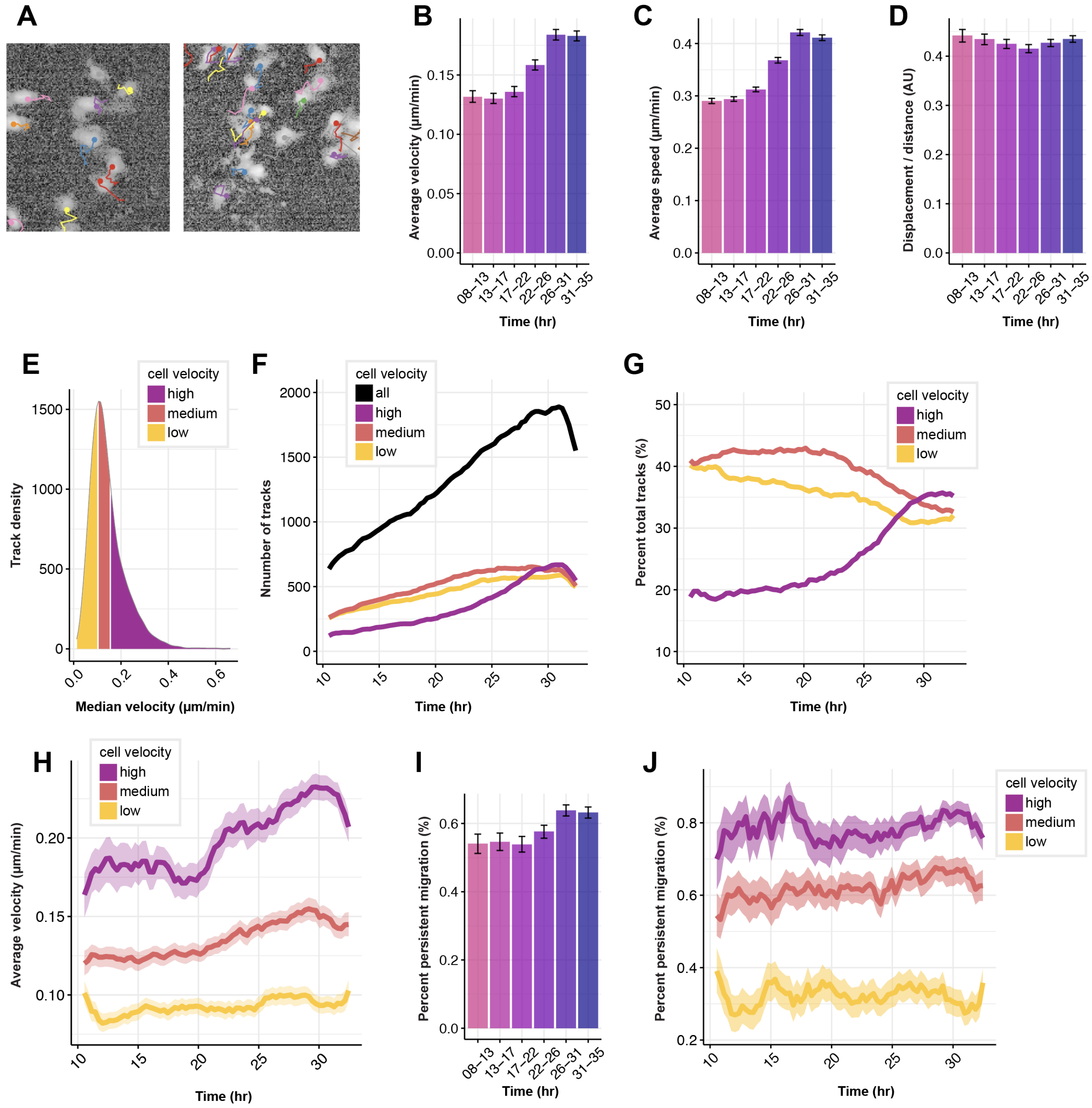

Figure 4.16: **Single-cell tracking of optoWnt cells in optoWnt/WT co-cultures shows increased cell migration and no change in cell persistence**

A Representative images of single-cell trajectories of mVenus-NLS+ optoWnt cells. Track color distinguishes different cells in field of view. **B)** Average cell velocities at indicated time intervals after onset of light stimulation. Graph shows mean (>1,000 tracks over 5 fields of view) ± 95% confidence interval. **C)** Average cell speed at indicated time intervals after onset of light stimulation. Graph shows mean (>1,000 tracks over 5 fields of view) ± 95% confidence interval. *Caption continued on next page*

Figure 4.16: **D)** Average ratio of cell displacement over distance at indicated time intervals after onset of light stimulation. Graph shows mean (>1,000 tracks over 5 fields of view) ± 95% confidence interval. **E)** Distribution of median cell velocities across all cell tracks. Tracks were binned into three equal groups by median velocity (low: 0-0.15 $\mu m min^{-1}$; medium: 0.15-0.18 $\mu m min^{-1}$; high: 0.18-0.6 $\mu m min^{-1}$) as indicated. **F)** Number of tracks in each median velocity bin over time. **G)** Tracks in each velocity bin over time, shown as percentage of total tracks. **H)** Average cell velocity over time, binned by median cell velocity. Graph shows mean ± 95% confidence interval. **I)** Average percent of cells undergoing persistent migration at indicated time intervals. Graph shows mean percentage ± 95% confidence interval. **J)** Average percent of cells undergoing persistent migration over time, binned by median cell velocity. Graph shows mean percentage ± 95% confidence interval.

Figure 4.17: **Gene knockdown of EMT regulator SNAI1 in optoWnt cells shows decreased cell self-organization in 2D co-cultures**
A Western blot (left) for SLUG protein levels in indicated WT and optoWnt cell lines in response to shRNA knockdown. Cell lines labelled +FACS designates that lines were sorted for GFP+ expression, which marks cells infected with shRNA construct. WB quantification (right), normalized to β-actin loading control. The optoWnt line expressing shRNA snai2 #2 (+FACS) was used for subsequent experiments. **B)** Western blot (left) for SNAIL protein levels in indicated WT and optoWnt cell lines in response to shRNA knockdown. WB quantification (right), normalized to β-actin loading control. shRNA snai1 #1 (+FACS) was used for subsequent experiments. **C)** Representative images of 2D optoWnt/WT co-cultures (left column) in the dark and after 48 hrs illumination. OptoWnt cells express scrambled shRNA (shSCRAM, top panel) or SNAI1 shRNA (shSNAI1, bottom panel). mCherry fluorescence marks optoWnt cells, GFP nuclear fluorescence marks WT cells. Sample images from cell neighbor analysis in CellProfiler (right column) show nuclear outline of mCh+ cells (green) overlaid on mCh channel image. Scale bar 100 μm. **D)** Cell neighbor analysis of optoWnt (mCh+) cells in optoWnt-shSCRAM/WT or optoWnt-shSNAI1/WT co-cultures kept the dark or illuminated for 48 hrs. Graph shows the count of total cell neighbors vs. count of mCh+ cell neighbors across total population of analyzed mCh+ cells (72,338 cells analyzed, pooled analysis from n=3 biological replicates). Area and color of points is proportional to the fraction of total population. Constant ratios of mCh+ to total neighbors are highlighted with pink and grey lines. **E)** Quantification of fraction of optoWnt (mCh+) cells whose neighbors are all mCh+ in optoWnt-shSCRAM/WT and optoWnt-shSNAI1/WT co-cultures. Each point represents an analyzed field of view (72 fields of view analyzed, n=3 biological replicates). Unpaired two-samples Wilcoxon test (p = 0.0033). **F)** Histogram of total cell neighbor counts (bottom) and mCh+ cell neighbor counts (top) across all analyzed cells show comparable cell densities between light and dark conditions, as well as between optoWnt-SCRAM/WT and optoWnt-SNAI1/WT co-cultures.

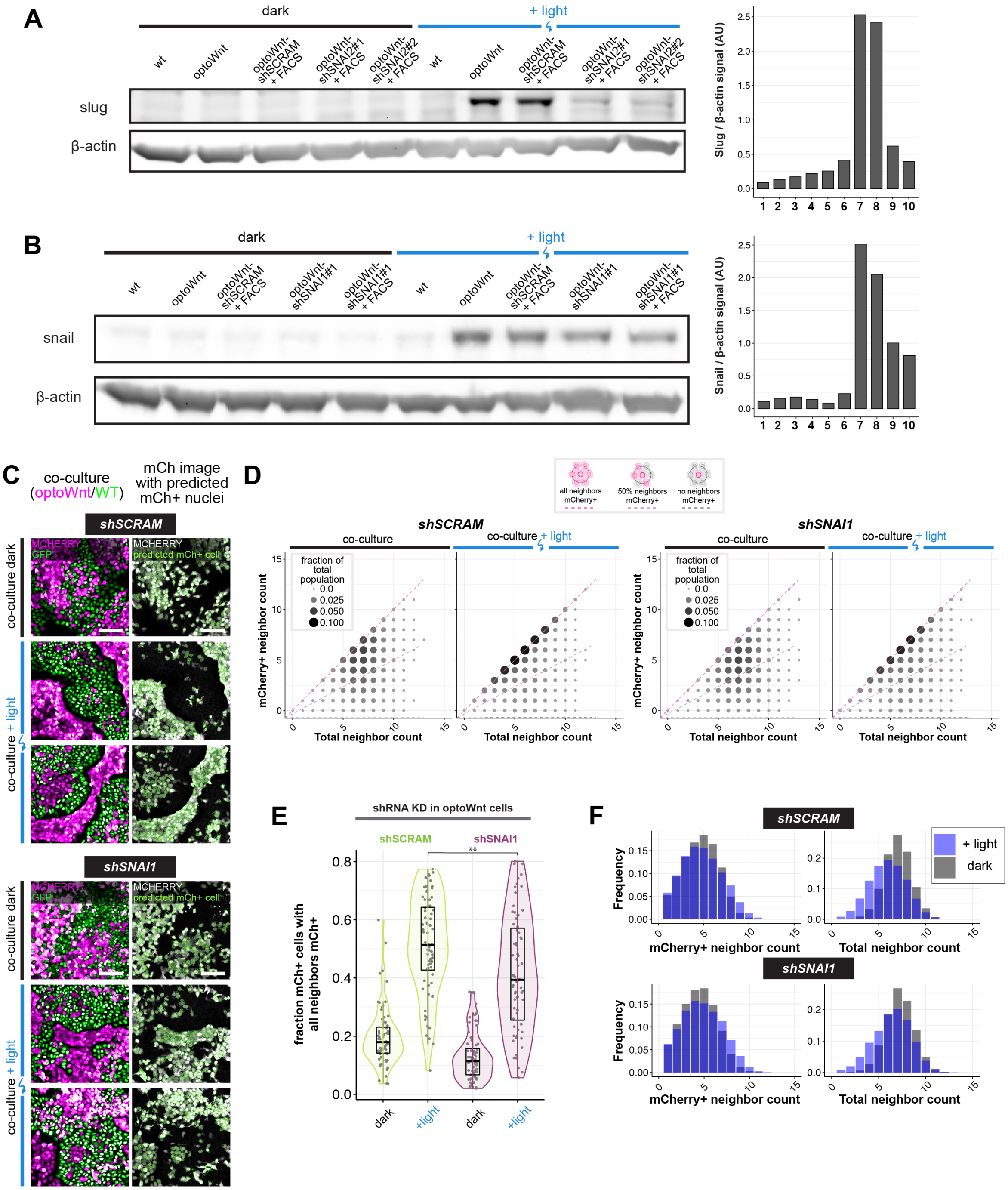

Figure 4.17: *See previous page for caption.*

4.3 Discussion

Amidst the signaling complexity of the early epiblast and ESC-based models for gastrulation, it has been difficult to tease out the signaling factors responsible for morphogenesis (*20*). Wnt signaling induces ESC differentiation and EMT (*52*, *55*, *62*), but whether this can direct the movement of cell subpopulations relative to one another, to generate an organized structure, is unknown. In this study, we combined genetic perturbation, optogenetic stimulation, and live-cell migration tracking to establish a model system for studying early human embryonic patterning. Through optogenetic control of canonical Wnt activity in subpopulations of hESCs, we show that cell-to-cell variation in Wnt signaling is sufficient for inducing cell self-organization and morphogenesis reminiscent of human gastrulation in an EMT-dependent manner.

As biological models become increasingly complex, there is an increased need for tools that can precisely and dynamically perturb a signal input. Previous methods rely on uniform addition of signal pathway agonists or inhibitors, which lack spatial control and are confounded by variations in molecule diffusion and receptor expression (*5*, *34*). This problem is particularly evident in previous ESC-based organoid or gastruloid models where spontaneous differentiation along heterogeneous cell lineages results in signaling and cell interactions that are poorly controlled (*21*, *26*). Microfluidics-based approaches can achieve intricate temporal control of morphogen signaling (*63*), but such approaches are limiting in their complexity and throughput. In contrast, optogenetics offers the ability to precisely control intracellular signaling pathways in space and time with light. Using engineered methods for optically shaping the illumination pattern, optogenetic control has been recently applied to several developmental systems and achieved spatiotemporal control of ERK signaling in the Drosophila embryo (*38*, *39*) and cell migration in the zebrafish embryo through non-canonical Wnt signaling (*42*). Our work extends the optogenetic toolkit to morphogen signaling in mammalian development. Rather than optically shaping the illumination pattern, we introduced subpopulations of optoWnt cells into WT cultures to act as local Wnt signaling hubs upon uniform illumination. By controlling the number or ratio of light-responsive cells in the co-culture, the spatial limits for local signaling density can be investigated. In the future, cell mixing could be combined with cell and light patterning techniques (*36*, *64*) to achieve intricate geometries and controlled positioning of cells.

Targeting Wnt activation in cell subpopulations allowed us to model several key processes of early embryonic development. First, light stimulation of co-cultures mimicked the presentation of Wnt ligand in the epiblast, which occurs prior to primitive streak formation (*9*, *65*, *66*). From studies of mouse embryogenesis and mESC model systems, Wnt signal induction from a localized source in extraembryonic tissue is thought to break anterior-posterior symmetry of the epiblast (*9*, *22*, *29*), though the source of Wnt signaling remains ambiguous (*65*, *66*). Alternatively, cell-to-cell variability in the early embryo could also sensitize certain cells to a signal input or elicit spontaneous emergence of collective cell behavior (*3*, *18*, *67*). Our hESC co-cultures model the latter scenario, where individual cells randomly mixed in a population are stimulated with a Wnt signal. That co-cultures are able to self-organize despite their initial salt-and-pepper distribution shows that even in the absence of directional cues, such as gradients of Wnt signaling, heterogeneous activation of Wnt is sufficient for self-organization and mesendoderm migration away from an epithelial cell population (Figure 4.15). Consequently, emergence of cell-to-cell heterogeneity in Wnt signaling may contribute to tissue organization. This result sheds light on the spontaneous and unexplained self-organization of ESC gastruloid models that occurs in the absence of a localized source of Wnt signaling (*21*, *26*, *27*). Our results suggest that such spontaneous self-organization can emerge from heterogeneous Wnt pathway activation, for example due to variable cell sensitivity to Wnt treatment. Indeed, it has been reported that within a population of ESCs, cells show heterogeneous β-catenin activity (*52*, *62*, *68*) and sensitivity to Wnt agonists (*52*), likely a result of inherent gene expression variability or asymmetries in the cell environments. In an embryonic context, epiblast cell heterogeneity is similarly present prior to primitive streak formation (*17*, *18*) and may thereby help ensure successful morphogenesis in response to a localized Wnt signal.

A second process that our optoWnt/WT co-culture system models is the emergence of a subpopulation of Bra-positive cells adjacent to a subpopulation of Bra-negative cells, mimicking the spatial arrangement of cells at the primitive streak. This model system thus allows studies of the cell-cell interactions and dynamic cell rearrangement between these two populations. Future work may explore the role of cell adhesion proteins in migration and segregation, given their known role in cell sorting (*6*, *7*) (*69*). In addition, the directionality of migration in the 3D spheroid cultures is consistent with the mouse embryo, where the lumenized epiblast forms a basal lamina on the outer surface of the spheroid through which the mesendoderm cells migrate (*57*). However, the absence of a second epithelial layer, equivalent to a hypoblast layer, allows optoWnt cells to continue migrating radially outward instead of becoming spatially confined as in mESC model systems that are bounded by extraembryonic tissues (*22*) or as in our 2D co-culture model that becomes bounded by cell density (Figure 4.7). Interestingly, since single-cell tracking showed no change in directionality of migration during 2D segregation, the directional migration in 3D cultures is likely a result of the organized epithelial cell polarity of spheroids and/or optoWnt cell interaction with the extracellular matrix. Furthermore, single-cell analysis revealed heterogeneity in optoWnt migration velocity (0.1-0.3 $\mu m min^{-1}$) in response to optoWnt signaling (Figure 4.17). In the mouse epiblast, cells display similarly heterogeneous migration speeds (*13*, *19*), with temporal order of migration through the streak and cell displacement correlating with cell fate outcome (*13*, *15*). Though migration speed heterogeneity in our co-culture models is anticipated due to different local cell densities and confinement in 2D culture, an intriguing developmental analogy could be the spatial patterning of mesoderm fates as cells migrate from the primitive streak to the mesodermal wings.

In conclusion, we establish a framework for studying tissue self-organization in early development through optogenetic control of Wnt signaling. As the mechanisms of cell patterning remain poorly understood, this model can be used for further studies of cell-cell interactions and intracellular regulation of cell polarity and migration. We propose that our optogenetic approach can be applied to a variety of stem cell models for mechanistic studies of Wnt signaling dynamics and spatiotemporal signaling thresholds, which would shed light on the ubiquitous Wnt-mediated tissue patterning in developmental and stem cell biology.

4.4 Methods

4.4.1 DNA vector assembly

All vectors were constructed using Gibson assembly or standard restriction enzyme cloning. Full sequences and descriptions of constructs used are provided in Supplementary Data. To make all the AAVS1-Pur-CAG-optoWnt plasmids, AAVS1-Pur-CAG-EGFP (Addgene plasmid # 80945) was digested with SalI and MluI and the Cry2-LRP6c construct, containing the photolyase homology region of the A. thaliana Cry2 protein (*45*), was inserted with standard restriction enzyme cloning. To generate β-catenin luciferase reporter lines, the 7xTFP vector (Addgene plasmid #24308) was modified to replace puromycin resistance with hygromycin resistance. To generate the Brachyury-2A-eGFP donor plasmid (manuscript under revision), DNA fragments of ∼2 kbp in length were PCR-amplified from the endogenous genomic T locus, before and after the stop codon, and were cloned into the OCT4-2A-eGFP donor plasmid (Addgene plasmid #31938). Two sgRNAs targeting at or near T stop codon (1: CACTGCATCTTTCGGGACCTGGG and 2: TGGCGACACAGGTGTCCATGAGG) were cloned into the CRISPR-GFP plasmid (*70*) via T4 ligation. To generate shRNA knockdown lines, shRNA sequences (Table S3) were subcloned into the pLKO.1 lentiviral expression vector digested with AgeI and EcoRI and modified to express the blastocydin resistance gene and eGFP.

4.4.2 hESC cell culture

For routine culture and maintenance, all optogenetic and WT hESC lines (H9, WiCell) (*30*) and iPSC lines (19-9-7, WiCell) (*71*) were grown on Matrigel (Corning, lot # 7268012, 7275006) coated plates in mTeSR1 medium (STEMCELL Technologies) and 1% penicillin / streptomycin (Life Technologies) at 37 °C and 5% CO2 with daily media changes. Optogenetic cells were cultured with hood lights off. For illumination experiments, cells were singularized with Accutase (STEMCELL Technologies) at 37 °C for 5 min and seeded onto Matrigel-coated 24-well plates in media containing 5 μM ROCK inhibitor Y-27632 (Selleckchem). Cells were seeded at a density of 35k – 70k cell cm-2. For co-culture experiments, WT and optoWnt cells were mixed in a 1:1 ratio and seeded at a density of 35k cell cm-2. After 20-24 hrs, media was changed to E8 (STEMCELL Technologies), E6 (ThermoFisher), or APEL 2 (STEMCELL Technologies) media without ROCK inhibitor and plates were placed onto LAVA illumination devices and subjected to experimental conditions (*49*). When indicated, Wnt agonist CHIR99021 (Stemgent) or recombinant Wnt3a protein (StemRD) was diluted in E8 media and added to cells. To generate 3D cell spheroids, hESCs (WT H9s and optoWnt cells) were passaged to single cell suspensions with Accutase. A 1:1 ratio of H9s and optoWnt cells in E8 media containing 10 μM ROCK inhibitor were added to PDMS inverse-pyramidal microwells to generate 250-cell aggregates (72). After overnight incubation, aggregates were dislodged from microwells by gentle pipetting. Aggregates were then resuspended in 100% Matrigel and 150 aggregates in 50 μL Matrigel were transferred to 24-well plates. After 10 minutes incubation at 37 °C, pre-warmed E8 was added to each well and exchanged every day for the remainder of the experiment.

4.4.3 Generation of hESC and iPSC cell lines

Clonal knock-in lines were generated through CRISPR/Cas9-mediated recombination. Prior to nucleofection, hESCs were pre-treated with 10 μM ROCK inhibitor for 3 to 4 hours or 5 μM Y27632 overnight. Accutase-digested single hESCs were collected and 2.5 - 3.5 million cells were nucleofected with 2.5 μg gRNA AAVS1-T2 (Addgene #41818), 4.5 μg pCas9-GFP (Addgene #44719), and 6 μg optoWnt donor plasmid in 200 μL room temperature PBS -/- using a NucleofectorTM 2b (Lonza) with program B-016. The resulting cells were plated onto Matrigel-coated 6-well plates containing 3 mL pre-warmed mTeSR1 with 10 μM ROCK inhibitor. Once the cells grew to confluency, they were subjected to selection with 1 $\mu g m L^{-1}$ puromycin in mTeSR1 media for approximately 2 weeks. Clonal lines were generated by picking single-cell clones into wells of a Matrigel-coated 96-well plate that were expanded for 1-2 weeks and subjected to PCR genotyping. As for the Bra-2A-eGFP reporter line, 3 μg T gRNA1, 3 μg T gRNA2 and 6 μg Bra-2A-eGFP donor plasmid were used. After the genotyping, targeted clone was treated with TAT-Cre to remove the PGK-PuroR cassette (manuscript under revision). Dual OptoWnt/Bra reporter lines were generated by CRISPR/Cas9-mediated knock-in of Cry2-LRP6c-2A-mCherry into the AAVS1 locus of Bra eGFP reporter cells, as described above.

Knock-in at the AAVS1 locus was verified through PCR on genomic DNA extracted with a Quick-DNA kit (D3024, Zymo Research). For the positive knock-in screen, a band size of 1.1kb was expected using F/R primers 5' CTGTTTCCCCTTCCCAGGCAGGTCC / 5' TCGTCGCGGGTGGCGAGGCGCACCG. For determination of zygocity, a band size of 0.2kb was expected for heterozygous clones using F/R primers 5' CGGTTAATGTGGCTCTGGTT / 5' GAGAGAGATGGCTCCAGGAA.

The β-catenin luciferase reporter lines were generated through lentiviral infection of WT and optoWnt hESCs with 7x TFP lentivirus packaged and purified from HEK 293T cells. Cells were infected with a multiplicity of infection less than 1 and selected with 50-100 $\mu g m L^{-1}$ hygromycin for three weeks. Knock-down lines were generated by lentiviral infection of optoWnt hESCs with shRNA against target genes (Table S3). Infected cells were isolated by FACS sorting for eGFP expression. Knock-down was verified through western blot for target genes.

4.4.4 Optogenetic stimulation

Cells were seeded on matrigel-coated 24-well plates (0030741021, Eppendorf, black-walled with 170μm coverglass bottom) and placed onto LAVA illumination devices kept in standard 37°C tissue culture incubators (*49*). In brief, user-defined illumination patterns were uploaded to the LAVA device for independent illumination control of each well. Unless otherwise noted, optogenetic stimulation was achieved with blue light emitted by arrays of 470nm LEDs continuously illuminating hESCs with 0.8 $\mu W mm^{-2}$ light for the duration of the experiment (1-48 hrs).

4.4.5 Immunostaining and imaging

For 2D cell cultures, cells were fixed with 3% paraformaldehyde (ThermoFisher) in PBS for 20 min at room temperature and subsequently washed three times with PBS, followed by blocking and permeabilization with 5% donkey serum (D9663, Sigma-Aldrich) and 0.3% Triton X-100 (Fisher Scientific) in PBS (PBS-DT) for 1 hour. Cells were incubated with primary antibodies (Table S2) at 4 °C overnight, then washed three times with PBS, and incubated with fluorescently conjugated secondary antibodies (Invitrogen) at 1:250 dilution for 1 hour at room temperature. Both primary and secondary antibodies were diluted in PBS-DT. Cells were washed with PBS and stained with 0.1 $\mu g mL^{-1}$ DAPI nuclear stain (ThermoFisher) prior to imaging. For 3D spheroid cultures, each incubation and wash step was performed overnight at 4 °C overnight to allow for diffusion through Matrigel.

Cell proliferation analysis with EdU was performed by treating cells with 10 μM EdU for 20 min prior to fixation. Staining for EdU was performed using a Click-iT EdU Alexa Fluor 647 kit (Invitrogen) following manufacturer specifications.

Confocal imaging was performed on a Perkin Elmer Opera Phenix system (QB3 High-Throughput Screening Facility). Brightfield and widefield fluorescence imaging was performed on a Zeiss AxioObserver epi-fluorescent microscope and a Molecular Devices Image Xpress Micro imaging system (CIRM/QB3 Shared Stem Cell Facility). Two-photon imaging of 3D spheroids was performed on a Zeiss LSM 780 AxioExaminer with a Spectra-Physics Mai Tai laser (CRL Molecular Imaging Center).

4.4.6 Live single-cell imaging and tracking

Co-cultures were treated with CellTracker Red (ThermoFisher) dye diluted 5,000x in mTeSR1 media for 15 min and washed two times. A sealing membrane (Breathe-Easy, Sigma-Aldrich) was applied to plates prior to imaging. Plates were imaged on a Molecular Devices Image Xpress Micro (IXM) imaging system with environmental control (37 °C, 5% CO2, and humidity control) using a 10x objective. For each experiment, 4-8 sites were imaged at 10-30 min intervals. For single-cell tracking experiments, cells were imaged at 18 min intervals. Optogenetic stimulation was delivered from the fluorescence light source (SOLA Light Engine, Lumencor) set to 5% intensity, passing through the 10x objective and GFP filter set

(472/30nm). Measured power at the sample was 2.82 mW. Optogenetic stimulation was delivered for 3 min at each site prior to imaging of each timepoint (i.e. for 3 min every 10-30 min) in a sequence of short light pulses (500 ms on-pulse, 10 s off-pulse).

Single-cell tracking analysis was performed as follows. To extract cell positions, each the contrast on each image was corrected using adaptive histogram equalization, then the image background was removed using a difference of gaussians filter. Peaks at least 20% above background in the resulting foreground image were then detected using non-local maximum suppression (*73*) with a minimum radius of 2.6 μm. The cell counts were then fit to an exponential model of cell growth, and frames with anomalous ($R^2 > 2500\ cells^2$) segmentations were discarded. This resulted in a dataset of individual cell detections in 5 fields of view spanning 90 frames between approximately hours 8 and 36 of the stimulation experiment.

Individual cell detections were linked to their nearest neighbor in a radius up to 32.4 μm from their previous position both forwards and backwards in time with both a global maximum velocity and neighborhood quasi-rigidity penalty (*74*). The resulting track fragments were then iteratively merged with overlapping tracks within 3.4 μm and 18 minutes of each other. This process converged after 10 iterations, generating 4,127 total tracks with mean length of 13.5 hours (standard deviation 6.4 hours). For each track, instantaneous velocity magnitude and direction were approximated using finite differences and then smoothed with a 15 point (4.5 hour) rolling window filter. Cell migration distance was calculated by integrating over finite differences of cell position. Track turning angle was calculated by phase unwrapping change in velocity direction. Finally, periods of persistent migration were determined as those times where a cell was both migrating at least 0.1 $\mu m min^{-1}$ and turning no more than 2 degrees/min from its previous velocity direction. Both changes in instantaneous traces and binned values were assessed based on 95% confidence intervals around the mean, as determined by 1000 iterations of bootstrap sampling.

4.4.7 Image analysis

Microscopy image processing, including stitching and z-slice projection, was performed in Fiji (*75*) and image quantification was performed in CellProfiler (*76*) with custom analysis pipelines detailed below.

For nuclear detection of β-catenin, nuclei stained with DAPI were identified and used to generate a binary mask applied to the β-catenin image channel. The mean β-catenin intensity per cell nucleus was calculated for each cell in a given field of view. A similar quantification strategy was adopted for quantification of percent positive cells for a given nuclearly-localized cell fate marker (e.g. BRA, SOX2, OCT4, NANOG) with a threshold defining 'positive' cells determined from signal intensity of negative controls (see Figure 4.4).

Quantification of cell segregation in 2D cultures was performed as follows. Nuclear outlines for all cells were identified using the DAPI channel images. Each nucleus was then classified as either mCherry positive or negative based on its mean mCherry nuclear intensity. For each mCherry-positive (mCh+) nucleus, the number of total nuclei and the number of mCh+ nuclei that neighbored the cell nucleus within a 15 μm expanded perimeter was calculated using the MeasureObjectNeighbors module in CellProfiler. The distribution of total neighbors vs. mCh+ neighbors was then plotted directly and was also used to calculate the neighbor fraction (i.e. mCh+ neighbors / total neighbors) for each mCh+ nucleus. Next, for each field of view (16-54 per biological replicate), the mCh+ cells whose neighbors were all mCh+ (i.e. neighbor fraction = 1) and who had more than 2 neighbors were counted and normalized to the total number of mCh+ cells in the field of view. This value, fraction mCh+ cells with all neighbors mCh+, was used as a metric for quantifying cell segregation. In a well-mixed population, a small fraction of cells should have a neighbor fraction equal to 1, whereas in a perfectly segregated population, all cells except those located at boundary edges should have a neighbor fraction equal to 1.

Radial quantification of cell distribution in 3D co-culture spheroids was performed in Matlab. First, the center of individual spheroid was calculated. From the center, the pixel intensity of the dsRed or mVenus signal, corresponding to the WT and optoWnt cells, respectively, was determined at 10μm intervals in the radial direction. Locally estimated scatterplot smoothing (Loess) was performed to smooth curves and peak dsRed and mVenus signal was determined by finding the maximum of these curves.

4.4.8 Luciferase assay

WT and β-catenin reporter hESCs were rinsed with PBS, lysed with lysis buffer (E1531, Promega), and centrifuged to pellet debris. Firefly luciferase expression was quantified by adding 100 μL Luciferase Assay Reagent (E1500, Promega) to wells of an opaque 96-well plate containing 20 μL lysate supernatant, with resulting luminescence immediately detected on a luminometer (SpectraMax, Molecular Devices). Luminescence intensity was normalized to total protein concentration (Pierce BCA protein assay, Thermo Scientific) to account for proliferation or seeding density variability between samples.

4.4.9 Flow cytometry and analysis

Cells were lifted with Accutase at 37 °C for 5 min, centrifuged, and resuspended in flow buffer (0.5% bovine serum albumin in PBS (w/v)) for analysis. Flow analysis and FACS sorting was performed on a BD Fortessa X20 or BD Aria cell sorter, respectively (CRL Flow Cytometry Facility). Cell counting for proliferation assays was performed using a ThermoFisher Attune (CIRM/QB3 Shared Stem Cell Facility) by measuring the number of cells per unit volume.

Data analysis was performed with FlowJo 10 software. To determine the fraction of BRA-eGFP+ cells after light treatment, gating was set such that less than 0.5% of undifferentiated WT hESCs were positive for eGFP or mCherry.

4.4.10 RNA extraction, reverse transcription, and qPCR

Cells were lifted with Accutase at 37 °C for 5 min, centrifuged, and resuspended in TRI reagent (Zymo Research). To achieve higher RNA yields, two to three wells were pooled, constituting a single biological replicate. RNA was purified using an RNA extraction kit (R2051, Zymo Research) as per manufacturer recommendations with an on-column DNase digestion to remove residual genomic DNA. After measurement of total RNA concentration, 1 μg of RNA was converted to cDNA using an iScript cDNA synthesis kit (Bio-Rad). Finally, 10 ng of cDNA was used for each SYBR Green qPCR reaction, run in 96-well plate format with a 0.1 μM final forward and reverse primer concentration (Table S3). qPCR was conducted for 50 cycles at an annealing temperature of 56 °C on a CFX Connect Real-Time PCR Detection System (Bio-Rad). A melt curve was generated at the end of the PCR reaction and a subset of reactions were run on a 1% agarose gel to ensure that only one product of the expected size was amplified per primer pair. qPCR analysis was conducted by the ddCt method. For each cDNA sample, gene expression was internally normalized to the expression of a human housekeeping gene (RPS18) run on the same qPCR plate. Next, for each gene, expression was normalized to the expression level of WT untreated hESCs. The log of relative expression over this WT control (i.e. log_2(fold change)) was graphed as a heatmap where color corresponds to mean value of biological replicates. The variability in gene expression was assessed with histogram graphs that show mean and standard deviation of fold change for 3 biological replicates, with at least 2 technical replicates for each biological replicate.

4.4.11 RNA sequencing and data analysis

RNA was purified as described above, with three biological replicates per experimental condition, and stored at -80 °C until library preparation. Library preparation, sequencing, and data pre-processing were performed by MedGenome Inc (Foster City, CA). In short, libraries were generated with the TruSeq Stranded mRNA Library Prep Kit (Illumina) and sequencing was performed on an Illumina HiSeq 4000 with a sequencing depth of ∼35-65 million aligned reads per sample. Quality of reads was evaluated using the FASTQC tool. Adapter trimming was performed using Fastq-mcf and Cutadapt, followed by contamination removal using Bowtie2. Paired-end reads were aligned to the reference human genome (GRCh38, Ensemble database) using STAR alignment software and raw read counts were estimated using HTSeq. Normalization and differential expression analysis were performed in DESeq2 (*77*). Genes with an adjusted P-value less than 0.05 and fold change greater than 2 were identified as differentially expressed genes (DEGs). PCA analysis, heatmaps, and volcano plots were generated in R. Unless otherwise stated, fold change in heatmaps was normalized to the WT unilluminated control and calculated using normalized read count + 1 values.

4.4.12 Western blotting

Cells were lysed in RIPA buffer (Sigma) with phosphatase and protease inhibitors (EMD Millipore). Protein content was measured by bicinchoninic acid (BCA) assay and used to normalize samples to the lowest concentration. Lysates were heated to 95 °C and run on a 4–12% Bis–Tris gel (Life Technologies) and transferred to a nitrocellulose membrane. Membranes were blocked in Odyssey blocking buffer (Li-Cor) and incubated with primary antibody at 4 °C overnight (Table S2). All membrane wash steps were performed using tris-buffered saline with 0.1% Tween-20. Membranes were incubated with secondary antibody, IRDye 800 goat anti-mouse IgG and IRDye 700 goat anti-rabbit IgG (Li-Cor), at a 1:10,000 dilution in blocking buffer for 1 hr at room temperature. Blot fluorescence was visualized using an Odyssey CLx system (Li-Cor) and quantified with the built-in gel analyzer tool in ImageJ.

4.4.13 Statistical analysis and graphing

Data are presented as mean ± 1 standard deviation (s.d.) unless otherwise specified. Statistical significance was determined by Student's t-test (two-tail) between two groups, and three or more groups were analyzed by one-way analysis of variance (ANOVA) followed by Tukey test. The unpaired two-samples Wilcoxon test was performed for data that was not normally distributed. $P < 0.05$ was considered statistically significant (NS $P>0.05$, $*P<0.05$, $**P<0.01$, $***P<0.001$). Statistical analysis and data plotting was performed in R.

References

1. Wennekamp, S., Mesecke, S., Nédélec, F. & Hiiragi, T. A self-organization framework for symmetry breaking in the mammalian embryo. *Nat. Rev. Mol. Cell Biol.* **14,** 452–459 (2013).
2. Eldar, A. & Elowitz, M. B. Functional roles for noise in genetic circuits. *Nature* **467,** 167–173 (2010).
3. Snijder, B. & Pelkmans, L. Origins of regulated cell-to-cell variability. *Nat. Rev. Mol. Cell Biol.* **12,** 119–125 (2011).
4. Arnold, S. J. & Robertson, E. J. Making a commitment: cell lineage allocation and axis patterning in the early mouse embryo. *Nat. Rev. Mol. Cell Biol.* **10,** 91–103 (2009).
5. Etoc, F. *et al.* A Balance between Secreted Inhibitors and Edge Sensing Controls Gastruloid Self-Organization. *Dev. Cell* **39,** 302–315 (2016).
6. Steinberg, M. S. & Takeichi, M. Experimental specification of cell sorting, tissue spreading, and specific spatial patterning by quantitative differences in cadherin expression. *Proceedings of the National Academy of Sciences* **91,** 206–209 (1994).
7. Lecuit, T. & Lenne, P.-F. Cell surface mechanics and the control of cell shape, tissue patterns and morphogenesis. *Nat. Rev. Mol. Cell Biol.* **8,** 633–644 (2007).
8. Liu, P. *et al.* Requirement for Wnt3 in vertebrate axis formation. *Nat. Genet.* **22,** 361–365 (1999).
9. Rivera-Pérez, J. A. & Magnuson, T. Primitive streak formation in mice is preceded by localized activation of Brachyury and Wnt3. *Developmental Biology* **288,** 363–371 (2005).
10. Lawson, K. A. *et al.* Bmp4 is required for the generation of primordial germ cells in the mouse embryo. *Genes Dev.* **13,** 424–436 (1999).
11. Brennan, J. *et al.* Nodal signalling in the epiblast patterns the early mouse embryo. *Nature* **411,** 965–969 (2001).
12. Ciruna, B. & Rossant, J. FGF signaling regulates mesoderm cell fate specification and morphogenetic movement at the primitive streak. *Dev. Cell* **1,** 37–49 (2001).
13. Saykali, B. *et al.* Distinct mesoderm migration phenotypes in extra-embryonic and embryonic regions of the early mouse embryo. *eLife* **8,** 91 (2019).
14. Dumortier, J. G., Martin, S., Meyer, D., Rosa, F. M. & David, N. B. Collective mesendoderm migration relies on an intrinsic directionality signal transmitted through cell contacts. *Proceedings of the National Academy of Sciences* **109,** 16945–16950 (2012).
15. Kinder, S. J. *et al.* The orderly allocation of mesodermal cells to the extraembryonic structures and the anteroposterior axis during gastrulation of the mouse embryo. *Development* **126,** 4691–4701 (1999).

16. Lawson, K. A., Meneses, J. J. & Pedersen, R. A. Clonal analysis of epiblast fate during germ layer formation in the mouse embryo. *Development* **113,** 891–911 (1991).

17. Scialdone, A. *et al.* Resolving early mesoderm diversification through single-cell expression profiling. *Nature* **535,** 289–293 (2016).

18. Mohammed, H. *et al.* Single-Cell Landscape of Transcriptional Heterogeneity and Cell Fate Decisions during Mouse Early Gastrulation. *Cell Rep* **20,** 1215–1228 (2017).

19. McDole, K. *et al.* In Toto Imaging and Reconstruction of Post-Implantation Mouse Development at the Single-Cell Level. *Cell* **175,** 859–876.e33 (2018).

20. Shahbazi, M. N. & Zernicka-Goetz, M. Deconstructing and reconstructing the mouse and human early embryo. *Nat. Cell Biol.* **20,** 878–887 (2018).

21. Beccari, L. *et al.* Multi-axial self-organization properties of mouse embryonic stem cells into gastruloids. *Nature* **5,** 277 (2018).

22. Sozen, B. *et al.* Self-assembly of embryonic and two extra-embryonic stem cell types into gastrulating embryo-like structures. *Nat. Cell Biol.* **20,** 979–989 (2018).

23. Rivron, N. C. *et al.* Blastocyst-like structures generated solely from stem cells. *Nature* **557,** 106–111 (2018).

24. Martin, G. R. Isolation of a pluripotent cell line from early mouse embryos cultured in medium conditioned by teratocarcinoma stem cells. *Proceedings of the National Academy of Sciences* **78,** 7634–7638 (1981).

25. Evans, M. J. & Kaufman, M. H. Establishment in culture of pluripotential cells from mouse embryos. *Nature* **292,** 154–156 (1981).

26. Ten Berge, D. *et al.* Wnt Signaling Mediates Self-Organization and Axis Formation in Embryoid Bodies. *Cell Stem Cell* **3,** 508–518 (2008).

27. Turner, D. A. *et al.* Anteroposterior polarity and elongation in the absence of extra-embryonic tissues and of spatially localised signalling in gastruloids: mammalian embryonic organoids. *Development* **144,** 3894–3906 (2017).

28. Van den Brink, S. C. *et al.* Symmetry breaking, germ layer specification and axial organisation in aggregates of mouse embryonic stem cells. *Development* **141,** 4231–4242 (2014).

29. Harrison, S. E., Sozen, B., Christodoulou, N., Kyprianou, C. & Zernicka-Goetz, M. Assembly of embryonic and extra-embryonic stem cells to mimic embryogenesis in vitro. *Science,* eaal1810 (2017).

30. Thomson, J. A. *et al.* Embryonic stem cell lines derived from human blastocysts. *Science* **282,** 1145–1147 (1998).

31. Warmflash, A., Sorre, B., Etoc, F., Siggia, E. D. & Brivanlou, A. H. A method to recapitulate early embryonic spatial patterning in human embryonic stem cells. *Nat. Methods* **11,** 847–854 (2014).

32. Martyn, I., Brivanlou, A. H. & Siggia, E. D. A wave of WNT signalling balanced by secreted inhibitors controls primitive streak formation in micropattern colonies of human embryonic stem cells. *Development,* dev.172791 (2019).

33. Martyn, I., Kanno, T. Y., Ruzo, A., Siggia, E. D. & Brivanlou, A. H. Self-organization of a human organizer by combined Wnt and Nodal signalling. *Nature* **558,** 132–135 (2018).

34. Carpenedo, R. L. *et al.* Homogeneous and organized differentiation within embryoid bodies induced by microsphere-mediated delivery of small molecules. *Biomaterials* **30,** 2507–2515 (2009).

35. Guillaume, B. *et al.* Geometrical confinement controls the asymmetric patterning of Brachyury in cultures of pluripotent cells. *Development,* dev.166025 (2018).

36. Repina, N. A., Rosenbloom, A., Mukherjee, A., Schaffer, D. V. & Kane, R. S. At Light Speed: Advances in Optogenetic Systems for Regulating Cell Signaling and Behavior. *Annual review of chemical and biomolecular engineering* **8,** 13–39 (2017).

37. Deisseroth, K. & Hegemann, P. The form and function of channelrhodopsin. *Stem cells and healthy aging.* **357,** eaan5544 (2017).

38. Johnson, H. E. *et al.* The Spatiotemporal Limits of Developmental Erk Signaling. *Dev. Cell* **40,** 185–192 (2017).

39. Johnson, H. E. & Toettcher, J. E. Signaling Dynamics Control Cell Fate in the Early Drosophila Embryo. *Dev. Cell* **48,** 361–370.e3 (2019).

40. Huang, A., Amourda, C., Zhang, S., Tolwinski, N. S. & Saunders, T. E. Decoding temporal interpretation of the morphogen Bicoid in the early Drosophila embryo. *eLife* **6,** 197 (2017).

41. Izquierdo, E., Quinkler, T. & De Renzis, S. Guided morphogenesis through optogenetic activation of Rho signalling during early Drosophila embryogenesis. *Nat Commun* **9,** 2366 (2018).

42. Čapek, D. *et al.* Light-activated Frizzled7 reveals a permissive role of non-canonical wnt signaling in mesendoderm cell migration. *eLife* **8,** 1025 (2019).

43. Sako, K. *et al.* Optogenetic Control of Nodal Signaling Reveals a Temporal Pattern of Nodal Signaling Regulating Cell Fate Specification during Gastrulation. *Cell Rep* **16,** 866–877 (2016).

44. Wang, X., He, L., Wu, Y. I., Hahn, K. M. & Montell, D. J. Light-mediated activation reveals a key role for Rac in collective guidance of cell movement in vivo. *Nat Cell Biol* **12,** 591–597 (2010).

45. Bugaj, L. J., Choksi, A. T., Mesuda, C. K., Kane, R. S. & Schaffer, D. V. Optogenetic protein clustering and signaling activation in mammalian cells. *Nat. Methods* **10,** 249–252 (2013).

46. Bilic, J. *et al.* Wnt induces LRP6 signalosomes and promotes dishevelled-dependent LRP6 phosphorylation. *Science* **316,** 1619–1622 (2007).

47. Clevers, H., Loh, K. M. & Nusse, R. Stem cell signaling. An integral program for tissue renewal and regeneration: Wnt signaling and stem cell control. *Science* **346,** 1248012–1248012 (2014).

48. Smith, J. R. *et al.* Robust, persistent transgene expression in human embryonic stem cells is achieved with AAVS1-targeted integration. *Stem Cells* **26,** 496–504 (2008).

49. Repina, N. A., McClave, T., Bao, X., Kane, R. S. & Schaffer, D. V. Engineered illumination devices for optogenetic control of cellular signaling dynamics. *bioRxiv* **8,** 675892 (2019).

50. Fuerer, C. & Nusse, R. Lentiviral Vectors to Probe and Manipulate the Wnt Signaling Pathway. *PLoS ONE* **5,** e9370 (2010).

51. Lindsley, R. C., Gill, J. G., Kyba, M., Murphy, T. L. & Murphy, K. M. Canonical Wnt signaling is required for development of embryonic stem cell-derived mesoderm. *Development* **133,** 3787–3796 (2006).

52. Davidson, K. C. *et al.* Wnt/β-catenin signaling promotes differentiation, not self-renewal, of human embryonic stem cells and is repressed by Oct4. *Proceedings of the National Academy of Sciences* **109,** 4485–4490 (2012).

53. Yamaguchi, T. P., Takada, S., Yoshikawa, Y., Wu, N. & McMahon, A. P. T (Brachyury) is a direct target of Wnt3a during paraxial mesoderm specification. *Genes Dev.* **13,** 3185–3190 (1999).

54. Arnold, S. J. *et al.* Brachyury is a target gene of the Wnt/β-catenin signaling pathway. *Mechanisms of Development* **91,** 249–258 (2000).

55. Sumi, T., Tsuneyoshi, N., Nakatsuji, N. & Suemori, H. Defining early lineage specification of human embryonic stem cells by the orchestrated balance of canonical Wnt/beta-catenin, Activin/Nodal and BMP signaling. *Development* **135,** 2969–2979 (2008).

56. Shahbazi, M. N. *et al.* Pluripotent state transitions coordinate morphogenesis in mouse and human embryos. *Nature* **552,** 239–243 (2017).

57. Williams, M., Burdsal, C., Periasamy, A., Lewandoski, M. & Sutherland, A. Mouse primitive streak forms in situ by initiation of epithelial to mesenchymal transition without migration of a cell population. *Developmental dynamics : an official publication of the American Association of Anatomists* **241,** 270–283 (2012).

58. Scarpa, E. & Mayor, R. Collective cell migration in development. *J. Cell Biol.* **212,** 143–155 (2016).

59. Huelsken, J. *et al.* Requirement for β-Catenin in Anterior-Posterior Axis Formation in Mice. *A light-triggered protein secretion system.* **148,** 567–578 (2000).

60. Carver, E. A., Jiang, R., Lan, Y., Oram, K. F. & Gridley, T. The mouse snail gene encodes a key regulator of the epithelial-mesenchymal transition. *Mol. Cell. Biol.* **21,** 8184–8188 (2001).

61. Jiang, R., Lan, Y., Norton, C. R., Sundberg, J. P. & Gridley, T. The Slug gene is not essential for mesoderm or neural crest development in mice. *Developmental Biology* **198,** 277–285 (1998).

62. Turner, D. A., Rué, P., Mackenzie, J. P., Davies, E. & Martinez Arias, A. Brachyury cooperates with Wnt/β-catenin signalling to elicit primitive-streak-like behaviour in differentiating mouse embryonic stem cells. *BMC Biol.* **12,** 63 (2014).

63. Sonnen, K. F. *et al.* Modulation of Phase Shift between Wnt and Notch Signaling Oscillations Controls Mesoderm Segmentation. *Cell* **172,** 1079–1090.e12 (2018).

64. Chen, S. *et al.* Interrogating cellular fate decisions with high-throughput arrays of multiplexed cellular communities. *Interrogating cellular fate decisions with high-throughput arrays of multiplexed cellular communities* **7,** 10309 (2016).

65. Yoon, Y. *et al.* Extra-embryonic Wnt3 regulates the establishment of the primitive streak in mice. *Developmental Biology* **403,** 80–88 (2015).

66. Tortelote, G. G. *et al.* Wnt3 function in the epiblast is required for the maintenance but not the initiation of gastrulation in mice. *Developmental Biology* **374,** 164–173 (2013).

67. Dietrich, J.-E. & Hiiragi, T. Stochastic patterning in the mouse pre-implantation embryo. *Development* **134,** 4219–4231 (2007).

68. Blauwkamp, T. A., Nigam, S., Ardehali, R., Weissman, I. L. & Nusse, R. Endogenous Wnt signalling in human embryonic stem cells generates an equilibrium of distinct lineage-specified progenitors. *Nat Commun* **3,** 1070 (2012).

69. Libby, A. R. *et al.* Spatiotemporal mosaic self-patterning of pluripotent stem cells using CRISPR interference. *eLife* **7,** 3731 (2018).

70. Bao, X. *et al.* Long-term self-renewing human epicardial cells generated from pluripotent stem cells under defined xeno-free conditions. *Nature Biomedical Engineering* **1,** 0003 (2016).

71. Yu, J. *et al.* Human induced pluripotent stem cells free of vector and transgene sequences. *Science* **324,** 797–801 (2009).

72. Hookway, T. A., Butts, J. C., Lee, E., Tang, H. & McDevitt, T. C. Aggregate formation and suspension culture of human pluripotent stem cells and differentiated progeny. *Methods* **101,** 11–20 (2016).

73. Van der Walt, S. *et al.* scikit-image: image processing in Python. *PeerJ* **2,** e453 (2014).

74. Kim, H.-B. & Lee, S.-J. Performance improvement of two-frame particle tracking velocimetry using a hybrid adaptive scheme. *Measurement Science and Technology* **13,** 573–582 (2002).

75. Schindelin, J. *et al.* Fiji: an open-source platform for biological-image analysis. *Nat. Methods* **9,** 676–682 (2012).
76. Carpenter, A. E. *et al.* CellProfiler: image analysis software for identifying and quantifying cell phenotypes. *Genome biology* **7,** R100 (2006).
77. Love, M. I., Huber, W. & Anders, S. Moderated estimation of fold change and dispersion for RNA-seq data with DESeq2. *Genome biology* **15,** 550 (2014).

Chapter 5

Conclusion and future directions

In this dissertation, we sought to address the critical need for tools that control the location and timing of morphogen signaling in stem cell-based models for embryonic development. We used the optoWnt optogenetic system, which relies on light-induced photosensor oligomerization, to induce Wnt/β-catenin morphogen signaling in human embryonic stem cells. In parallel, we engineered two photostimulation technologies to activate signaling in hESC cultures with patterns of light: (1) LAVA boards, which allow high-throughput activation of multiwell plates with programmable intensity, temporal, and spatial patterns and (2) the opto-SIM microscope, which allows high-resolution and dynamic photostimulation and simultaneous fluorescence imaging. Using these engineered systems, we show that optoWnt activation in subpopulations of hESCs is sufficient for cell self-organization and morphogenesis. We thus create a platform for studying the signaling dynamics of Wnt-mediated cell fate commitment during early embryonic development.

Future work will continue to investigate the molecular mechanisms and cell-cell interactions that govern such Wnt-mediated cell self-organization. As one exciting direction, we posited that activated optoWnt cells may pattern the fate of their neighbors. Transcriptomic analysis showed that optogenetic stimulation induced downstream expression of morphogens such as BMP, Wnt, and FGF agonists and antagonists that may signal to neighboring cells through paracrine signals (Figure 5.1A). To determine whether neighboring hESCs are affected by such signaling from optoWnt cells, we performed global RNA sequencing analysis to detect any transcriptional changes between hESCs grown in monoculture vs. hESCs grown in co-culture with optoWnt cells (Figure 5.1B). After co-culture and self-segregation of the two cell populations, we performed FACS sorting to separate the optoWnt and wild-type (WT) hESCs for RNA sequencing (Figure 5.1C). Sequencing results showed that WT cells grown in co-culture with optoWnt cells had signficant transcriptomic changes. Principal component analysis (PCA) showed clustering of biological triplicates for each condition and a shift of the $WT^{cocult} + light$ population away from all other WT conditions (Figure 5.2A). Gene expression analysis revealed that this $WT^{cocult} + light$ population expressed genes such as T, EOMES, and WNT (Figure 5.2B). Further analysis with the gene clustering software IPA and GSEA identified that the TGFβ pathways was strongly upregulated in this population (Figure 5.2C). We hypothesized that hallmarks of the TGFβ pathway could be induced from secreted BMP or Nodal/TGFβ from illuminated optoWnt cells. To validate RNA sequencing results on a protein level, and to probe for postranslational protein modification, we performed immunostainining for phosphorylated SMAD proteins in 2D culture, which are downstream signal targets of TFGβ signaling. Indeed, we saw that in co-cultures kept in the dark, WT cells did not express phospho-SMAD 1/5, whereas upon illumination both the optoWnt and WT populations showed strong fluorescence staining (Figure 5.2D). These results confirm that differentiating mesendoderm cells can signal to the neighboring epiblast cells to the pattern their cell fate. In the future, we will extend such studies to 3D hESC cultures and use pathway inhibitors to identify the specific molecular signals responsible for the observed patterning and TGFβ signal induction. We hypothesize that these findings may identify novel mechanisms for tissue patterning during early human gastrulation.

In the future, biological studies that similarly take advantage of specific targeting of cell subpopulations and/or signal dynamics can be extended to other tissue types and organisms. Varying Wnt signal intensities can, for example, drive dose-dependent or divergent lineage specification during neural fate commitment (*1, 2*), hematopoiesis (*3*), and mesoderm differentiation (*4, 5*). Wnt signaling also plays key roles in regulating intestinal development (*6*), cardiac differentiation (*7–9*), and neural tube patterning (*10, 11*). Thus, tissue patterning and Wnt signal dynamics can be readily studied in a variety of organoid and stem-cell based model systems using the optoWnt system and in combination with our engineering photostimulation technologies.

As our methods for controlling cell signaling and performing single-cell analysis become more sophisticated, so can the questions we begin to ask. Optogenetic studies can be combined with advanced imaging techniques, such as lightsheet microscopy (*12–14*), SIM imaging (*15, 16*), or single-particle tracking (*17*) to gain mechanistic insight of cell-cell interactions and transcriptional regulation. An exciting application of such studies is in the *in vivo* embryo, where photostimulation with spatially-varying light patterns can be used to mimic and perturb Wnt signaling in specific cell populations. Such work could elucidate the role of Wnt signaling from extraembryonic tissues, the mechanisms of Wnt signal propagation through the tissue, and non-cell-autonomous fate patterning. Lastly, subcellular control of signaling will allow intricate studies of duration, intensity, and spatial thresholds for Wnt-mediated asymmetric division (*18*). The combination of optogenetics, imaging, and developmental biology holds a promising future for expanding our understanding of early embryogenesis.

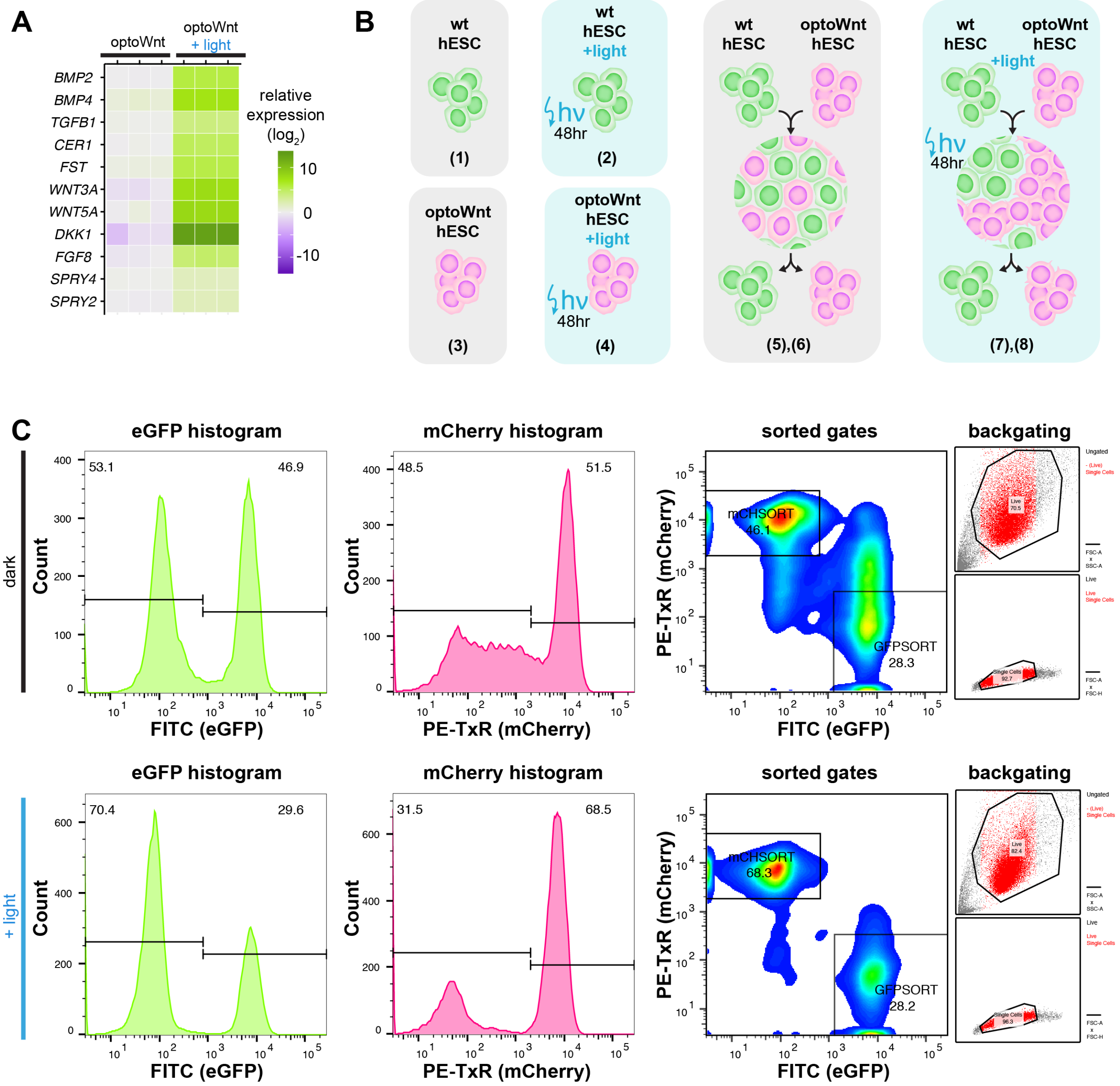

Figure 5.1: **RNA sequencing study design to determine whether WT hESCs are patterned by Wnt-activated mesendoderm cells**

A) RNA sequencing results from optoWnt monocultures show morphogen upregulation upon illumination. **B)** Schematic of RNA sequencing study design. **C)** Flow cytometry of co-cultures kept in the dark (top row) or after 48 hrs of illumination (bottom row) show separation of the two populations: WT hESCs (GFP+) and optoWnt hESCs (mCherry+).

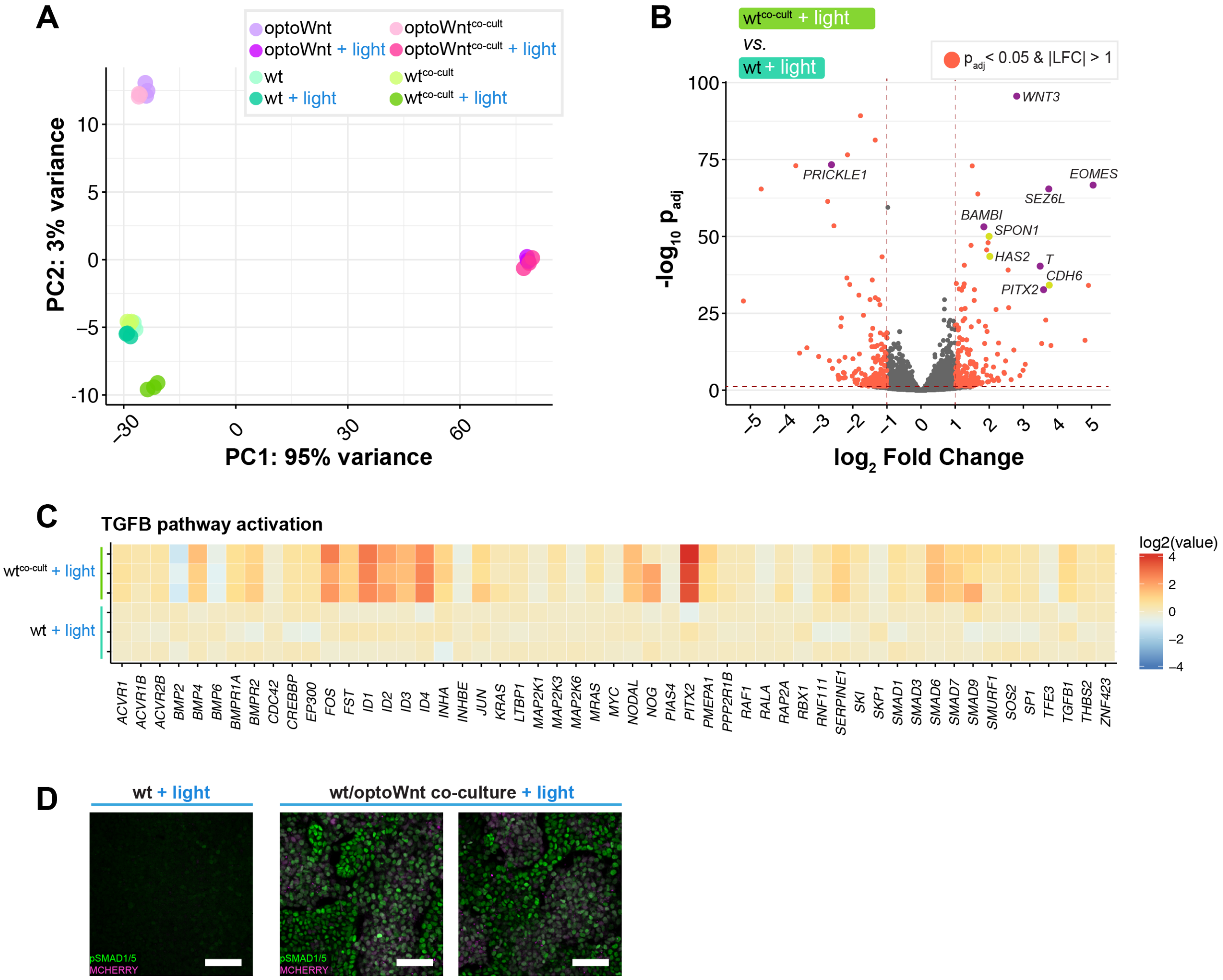

Figure 5.2: **OptoWnt cells pattern WT hESCs in co-culture**
A) PCA of RNA-seq results. Colors designate the eight experimental conditions. Each point is a biological replicate. **B)** Volcano plot of RNA-seq differential expression analysis, with DEGs (adjusted p-value < 0.05 and log_2 fold change > 1) highlighted red. Plot shows WT monocolture cells compared to WT cells in co-culture with optoWnt cells. **C)** Heatmap of TGFβ pathway hallmark gene expression. Biological triplicates displayed for each experimental condition. **D)** Sample immunostaining images for phospho-SMAD1/5 (green). mCherry fluorescence (magenta) marks optoWnt cells.

References

1. Kirkeby, A. *et al.* Generation of regionally specified neural progenitors and functional neurons from human embryonic stem cells under defined conditions. *Cell Rep* **1,** 703–714 (2012).
2. Kiecker, C. & Niehrs, C. A morphogen gradient of Wnt/beta-catenin signalling regulates anteroposterior neural patterning in Xenopus. *Development* **128,** 4189–4201 (2001).
3. Luis, T. C. *et al.* Canonical wnt signaling regulates hematopoiesis in a dosage-dependent fashion. *Cell Stem Cell* **9,** 345–356 (2011).
4. Davidson, K. C. *et al.* Wnt/β-catenin signaling promotes differentiation, not self-renewal, of human embryonic stem cells and is repressed by Oct4. *Proceedings of the National Academy of Sciences* **109,** 4485–4490 (2012).
5. Kempf, H. *et al.* Bulk cell density and Wnt/TGFbeta signalling regulate mesendodermal patterning of human pluripotent stem cells. *Nat Commun* **7,** 13602 (2016).
6. Clevers, H. Modeling Development and Disease with Organoids. *Cell* **165,** 1586–1597 (2016).
7. Bao, X. *et al.* Long-term self-renewing human epicardial cells generated from pluripotent stem cells under defined xeno-free conditions. *Nature Biomedical Engineering* **1,** 0003 (2016).
8. Lian, X. *et al.* Robust Cardiomyocyte Differentiation from Human Pluripotent Stem Cells via Temporal Modulation of Canonical Wnt Signaling. *Proceedings of the National Academy of Sciences* **109,** E1848–E1857 (2012).
9. Lian, X. *et al.* Directed Cardiomyocyte Differentiation from Human Pluripotent Stem Cells by Modulating Wnt/β-Catenin Signaling under Fully Defined Conditions. *Nature Protocols* **8,** 162–175 (2013).
10. Mulligan, K. A. & Cheyette, B. N. R. Wnt Signaling in Vertebrate Neural Development and Function. *Journal of neuroimmune pharmacology : the official journal of the Society on NeuroImmune Pharmacology* **7,** 774–787 (2012).
11. Ikeya, M. & Takada, S. Wnt Signaling from the Dorsal Neural Tube Is Required for the Formation of the Medial Dermomyotome. *Development (Cambridge, England)* **125,** 4969–4976 (1998).
12. McDole, K. *et al.* In Toto Imaging and Reconstruction of Post-Implantation Mouse Development at the Single-Cell Level. *Cell* **175,** 859–876.e33 (2018).
13. Huisken, J., Swoger, J., Del Bene, F., Wittbrodt, J. & Stelzer, E. H. K. Optical Sectioning Deep inside Live Embryos by Selective Plane Illumination Microscopy. *Science (New York, N.Y.)* **305,** 1007–1009 (2004).

14. Keller, P. J., Schmidt, A. D., Wittbrodt, J. & Stelzer, E. H. K. Reconstruction of Zebrafish Early Embryonic Development by Scanned Light Sheet Microscopy. *Science (New York, N.Y.)* **322,** 1065–1069 (2008).

15. Gustafsson, M. G. L. Surpassing the Lateral Resolution Limit by a Factor of Two Using Structured Illumination Microscopy. *Journal of Microscopy* **198,** 82–87 (2000).

16. Gustafsson, M. G. L. *et al.* Three-Dimensional Resolution Doubling in Wide-Field Fluorescence Microscopy by Structured Illumination. *Biophysical Journal* **94,** 4957–4970 (2008).

17. Liu, Z., Lavis, L. D. & Betzig, E. Imaging Live-Cell Dynamics and Structure at the Single-Molecule Level. *Molecular Cell* **58,** 644–659 (2015).

18. Loh, K. M., van Amerongen, R. & Nusse, R. Generating Cellular Diversity and Spatial Form: Wnt Signaling and the Evolution of Multicellular Animals. *Dev. Cell* **38,** 643–655 (2016).